

DEVELOPMENT OF A CYCLONE RICE DRYER

by

Pracha Bunyawanichakul

B.Eng, Kasetsart University; M.Eng, AIT Thailand

School of Engineering

Submitted in fulfillment of the requirement for the degree of

Doctor of Philosophy



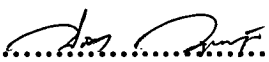
University of Tasmania

Faculty of Science, Engineering and Technology

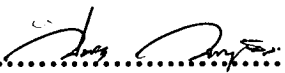
September 2006

Signed Statements

This work contains no material which has been accepted for the award of any other degree or diploma in any University or other institution and, to the best of my knowledge and belief, contains no material previously published or written by another person, excepted where due reference has been made in the text.

Signed.....Date.....28/09/06.....
Pracha Bunyawanicakul Revised 19/09/07

This thesis may be made available for loan and limited copying in accordance with the Copyright Act 1968

Signed.....Date.....28/09/06.....
Pracha Bunyawanicakul Revised 19/09/07

ABSTRACT

This thesis evaluates the suitability of a cyclone dryer for the drying of paddy (rice grain). The design aim is to reduce the moisture content of paddy from a fresh harvest level of 33% dry-basis to a more manageable level of 22% of dry basis, and to replace all classical methods of drying. The cyclone dryer consists of a cylindrical tower containing a series of inverted conical baffles with central orifices that divide the tower into chambers. The moist particulate matter is fed into a stream of hot, dry air which enters tangentially at the base of the tower, creating a rotating flow within the dryer. The central vortex and through-flow jet transport the particles upwards from chamber to chamber until discharged tangentially at the top. Recirculation of flow within the chambers lengthens the particle residence time

Single-phase numerical calculations with the commercial RANS-based Computational Fluid Dynamics (CFD) code CFX 5.7 are used for flow field and pressure drop predictions. Experimental observations in a small scale laboratory model are used for validation. Useful descriptions of the axial and tangential velocity distributions are obtained, and the pressure drop across the cyclone dryer chamber is predicted to about 20% accuracy.

Particle residence time in the laboratory model cyclone dryer is measured by the pulse tracer stimulus response technique. Observations using paddy grain and spherical silica gel particles show the mean residence time to vary quadratically with particle concentration. The residence time distribution (RTD) is explained well by a tank-in-series model. Numerical predictions of particle residence time obtained from one-way coupled particle transport modelling without particle dispersion using a Lagrangian/Eulerian approach produce RTDs differing significantly from the experimental observations. However, the trends of mean residence time variations in response to changes in inlet air velocity and number of cyclone chambers are correctly predicted.

Single-pass drying tests with paddy grain demonstrate maximum moisture reductions of 2.6-6.5% dry-basis obtained at inlet air temperatures of 82-89 °C and paddy grain feed rate of 0.03 kg/s. The specific energy consumption (SPEC) varies between 7.5-20.5 MJ/kg of water evaporated, depending on the initial moisture content of paddy grain. Compared with fluidised bed and spouted bed paddy dryers employing 50-70% exhaust air recycling, the cyclone dryer gives a lower moisture reduction and a higher SPEC. This indicates that practical application of the model-scale cyclone dryer would require multi-pass operation with exhaust air recycling to be sufficiently economic.

Multi-pass laboratory tests show three-pass drying in a four-chamber cyclone dryer with inlet air temperature of about 80°C and 0.03 kg/s paddy grain feed rate to reduce the moisture content of paddy grain by about 11% dry-basis, with an SPEC of 13 MJ/kg of water evaporated. Recycling about 90% of the air would give a 70-75% reduction in SPEC compared to non-recycled air operation, and 3.5-4 MJ/kg water evaporated. This is comparable to fluidised bed paddy dryer operation for similar initial moisture content of the paddy grain.

Numerical simulations of silica gel particle drying based on two-way coupled particle transport modelling with a Lagrangian/Eulerian approach are also reported. The simulations consistently overpredict the moisture and heat transfer observed experimentally using silica gel particle 3.25 mm in average diameter. As the mean particle residence time was underpredicted, it is concluded that the water evaporation model used here gives a much higher moisture transfer rate than that observed experimentally.

Computational studies of the increase in residence time with geometric scale-up of the dryer indicate that a commercial scale unit small enough to be field portable could achieve the desired moisture reduction of paddy grain with single pass operation.

Acknowledgements

The author wishes to express his sincere appreciation and gratitude to his supervisor, Dr. Greg Walker, for his guidance, encouragement and advice throughout the duration of his study and research. Grateful thanks are also due to his co-supervisors, Dr. Michael Kirkpatrick and Dr. Jane Sargison for their valuable suggestions, advice and great support. Thanks for kind help and suggestions on CFX techniques from Dr. Alan Henderson. Sincere thanks are extended to the initial-supervisor, Associate Professor Dr. Peter Doe for his suggestions and advice on the pneumatic drying studies. Special thank for Dr. Neville Mendham, for his advice on the paddy supply source. The author wishes to acknowledge and thank his scholarship provider, Srinakharinwirot University, for all the support which enabled him to complete the Ph.D at University of Tasmania (UTAS). The support of ANSYS Inc. for the CFX academic software licence is gratefully acknowledged.

He is most grateful to technical staff of the School of Engineering, UTAS for assistance in making available facilities needed in conducting experiments. Thanks also to Mr. Ron Burton, Production Manager, Sunrice Leeton Mill, for kindly supplying paddy for the experiments. His deep gratitude is extended to Ms. Diane Smith, Senior International Student Advisor, UTAS for her kind assistance during the time spent in Tasmania.

The author would like to express deep appreciation to Mr. Setta Sadsananan, his colleague, for all special help, support and advice. Sincere appreciation is extended to all of his colleagues from Srinakharinwirot University: Dr. Tossapol Kietchareanpol, Mr. Chainarong Klaimanee, Mr. Siradej Chartniyom, Miss Pilada Wangpanich and Mr. Chanchai Thaijiem. Many thanks to fellow post graduate student Tzuu Bin Ng for his help and discussion.

Above all, the author extends his deep love to his lovely family for their help and support throughout this study. Finally, the author wishes to dedicate this work to his beloved mom who passed away in 2001, one year before he started study at UTAS.

Supporting Publications

Bunyawanchakul, P., Kirkpatrick, M.P., Sargison, J.E. and Walker, G.J., 2006, *Numerical and experimental studies of the flow field in a cyclone dryer*. ASME Journal of Fluids Engineering, Vol. 28(6), pp.1240-1250.

Bunyawanchakul, P., Sargison, J.E. and Walker, G.J., 2007, *Modelling and simulation of paddy (rice) drying in a simple pneumatic dryer*. Biosystems Engineering, Vol. 96(3), pp. 335-344.

Bunyawanchakul, P., Kirkpatrick, M.P., Sargison, J.E. and Walker, G.J. *A three-dimensional simulation of a cyclone dryer*. CFD 2006 the 5th International Conference on Computational Fluid Dynamics in Industrial Processes, Melbourne, Australia, 13-15 December 2006, CD ROM, 10 pp.

Table of Contents

<i>Signed Statements</i>	<i>i</i>
<i>Abstract</i>	<i>ii</i>
<i>Acknowledgements</i>	<i>iv</i>
<i>Supporting Publications</i>	<i>v</i>
<i>Table of Contents</i>	<i>vi</i>
<i>List of Figures</i>	<i>xii</i>
<i>List of Tables</i>	<i>xix</i>
<i>List of Symbols</i>	<i>xx</i>
 Chapter 1 INTRODUCTION	 1
1.1 NEED.....	1
1.2 PROCESS.....	1
1.3 CURRENT METHODS.....	2
1.4 PROBLEMS WITH CURRENT METHODS.....	3
1.5 TARGET USERS.....	3
1.6 THESIS OUTLINE.....	4
 Chapter 2 OVERVIEW OF PADDY DRYING IN THAILAND	 6
2.1 INTRODUCTION AND DEFINITION.....	6
2.1.1 Fixed Bed Dryers.....	7
2.1.2 Moving Bed Dryers.....	7
2.1.3 Boiling Bed Dryers.....	7
2.1.4 Suspension Bed Dryers.....	7
2.2 BACKGROUND AND DEVELOPMENT.....	8
2.2.1 Batch Type Paddy Dryers.....	9
2.2.2 Solar Paddy Dryer.....	9
2.2.3 Rotary Paddy Dryer.....	15
2.2.4 Mixed Flow Paddy Dryer.....	17
2.2.5 Fluidised Bed Paddy Dryer.....	18
2.2.6 Spouted Bed Paddy Dryer.....	23
2.3 COMMERCIAL PADDY DRYERS.....	24
2.4 EFFECT OF OPERATING PARAMETERS ON RICE QUALITY.....	28

2.5 POTENTIAL TECHNOLOGY FOR PADDY DRYING.....	37
<i>Chapter 3 MATHEMATICAL MODEL FOR PADDY DRYING IN A SIMPLE PNEUMATIC DRYER.....</i>	<i>40</i>
3.1 INTRODUCTION.....	40
3.2 PNEUMATIC DRYER.....	41
3.3 THEORETICAL MODEL DEVELOPMENT.....	43
3.4 SOLUTION TECHNIQUE.....	48
3.5 SIMULATION RESULTS.....	50
3.5.1 Introduction.....	50
3.5.2 Effect of Dryer Diameter on Moisture and Temperature of Air and Paddy.....	51
3.5.3 Effect of Paddy Feed Rate on Moisture and Temperature of Air and Paddy....	52
3.5.4 Effect of Inlet Air on Moisture and Temperature of Air and Paddy.....	56
3.6 DISCUSSION AND EVALUATION OF THE PNEUMATIC DRYER FOR PADDY DRYING.....	57
3.7 CONCLUSIONS.....	59
<i>Chapter 4 CYCLONE TECHNOLOGY FOR GRAIN DRYING.....</i>	<i>62</i>
4.1 INTRODUCTION.....	62
4.2 CYCLONE SEPARATOR.....	63
4.2.1 Flow Behaviour.....	63
4.2.2 Particle Terminal Velocity.....	66
4.2.3 Particle Deposition Velocity.....	67
4.3 THE WORKING PRINCIPLE OF A CYCLONE DRYER.....	68
4.4 CYCLONE DRYER APPARATUS DESIGN AND DEVELOPMENT.....	69
4.4.1 Outline and Basic Assumptions.....	69
4.4.2 Drying Chamber.....	71
4.4.3 Blower Selection.....	73
4.4.4 Rated Capacity of Heater.....	73
4.4.5 Separation Chamber.....	74
4.5 PRELIMINARY-STUDY OF CYCLONE DRYER.....	75
4.5.1 Introduction	75
4.4.1 Effect of Velocity on Cyclone Dryer Pressure Drop	75
4.4.2 Flow Characteristics of Grain Inside Cyclone Dryer and Minimum Working Velocity.....	76
4.6 CONCLUDING REMARKS.....	78

Chapter 5 CYCLONE DRYER FLOW FIELD: EXPERIMENTAL AND NUMERICAL STUDIES.....	76
5.1 INTRODUCTION.....	79
5.2 EXPERIMENTAL INVESTIGATIONS.....	82
5.2.1 Flow Geometry and Physical Model.....	82
5.2.2 Measurement Techniques.....	83
5.2.3 Experimental Results.....	86
5.3 NUMERICAL SIMULATION AND VALIDATION.....	88
5.3.1 Basic Governing Equations.....	88
5.3.1.1 Two-equation turbulence model.....	89
5.3.1.1 Reynolds stress turbulence model.....	90
5.3.2 Numerical Set-up and Solution Technique.....	92
5.3.3 Simulation Results and Validation.....	93
5.3.3.1 Advection (differencing) scheme.....	95
5.3.3.2 Grid sensitivity.....	98
5.3.3.3 Turbulence model.....	103
5.3.3.4 Optimised numerical model.....	108
5.4 NUMERICAL PREDICTIONS.....	108
5.4.1 Effect of Inlet Air Velocity.....	108
5.4.2 Effect of Number of Chambers.....	113
5.5 CONCLUSIONS.....	117
Chapter 6 SOLID-GAS FLOW BEHAVIOUR AND PARTICLE RESIDENCE TIME DISTRIBUTION OF A CYCLONE DRYER.	119
6.1 INTRODUCTION.....	119
6.2 RESIDENCE TIME DISTRIBUTION (RTD) OF PARTICLES IN A CYCLONE DRYER.....	122
6.2.1 RTD Theory.....	123
6.2.2 Experimental Evaluation of RTD.....	125
6.2.3 RTD Modelling for Non-Ideal Flow.....	126
6.2.3.1 Dispersion model.....	126
6.2.3.2 Tank-in-Series model.....	127
6.3 EXPERIMENTAL INVESTIGATION.....	127
6.3.1 Experimental Set-up.....	129
6.3.1.1 Intake system.....	129
6.3.1.2 Particle feeder.....	129

6.3.1.3 Cyclone dryer chamber.....	130
6.3.1.4 Separation chamber.....	131
6.3.2 Experimental Procedure.....	132
6.3.3 Experimental Results.....	132
6.3.3.1 Effect of inlet air velocity.....	135
6.3.3.2 Effect of particle feed rate.....	135
6.3.3.3 Effect of number of cyclone chambers.....	138
6.3.3.4 Effect of particle density.....	138
6.3.3.5 Comparison with ideal flow models.....	140
6.4 NUMERICAL SIMULATION.....	143
6.4.1 Mathematical Modelling.....	143
6.4.2 Numerical Procedure.....	144
6.4.3 Numerical Results.....	145
6.4.3.1 Effect of turbulent dispersion model.....	145
6.4.3.2 Comparison of numerical residence time predictions with experimental results.....	147
6.5 CONCLUSIONS.....	151

***Chapter 7 EXPERIMENTAL AND NUMERICAL STUDIES OF CYCLONE
DRYER PERFORMANCE..... 155***

7.1 INTRODUCTION.....	155
7.2 EXPERIMENTAL STUDIES.....	158
7.2.1 Experimental Apparatus and Instrumentation.....	158
7.2.2 Experimental Procedure.....	159
7.2.3 Experimental Heat and Mass Transfer.....	160
7.2.4 Results and Discussion.....	162
7.2.4.1 Moisture reduction.....	162
7.2.4.2 Heat transfer.....	163
7.2.4.3 Mass transfer.....	171
7.2.4.4 Specific energy consumption.....	175
7.2.4.5 Summary of experimental results for single pass drying and comparison with other paddy dryers.....	180
7.2.5 Strategy for Paddy Drying with the Model Cyclone Dryer.....	183
7.2.5.1 Characteristics of multi-pass drying in the model dryer.....	183
7.2.5.2 Predicted effect of air recycling.....	185
7.2.5.3 Summary of paddy drying strategy in the model scale cyclone dryer.....	187

7.3 NUMERICAL STUDIES.....	189
7.3.1 Mathematical Model.....	190
7.3.1.1 Governing conservation equations for the continuous phase.....	190
7.3.1.2 Governing equations for the dispersed phase.....	191
7.3.1.3 Heat and mass transfer.....	191
7.3.2 Modelling Set-up.....	192
7.3.3 Simulation Results.....	193
7.3.3.1 Particle trajectories.....	194
7.3.3.2 Velocity distribution.....	195
7.3.3.3 Temperature and humidity distributions.....	195
7.3.4 Numerical Validations.....	196
7.4 PROJECTED COMMERCIAL SCALE PROTOTYPE PERFORMANCE.....	202
7.4.1 Scale Up Considerations.....	203
7.4.2 Numerical Results and Discussion.....	204
7.4.3 Cyclone Dryer Scale Up Strategy.....	206
7.5 CONCLUSIONS.....	206
 <i>Chapter 8 SUMMARY AND RECOMMENDATIONS.....</i>	 210
8.1 INTRODUCTION.....	210
8.2 SUMMARY.....	211
8.2.1 Apparatus Design and Preliminary Investigation.....	211
8.2.2 RTD of Solid Particles in the Model Cyclone Dryer.....	212
8.2.3 Performance of the Model Cyclone Dryer during Continuous Operation.....	212
8.2.4 Applicability of CFD for Cyclone Dryer Design.....	213
8.3 RECOMMENDATIONS.....	215
 <i>References.....</i>	 216
 <i>Appendices (in separate volume)</i>	
 <i>Appendix A. MATLAB Source Program for Pneumatic Dryer Simulation.....</i>	 226
 <i>Appendix B. Drawing of Cyclone Dryer, Rotary Feeder, Heater and Settling Chamber.....</i>	 235

<i>Appendix C. Calculation of the Required Air Flow and Total Pressure Drop</i>	264
<i>Across the Drying System.....</i>	
C.1 Air flow rate.....	265
C.2 System pressure drop.....	265
<i>Appendix D. Three Hole Probe Calibration.....</i>	271
D.1 Probe Construction.....	272
D.2 Detail of Probe Calibration.....	272
D.3 Calibration Results and Data Fitting.....	273
D.4 Error of Fitted Surface.....	277
<i>Appendix E. Experimental Results of Paddy Grain and Silica Gel Particle</i>	
<i>Drying and Initial Conditions for Cyclone Dryer Simulations....</i>	280

List of Figures

2.1	Paddy dryer developed by AED (Singhagajen, 1981).....	10
2.2	AIT Solar Paddy dryer (Exell et al., 1979).....	12
2.3	Solar rice dryer with forced air circulation (Tongprasert, 1978).....	13
2.4	Integrated paddy-drying/storage solar hut (Soponronnarit, 1985).....	14
2.5	Natural convective rotary dryer (Puechkamutr, 1985).....	16
2.6	Drying Chamber of the Louisiana State University Dryer.....	17
2.7	Diagram of fluidised bed paddy dryer (Soponronnarit et al., 1996a).....	19
2.8	Fluidised bed paddy dryer (Soponronnarit et al., 1996b).....	20
2.9	Mobile fluidised bed paddy dryer (Soponronnarit et al., 1998).....	21
2.10	Diagram of vibro-fluidised bed paddy dryer (Soponronnarit et al., 2001).....	22
2.11	Industrial-scale prototype spouted bed dryer (Madhiyanon et al., 2001).....	24
2.12	Paddy drying system in Supanthaanya rice mill (Rordprapat et al., 1999).....	26
2.13	Paddy drying System in Poonsinthaï rice mill (Rordprapat et al., 1999).....	27
2.14	Paddy drying System in Taweerungruang rice mill (Rordprapat et al., 1999).....	28
2.15	Head rice yield as a function of final moisture content of paddy (agitation speed, 14 rpm; feed rate 30 kg/min) (Jindal et al., 1986).....	30
2.16	Head rice yield as a function of final moisture content of paddy (agitation speed, 30 rpm; feed rate 30 kg/min) (Jindal et al., 1986).....	30
2.17	Head rice yield as a function of final moisture content of paddy (agitation speed, 40 rpm; feed rate 30 kg/min) (Jindal et al., 1986).....	31
2.18	Relationship between relative head rice yield and final moisture content in fluidised bed drying at different temperatures (Initial moisture content 45.3% dry- basis) (Soponronnarit et al., 1994).....	31
2.19	Relationship between Relative whiteness and final moisture content in fluidised bed drying at different temperature (Initial moisture content 45.3% dry- basis) (Soponronnarit et al., 1994).....	32
2.20	Relative head rice yield at different initial moisture contents Inlet air temperature 150 °C (Wetchacama et al., 1999).....	33
2.21	Relative head rice yield at different inlet air temperatures Initial moisture content 31.1 % db. (Wetchacama et al., 1999).....	34
2.22	Relative rice whiteness at different initial moisture contents (Wetchacama et al., 1999)....	35
2.23	Relative rice whiteness at different inlet air temperatures (Wetchacama et al., 1999).....	35
2.24	Sun drying of paddy on a concrete floor.....	38
3.1	Diagram of a simple pneumatic dryer.....	43
3.2	Elemental layer of a concurrent flowing pneumatic dryer.....	44

3.3	Flow diagram of the pneumatic dryer simulation.....	49
3.4	Development of dimensionless quantities over the dryer length.....	51
3.5	Variation of slip velocity over dryer length with paddy feed rate of 0.75 kg/s and inlet air velocity of 23 m/s for three dryer diameters.....	52
3.6	Development of : (a) paddy and air temperatures; and (b) paddy moisture content and air Humidity, over the dryer length with paddy feed rate of 0.75 kg/s and inlet air velocity of 23 m/s for three dryer diameters.....	53
3.7	Variation of slip velocity over dryer length with dryer diameter of 0.203 m and inlet air velocity of 23 m/s for three paddy feed rates.....	54
3.8	Development of : (a) paddy and air temperatures; and (b) paddy moisture content and air humidity over, the dryer length with dryer diameter of 0.203 m and inlet air velocity of 23 m/s for three paddy feed rates.....	55
3.9	Variation of slip velocity over dryer length with dryer diameter diameter of 0.203 m and inlet air velocity of 23 m/s for three inlet air velocity values.....	56
3.10	Development of : (a) paddy and air temperatures; and (b) paddy moisture content and air humidity over, the dryer length with, dryer diameter of 0.203 m and inlet paddy feed rate of 0.5 kg/s for three inlet air velocities.....	58
3.11	Variation of equilibrium temperature with: (a) dryer diameter; and (b) paddy feed rate, for three inlet air velocities.....	60
3.12	Required dryer length to achieve different final moisture contents. ($T_{\text{fi}} = 30\text{ }^{\circ}\text{C}$, $M_i = 0.33\text{ kg water/ kg dry material}$, $D = 0.203\text{ m}$, $F = 0.25\text{ kg/s}$, $v_f = 23\text{ m/s}$).....	61
4.1	Flow pattern inside tangential inlet cyclone (Hoffmann et al., 2002).....	63
4.2	Control surface (CS) of cyclone (Hoffmann et al., 2002).....	64
4.3	Multi-chamber cyclone dryer (Korn, 2001).....	69
4.4	Schematic diagram for model cyclone dryer used in this study.....	70
4.5	Geometry of cyclone dryer chamber used in the present investigation.....	72
4.6	Drawing of model cyclone dryer system.....	74
4.7	Variation of cyclone dryer total pressure drop coefficient with Reynolds number.....	76
4.8	Paddy grain behaviour at 0.09 m ³ /s air flow rate (Estimated jet velocity 11.5 m/s).....	77
4.9	Paddy grain behaviour at 0.11 m ³ /s air flow rate (Estimated jet velocity 14 m/s).....	78
5.1	Model cyclone dryer geometry in x-z and x-y planes. The configuration geometric ratios and measuring positions are also shown.....	83
5.2	Three-hole modified wedge probe. (support diameter 6.35 mm).....	85
5.3	Radial profiles of velocity components at elevations $z = 0.055\text{ m}$ and 0.255 m : (a) axial velocity; (b) tangential velocity.....	87
5.4	Series of meshes of different fineness used for grid sensitivity studies: (a) 864,185 nodes; (b) 419,928 nodes; (c) 190,057 nodes; (d) 86,555 nodes.....	94

5.5	Influence of differencing scheme on predicted velocity distributions at $z = 0.055$ m: (a) axial velocity; (b) tangential velocity.....	96
5.6	Influence of differencing scheme on predicted velocity distributions at $z = 0.255$ m: (a) axial velocity; (b) tangential velocity.....	97
5.7	Influence of mesh resolution on predicted velocity distributions at $z = 0.055$ m for RNG k- ϵ turbulence model: (a) axial velocity; (b) tangential velocity.....	99
5.8	Influence of mesh resolution on predicted velocity distributions at $z = 0.255$ m for RNG k- ϵ turbulence model: (a) axial velocity; (b) tangential velocity.....	101
5.9	Predicted near-wall tangential velocity distributions for different mesh resolutions using the RNG k- ϵ turbulence model: (a) inlet pipe side; (b) outlet pipe side. Values plotted at computational nodes.....	102
5.10	Influence of mesh resolution on predicted velocity distributions at $z = 0.055$ m for SSG Reynolds stress turbulence model: (a) axial velocity; (b) tangential velocity.....	104
5.11	Influence of mesh resolution on predicted velocity distributions at $z = 0.255$ m for SSG Reynolds stress turbulence model: (a) axial velocity; (b) tangential velocity.....	105
5.12	Predicted near-wall tangential velocity distributions for different mesh resolutions using the SSG Reynolds stress turbulence model: (a) inlet pipe side; (b) outlet pipe side. Values plotted at computational nodes.....	107
5.13	Influence of different turbulence models on predicted velocity distributions at $z = 0.055$ m: (a) axial velocity; (b) tangential velocity.....	109
5.14	Influence of different turbulence models on predicted velocity distributions at $z = 0.255$ M: (a) axial velocity; (b) tangential velocity.....	110
5.15	Pressure drop characteristics from simulation and experiment.....	111
5.16	Comparison of axial and tangential velocity profiles predicted by RNG k- ϵ turbulence model at different inlet velocities (8, 10 and 13 m/s): (a) axial velocity; (b) tangential velocity.....	112
5.17	Velocity vector plot and pressure contour of three-chamber cyclone dryer: (a) velocity vector plot of x-z cut plane at $y=0$; (b) pressure contour plot of x-z cut plane at $y=0$; (c), (d) and (e) velocity vector and pressure contour plots of x-y plane at $z = 0.055$ m, 0.255 M and 0.455m.....	114
5.18	Velocity vector plot and pressure contours of four-chamber cyclone dryer: (a) velocity vector plot of x-z cut plane at $y=0$; (b) pressure contour plot of x-z cut plane at $y=0$; (c), (d), (e) and (f) velocity vector and pressure contour plots of x-y cut plane at $z = 0.055$ m, 0.255 m, 0.455 m and 0.655 m.....	115
6.1	The two ideal types of reactor: (a) plug flow; (b) mixed flow.....	122
6.2	Cumulative age distribution, or $F(t)$ curve.....	123
6.3	The exit age distribution curve, $E(t)$ for particle flow through the dryer, also called the	

residence time distribution or RTD (Levenspiel 1972).....	124
6.4 Effect of model parameters on the RTD curve, indicating various degrees of mixing :	
(a) Dispersion model: influence of dispersion number, D/uL ;	
(b) Tank-in-series model: influence of number of tanks, n (Levenspiel, 1972).....	128
6.5 Paddy flow rates versus motor frequency at different sliding plate openings.....	130
6.6 Silica gel flow rates versus motor frequency at different sliding plate openings.....	131
6.7 Cumulative age distribution, $F(t)$, of silica gel particles.....	134
6.8 Cumulative age distribution, $F(t)$, of paddy grain.....	134
6.9 Influence of inlet air velocity on cumulative age distribution of silica gel particles.....	136
6.10 Influence of inlet air velocity on cumulative age distribution of paddy grain.....	136
6.11 Influence of particle feed rate on cumulative age distribution of silica gel particles.....	137
6.12 Influence of particle feed rate on cumulative age distribution of paddy grain.....	137
6.13 Influence of mass concentration on mean residence time of paddy grain for three- and four-chamber cyclone dryers.....	139
6.14 Influence of mass concentration on mean residence time of silica gel particles for three- and four-chamber cyclone dryers.....	139
6.15 Comparison of best fit tank-in-series and dispersion models with experimental RTD for paddy grain. Test case 1.....	141
6.16 Comparison of best fit tank-in-series and dispersion models with experimental RTD for silica gel. Test case 11.....	141
6.17 Comparison of experimental and numerical cumulative age distributions of silica gel particles in a three-chamber cyclone dryer (Silica gel feed rate = 0.0778 kg/s).....	148
6.18 Comparison of experimental and numerical cumulative age distributions of silica gel particles in a four-chamber cyclone dryer (Silica gel feed rate = 0.0778 kg/s).....	148
6.19 Comparison of experimental and numerical cumulative age distributions of paddy grain in a three-chamber cyclone dryer (Silica gel feed rate = 0.0778 kg/s).....	149
6.20 Comparison of experimental and numerical cumulative age distributions of paddy grain in a four-chamber cyclone dryer (Silica gel feed rate = 0.0778 kg/s).....	149
6.21 Comparison of numerical and experimental age distributions, $E(t)$, for silica gel particles in three-chamber cyclone dryer, showing influence of inlet air velocity.....	152
6.22 Comparison of numerical and experimental age distributions, $E(t)$, for silica gel particles in four-chamber cyclone dryer, showing influence of inlet air velocity.....	152
6.23 Comparison of numerical and experimental age distributions, $E(t)$, for paddy grain in three- chamber cyclone dryer, showing influence of inlet air velocity.....	153
6.24 Comparison of numerical and experimental age distributions, $E(t)$, for paddy grain in four-chamber cyclone dryer, showing influence of inlet air velocity.....	153

7.1	Variation of percentage of moisture reduction (MR) with inlet air temperature (T_{fi}) at different paddy feed rates: (a) three-chamber cyclone dryer; (b) four-chamber cyclone dryer.....	164
7.2	Variation of percentage of moisture reduction (MR) with inlet air temperature (T_{fi}) at different silica gel feed rates: (a) three-chamber cyclone dryer; (b) four-chamber cyclone dryer.....	165
7.3	Comparison of moisture reduction (MR) for three- and four-chamber cyclone dryers at different feed rates: (a) low feed rate; (b) medium feed rate; (c) high feed rate.....	167
7.4	Variation of dimensionless heat transfer coefficient (Nu) with inlet air temperature for different paddy feed rates; (a) three-chamber cyclone dryer; (b) four-chamber cyclone dryer.....	168
7.5	Variation of dimensionless heat transfer coefficient (Nu) with inlet air temperature for different silica gel feed rates: (a) three-chamber cyclone dryer; (b) four-chamber cyclone dryer.....	169
7.6	Comparison of dimensionless heat transfer coefficient (Nu) variation with inlet air Temperature for three- and four-chamber cyclone dryer operation at different feed rates: (a) low feed rate; (b) medium feed rate; (c) high feed rate.....	171
7.7	Variation of dimensionless mass transfer coefficient (Sh) with inlet air temperature for different paddy feed rates: (a) three-chamber cyclone dryer; (b) four-chamber cyclone dryer.....	172
7.8	Variation of dimensionless mass transfer coefficient (Sh) with inlet air temperature for different silica gel feed rates: (a) three-chamber cyclone dryer; (b) four-chamber cyclone dryer.....	173
7.9	Comparison of dimensionless mass transfer coefficients (Sh) for paddy grain and silica gel particle drying: (a) low feed rate; (b) medium feed rate; (c) high feed rate.....	175
7.10	Variation of specific energy consumption (SPEC) with inlet air temperature at different paddy feed rates: (a) three-chamber cyclone dryer; (b) four-chamber cyclone dryer.....	176
7.11	Variation of specific energy consumption (SPEC) with inlet air temperature at different silica gel feed rates: (a) three-chamber cyclone dryer; (b) four-chamber cyclone dryer.....	177
7.12	Comparison of specific energy consumption (SPEC) for paddy grain and silica gel particle drying: (a) low feed rate; (b) medium feed rate; (c) high feed rate.....	179
7.13	Influence of initial moisture content of particles on the SPEC.....	180
7.14	Schematic diagram of cyclone dryer with system of air recycling system.....	186
7.15	Influence of mixing moisture content on fraction of air recycled and SPEC.....	188
7.16	Variation of SPEC with fraction of air recycled.....	188

7.17	Typical particle trajectories: (a) three-chamber cyclone dryer; (b) four-chamber cyclone Dryer. Colour contours indicate residence time in seconds.....	194
7.18	Influence of silica gel feed rate on predicted tangential velocity profiles for three- chamber cyclone dryer at: (a) 0.055 m elevation ;(b) 0.255 m elevation (Inlet air temperature 57.43 °C; initial moisture content of silica gel 21 % db.).....	198
7.19	Influence of inlet air temperature on predicted tangential velocity profiles for three- chamber cyclone dryer: (a) 0.055 m elevation; (b) 0.255 m elevation (Silica gel feed rate 0.0256 kg/s; initial moisture content of silica gel 21 % db.).....	198
7.20	Influence of initial moisture content of silica gel on predicted tangential velocity profiles for three-chamber cyclone dryer: (a) 0.055 m elevation; (b) 0.255 m elevation (Inlet air temperature 57.43 °C; silica gel feed rate 0.0256 kg/s).....	199
7.21	Influence of silica gel feed rate on predicted temperature profiles for three-chamber cyclone dryer: (a) 0.055 m elevation; (b) 0.255 m elevation (Inlet air temperature 57.43 °C; initial moisture content of silica gel 21 % db.).....	199
7.22	Influence of inlet air temperature on predicted temperature profiles for three- chamber cyclone dryer: (a) 0.055 m elevation; (b) 0.255 m elevation; (Silica gel feed rate 0.0256 kg/s; initial moisture content of silica gel 21 % db.).....	200
7.23	Influence of initial moisture content of silica gel on predicted temperature profiles for three-chamber cyclone dryer: (a) 0.055 m elevation; (b) 0.255 m elevation (Inlet air temperature 57.43 °C; silica gel feed rate 0.0256 kg/s).....	200
7.24	Influence of silica gel feed rate on predicted humidity profiles for three-chamber cyclone dryer: (a) 0.055 m elevation; (b) 0.255 m elevation (Inlet air temperature 57.43 °C; initial moisture content of silica gel 21 % db.).....	201
7.25	Influence of inlet air temperature on predicted humidity profiles for three-chamber cyclone dryer: (a) 0.055 m elevation; (b) 0.255 m elevation (Silica gel feed rate 0.0256 kg/s; initial moisture content of silica gel 21 % db.).....	201
7.26	Influence of initial moisture content of silica gel on predicted humidity profiles for three-chamber cyclone dryer: (a) 0.055 m elevation; (b) 0.255 m elevation (Inlet air temperature 57.43 °C; silica gel feed rate 0.0256 kg/s).....	202
7.27	Influence of geometric scale factor on RTDs of silica gel particles.....	205
7.28	Predicted variation of mean residence time with geometric scale factor.....	205
C-1	Operating point at various speeds of the selected blower.....	269
C-2	Characteristic curve of selected blower at 2880 rpm.....	270
D-1	f1plotted against probe angle at different Re.....	274
D-2	f2plotted against probe angle at different Re.....	274
D-3	f3plotted against probe angle at different Re.....	275
D-4	Error of f1.....	278

D-5	Error of f_2	278
D-6	Error of f_3	278
D-7	Error of Calibration Angle	279
D-8	Error of Air Velocity.....	279

List of Tables

4.1	Characteristic of cyclone dryer pilot plant (Korn, 2001).....	71
5.1	Pressure scanner channel set-up during flow field measurement of Cyclone dryer.....	85
5.2	Effect of differencing scheme on predicted total pressure drop coefficient using mesh of 86,555 nodes and RNG k- ϵ turbulence model.....	98
5.3	Comparison of predicted total pressure drop coefficient and RMS residual value for different mesh resolutions using RNG k- ϵ turbulence model with second-order differencing scheme.....	103
5.4	Comparison of predicted total pressure drop coefficient and RMS residual value for different mesh resolutions using SSG Reynolds stress turbulence model with second-order differencing scheme.....	106
5.5	Predicted influence of number of chambers on total pressure drop coefficient for model cyclone dryer.....	117
6.1	Influence of cyclone geometry and operating conditions on residence time distributions for silica gel particles and paddy grain.....	133
6.2	Best fit to experimental residence time distribution for tank-in-series and dispersion models for cases specified in Table 6.1.....	142
6.3	Stokes number of paddy grain and silica gel particles at different inlet air velocity.....	147
6.4	Comparison of experimental and numerical by simulated mean particle residence times...	150
7.1	Comparison of working performance between the model cyclone dryer and other commercial paddy dryers.....	182
7.2	Results of multi-pass drying of paddy grain in a three-chamber cyclone dryer.....	184
7.3	Results of multi-pass drying of paddy grain in a four-chamber cyclone dryer.....	184
7.4	Overall average values for multi-pass paddy drying tests.....	184
7.5	Comparison of numerical and experimental results for overall air temperature and humidity changes in silica gel drying.....	197
7.6	Influence of geometric scale-up factor mean residence time.....	206
D-1	Coefficient of $f_1(\alpha, Re)$	276
D-2	Coefficient of $f_2(\alpha, Re)$	276
D-3	Coefficient of $f_3(\alpha, Re)$	276
E.1	Experimental results of paddy drying in three-chamber cyclone dryer.....	281
E.2	Experimental results of paddy drying in four-chamber cyclone dryer.....	282
E.3	Experimental results of silica gel drying in three-chamber cyclone dryer.....	283
E.4	Experimental results of silica gel drying in four-chamber cyclone dryer.....	284
E.5	Summary of simulation cases for silica gel drying in three-chamber cyclone dryer.....	285
E.6	Summary of simulation cases for silica gel drying in four-chamber cyclone dryer.....	386

List of Symbols

A	Projected area of body normal to relative flow direction	m^2
\mathbf{a}	Anisotropic tensor	$m\ s^{-1}$
a_p	Specific surface area	$m^2\ m^{-3}$
b, b_0, b_1	Constants	-
b_2, b_3, b_4	Constants	-
C	Concentration	$kg\ kg^{-1}$
C_D	Drag coefficient	-
C_e	Equilibrium concentration	$kg\ kg^{-1}$
C_1, C_2	Constants for k- ϵ turbulence model	-
C_{r1}, C_{r2}, C_{r3}	Constants for Reynolds stress turbulence model	-
C_{r4}, C_{r5}	Constants for Reynolds stress turbulence model	-
C_S, C_{S1}, C_{S2}	Constants for Reynolds stress turbulence model	-
$C_\epsilon, C_{\epsilon1}, C_{\epsilon2}$	Constants for Reynolds stress turbulence model	-
$C_{\epsilon1RNG}$	Constant for RNG k- ϵ turbulence model	-
$C_{\epsilon2RNG}$	Constant for RNG k- ϵ turbulence model	-
C_μ	Constant for k- ϵ turbulence model	-
$C_{\mu RNG}$	Constant for RNG k- ϵ turbulence model	-
$C_{\Delta P}$	Total pressure drop coefficient	-
c_1, c_2	Constants	-
c_f	Heat capacity of air	$kJ\ kg^{-1}\ K^{-1}$
c_i	Measured tracer concentration	$kg\ kg^{-1}$
c_p	Heat capacity of particles	$kJ\ kg^{-1}\ K^{-1}$
c_{pi}	Heat capacity of particles at initial state	$kJ\ kg^{-1}\ K^{-1}$
c_w	Heat capacity of saturated water	$kJ\ kg^{-1}\ K^{-1}$
c_v	Heat capacity of water vapour	$kJ\ kg^{-1}\ K^{-1}$
D	Dryer diameter	m
D_{eff}	Coefficient of diffusion	$m^2\ s^{-1}$
D_{eq}	Equivalent diameter	m
D_o	Outlet diameter	m
D_p	Axial dispersion coefficient	-
D_{v-a}	Diffusivity of water in air	$m^2\ s^{-1}$
d_p	Particle diameter	m
$E(t)$	Exit age distribution, or residence time distribution	s^{-1}
$E(\theta)$	Dimensionless exit age distribution	-

E_m	Mean deviation	-
F	Feed rate of particles	kg s^{-1}
$F(t)$	Cumulative age distribution	s^{-1}
$F(\theta)$	Dimensionless cumulative age distribution	s^{-1}
\bar{F}	Average particle feed rate	kg s^{-1}
F	Friction factor	-
f_η	Constant	-
f'	Modified friction factor	-
g	Gravitational acceleration	m s^{-2}
h	Heat transfer coefficient	$\text{W m}^{-2} \text{K}^{-1}$
h_{CS}	Height of control surface	m
h_{fg}	Latent heat of vaporisation	kJ kg^{-1}
\mathbf{I}	Kronecker delta	-
K_m	Mass transfer coefficient	kg s^{-1}
k	Turbulence kinetic energy	$\text{m}^2 \text{s}^{-2}$
L	Length	m
l_d	Diffuser length	m
M	Moisture content of particles (dry basis)	kg kg^{-1}
M_{cr}	Critical moisture content	kg kg^{-1}
M_{eq}	Equilibrium moisture content	kg kg^{-1}
M_i	Initial moisture content	kg kg^{-1}
M_o	Moisture content at outlet	kg kg^{-1}
MR	Moisture reduction	% db.
m_f	Mass flow rate of air	kg s^{-1}
\dot{m}_f	Mass flux of air	$\text{kg m}^{-2} \text{s}^{-1}$
m_p	Mass flow rate of particles	kg s^{-1}
\dot{m}_p	Mass flux of particles	$\text{kg m}^{-2} \text{s}^{-1}$
m_w	Mass of water in particles	kg
NP_i	Number of particles having left calculation domain at time t_i	-
Nu	Nusselt number	-
n	Number of tank for tanks-in-series RTD model	-
n_o	Number of particles initially injected into calculation domain	-
P	Pressure	Pa
P_k	Shear production for k- ϵ turbulence model	kg m s^{-3}
P_s	Shear production for Reynolds stress turbulence model	kg m s^{-3}
P_w	Partial pressure of vapour in air	Pa

P_{ws}	Saturated vapour pressure	Pa
Pr	Prandtl number	-
Q	Volumetric flow rate	$m^3 s^{-1}$
\dot{Q}	Heat transfer rate	$kJ s^{-1}$
\dot{Q}_m	Mass transfer rate	$kg s^{-1}$
R	Radius	m
\bar{R}	Vector directed from the axis of rotation	-
R_c	Radius of vortex finder	m
$R_{cyclone}$	Radius of cyclone dryer	m
R_x	Radius of vortex core	m
Re	Reynolds number	-
Re_p	Particle Reynolds number	-
R_e	Surface roughness	m
Re'	Modified particle Reynolds number	-
RH	Relative humidity	%
r	Radial coordinate	m
r_c	Continuous phase volume fraction	-
r_f	Fraction of mass in continuous phase	-
r_p	Fraction of mass in particulate phase	-
S	Strain rate	$m s^{-1}$
S_E	Energy source	$kg m^{-1} s^{-1}$
S_M	Momentum source	$kg m^{-2} s^{-1}$
S_{MS}	Mass source	$kg m^{-3} s^{-1}$
Sh	Sherwood number	-
SP_{air}	Specific air flow rate	$m^3 kg^{-1}$
St_v	Stokes number	-
T	Temperature	K
T_{eq}	Equilibrium temperature	K
T_f	Air temperature	K
T_{fi}	Air temperature at inlet	K
T_{fo}	Air temperature at outlet	K
T_p	Particle temperature	K
T_{pi}	Particle temperature at inlet	K
T_{po}	Particle temperature at outlet	K
T_{∞}	Ambient temperature	K
t	Time	s

t_f	Air temperature	$^{\circ}\text{C}$
\bar{t}_i	Mean residence time in one tank	s
\bar{t}	Mean residence time in n tanks	s
\mathbf{u}	Velocity vector	m s^{-1}
\mathbf{u}'	Fluctuating velocity component in turbulence flow	m s^{-1}
V	Volume	m^3
v	Velocity	m s^{-1}
$v_{a,d}$	Average downward axial velocity	m s^{-1}
v_d	Bed voidage	%
$v_{a,u}$	Average upward inlet velocity	m s^{-1}
v_p	Velocity of particle	m s^{-1}
v_{po}	Initial velocity of particle	m s^{-1}
v_f	Velocity of air, fluid	m s^{-1}
v_r	Radial velocity	m s^{-1}
v_{rCS}	Radial velocity at control surface	m s^{-1}
v_t	Terminal velocity of particle	m s^{-1}
v_{θ}	Tangential velocity	m s^{-1}
v_m	Minimum superficial pipe velocity	m s^{-1}
W	Humidity of air	kg kg^{-1}
W_d	Weight of bone-dry material	kg
W_i	Humidity at inlet	kg kg^{-1}
W_m	Weight of moist material	kg
W_o	Humidity at outlet	kg kg^{-1}
W_{sat}	Saturated humidity	% db.
WP	Wetted perimeter	m
x_o	Initial displacement of particle	m
x_n	Displacement of particle at n^{th} stage	m
z	Height of dryer	m
α	Transition angle	degree
β	Constant for k- ϵ turbulence model	-
β_{RNG}	Constant for RNG k- ϵ turbulence model	-
χ	Constant	-
δ	Constant	-
ϵ	Dissipation rate	$\text{m}^2 \text{s}^{-3}$
ϕ_i	The solution of relevant quantity	-
γ	Constant	-

λ	Thermal conductivity	$\text{W m}^{-2} \text{K}^{-1}$
μ	Molecular viscosity	$\text{kg m}^{-1} \text{s}^{-1}$
μ_{eff}	Effective viscosity	$\text{kg m}^{-1} \text{s}^{-1}$
μ_T	Turbulent viscosity	$\text{kg m}^{-1} \text{s}^{-1}$
μ_w	Air viscosity at surface temperature	$\text{kg m}^{-1} \text{s}^{-1}$
μ_∞	Air viscosity at bulk temperature	$\text{kg m}^{-1} \text{s}^{-1}$
η	Constant for RNG k- ϵ turbulence model	-
θ	Dimensionless time	-
ρ_p	Density of particles	kg m^{-3}
ρ_f	Density of air, fluid	kg m^{-3}
σ	Standard deviation of residence time distribution	s^{-2}
$\sigma_k, \sigma_\epsilon$	Constant for k- ϵ turbulence model	-
$\sigma_{\epsilon \text{RNG}}$	Constant for RNG k- ϵ turbulence model	-
τ	Mean residence time	s
τ_v	Momentum response time	s
τ_T	Characteristic convective time for the flow field	s
ω	Vorticity	Red s^{-1}
ξ	Fitting pressure loss coefficient	-
Γ_t	Eddy diffusivity	$\text{kg m}^{-1} \text{s}^{-1}$
ΔP	Total pressure loss	Pa
Π	Pressure strain term for Reynolds stress turbulence model	kg m s^{-3}
\mathfrak{R}	Gas constant	$\text{Nm kg}^{-1} \text{K}^{-1}$
$\frac{D}{uL}$	Dispersion number	-

Chapter 1

INTRODUCTION

1.1 NEED

The rice yield of farming systems in Thailand is increasing due to many factors, such as high-yielding non-photoperiodic varieties, irrigated farms, high fertiliser inputs and the development of agricultural machinery, etc., which result in double or triple cropping systems.

At least one paddy (rice) crop is harvested during the rainy season, and there are many difficulties associated with this wet crop production. Because of the large crop production, some of the products cannot be harvested on time. This has resulted in losses of product stability, which can lead to biochemical deterioration of grain. This deterioration takes the form of general discolouration, yellowing, germination and damage to milling quality. Immediate threshing and drying of the wet harvest is the only practical method to arrest deterioration.

1.2 PROCESS

During 2000-01, 25.608 Mt of paddy was produced in Thailand. This comprised 19.552 Mt from the main year crop and 6.055 Mt from the second crop (Agricultural

statistics crop year 2000-01, Office of Agricultural Economies, Thailand, 2002). The main year crop is harvested in the dry season, while the second crop is harvested in the rainy season. The combine harvester does most of the harvesting work. The plant is cut and threshed in the combine harvester. Then, the paddy is sold to the rice millers or transported to the barn. Most farmers sell the paddy to rice millers immediately, because they have no storage facilities or need to obtain the cash. Furthermore, the grain deteriorates more quickly in the rainy season.

During the harvesting season of the second crop, a high moisture content is usually found in the air. Rice harvested from the field contains about 24-28% moisture content wet-basis (De Padua et al., 1985), while a general moisture content of 14 % wet-basis gives the paddy a longer storage life and higher milling quality (Kunze et al. 1980). An 18 % moisture content wet-basis of threshed rice is generally preferable to the rice miller, and the price decreases when the moisture content increases. The drying process plays an important role to maintain the quality and increase the price of paddy.

1.3 CURRENT DRYING METHODS

Solar drying is usually practised. In this method, a thin layer of grain is spread on an apron in the ambient air. This method is still the most commonly used in Thailand. In the dry season, paddy grain can be dried within a few days by solar drying. However, it is problematic in the rainy season, which is why the products are then distributed out to the rice millers as fast as possible. The rice millers have better facilities, such as high-speed mechanical dryers or sun drying on a concrete apron, to dry paddy.

Heated air-drying has been developed in Thailand within the last few decades. The dryers which have been developed were mostly batch types and use solar energy, fuel oil or agricultural waste as energy supplies. However, solar drying is the most popular method to eliminate the moisture content in paddy, because it is cheapest.

1.4 PROBLEMS WITH CURRENT METHODS

Traditional solar drying of spread-out paddy grain is an effective means of reducing moisture in the dry season. Wet season crops require forced-air drying with heated or ambient temperature air. In both wet and dry seasons, paddy grain may be treated by variety of methods, all of which require great care. Drying is a complex process requiring considerable skill and effort on the part of the farmer; the success with which the grain is preserved over shorter or longer periods depends on the care and attention given to the drying and subsequent storage.

Over-heating, under-heating and too-rapid drying can occur during the sun drying process. The temperature of the sun drying floor surface and the paddy may increase to as high as 60 to 70 °C. This high, uncontrolled temperature induces severe temperature and moisture gradients within the paddy kernels resulting in a rapid drying rate and, consequently, stress checks and cracks. The resulting “sun checking” of the paddy is a common and, unfortunately, too often accepted form of loss of rice quality. On the other hand, slow drying results in deterioration due to fungi and bacteria, and also leads to losses of paddy grain. Solar drying is undoubtedly a low-cost method, but there are problems associated with sun drying which often result in a poor quality product: no control over the drying process, possible contamination of the product, and its labour intensiveness.

1.5 TARGET USERS

As mentioned in the previous section, the drying process plays an important role to maintain the quality and increase the price of paddy. For the farmers, a better purchasing price will be obtained at 18 % moisture content wet-basis. For rice millers, the length of storage life depends on the moisture content in paddy grain, and 14 % moisture content wet-basis is the best. Therefore, the development of rice dryers is needed not only for farmers but also for rice millers. The development of rice dryers requires the following steps:

-
1. First determine the quantity and nature of the product to be dried and the particular consumer requirements. By determining what the initial and final moisture content are and the maximum drying time, quantity to be dried per batch, dryer bed size, amount of moisture to be removed, and heat required to remove moisture, a required air flow rate can be established.
 2. A prototype dryer should be built and initial tests carried out, and a consumer-acceptance analysis should be conducted.
 3. Feedback data from consumers should be used in prototype modification until the prototype is suitable for the drying of a high-quality product acceptable to the consumer.

1.6 THESIS OUTLINE

The thesis outlines the development of a forced air rice dryer based on the previously discussed requirements. The remaining chapters are structured as follows.

Chapter 2 reviews rice (paddy) dryers used in Thailand and their commercialisation. The effect of their operating parameters on rice quality is also reviewed. The most promising dryer for paddy grain is identified.

Chapter 3 develops mathematical modeling of heat and mass balance between air and rice (paddy) and tests the applicability of a simple pneumatic dryer for rice (paddy) drying. Simulation results for different operating parameters are discussed.

Chapter 4 introduces the design and development of a proposed cyclone dryer. Preliminary studies of rice grain flow inside a model cyclone dryer chamber are reported.

Chapter 5 details a series of single-phase flow field simulations inside the cyclone dryer chamber with the commercial RANS-based computational fluid dynamics

(CFD) package CFX 5.7. The Numerical results are validated using experimental results obtained from the laboratory scale model cyclone dryer.

Studies of solid-gas flow in the model cyclone dryer using paddy grain and silica gel particles are reported in Chapter 6. Experimental results with different operating parameters are discussed. Numerical simulations for paddy grain and silica gel particles are presented and compared with experimental results.

Experimental and numerical results for heat and mass transfer in the laboratory scale cyclone dryer are reported in Chapter 7. A strategy for scaling up the model cyclone dryer to a commercial sized unit is identified.

Chapter 8 gives the conclusions and recommendations for the study.

All references are located at the back of the thesis.

The appendices are placed in a separate volume.

Chapter 2

OVERVIEW OF PADDY DRYING IN THAILAND

2.1 INTRODUCTION AND DEFINITIONS

“Drying” is the word commonly used to describe any process in which water is removed from a substance. Drying may be defined as the removal of volatile substances by heat from a mixture to yield a solid product. Commonly, the principal volatile substance is water. Many agricultural products, especially cereal grains, must be dried to preserve their quality.

There are various ways to classify a grain dryer. An important technological characteristic of convective grain dryers is the state of the grain layer during drying, which, to a great extent, governs the heat and mass transfer parameters of the drying process. Based on this, all convective grain driers may be classified into four types:

- 1) Dryers with grain in a stationary or fixed bed;
- 2) Dryers with grain in a moving bed;
- 3) Dryers with grain in a “boiling” or fluidised bed layer;
- 4) Dryers with grain in suspension.

2.1.1 Fixed Bed Dryers

Grain drying in a stationary layer is characterised by the fact that the velocity of grain (v_p) is zero and the velocity of the drying agent (v_f) is less than the terminal velocity of grain (v_t). Dryers in which drying is conducted in a fixed bed are operated intermittently and are simple in construction. They are suitable for small farm usage because they do not need large capital investment and they provide long service. Moreover, they may also be used as storage bins after drying. This type of grain dryer may be further classified into tray dryers, through dryers, chamber dryers, belt dryers and forced circulation dryers.

2.1.2 Moving Bed Dryers

In moving bed dryers, the velocity of the grain is greater than zero ($v_p > 0$) and the velocity of the drying agent is less than the terminal velocity ($v_f < v_t$). Examples of this dryer type are the drum (rotary) dryer, vibrating grain dryer, shaft dryer and louvered dryer.

2.1.3 Boiling Bed Dryers

In boiling bed dryers, the velocity of the grain is varied from zero to the terminal velocity ($0 < v_p < v_t$) and the velocity of the drying agent is greater than the terminal velocity ($v_f > v_t$). The force exerted by the drying agent moves grains in the dryer. The grain layer swells and its height and volume increase to some extent. When the weight of individual grains is balanced by the drag force, the grain velocity is zero. Grain drying in a boiling bed may be achieved in a spouted bed dryer or a fluidised bed dryer.

2.1.4 Suspension Dryers

Suspension dryers have the velocity of grain (v_p) equal to the velocity of the drying agent (v_f), which is much greater than the terminal velocity ($v_f \gg v_t$). Grains are

moving along with the drying agent in the dryer. This type of dryer is called a pneumatic dryer or stream dryer.

As mentioned in Chapter 1, various types of paddy dryer have been developed and tested in Thailand over the last few decades. Most of them used heated air as the drying agent. The primary design criterion was simplicity in construction and operation. The earlier machines were fixed bed dryers that used solar energy or agricultural waste as a heat source. They were implemented in rural areas of Thailand but none was attractive for the Thai farmer. Later developments included moving bed and boiling bed paddy dryers. Commercial rice millers adopted some of them, but there is still no acceptance of these types by farmers.

The purpose of this chapter is to review the present state of the art in the development of paddy dryers in Thailand. Their design, operation and performance in terms of capacity, energy consumption and product quality will be analysed; the constraints and problems with each type of dryer will be reported. Their capacity is expressed in terms of 'hold-up', which means the amount of drying material remaining in the drying chamber during steady state operation. The product quality is measured by percent of head rice yield, which is defined as the ratio of the mass of rice kernels having a length at least 8/10 of an intact rice kernel to the total mass of rice. It is usually measured by random sampling from the processed rice.

2.2 BACKGROUND AND DEVELOPMENT

In 1976, the Agricultural Engineering Division (AED), Department of Agriculture of the Government of Thailand, began work on post harvest technology with the support of the International Development Research Centre (IDRC). The survey on post harvest practices of farms conducted in that year indicated that the introduction of a farm grain dryer was essential because of the government support for second cropping in various part of country. The second crop was harvested during the wet season; this caused quality losses because of mould infection and changes in colour, giving a low milling yield.

2.2.1 Batch Type Paddy Dryers

A batch type fixed, flatbed paddy dryer with capacity 1-2 t was developed and tested by AED in 1977. The design basic for this dryer was simplicity of operation and construction, and an ability to be constructed using local materials and labour. Figure 2.1 shows the design and construction of the AED batch type dryer.

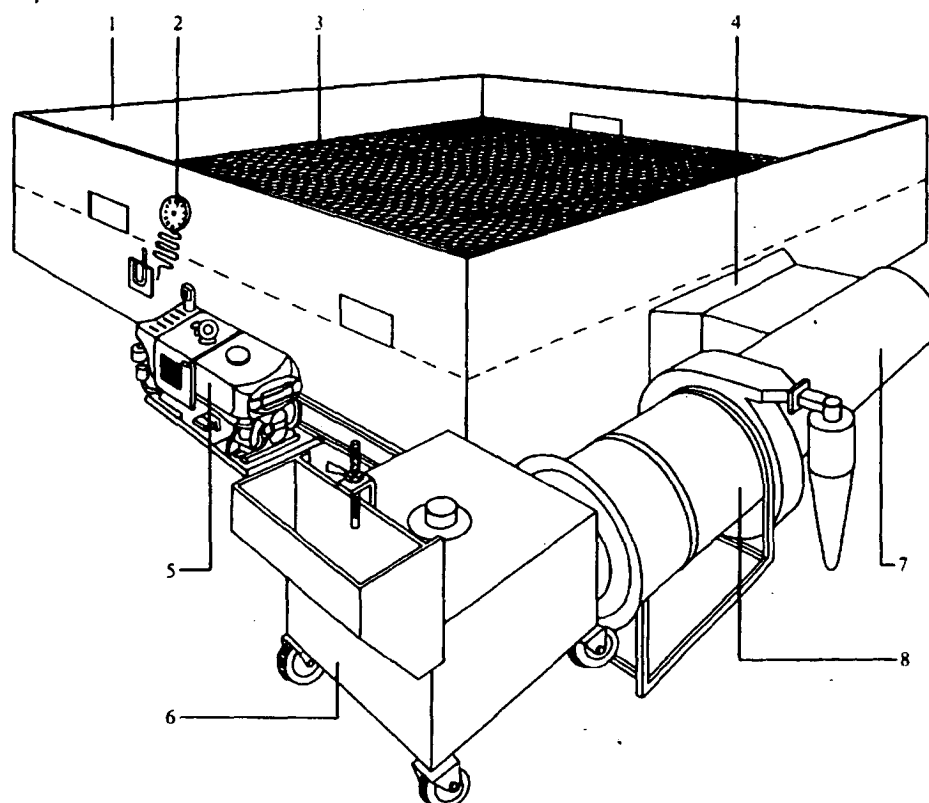
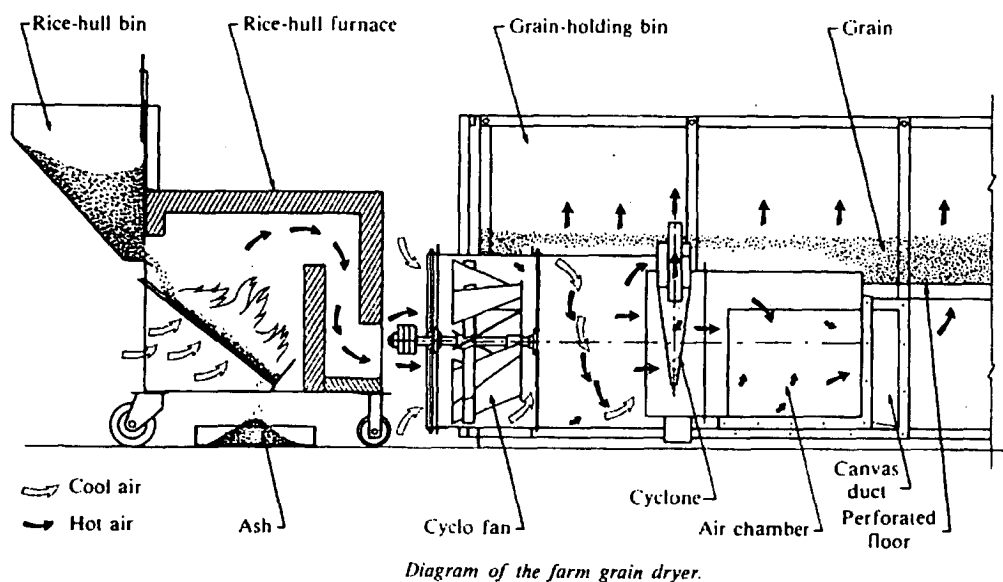
Grain was dried by hot air at a temperature of 43-38 °C. Heat was supplied by burning diesel oil or rice hull. When a 1 t/batch of paddy was dried with an air flow rate 107 m³/h, it took 3-6 hours to reduce the moisture content of paddy from 20-26 % to 14 %. The rate of drying was about 2 % of moisture content per hour. Fuel consumption was estimated to be 0.7-1.07 ℓ / t of paddy / 1 % (wet basis) of moisture reduction, for a 6 kW diesel engine and burner (Singhagajen, 1981).

A study made by the Philippines National Post Harvest Institute for Research and Extension (NAPHIRE) with the assistance of the IDRC documented the constraints perceived by both users and non-users of this dryer in the private sector. There were frequent complaints against heated-air dryers as follows (De Padua, 1985):

- 1) Dryer capacity is too great or too small: a 2-ton batch dryer was observed to be too large for farmers' requirements, but too small for rice millers;
- 2) High fixed cost required and/or limited capital available;
- 3) High operating cost for the fuel burner;
- 4) Claims of poorer quality milled rice than with sun drying, higher percentages of broken grains in milled rice, darker colour, and non-uniform drying;
- 5) Dryers said to be inconvenient. (Heat and dust are mentioned.)

2.2.2 Solar Paddy Dryer

Exell et al. (1979) have developed a simple solar dryer designed to provide the rice farmer in Thailand with a cheap and simple but efficient method for drying in the wet season. Their dryer and components are shown in Figure 2.2.



Components of the paddy dryer: (1) grain bin (244 × 244 × 122 cm), (2) thermometer, (3) screen (no. 8½), (4) canvas air duct, (5) engine (6 kW), (6) rice-hull furnace, (7) air duct, and (8) cyclo fan.

Figure 2.1 Paddy dryer developed by AED (Singhagajen, 1981)

The three main components are the solar collector, paddy box and chimney. The solar collector consists of a matte-black substance spread on the ground and provided with transparent top and side covers. The dryer was initially designed with a bed of burnt rice husk as an absorber and clear UV-stabilised polyethylene plastic sheet as the transparent cover. However, these could be substituted with locally-available materials such as charcoal, black plastic or black-painted metal sheets, dark coloured pebbles, etc.

The paddy box, located at waist level, is made of perforated material which allows air to pass through easily but is able to contain the grain. A door is provided to load and unload paddy at the back. The roof and sides of the box are covered with clear material, such as polyethylene plastic sheet. The box can be made of straw, but should be strong enough to hold paddy up to a depth of about 100 mm.

The chimney consists of a light, strong frame covered with a matte-black material. A top cover above the chimney keeps out the rain. The black material could be black plastic or black-painted metal sheet.

The principle of operation of this dryer is very simple. Sunlight passes through the clear plastic sheet and is absorbed by the black absorber bed, which in turn heats up the air inside the solar collector. The warm air then rises and passes up through the paddy box. The chimney gives a tall column of warm air to increase the airflow through the paddy by natural convection. The airflow is increased further if the air inlet to the bottom of dryer faces the direction of the prevailing wind. The paddy in the box is also heated up by direct absorption. Drying is thus by both direct and indirect heating modes. Experiments conducted during the wet season (Boonthumjinda, 1983) showed that:

- drying was faster in the top and bottom layers because of the subsequent increase in humidity of the air during its passage through the paddy bed and the direct heating effect of the top layer;
- stirring of the paddy bed reduced drying times by half;
- optimum bed depth during the wet season was 100 mm
- the use of a chimney reduced drying time by about 10%.

Boonthumjinda et al. (1983) reported that the main problems encountered during field tests of this solar dryer conducted in Thailand were:

- damage of plastic sheets caused by vandals, dogs, strong wind and heavy rain;
- short life span of the polyethylene sheets used and hence frequent replacement costs,
- loading and unloading was found to be slow and tedious.

The general experiences and opinions of farmers who participated in the field tests could be summarised as follows:

- construction materials should be changed in order to lengthen the life of the dryer and reduce general maintenance requirements;
- the dryer should be made transportable to simplify bringing the dryer to the paddy field;
- capacity should be increased to 2-5 tonnes to cope with the harvest.

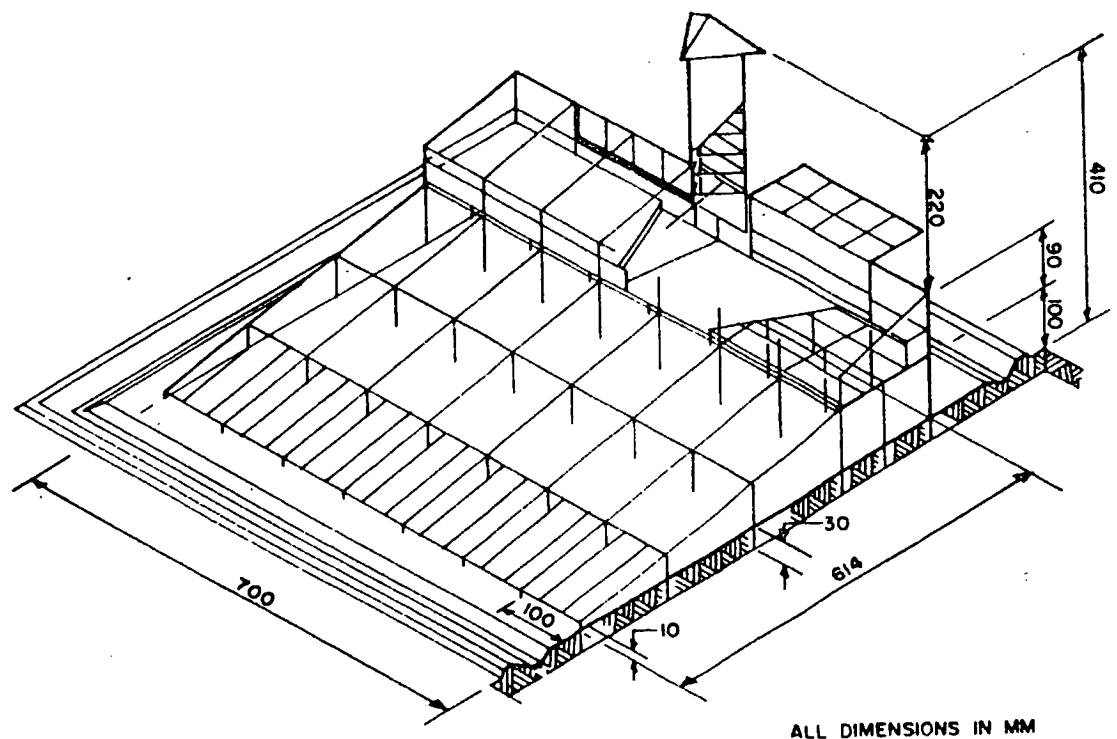


Figure 2.2 AIT solar paddy dryer (Exell et al., 1979)

Tongprasert (1978) has presented a theoretical evaluation of the performance of a forced circulation type solar paddy dryer. A mathematical model of the system comprising a drying chamber and solar air heater was formulated. A computer program was used to predict the system drying performance, which was checked by a small-scale experimental model. Results indicated that, with a collector area of 1 m^2 , the system could reduce the moisture content of 50 kg of wet paddy grain from about 22% to 16 % within 3.6 hours. A proposed prototype is shown in Figure 2.3. Grain handling could be greatly simplified by using this system.

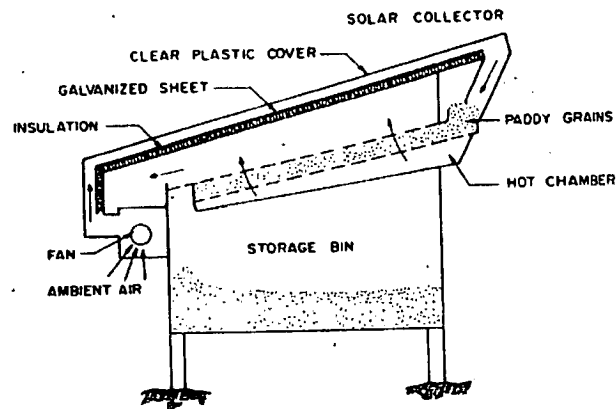


Figure 2.3 Solar rice dryer with forced air circulation (Tongprasert, 1978)

Soponronnarit (1985) evaluated a 1 t forced convection solar hut dryer. The dryer consisted of a drying-cum-storage barn with a roof-cum-collector flat-plate solar air heater as shown in Figure 2.4.

This integrated paddy-drying/storage solar hut comprised an 18.6 m^2 flat-plate solar air heater, two drying/storage rooms, a fan, and an air duct system. The solar heater was built on the roof of the hut from corrugated, galvanized steel sheets (the absorber). In order to simplify construction, it had no transparent cover. Air flowed through a 20 mm gap between the absorber and 25 mm thick Styrofoam.

The space inside the hut was divided into two rooms having perforated floor areas of 2.9 and 5.8 m^2 . About 1 t paddy (0.6 m deep) was transferred to the larger room for

storage. However, both could be used for drying and/or storage. The maximum storage capacity was about 10 t at a depth of 2 m.

A 0.3 m centrifugal fan with forward-curved blades, driven by a 3.7 kW diesel engine, was used to draw heated air from the solar air heater and pass it through the paddy in which drying took place. The fan could be driven by a power tiller engine or an electric motor. Normally, it was operated during the daytime at 1500-1900 rpm, corresponding to an engine speed of 1200-1500 rpm and a power requirement of 2.2-2.9 kW.

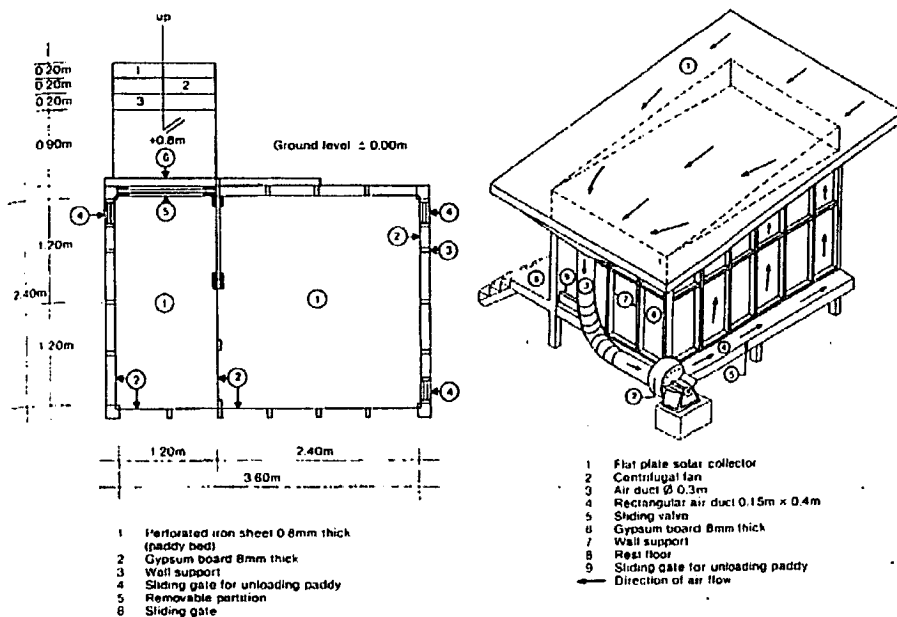


Figure 2.4 Integrated paddy-drying/storage solar hut (Soponronnarit, 1985)

The efficiency of the solar collector varied from 7-29% at airflow rates of 0.027-0.041 kg/s/m² of collector, with high variability due to changing of the wind velocity. Heat obtained from the solar air heater varied from 20 to 81 MJ/day when the global solar radiation was 15 MJ/m²/day.

Three runs of drying experiments were conducted during the wet season and 10 during the dry season. The resulting performance estimates indicated drying rates of 0.64 and 0.3 % wet-basis/t of dry paddy/h, and fuel consumption of the diesel engine driving the fan of 1.13 and 2.08 ℓ / t of dry paddy / 1 % wet-basis moisture reduction, for drying paddy during the dry and wet season, respectively.

The head rice yield after milling varied from 45-50 % and germination was greater than 92 %. About 7 t of paddy was stored in the solar hut for 5 months (January-May). It was found that the quality of the stored product remained high. There was no evidence of losses due to birds or rats.

The farmers who participated in this project were interested in drying wet paddy harvested during the wet season in order to prevent it from spoilage due to rain. They were also interested in storing paddy and selling it when the price was reasonably high. Their interest arose from the ease of operation of the hut and because it did not conflict with their traditional post harvest practices. However, they would not accept solar hut drying during the dry season because paddy could then be dried easily in the field within 2 or 3 days.

The integrated paddy drying and storage solar hut is seem to be an ideal dryer for the farmer who harvests about 10 t of paddy per season and grows two crops per year. However, energy consumption for drying is still high. This is due to the use of a centrifugal fan, which is needed to overcome the significant pressure loss in the system from the bed of paddy grain.

2.2.3 Rotary Paddy Dryer

Puechkamutr (1985) designed and constructed a natural convection rotary dryer for paddy. Components and details of this dryer are shown in Figure 2.5. The basic design concept was to dry free-flowing material such as grain by means of both conduction and convection heating from the pipe heat exchanger and the rotary cylinder itself during movement of the material. Air was heated by combustion of rice husks inside the furnace, and was passed through the pipe heat exchanger to avoid

direct contact of the fly ash and flue gas with the grain. The cylinder, having an inside diameter of 30 cm and 250 cm long, was arranged horizontally. Circular fins were fastened around the cylinder in the drying section to increase the heat transfer area in the dryer.

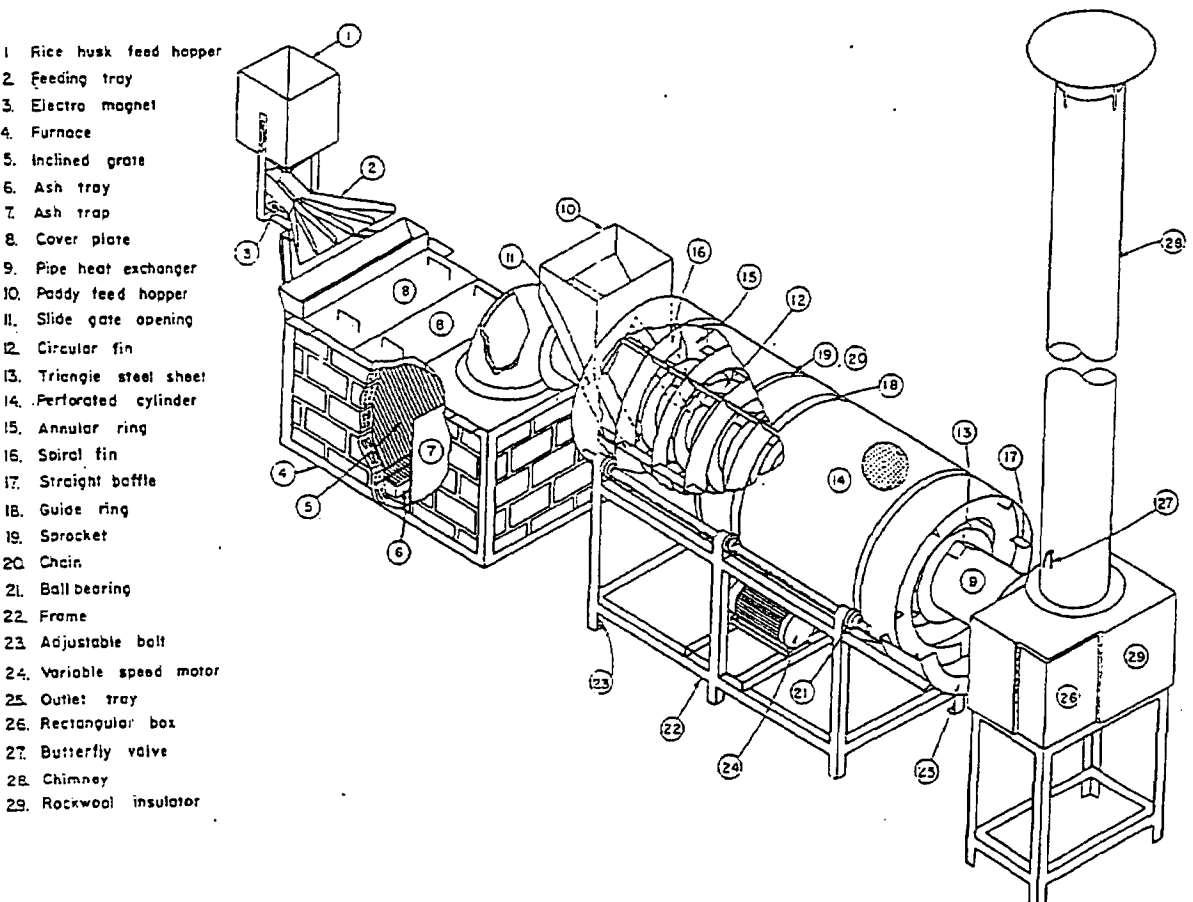


Figure 2.5 Natural convective rotary dryer (Puechkanutr, 1985)

2.2.4 Mixed Flow Paddy Dryer

In 1993, the government of Thailand set up two main projects for the use of mechanical dryers. The objective of the first project (duration of 2 years) was to extend loans with low interest rate to rice millers in order to purchase the Louisiana State University (LSU) type dryer, which had a capacity of 120 t/day. The objective of the second project (duration of 4 years) was to extend loans for 20 units of 100 t/day LSU-type dryers to government cooperative millers and 80 units of 20 t/day small-scale dryers, designed and developed by the AED for groups of farmers at the village level (Chamsingl et al., 2000).

The LSU dryer is a continuous flow, moving bed, heated-air, columnar, mixing type dryer. The drying chamber is shown in Figure 2.6. The flow of rice is diverted from a straight downward path by rows of baffles through which the heated air is introduced or exhausted. The pattern of airflow and path of rice flow for this dryer is illustrated in Figure 2.6.

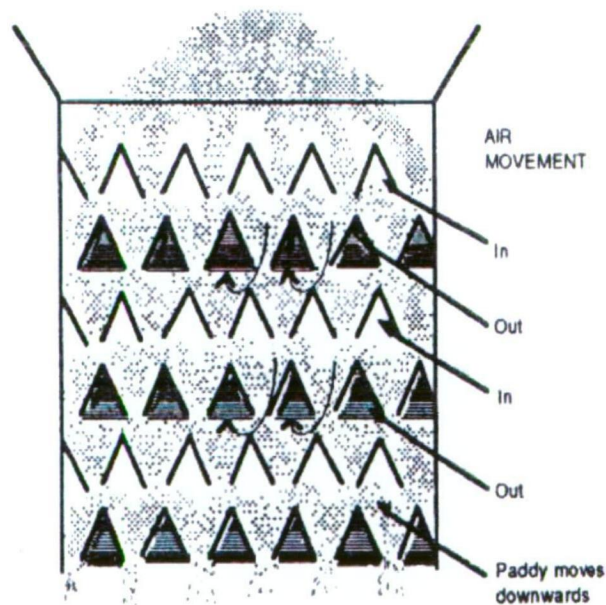


Figure 2.6 Drying chamber of the Louisiana State University dryer

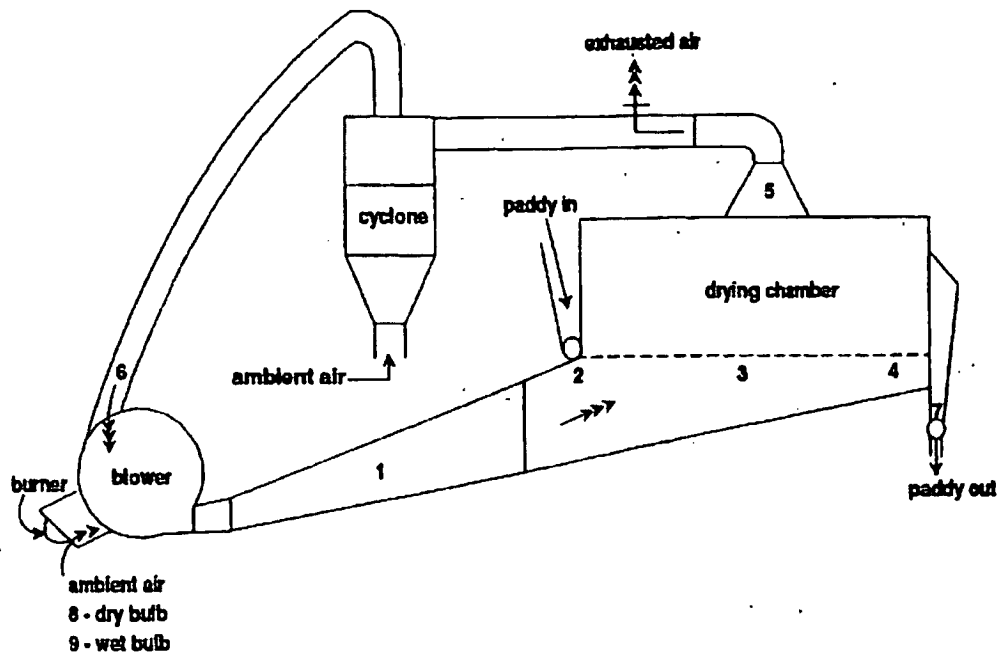


Figure 2.7 Diagram of fluidised bed paddy dryer (Soponronnarit et al., 1996a)

Throughout the wet season of 1994 the prototype fluidised bed dryer was used for drying high moisture content paddy. No repair was required. The owner of the rice mill assessed the unit as having:

- ease of use;
- very fast drying rate, especially at high moisture level;
- less energy consumption in terms of electricity and diesel fuel oil and more uniform product moisture compared to existing dryers.

Due to the success of the prototype, the owner of the rice mill where the prototype was tested ordered a larger fluidised bed dryer unit with an adjustable capacity of 2.5-5 t/h. Commercial fluidised bed paddy dryers with capacities of 5 t/h and 10 t/h were produced at the beginning of 1995 (Soponronnarit et al., 1996b). Figure 2.8 shows the components of the latter fluidised bed paddy dryer.

In order to make the fluidised bed paddy dryer more convenient to use, especially in harvesting areas remote from rice mills where electricity is not available, a project on

development of a mobile fluidised bed dryer with capacity of 2.5-4 t/h was proposed by Soponronnarit et al. (1998).

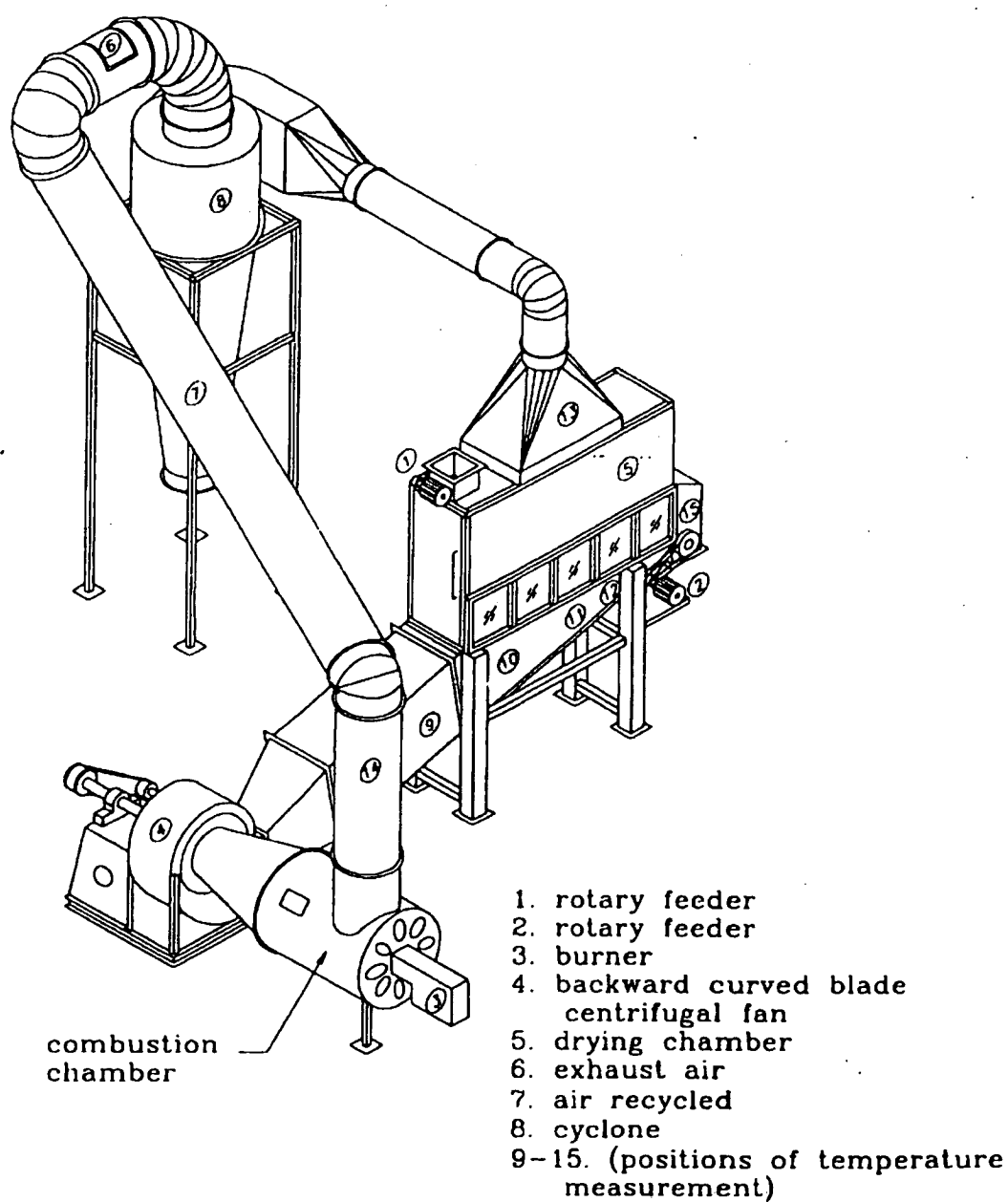


Figure 2.8 Fluidised bed paddy dryer (Soponronnarit et al., 1996b)

The mobile fluidised bed dryer was designed and constructed by the research group on drying technology at King Mongkut's Institute of Technology Thonburi. The capacity was 2.5-4 t/h. The dryer was installed on a 2x4 m trailer. It comprised a diesel burner, 0.6x2.1x0.8 m drying chamber and paddy hopper, backward-curved blade centrifugal fan driven by an 11.2 kW motor, 2 bucket elevators, cyclone and cyclo-fan as shown in Figure 2.9.

After construction, the unit was installed and tested at a private rice mill. Suitable drying conditions were recommended as follows:

- drying capacity 3.8 t/h;
- bed velocity 2.8 m/s;
- average drying air temperature 144°C;
- bed height 13.5 cm;
- fraction of air recycled 0.8;
- residence time of paddy approximately 1.3 minutes.

Test results showed that the moisture content of paddy was reduced from 32.6% to 25.8% dry basis. Consumption of electrical power and diesel fuel were 12.9 kW and 21.71 ℓ / h, respectively. Specific energy consumption was 4.2 MJ/kg water evaporated.

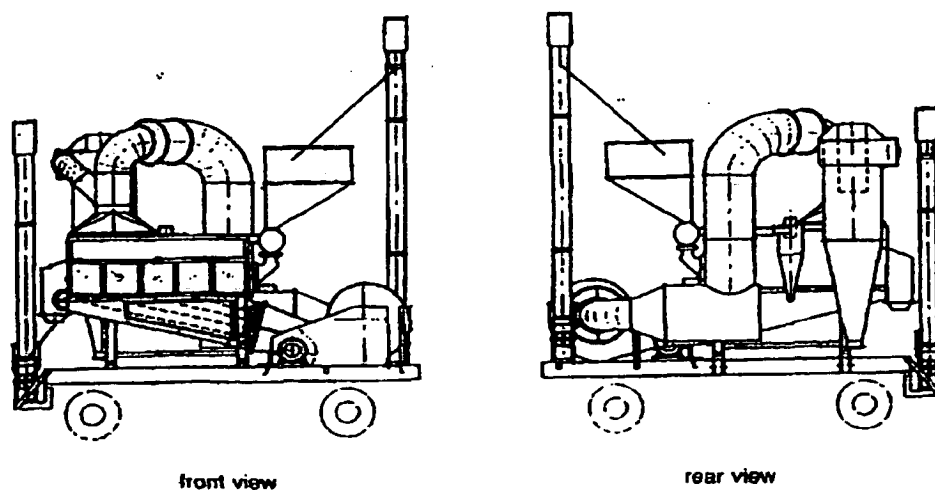


Figure 2.9 Mobile fluidised bed paddy dryer (Soponronnarit et al., 1998)

Due to the success of the fluidised bed paddy dryer development and the requirement to reduce electrical power of the blower motor, Soponronnarit et al. (2001) conducted research aimed at designing, constructing and testing a vibro-fluidised bed paddy dryer with capacity 2.5-5 t/h, and developed a mathematical model to determine optimum operating parameters.

A vibro-fluidised bed paddy dryer was fabricated and tested at a private rice mill. The unit comprised a diesel burner and combustion chamber, a backward-curved blade centrifugal fan driven by a 7.5 kW motor, 0.6x2.1x1.2 m drying chamber and 0.6x2.1 m perforated steel sheets with 0.5 mm thickness and 1.1 mm hole diameter. The vibration system comprised cams, coil springs, watch springs, a 1.5 kW vibration motor with vibration frequency of 7.3 Hz and vertical amplitude of 5 mm, hopper, rotary feeder, rotary discharger, recycle air duct and cyclone. A diagram of the vibro-fluidised bed paddy dryer is shown in Figure 2.10.

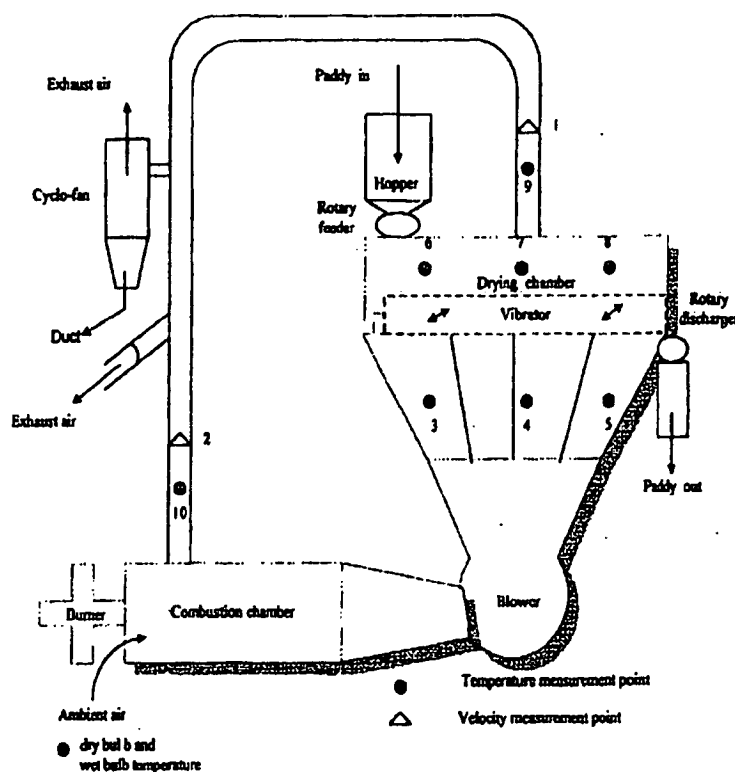


Figure 2.10 Diagram of vibro-fluidised bed paddy dryer

(Soponronnarit et al., 2001)

Experimental drying conditions were: airflow rate 1.7 m³/s; bed velocity 1.4 m/s; average drying air temperature 125-140°C; residence time of paddy approximately 1 minute; bed height 11.5 cm; fraction of air recycled 0.85; and vibration frequency 7.3 Hz and amplitude 5 mm. With a paddy feed rate of 4821 kg/h, moisture content was reduced from 28 to 23 % dry-basis. Specific energy consumption was 6.15 MJ/kg water evaporated. The total electrical power of the blower motor and vibration motor was 55% of the blower motor power used in fluidised bed drying without vibration.

2.2.6 Spouted Bed Paddy Dryer

Wetchacama et al. (1999) conducted experiments of paddy drying in a two-dimensional spouted bed dryer. Experimental results showed that a linear equation was suitable for describing the drying rate of paddy, which depends on the hold-up and drying temperature. The combination of two distinct hydrodynamic features, viz, the pneumatic transport of particles in the spouted bed (which allows intensive heating and moisture evaporation) and a falling bed in the downcomer (where tempering of particles takes place) are the main features of the spouted bed.

Madhiyanon et al. (2001) have studied drying of paddy in an industrial-scale prototype spouted bed dryer with capacity 3.5 t/h as shown in Figure 2.11. The dryer consisted of a vertical rectangular chamber 0.6 m in width, 1.45 m in height, and 2.1 m in length. The front wall and both of the sidewalls just above the slanting base of the drying chamber were fitted with glass windows to permit visualisation of the grain flow pattern. The slanting base was inclined at 60 ° to horizontal. The air entrance and spout widths were 0.04 and 0.06 m, respectively. The draft plates were centrally installed. The entrance height was varied to match the feed rate of paddy.

Heat derived from burning diesel fuel was supplied to heat the air before it entered the blower. The heated air was forced through the ductwork connected to the drying chamber. Hot and humid air leaving the drying chamber was discharged into a cyclone with some portion of it exhausted to atmosphere. The rest (approximately 60-70% of total circulated air) was recirculated and mixed with ambient air at the combustion chamber.

The paddy travelled upward through the draft channel before raining back onto the downcomers and moving vertically downward. The paddy movement alternated between spout and downcomer until paddy came out of the bottom of the drying chamber.

Experimental results showed that the prototype performed well in reducing the moisture content of the paddy and yielded high product milling quality. High temperatures up to 130-160 °C were applied to dry paddy from various initial moisture contents to the range of 14-25% dry-basis without significant change in quality. Specific energy consumption was 3.1-3.8 MJ/ kg water evaporated.

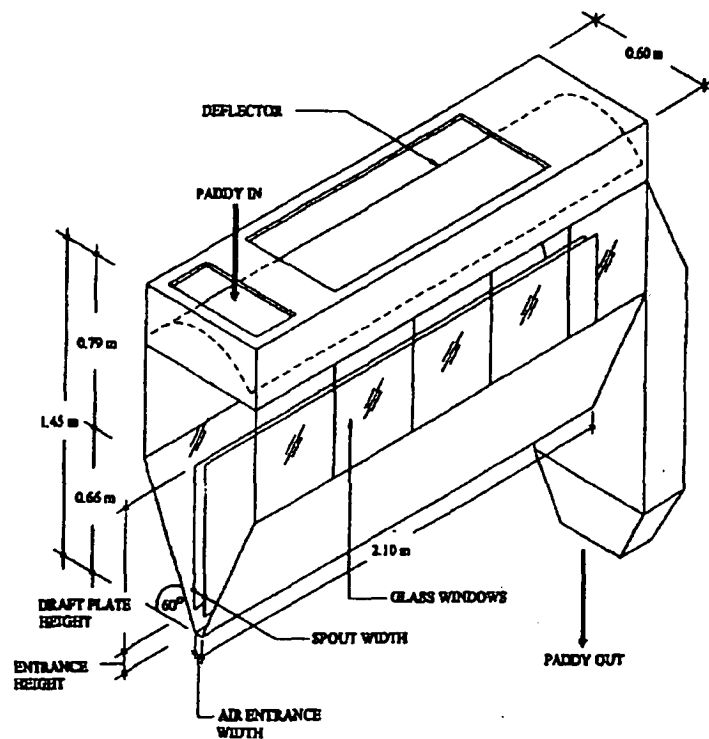


Figure 2.11 Industrial-scale prototype spouted bed dryer (Madhiyanon et al., 2001)

2.3 COMMERCIAL PADDY DRYERS

As stated in Section 2.3.2.1, many researchers and research groups in Thai universities and government institutes have evaluated dryer prototypes of varying

designs and capacity. These prototypes were tested for appropriateness at the farm level, and at cooperatives and commercial millers.

The greatest resistance to artificial drying is understandably at the farm level of operation. Government programs have generally encouraged the use of small flat bed dryers compatible with the volume of production in each farm, whose size typically ranges between 0.25 and 3 hectares. Despite the need for dryers at this critical level of operation, the acceptance of farm dryers was low. The major causes of this situation are (Fredericks et al., 1985):

- high acquisition costs beyond the reach of small-scale farmers due to low production volume;
- unsatisfactory performance of some drying systems introduced;
- lack of technical know-how in dryer operations, resulting in inefficiency and poor milling results;
- capacity of dryers incompatible with farm production and other processing equipment; and
- the price structure of paddy, which does not seem to reflect adequately the cost of drying.

A suitable farm dryer is one that is mobile, uses high temperature heat with very short exposure and residence time of the grain, and provides mixing of the grain. It can be made cost-effective when operated on a custom basis, as in the case of the mobile paddy thresher (Tumaming, 1987).

Commercial rice dryers seem to have been successfully developed at the cooperatives and commercial millers. The continuous moving bed dryer type called the LSU dryer was developed by Louisiana State University in the mid-1950s. This design was developed specially for rice, to ensure gentle treatment, good grain mixing, and good air-to-grain contact. The LSU dryer has become the most widely accepted mechanical paddy dryer for cooperatives and commercial millers in Thailand. Further development of the continuous dryer has resulted in the fluidised-bed dryer.

Commercial designs for fluidised-bed paddy dryers are now available. The principle of operation is to provide sufficient air pressure of fluidise a thin bed of grain, giving

excellent air/grain contact. Above a certain pressure, related to the weight per unit area of the paddy bed, the pressure drop across the bed becomes constant with volume flow rate, so that fast drying can be achieved. By combining high air temperatures and suitable grain tempering, the fluidised bed offers better economy, gentler grain handling, and reduced drying times over the LSU dryer.

A combination drying system, in which a single-pass fast-drying stage is followed by a multi-pass second stage, had been used in large rice mills of Thailand. The high moisture grain is dried rapidly to about 18% wet-basis using a fluidised-bed dryer in the first stage. The second-stage is done gently in an LSU type dryer (Rordprapat et al., 1999). The combination and arrangement of the fluidised-bed paddy dryer and LSU type dryer differs from rice mill to rice mill. Rordprapat et al. (1999) show the arrangements of paddy drying systems for three different rice mills (Figures 2.12-2.14).

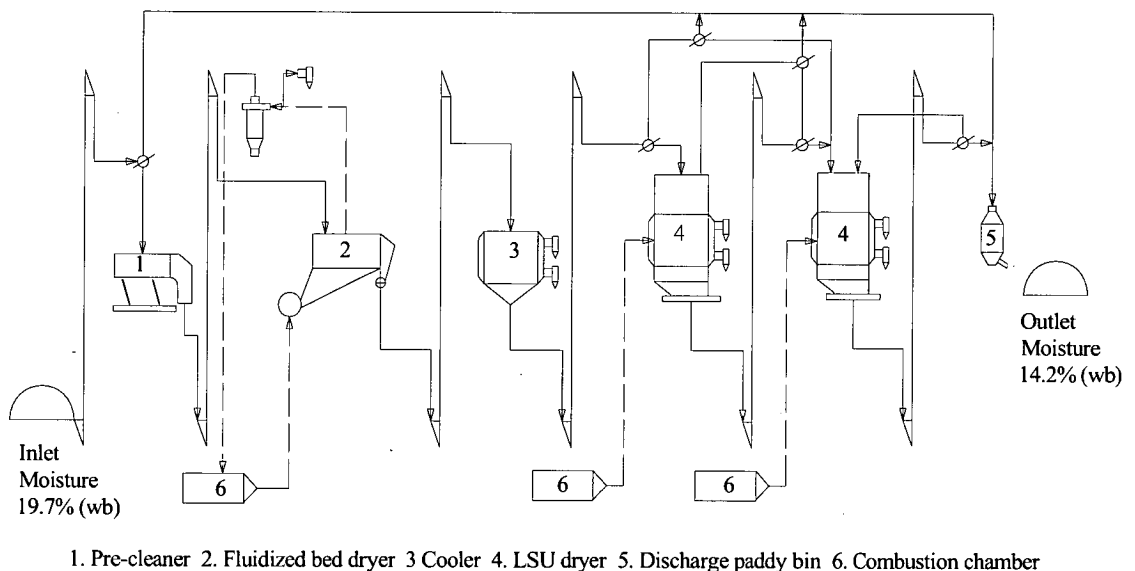


Figure 2.12 Paddy drying system in Supanthaanya rice mill (Rordprapat et al., 1999)

The first system arranges a fluidised-bed dryer, cooler and two LSU-type dryers in series. Paddy with bed depth 15 cm is exposed to 130 °C air in the fluidised-bed dryer; moisture content at the exit is 19.4 % wet-basis. It is then passed through the cooler for 10 minutes to reduce the temperature. The first and second LSU-type

dryers, each with a capacity of 6 t, provide second and third stages of drying at 100 °C and 90 °C air temperature, respectively. Moisture contents at exit from the first and second LSU dryers are 14.9 and 14.2 % wet-basis, respectively.

Another arrangement is shown in Figure 2.13. A fluidised-bed paddy dryer is connected to four parallel LSU-type dryers. Paddy with a bed depth of 15 cm is exposed to 110 °C air in the fluidised-bed dryer; moisture content at the exit is 18 % wet-basis. It is then passed through a cooler for 10 minutes to reduce the temperature. The following stage of drying is done in an LSU dryer with a capacity of 7 t. Paddy is passed through the LSU dryer four times at 75 °C air temperature; each pass takes 1 hour during which the paddy is tempered for 21 minutes. The final moisture content of paddy at exit is 14.9% wet-basis.

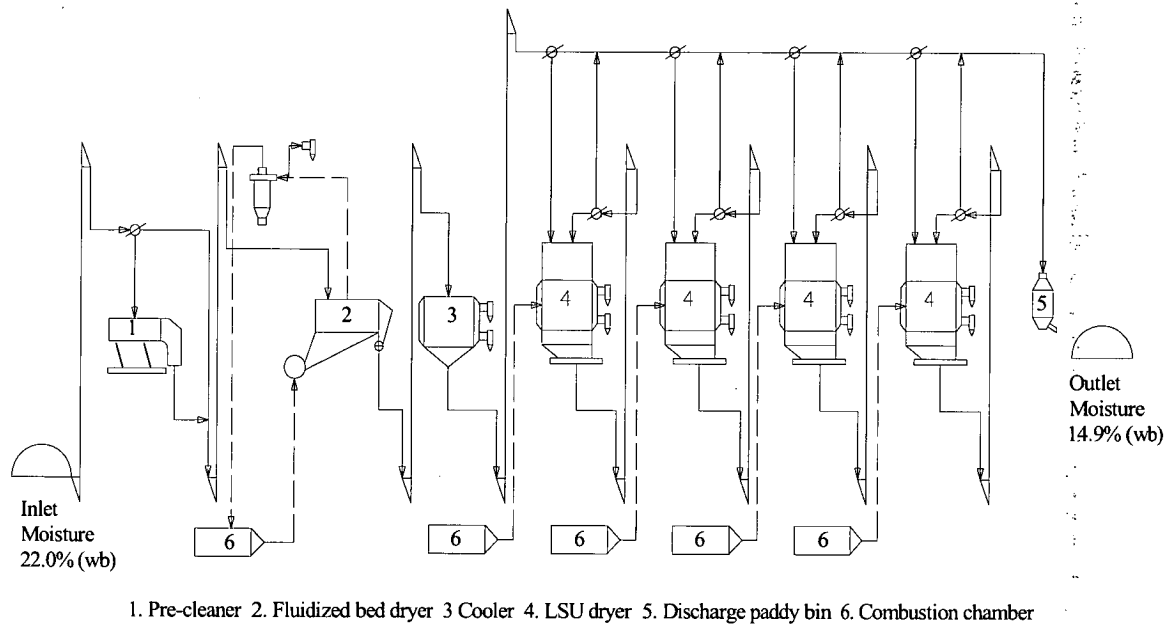
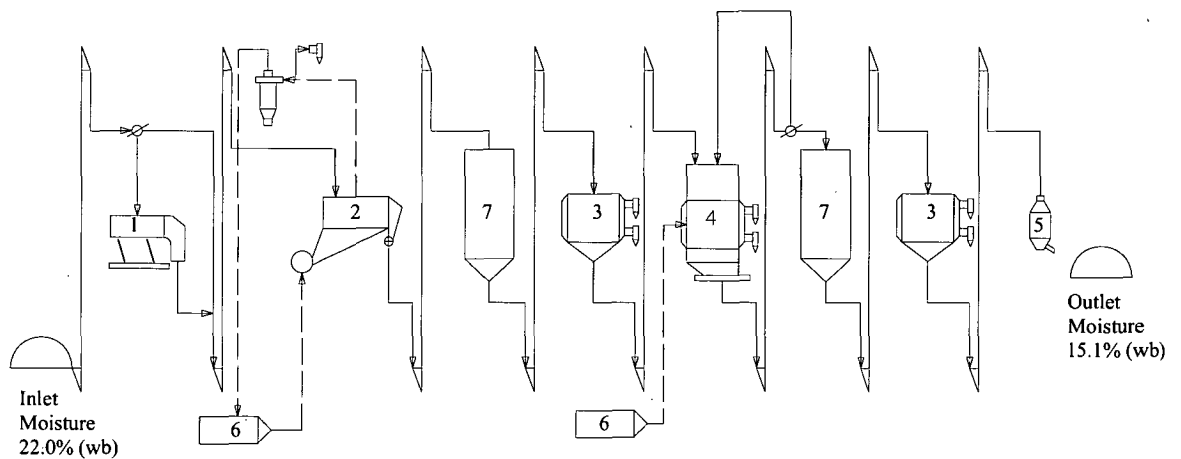


Figure 2.13 Paddy drying system in Poonsinthalai rice mill (Rordprapat et al., 1999)

The third arrangement shown in Figure 2.14 incorporates a tempering bin. A fluidised-bed paddy dryer and LSU-type dryer are arranged in series. They are followed by a tempering bin and cooler arranged in series. Paddy with a bed depth 15 cm is exposed to 110 °C air in the fluidised-bed dryer; moisture content at the exit is 17 % wet-basis. It then passes through the cooler to reduce the temperature and is kept in the tempering bin for 3.6 hours. The LSU-type dryer does the following stage of drying with 80 °C of air temperature; moisture content at exit is 15.6 % wet-basis.

Finally, paddy is kept in the tempering bin for 4.6 hours and cooled in the cooler, giving a final moisture content of 15.1% wet-basis.



1. Pre-cleaner 2. Fluidized bed dryer 3 Cooler 4. LSU dryer 5. Discharge paddy bin 6. Combustion chamber 7. Tempering bin

Figure 2.14 Paddy drying system in Taweerungruang rice mill

(Rordprapat et al., 1999)

The performance of the above three paddy drying systems with the same type of components but different arrangements was investigated by Rordprapat et al. (1999). The paddy quality and energy consumption of each dryer component in each system were studied. These studies found that the arrangement of dryers and temperature during each drying stage affected the overall performance of the drying system.

2.4 EFFECT OF OPERATING PARAMETERS ON RICE QUALITY

The drying operation is not merely considered as the removal of moisture content, as there are many factors that can be adversely affected by incorrect selection of drying conditions and equipment. The objective of the rice drying process is to maximise the drying capacity of a rice dryer with a minimum loss in head rice yield and a minimum consumption of energy, without affecting the colour and cooking characteristics of the rice.

The head rice yield is defined as the proportion of rice having a length at least 8/10 of the intact rice kernel. Percentage of head rice provides an estimate of the quality of head rice and total milled rice produced from a unit of paddy. Colour of rice is defined as kernel whiteness, which is measured by a colour difference meter. Low readings indicate the kernel is browning and will be graded as a low quality. Acceptable values of whiteness for commercial rice millers are not less than 37.

The head rice yield varies with final moisture content and exposure time during drying. Studies of the effect of drying on rice quality were conducted by Jindal et al. (1986) and Reyes et al. (1988). Their studies used a rotary conduction unit with various levels of moisture content and exposure time, and produced similar results. As indicated in Figures 2.15 to 2.17, heat-treated paddy samples showed an initial increase in head rice yield depending on the exposure time, heating surface temperature and initial moisture content. A marked improvement of head rice yield was observed in rice samples having an initial moisture content of 30% wet-basis. The increase in head rice yield was attributed to the gelatinisation of starch granules and cementing of fissures present in the kernel, which prevents excessive breakage during the milling operation. These results indicate that, in general, continuous rapid drying of high moisture paddy can be safely carried out to a final moisture content of about 16 % wet-basis.

The factors affecting rice quality during fluidised bed drying were investigated by Soponronnarit et al. (1994). Head rice yield was compared to a reference sample of paddy dried in ambient air. Figure 2.18 shows the relationship between relative head rice yield and final moisture content for an initial moisture content of 43.5% dry-basis. Head rice yield dropped rapidly when moisture content reached about 23-26% dry-basis. Due to the relatively fast drying rate, grain surfaces rapidly became hard, resulting in cracking of grain kernels with further drying. For a drying temperature of 150 °C, relative head rice yield increased when moisture content decreased. This was due to the gelatinisation effect observed by Jindal et al. (1986) and Reyes et al. (1988), in high temperature heat treatment of paddy by a rotary conduction dryer.

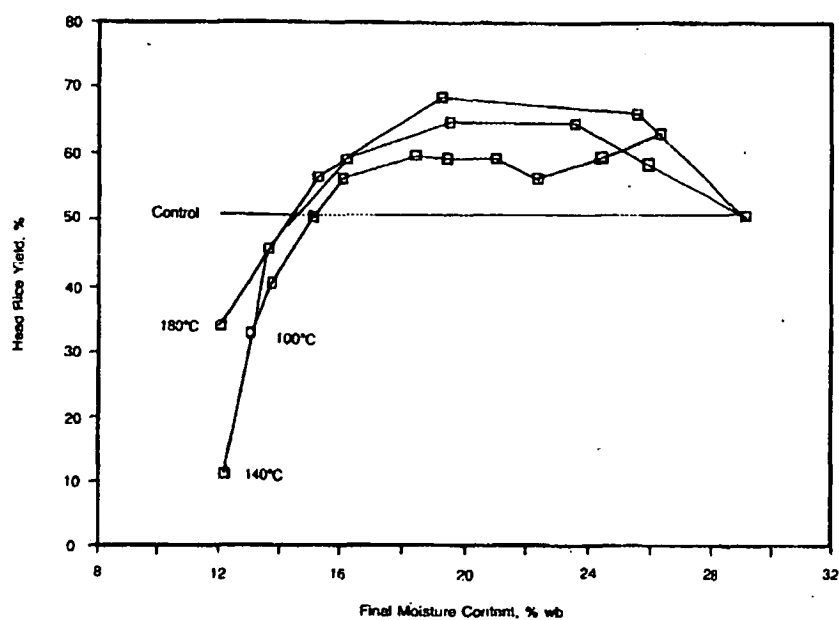


Figure 2.15 Head rice yield as a function of final moisture content of paddy (agitation speed 14 rpm; feed rate 30 kg/min) (Jindal et al., 1986)

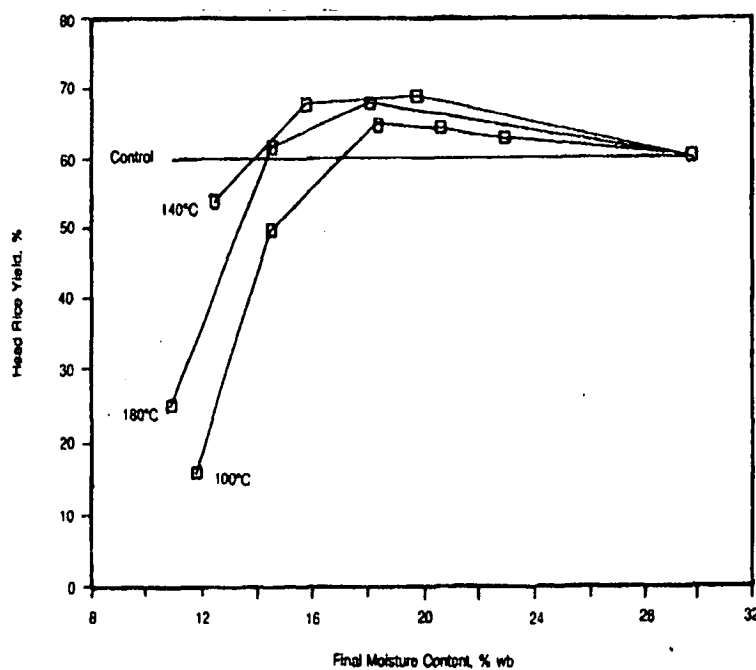


Figure 2.16 Head rice yield as a function of final moisture content of paddy (agitation speed 30 rpm; feed rate 30 kg/min) (Jindal et al., 1986)

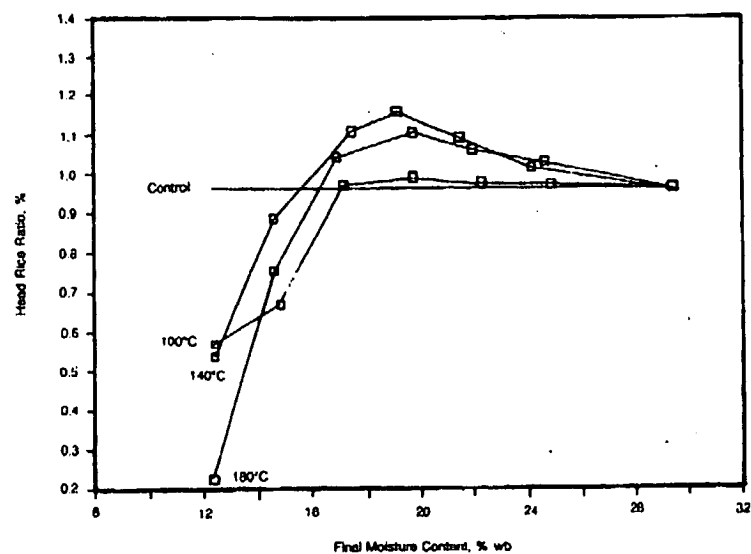


Figure 2.17 Head rice yield as a function of final moisture content of paddy (agitation speed 40 rpm; feed rate 30 kg/min) (Jindal et al., 1986)

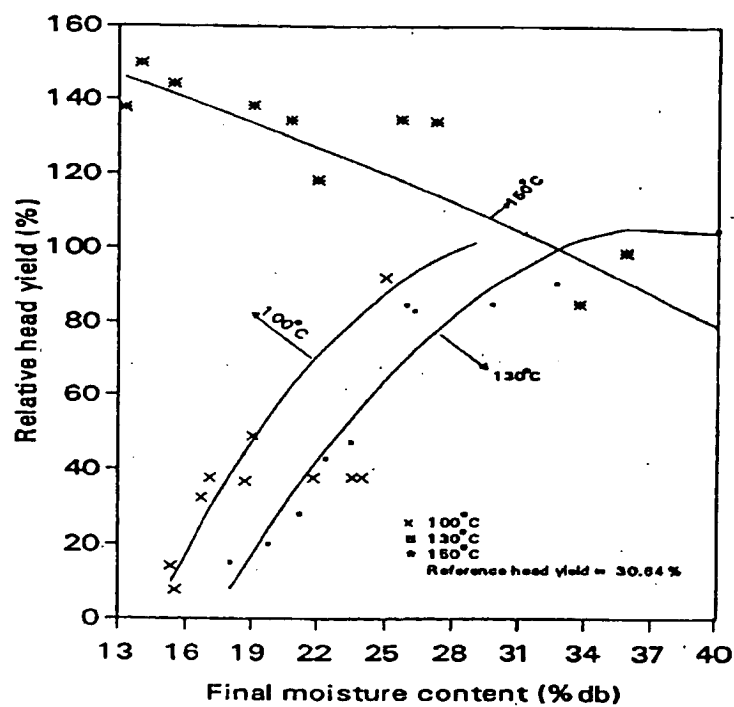


Figure 2.18 Relationship between relative head rice yield and final moisture content in fluidised bed drying at different temperatures (Initial moisture content 45.3% dry-basis) (Soponronnarit et al., 1994)

Figure 2.19 shows the relationship between relative whiteness and final moisture content for an initial moisture content of 45.3% dry-basis. The relative whiteness of rice kernels was still acceptable (relative whiteness more than 80%) for all final moisture content values when paddy was dried at 100 °C of heated air. For higher air temperatures (130, 150 °C), relative whiteness decreased rapidly with decreasing final moisture content. Drying temperature therefore needs to be limited to maintain whiteness of the rice kernel. Over-heating during drying causes rice kernels to turn yellow.

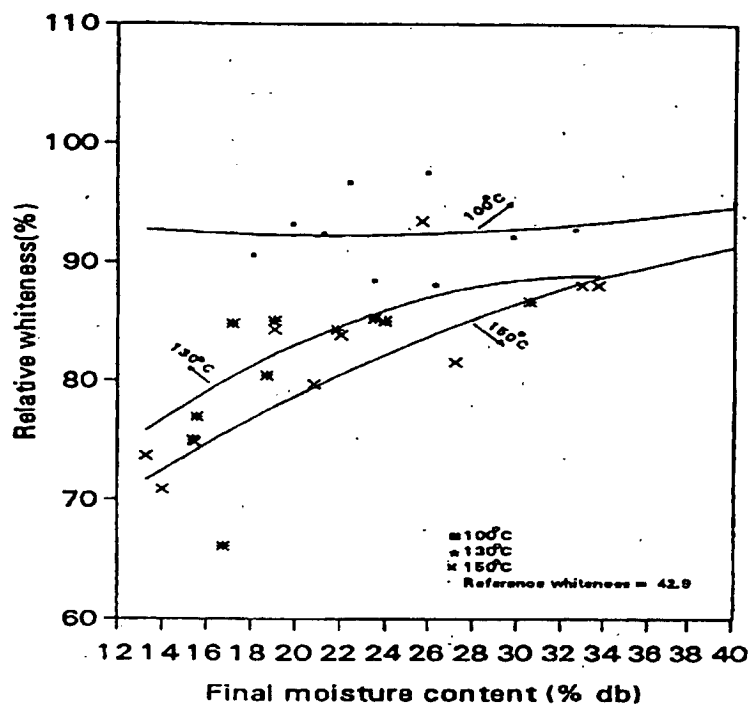


Figure 2.19 Relationship between relative whiteness and final moisture content in fluidised bed drying at different temperatures (Initial moisture content 45.3% dry-basis) (Soponronnarit et.al., 1994)

It was concluded from these results that air temperature during drying by the fluidised bed technique should not be higher than 115 °C to maintain whiteness of the rice kernel; the final moisture content should not be lower than 23% dry-basis to maintain the quality of head rice yield.

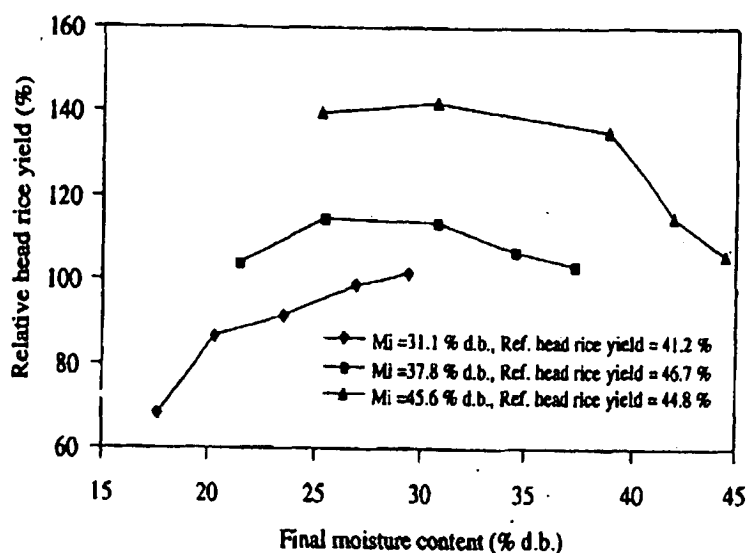


Figure 2.20 Relative head rice yield at different initial moisture contents.

Inlet air temperature 150 °C (Wetchakama et al., 1999)

Wetchakama et al. (1999) conducted experiments to investigate the quality of high moisture content paddy drying using the two-dimensional spouted bed technique. Figure 2.20 shows the relationships between the relative head rice yield and the final moisture content of paddy at an inlet air temperature of 150 °C, a hold-up of 30 kg, and initial moisture contents of 31.1, 37.8 and 45.6 % dry-basis. The relative head rice yield compared to the reference sample was higher for initial moisture contents of 37.8 and 45.6 % dry-basis, with values over 100 % indicated. The relative head rice yield reduced continuously with decreasing final moisture content for the case of an initial moisture content of 31.1% dry-basis. Such higher percentages of head rice yield can be explained by the gelatinisation effect in which molecules of the starch granules are vibrated and the chemical bonds are deformed, resulting in water molecules being transported to them and forming hydrogen bonds. Eventually, when both moisture and temperature levels are appropriate, gelatinisation occurs. For temperatures of 130 and 140 °C, and initial moisture contents of 37.8 and 45.6 % dry-basis, the results showed a similar trend to Figure 2.21, giving an increase of relative head rice yield.

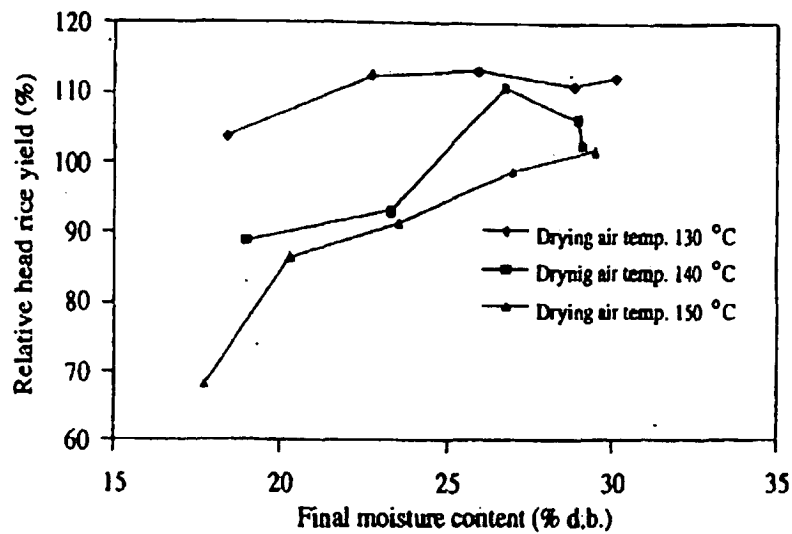


Figure 2.21 Relative head rice yield at different inlet air temperatures
Initial moisture content 31.1 % db. (Wetchacama et al., 1999)

The relative head rice yield for an initial moisture content of 31.1 % dry-basis reduced progressively with decrease of final moisture content, as shown in Figure 2.21. In this case, the inlet air temperature seriously affected relative head rice yield; significantly lower yields were obtained by using higher drying temperatures with the same final moisture level. This behaviour differs from that in Fig 2.20, particularly at moisture contents higher than 37.8 % dry-basis, where there is a remarkable increase of head rice yield during the reduction of moisture content. The reduction of head rice yield for paddy possessing lower moisture contents is due to large gradients of moisture inside the grain kernel leading to the formation of stress cracks.

Fig 2.22 shows the relationship between the relative rice whiteness and final moisture content. At initial moisture contents of 31.1-45.6 % dry-basis, a hold up of 30 kg and an inlet air temperature of 150 °C, the results indicated that the relative rice whiteness continuously decreased during periods of reducing moisture content. The relative rice whiteness curve for the initial moisture content of 45.6 % dry-basis showed a steep drop in colour values from 100 % at the start to 62 % at a moisture content of 25 % dry-basis, whereas the rice whiteness values for an initial moisture content of 31.1 % dry-basis changed insignificantly with the final moisture content. The reason for this

is the long drying time for removing the moisture content of 45.6 % dry-basis. The drying time clearly has a strong influence on the colour change of paddy.

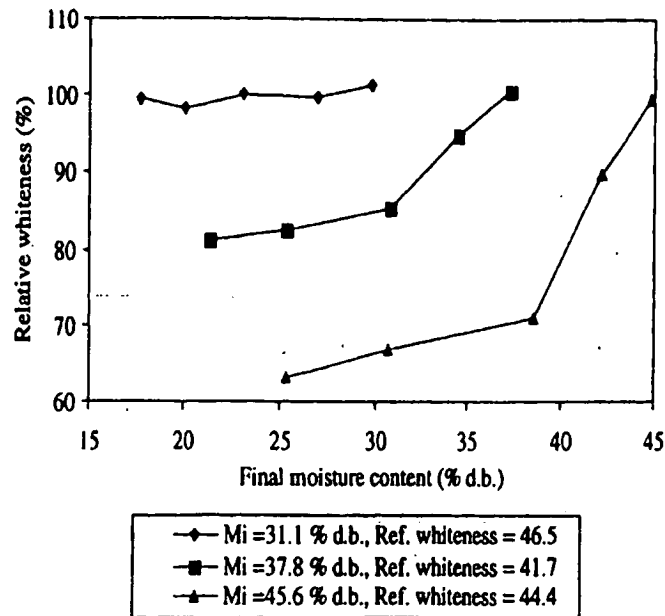


Figure 2.22 Relative rice whiteness at different initial moisture contents (Wetchacama et al., 1999)

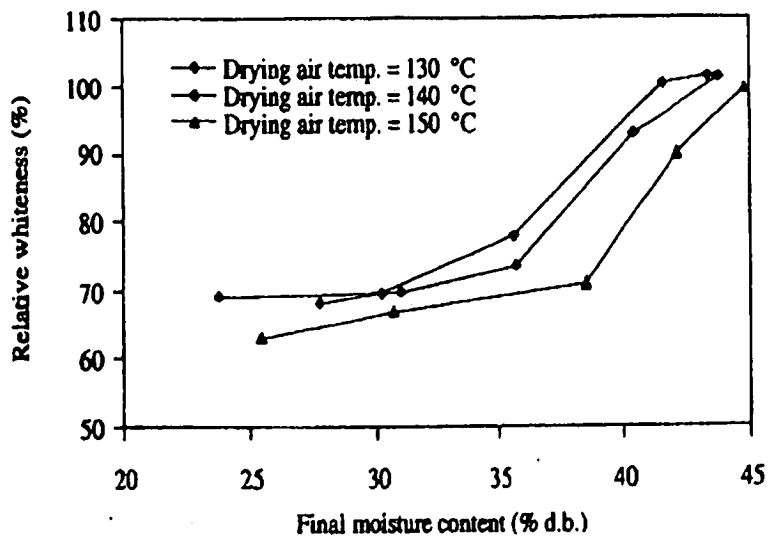


Figure 2.23 Relative rice whiteness at different inlet air temperatures (Wetchacama et al., 1999)

The influence of drying air temperature on rice whiteness is shown in Fig 2.23. It is clearly evident that for the same final moisture content the use of higher drying air temperatures produces lower values of relative rice whiteness, despite the shorter drying time. In all cases, the colour rapidly decreases during the initial period of drying and then slowly declines during the remainder of the drying period.

As stated by Kelnin et al. (1986), paddy is a cereal crop in which carbohydrates predominate. The structure and chemical composition of the seeds of cereal crops permit as much as 60 % moisture removal during one pass through a dryer. If a lower moisture content is required, further passes through the dryer can be needed. To avoid stress cracking of rice kernels, continuous flow dryers are used in association with tempering bins. After each drying pass of the grain, it is held in a tempering bin where the moisture within the kernel equalises as moisture diffuses from the interior to the surface.

The effects of tempering time on head rice yield and rice whiteness was studied by Taweerattanapanich (1999). A batch-type fluidised bed dryer was used in these experiments. Paddy was dried from moisture contents of 23-31 % wet-basis to 13-29 % wet-basis at air temperatures of 140-150 °C. Then the paddy was further dried in a tray dryer with ambient air to 14 % wet basis with and without tempering. The effect of tempering time on head rice yield and whiteness was investigated

Head rice yield was significantly increased when the paddy was tempered for 0-12 hours. The higher head rice yield of tempered paddy resulted from moisture redistribution during the tempering period which reduced the stress cracking during the subsequent tray drying. For 2-8 hour tempered paddy, whiteness was slightly decreased but it was still in the acceptable range for the rice trade. For tempering times longer than 8 hour, the whiteness of rice was further decreased and would have made the products less acceptable for sale.

2.5 POTENTIAL TECHNOLOGY FOR PADDY DRYING

As shown earlier in this chapter, a wide choice of technologies is available for drying paddy. For high moisture content paddy harvested in unfavourable weather conditions, especially during the wet season, it has been suggested that drying the grain in two stages can achieve acceptable results (Tumaming, 1987).

Two-stage drying can be done in various ways, depending upon the drying technology available, final grain quality desired, weather conditions in the area, and level of operation. The idea of two-stage drying is to rapidly dry the high moisture content down to a more manageable level (around 18% wet-basis) using high-speed dryers (e.g. batch dryer, continuous-flow dryer), or by sun drying if the weather is favourable. At this level, paddy may be held for up to three weeks in tropical climates before excessive deterioration occurs (Driscoll et al., 1986). The second stage of drying reduces moisture to the optimum moisture content of 14% wet-basis. The final drying to 14 %wb. is done in-plant using continuous-flow driers or by gentle drying in storage. Where solar drying is done properly, mechanical drying in combination with solar drying is an alternative two-stage drying system.

Sun drying is still the most widely used method of drying high moisture grain whenever the sun shines. In this method, paddy is spread into thin a layer over concrete floor and stirred periodically by a grader blade as shown in Figure 2.24.

Due to the unreliability of sun shine in the wet season, mechanical drying is the more sunshine effective method. The earliest form of mechanical dryer was the batch (fixed bed) dryer. It was developed for individual farmer operation, but found unattractive by farmers. Farmers who lacked understanding of the technical aspects of mechanical drying blamed the dryer for yielding poor quality processed grain, whereas the poor results were really due to improper adjustment of temperature, airflow and other drying conditions.



Figure 2.24 Sun drying of paddy on a concrete floor

Continuous-flow dryers that move the grain continuously through the dryer exist in many forms. They must be used with a multi-pass drying procedure to obtain higher drying capacity and good quality grain. They also require a system incorporating tempering bins and conveying equipment. Therefore, the potential users of continuous-flow dryers are commercial millers or farmer cooperatives. Large millers have also invested in these types of grain dryer, but the performance has been less than satisfactory, due to a lack of technical know-how in their operation. They are often installed without tempering bins and operated at higher drying temperatures for one-pass drying. This inevitably leads to a high percentage of broken grains.

Commercial designs for fluidised-bed paddy dryers now exist. By combining high air temperature and suitable grain tempering, the fluidised-bed offers better economy, gentler grain handling, and reduced drying time compared with continuous-flow dryers. Similar results occur during drying in a spouted-bed dryer. The whole bed of grain is continually being heated and dried, so the process is very energy-efficient and uniform, and the grain is automatically stirred in a spouted-bed dryer. The spouted-bed dryers process large volumes of wet grain quickly. They are used with conveying equipment, and are usually associated with bulk handling and storage systems and large potential users of continuous-flow dryers.

In spite of the many drying technologies resulting from past decades of research and development there is still work to be done, especially in designing drying systems compatible with specific drying requirements at the individual farmer level. This is especially true for the second crop when paddy is normally harvested at high moisture content (24-28 %wb). Drying of paddy from 24-28 %wb to 18 %wb is the only known method to prolong the storage life of grain and increase the selling price. A suitable dryer for this type of operation is one that is mobile, uses high temperature heat, and has very short exposure and residence time of the grain. It must be attractive for individual farmers, if it operated on a custom basis as for the mobile paddy thresher and combine harvester.

The type of dryer with the most potential for individual farmers' operation is the pneumatic dryer, in which solids are conveyed concurrently with the air stream. In the pneumatic dryer, the solid is dried while being transported. The basic and most commonly used form is the flash dryer. Drying takes place in a vertical tube up which warm air flows with velocity greater than the free-falling speed (terminal velocity) of the largest particles in the wet feed. The wet feed is introduced at the bottom of the tube by means of a suitable feeder.

At the top of the tube, dried product is collected by means of a cyclone or another collection device. The very short residence time of solids makes the flash dryer well suited to remove easily accessible surface moisture in the first drying stage, called the "constant rate period".

A mathematical model of paddy drying in a simple pneumatic dryer will be developed in the next chapter to investigate the drying behaviour of this kind of machine.

Chapter 3

MATHEMATICAL MODEL FOR PADDY DRYING IN A SIMPLE PNEUMATIC DRYER

3.1 INTRODUCTION

This chapter describes paddy grain (rice) drying in a pneumatic conveyor where gas-particle heat and mass transfer occur simultaneously with transporting and drying operations. A one-dimensional macroscopic drying model of the overall bed incorporating mass and energy balances, and drying kinetics of moisture diffusion inside the paddy grain is developed. The set of coupled non-linear ordinary differential equations is solved numerically to illustrate the evolution of moisture and temperature of the paddy grain and air stream throughout the dryer length. The effect of specific air flow rate, which depends on dryer diameter, paddy feed rate and inlet-air velocity on the final moisture content and temperature of the paddy grain and air stream is studied. The feasibility of paddy drying in a pneumatic conveyor for the first stage of a two-stage drying process is evaluated using the developed model, and found to be impractical because of the unduly large conveyor length requires.

As discussed in detail in Chapter 2, paddy grain is normally harvested from the field with a moisture content of about 24-28 % wet basis (wb), which results in high yields and prevents field loss due to dropping and shattering. However, this moisture content is too high for safe storage and the grain must be dried to a moisture content of 14 % wet basis to ensure long storage life and high milling quality. Owing to the high moisture content of the harvested paddy and unfavourable weather conditions, especially during the wet season, paddy drying is usually carried out in two stages. In the first stage, the high moisture content is rapidly reduced to a more manageable level (around 18-19 % wb) using fast rate drying. This is an appropriate final moisture content for fast rate drying because the percentage of head rice yield decreases significantly when the final moisture content is lower than 18-19 % wb. Excessive moisture removal during fast rate drying could induce stress cracking and lower the head rice yield.

At 18-19 % wb moisture content the paddy can keep for up to three weeks without excessive deterioration in quality. During that period, the moisture content of paddy can be reduced to 14 % wb using a second-stage slow rate dryer. For the individual farmer, immediate threshing and drying of wet harvested paddy to 18-19 % wb moisture content is a practical method to arrest deterioration and increase selling price. A suitable dryer for this purpose is a compact mobile unit that uses high temperature heating and has a very short grain exposure and grain residence time. It must be attractive for the individual farmer, if operated on a custom basis as for the mobile paddy thresher and combine harvester.

3.2 PNEUMATIC DRYERS

The pneumatic conveyor has been used extensively to convey various kinds of grain, for instance in post elevators transferring to/from ships. In industrial processes, wet particles can be dried by introducing inlet-heated air to the pneumatic conveyor. In principle, this dryer offers a number of advantages: very the short contact time and gas/solid concurrent flow make it possible to dry heat-sensitive materials; and low maintenance cost due to the small number of moving parts (Strumillo et al., 1986).

Figure 3.1 shows a schematic diagram of a simple pneumatic dryer. It consists of a heater, material feeder, dryer duct and material separator. Material is introduced into the gas stream by the material feeder, goes upward through the dryer duct and is separated at the material separator. The pneumatic dryer considered in the present study was designed to be part of a mobile threshing-drying-conveying machine using the thresher exhaust air as the heat source for the drying process.

Steady-state one-dimensional flow and uniform non-shrinking grain models have been developed to simulate the pneumatic drying process (Thorpe et al., 1973). The most simple moisture transfer model based on the rate of loss of moisture per unit mass of solid was used. The mass transfer between particle and air was assumed to be governed only by external convection. This model was later modified to take account of particle shrinkage in the pneumatic dryer (Pelegrina et al., 2001). In their model, the drying of a single particle was assumed to be controlled mainly by convection in the boundary layer at the particle-air interface. The drying rate depends on the material properties and the particle size, and the model application is restricted to sufficiently high water contents. This model can be used to predict the final particle conditions and provide a design tool; but more complex drying models must be used when the internal resistance for mass transfer is important. As mentioned by Strumillo et al. (1986), the rate of drying of hygroscopic material such as cereal grains is mainly governed by diffusion of moisture through the particle crust. The mathematical model of a pneumatic dryer for paddy grain to be developed here will take this effect into account.

Saastamoinen (1992) developed a one-dimensional steady state and uniform non-shrinking simulation for flash drying using a more complex model in which the drying rate was partially controlled by moisture migration to the surface. This model takes into account the internal resistance for both heat and mass transfer. Later, the model was applied to the drying process in a large-scale pneumatic dryer by taking into account shrinking effects on the particle diameter (Levy et al., 1999).

Experimental investigations of the mechanisms of heat and mass transfer in pneumatic dryers indicate that the heat and mass transfer coefficients are at a maximum in the acceleration region (Debrand, 1974). The latter study indicated three

locations where a high heat flux was observed between the gas and the particles: (a) the feeding point; (b) the elbow; and (c) the cyclone. The high flux at these locations was explained by high values of the slip velocity and a high intensity of turbulence. The slip velocity between particle and air stream is defined as the difference between the local air and particle velocities.

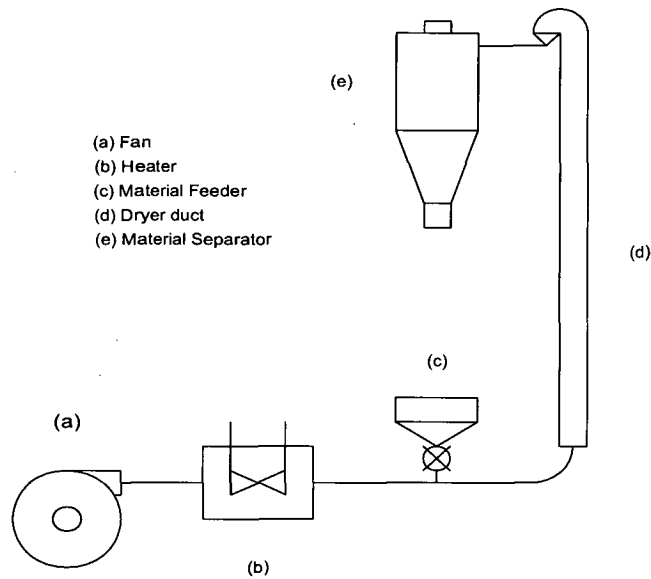


Figure 3.1 Diagram of a simple pneumatic dryer

Although extensive research has already been done on the pneumatic dryer, past efforts have been focussed on industrial drying. No work has been done on drying of paddy grain (rice). The objective of this Chapter is therefore to develop a model of paddy drying in a simple pneumatic dryer, and study the feasibility of using this device for first-stage drying

3.3 THEORETICAL MODEL DEVELOPMENT

To develop the present model, the volume of the pneumatic dryer was split longitudinally into elemental layers dz as shown in Figure 3.2, where z is the dryer length in m. The set of differential equations describing heat and mass conservation for different grain arrangements such as cross-flow, counter-flow and concurrent flow

proposed by Brooker et al.(1992) were applied. In this case, the differential equation for concurrent flow was used to describe the characteristics of the pneumatic dryer. The model is based on the following simplifying assumptions:

- (1) The paddy kernels are uniform in size and internally homogeneous, and can be approximated as isotropic spheres of 3.5 mm diameter;
- (2) The temperature gradients within the individual kernels are negligible, though not constant with time;
- (3) The volume shrinkage of paddy grain is negligible during the drying process. This model would be better applicable to dried grain;
- (4) Moisture diffusion dominates the drying process inside the grains. This means that the external convective resistance to mass transfer can be neglected, and the grain surface moisture assumed to attain instantaneous equilibrium with the drying air. Surface evaporation of moisture is inherent in this approach;
- (5) The effect of heat conduction and moisture transfer between grains, and heat losses through the dryer walls are considered negligible compared with the air-grain transfer rate;
- (6) The accumulation of thermal energy and water vapour of the air in the dryer duct is negligible;
- (7) The airflow and grain flow are plug-type, and the grain flow can be described by the Basset-Boussinesq-Oseen (BBO) equation (Crowe et al., 1997) in the simple form for one-dimensional flow with no rotation of individual grain particles.

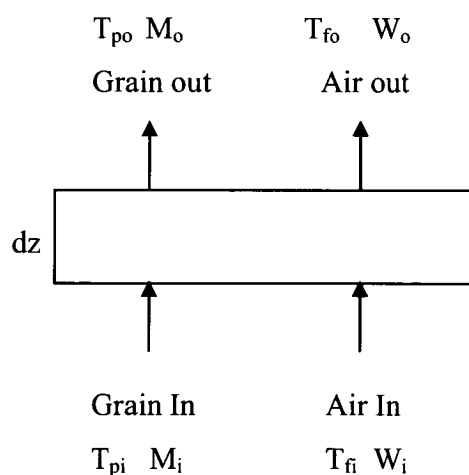


Figure 3.2 Elemental layer of a concurrent flowing pneumatic dryer

The mass conservation law can be written as

$$\dot{m}_p \frac{dM}{dz} = \dot{m}_f \frac{dW}{dz} \quad (3.1)$$

where \dot{m}_p and \dot{m}_f are the mass fluxes in kg/m²/s for the paddy and moist air, respectively; M is moisture content of paddy (dry basis) in kg water/ kg dry material; W is air humidity in kg water/ kg dry air.

From energy balances of grain and air, the air and grain temperature gradients with respect to dryer height are given by

$$\frac{dT_p}{dz} = \frac{h a_p (T_f - T_p)}{\dot{m}_p c_p + \dot{m}_p M c_w} + \frac{h_{fg} + c_v (T_f - T_p)}{c_p + M c_w} \frac{dM}{dz} \quad (3.2)$$

$$\frac{dT_f}{dz} = \frac{-h a_p (T_f - T_p)}{\dot{m}_f c_f + \dot{m}_f W c_v} \quad (3.3)$$

where T_p and T_f are temperatures in K for the paddy and moist air, respectively; h is the convective heat transfer coefficient in J/m²/K; a_p is surface area of paddy per unit of bed volume in m²/m³; c_p , c_w , c_v and c_f are specific heats in J/kg/K for paddy, water, vapour and moist air, respectively; h_{fg} is the latent heat of vaporisation in J/kg/K.

A differential equation in spherical coordinates based on Ficks' law is used to describe the moisture diffusion in paddy grain with appropriate initial and boundary conditions. These are written as (Steffe et al., 1982):

$$\frac{\partial M}{\partial t} = D_{eff} \left[\frac{\partial^2 M}{\partial r^2} + \left(\frac{2}{r} \right) \frac{\partial M}{\partial r} \right] \quad (3.4)$$

$$\frac{\partial M}{\partial t} = 0, \quad r = 0 \text{ and } t \geq 0 \quad (3.5)$$

$$M = M_{eq}, \quad r = d_p \text{ and } t \geq 0 \quad (3.6)$$

$$M = M_0, \quad 0 \leq r \leq d_p \text{ and } t = 0 \quad (3.7)$$

where t is time in s; D_{eff} is diffusion coefficient in m²/s; r is radial distance from the centre of a spherical particle in m; M_{eq} and M_0 are moisture contents of paddy (dry

basis) in kg water / kg dry material at equilibrium and initial states; d_p is equivalent diameter of paddy grain in m. The effective diffusion coefficient as a function of grain temperature is (Poomsaad et al., 2000):

$$D_{\text{eff}} = 5.68088 \times 10^{-6} e^{-3445.66/T_p} \quad (3.8)$$

The motion of paddy grain in the air stream can be calculated from the simplified BBO equation:

$$\frac{\pi d_p^3 \rho_p}{6} \frac{dv_p}{dt} = \frac{1}{8} \pi \rho_p d_p^2 C_D |v_f - v_p| (v_f - v_p) + \frac{1}{6} \pi d_p^3 (\rho_p - \rho_f) g \quad (3.9)$$

where ρ_p and ρ_f are densities in kg/m^3 for paddy and moist air, respectively; v_f and v_p are velocities in m/s for paddy and moist air, respectively; C_D is particle drag coefficient. The right hand side terms of the simplified BBO equation account for all the forces acting on each particle: particle drag, buoyancy and gravitation. The usual mode of flow in a pneumatic dryer is a dilute phase flow. Note that in the present study, a vertical dilute phase flow in a pneumatic dryer was investigated. As a consequence, the friction force between particle and wall, which is often encountered in two-phase flow, can be neglected in the present case.

The drag coefficient of spherical particles (assumption 1) at low Reynolds number (Re) can be computed analytically using Stoke's law:

$$C_D = \frac{24}{\text{Re}}, \quad \text{Re} \leq 1 \quad (3.10)$$

where Re is the Reynolds number based on the particle diameter and slip velocity. For particle Reynolds numbers sufficiently large for inertial effects to dominate viscous effects, the drag coefficient becomes independent of Reynolds number and

$$C_D = 0.44, \quad 1000 \leq \text{Re} \leq 2 \times 10^5 \quad (3.11)$$

In the transition region between the viscous and inertial regimes, the drag coefficient for a sphere can be determined from the Schiller-Naumann drag model for dilute solid particle flow

$$C_D = \frac{24}{\text{Re}} (1 + 0.15 \text{Re}^{0.687}) \quad (3.12)$$

The heat transfer in forced convection over a single sphere can be expressed as (Whitaker, 1972)

$$Nu = 2 + (0.4 Re^{0.5} + 0.06 Re)^{2/3} Pr^{0.4} (\mu_{\infty} / \mu_w) \quad (3.13)$$

where Nu is Nusselt number, hD/λ . Re is the particle Reynolds number; Pr is Prandtl number; μ_{∞} ; and μ_w are air viscosities in $kg/m/s$ evaluated at the bulk temperature and surface grain temperature, respectively. The surface area of particles available for heat transfer within each elemental layer is given by

$$a_p = \frac{6(1 - v_d)}{d_p} \quad (3.14)$$

$$v_d = 1 - \frac{v_p}{v_f + v_p} \quad (3.15)$$

where a_p is surface area of paddy per unit of bed volume in m^2/m^3 ; v_d is bed voidage. Complementary equations required in order to solve the physical and thermodynamic properties of paddy grain are summarised (Brooker et al., 1992; Laithong, 1987) as :

$$h_{fg} = (2502 - 2.386T_p)(1 + 2.496e^{-21.733M}) \times 10^3 \quad (3.16)$$

$$M_{eq} = \frac{1}{100} \left[\frac{\ln(1 - RH)}{-3.146 \times 10^{-6} T_p} \right]^{1/2.464} \quad (3.17)$$

$$c_p = 1.11 \times 10^{-3} + 4.48 \frac{M}{1 + M} \quad (3.18)$$

$$\rho_p = 1460.695 - 1.738M \quad (3.19)$$

where RH is relative humidity in percent. Thermophysical and transport properties of wet air are calculated from the following complementary equations (Mujumdar, 1995; Palowski et al., 1991; Wilhelm, 1976):

$$\rho_f = \frac{P(1 + 1.6078M)}{R \times T_f} \quad (3.20)$$

$$RH = \frac{P_w}{P_{ws}} \quad (3.21)$$

$$\ln(P_{ws}) = \frac{-7511.52}{T_f} + 89.63121 + 0.02399897T_f - 1.1654551 \times 10^{-5} T_f^2 - 1.2810336 \times 10^{-8} T_f^3 + 2.0998405 \times 10^{-11} T_f^4 - 12.150799 \ln(T_f) \quad (3.22)$$

$$P_w = \frac{P \times M}{0.62198 + M} \quad (3.23)$$

$$c_f = 1.00926 \times 10^{-3} - 4.043 \times 10^{-2} t_f + 6.1759 \times 10^{-4} t_f^2 - 4.097 \times 10^{-7} t_f^3 \quad (3.24)$$

$$\lambda = 2.425 \times 10^{-2} + 7.889 \times 10^{-5} t_f - 1.79 \times 10^{-8} t_f^2 - 8.57 \times 10^{-12} t_f^3 \quad (3.25)$$

$$\mu = 1.691 \times 10^{-5} + 4.984 \times 10^{-8} t_f - 3.187 \times 10^{-11} t_f^2 - 1.319 \times 10^{-14} t_f^3 \quad (3.26)$$

$$c_v = 1.883 \times 10^3 - 1.6737 \times 10^{-1} T_f + 8.4386 \times 10^{-4} T_f^2 - 2.6966 \times 10^{-7} T_f^3 \quad (3.27)$$

$$c_w = 2.8223 \times 10^3 + 11.828 T_f - 3.5043 \times 10^2 T_f^2 - 3.601 \times 10^{-5} T_f^3 \quad (3.28)$$

where λ is thermal conductivity in W/m/K; μ is air viscosity in kg/m/s; t_f is air temperature in °C.

3.4 SOLUTION TECHNIQUE

For integrating the drying equations, the dryer is represented as a series of elemental layers. Grain moves through the various layers with a constant volumetric flow rate. The conditions of grain leaving a previous layer are used as input conditions for grain entering the subsequent layer. The solution of the governing equations involves the following steps:

- (1) The time step required to transit a given elemental layer thickness is calculated from the mean velocity given by Equation (3.9) using one-step forward Euler integration. The initial velocity of a particle is assumed zero at the inlet of the pneumatic dryer.
- (2) The radial distribution of moisture inside the grain kernels and the change in average moisture content for a given time step are calculated from Equations (3.4) to (3.7). Equation (3.4) is solved numerically using the Crank-Nicholson implicit method. The average grain moisture content for each height step is calculated by Simpson integration over the entire radius of the paddy grain.
- (3) Knowing the inlet air humidity and the mass fluxes of grain and air, the outlet air humidity is determined from Equation (3.1).
- (4) The temperatures of grain and air at the exit of an elemental layer are calculated by solving Equations (3.2) and (3.3) using 4th order Runge-Kutta integration.
- (5) The entire procedure is repeated for subsequent layers until reaching the dryer exit.

A flow chart of the simulation procedure is shown in Figure 3.3. The MATLAB program in M-file format used for this simulation is presented in Appendix A.

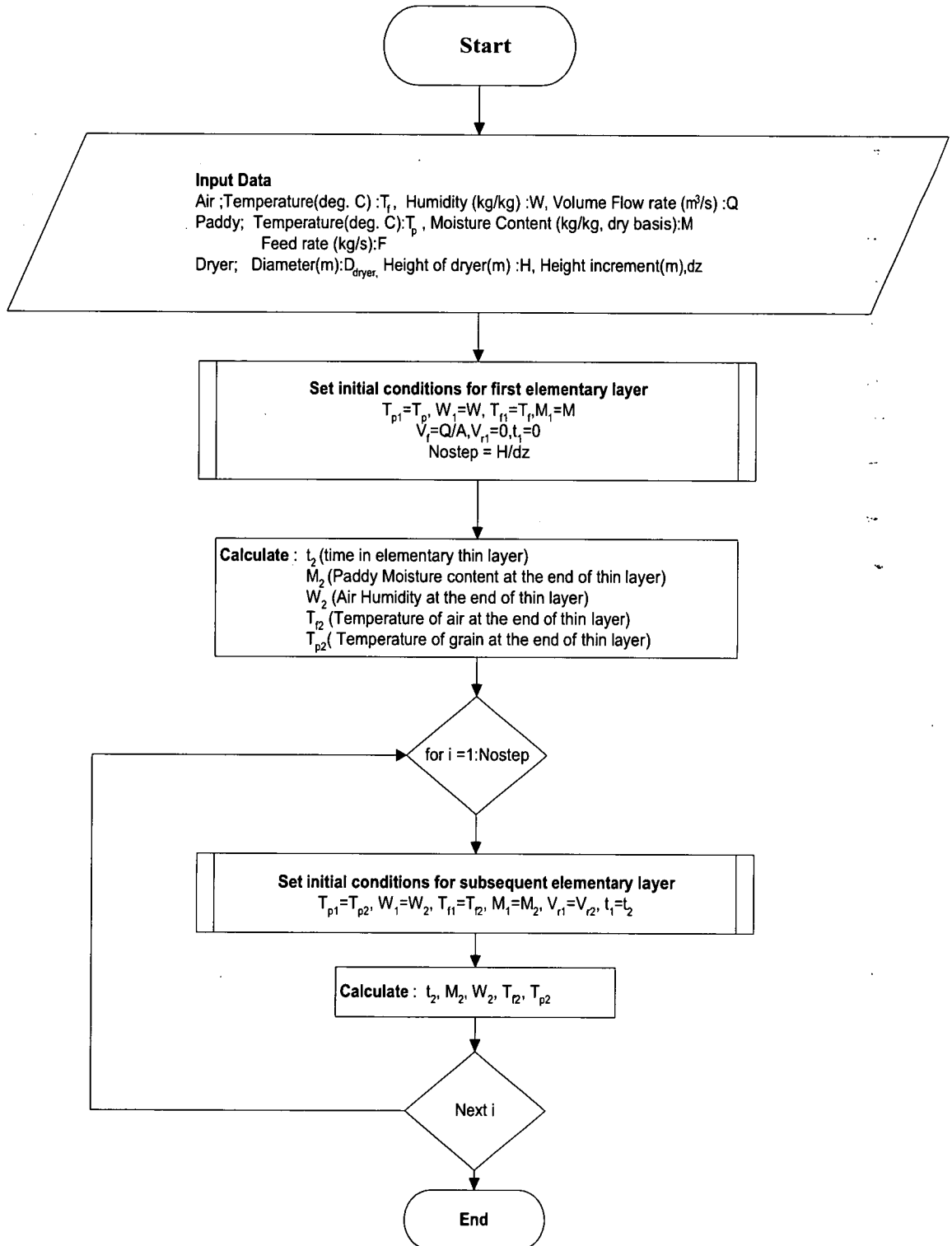


Figure 3.3 Flow diagram of the pneumatic dryer simulation

3.5 SIMULATION RESULTS

3.5.1 Introduction

To evaluate the potential of a pneumatic dryer for paddy drying, a series of simulations were performed. A dryer of 300 m length was divided into elemental layers of 0.005 m. The elemental layer thickness was decreased until the solutions for temperature and humidity distributions along the dryer converged. The calculations assumed paddy inlet temperature and moisture content values of 30 °C and 0.333 kg water / kg dry material, respectively. The inlet air temperature and humidity were fixed at 110 °C and 0.0215 kg water / kg dry air, respectively. To maintain stable operating conditions of the pneumatic dryer, the inlet air velocity must be higher than the minimum spouted bed velocity of paddy of 15 m/s (Wetchacama et al., 1999). Dryer diameters of 0.2032, 0.1524 and 0.1016 m, inlet air velocities of 15, 19 and 23 m/s, and paddy feed rates of 0.1, 0.75 and 0.5 kg/s were examined. The drying rate of paddy at various levels of specific air flow rate was evaluated by changing the dryer diameter and paddy feed rate at constant inlet air velocity. The variations of moisture content and temperature of air and grain at various levels through the pneumatic dryer were calculated. Figure 3.4 shows the resulting simulated distributions of velocity, temperature and moisture content along the dryer length expressed in terms of the dimensionless variables v/v_{fi} , $(T-T_{pi})/(T_{fi}-T_{pi})$, W/W_i and M/M_i .

After the entrance region, in which grain particles are accelerated, the grain velocity curve runs almost parallel to the air velocity curve. In the initial stage, corresponding to the acceleration zone, the drying rate reaches a maximum. Air temperature decreases sharply as in all concurrent flow systems, while paddy temperature rises rapidly from its initial value up to the equilibrium temperature. The paddy moisture content decreases markedly and air humidity concurrently increases. After reaching the equilibrium stage, the product temperature tends to decrease keeping equilibrium with the air. The paddy moisture content then becomes essentially constant, while the air humidity also tends to plateau.

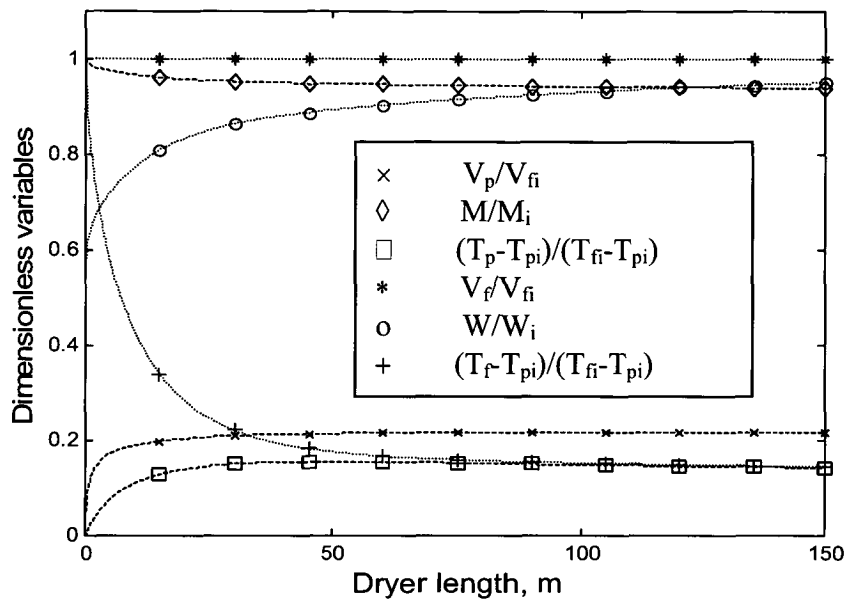


Figure 3.4 Development of dimensionless quantities over the dryer length.

3.5.2 Effect of Dryer Diameter on Moisture and Temperature of Air and Paddy

The aerodynamics of pneumatic transport, and the heat and mass transfer of paddy grains in vertical drying ducts of 0.1016, 0.1524 and 0.2032 m diameter were studied by means of the simulation program. Simulation results with values for v_f of 23 m/s, F of 0.75 kg/s and L of 300 m at different dryer diameters are shown in Figures 3.5 and 3.6.

As shown in Figure 3.5, the slip velocity between grain and air increases with dryer diameter, which results in a higher specific air flow ratio. Figure 3.6 (a) indicates that the final equilibrium temperatures of paddy and air both increase with dryer diameter. This leads to higher grain temperature and moisture diffusion rate, and a lower final moisture content of paddy grain. A comparison of paddy moisture content and air humidity is shown in Figure 3.6 (b). The air humidity in the entrance region is higher with a smaller dryer diameter. However, the final paddy moisture content decreases and the final air humidity increases with dryer diameter after reaching the equilibrium temperature.

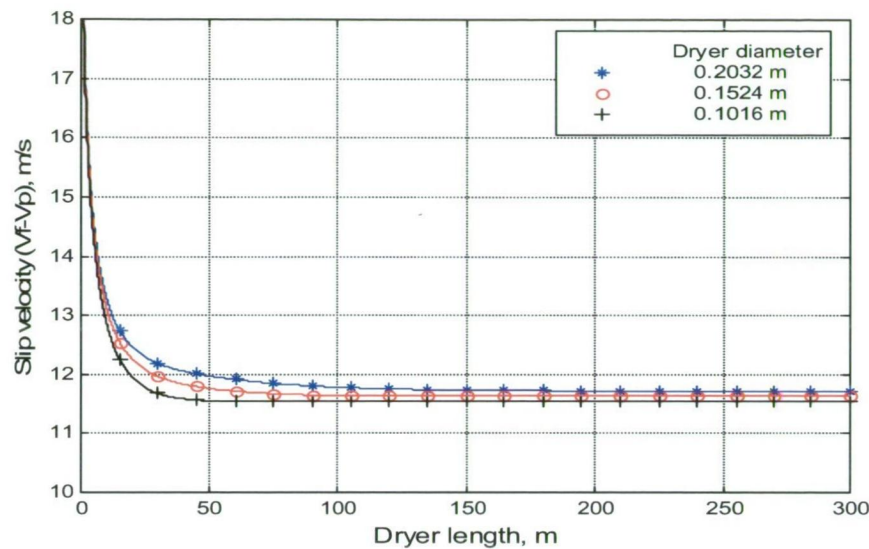


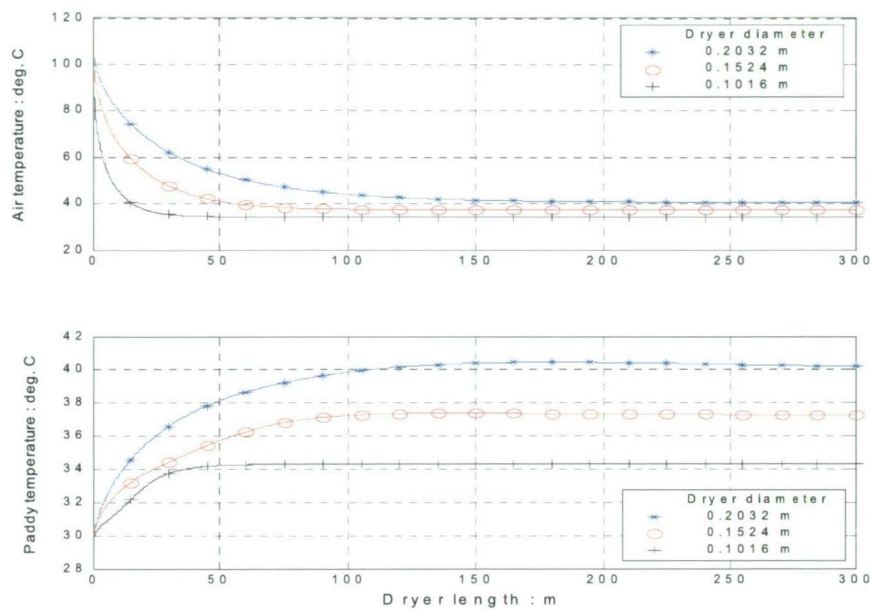
Figure 3.5 Variation of slip velocity over dryer length with paddy feed rate of 0.75 kg/s and inlet air velocity of 23 m/s for three dryer diameters

Thus, at constant inlet air velocity and paddy feed rate, the drying capacity is predicted to decrease with dryer diameter. The final moisture content of paddy decreases with dryer diameter, but the final air absolute humidity and equilibrium temperature T_{eq} both increase with increasing dryer diameter.

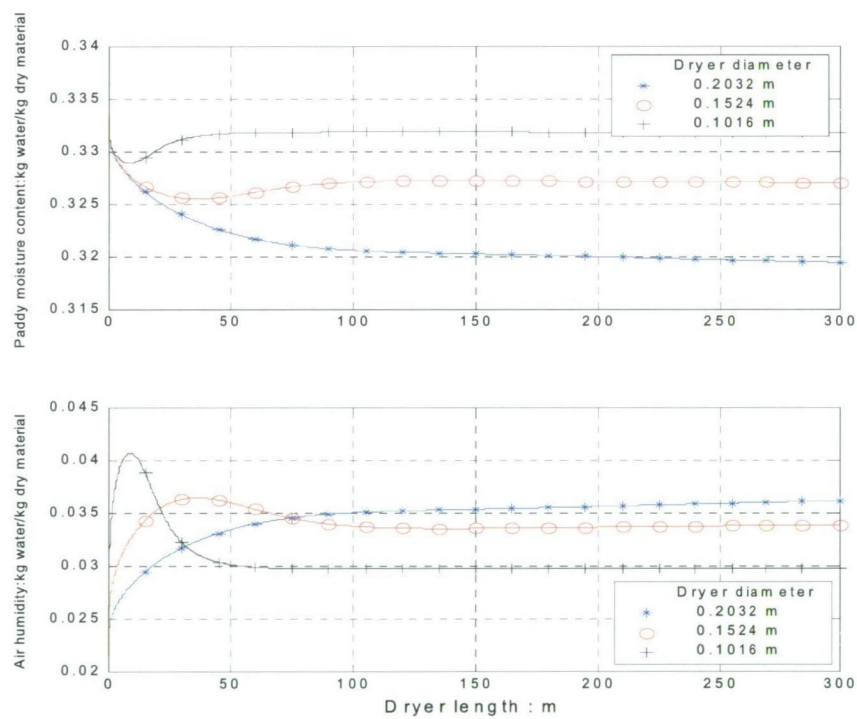
3.5.3 Effect of Paddy Feed Rate on Moisture and Temperature of Air and Paddy

Figures 3.7 and 3.8 show the effect of paddy feed rate on the variation of slip velocity and the distributions of temperature and moisture content of air and grain over the dryer length. The pneumatic drying model was solved for a vertical dryer ($D = 0.2032$ m, $L = 300$ m, $v_f = 23$ m/s) at different paddy feed rates ($F = 1.0, 0.75$ and 0.5 kg/s.).

Figure 3.7 indicates that the slip velocity increases when the paddy feed rate decreases. The higher slip velocity leads to an increased specific air flow ratio at the same dryer diameter and inlet air velocity, which results in a higher equilibrium temperature T_{eq} .



(a)



(b)

Figure 3.6 Development of: (a) paddy and air temperatures; and (b) paddy moisture content and air humidity, over the dryer length with paddy feed rate of 0.75 kg/s and inlet air velocity of 23 m/s for three dryer diameters.

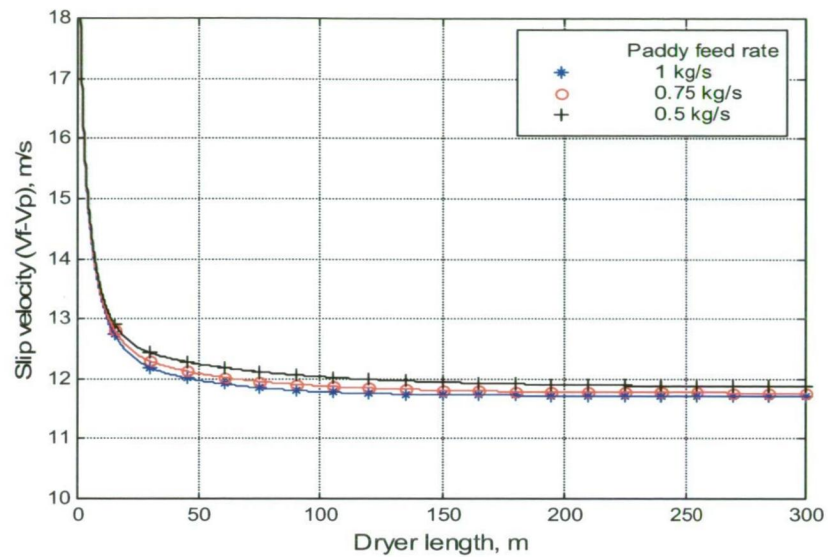
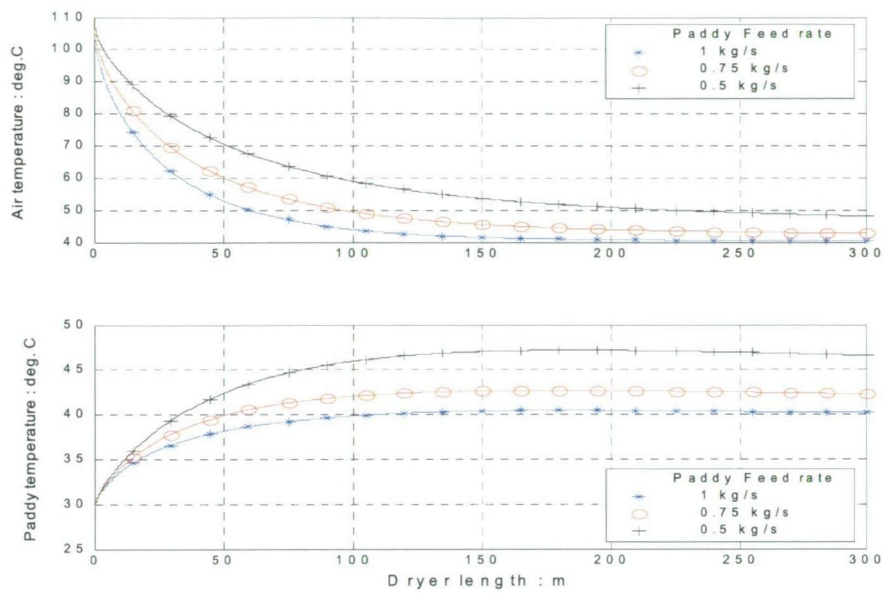


Figure 3.7 Variation of slip velocity over dryer length with dryer diameter of 0.203 m and inlet air velocity of 23 m/s for three paddy feed rates

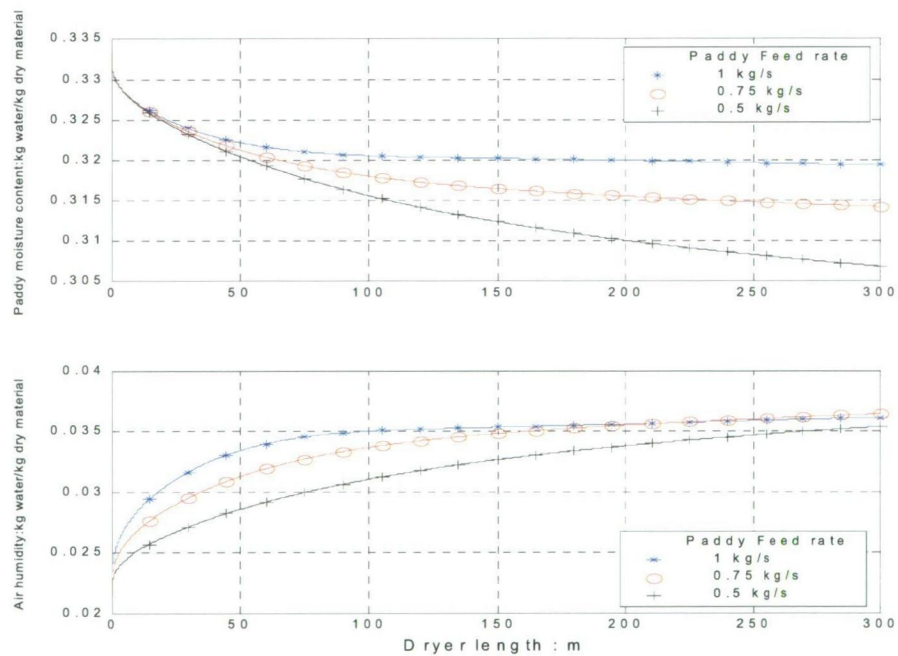
As shown in Figure 3.8 (a), the final air and paddy grain temperatures increase when the paddy feed rate decreases. This results in a higher moisture diffusion at lower paddy feed rates. As a result of higher moisture diffusion, the final moisture content of paddy grain decreases sharply with the decrease of paddy feed rate (as clearly seen in Figure 3.8 (b)).

Due to the increasing moisture transfer, the air humidity (in kg water / kg dry air) would be expected to increase as the paddy feed rate decreases. This equates to an improvement in drying performance demonstrated by a lower paddy moisture content. The temperature charts in Figure 3.8 (a) demonstrate that the system has reached equilibrium by a dryer length of 200 m for highest feed rate, but has not reached equilibrium by 300 m for the other feed rates.

This is also indicated in Figure 3.8 (b) by the continuing variation in humidity and moisture content with dryer length for the 0.75 and 0.5 kg/s solid feed rates. The air humidity for 0.75 and 0.5 kg/s has not reached a steady level by 300 m; and the slope of these lines indicates that the equilibrium level will be highest for the lowest paddy feed rate, even though the simulation was not extended to a dryer length beyond 300 m.



(a)



(b)

Figure 3.8 Development of: (a) paddy and air temperatures; and (b) paddy moisture content and air humidity over, the dryer length with dryer diameter of 0.203 m and inlet air velocity of 23 m/s for three paddy feed rates.

3.5.4 Effect of Inlet Air Velocity on Moisture and Temperature of Air and Paddy

The influence of inlet air velocity on the variations of slip velocity and the temperature and moisture content of air and paddy grain over the dryer length were investigated by simulations for air velocities of 15, 19 and 23 m/s. All simulations were conducted with $D = 0.2032$ m, $L = 300$ m and $F = 0.5$ kg/s. The results are presented in Figures 3.9 and 3.10.

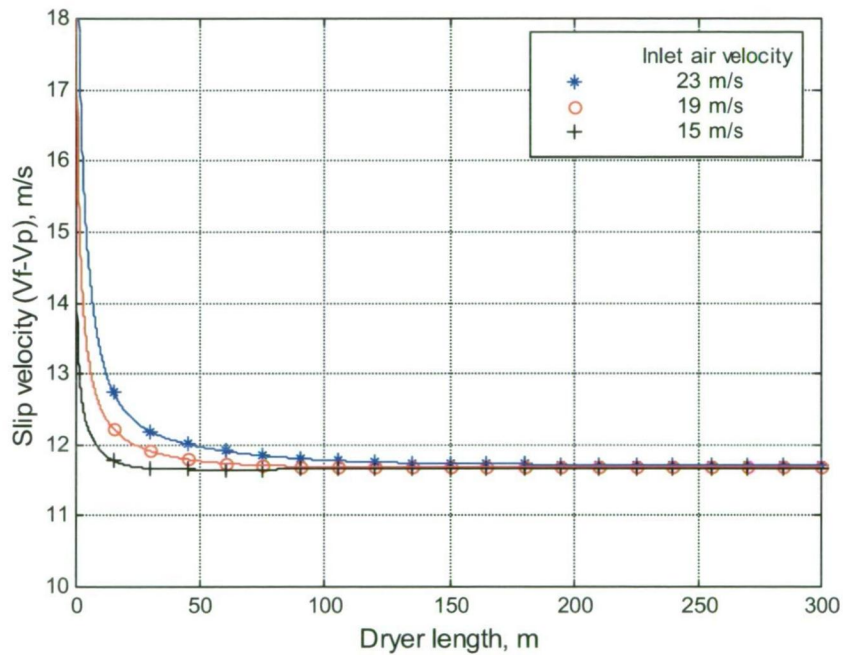


Figure 3.9 Variation of slip velocity over dryer length with dryer diameter of 0.203 m and paddy feed rate of 0.5 kg/s for three inlet air velocity values.

Figure 3.9 shows that slip velocity increases with inlet air velocity. At the same dryer diameter and paddy feed rate, increasing the inlet air velocity leads to an increased specific air flow ratio. This results in a higher convective transport of heat and mass, which increases the equilibrium temperature T_{eq} of air and grain.

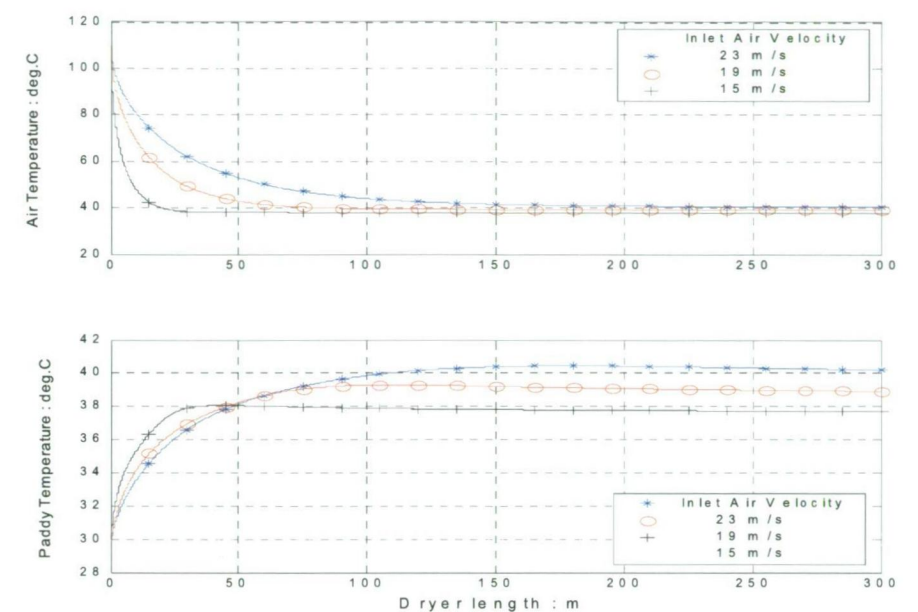
As shown in Figure 3.10 (a), the air and grain reach their equilibrium temperatures within 100 m with an air inlet velocity of 15 m/s. The temperature distribution should display similar trends at higher inlet air velocity, but did not reach equilibrium temperature within 300 m. A higher moisture diffusion results when the inlet air velocity is increased.

The paddy grain temperature rises faster from its initial value and reaches equilibrium within 300 m at the lower inlet air velocity, but is unable to achieve the equilibrium temperature within this length at higher inlet air velocities. Figure 3.10 (b) shows that the paddy moisture content at 15 m/s inlet air velocity reduces rapidly in the acceleration zone and more gradually after reaching thermal equilibrium. The paddy moisture content at higher inlet air velocity reduces faster along the dryer length and does not reach equilibrium. Therefore, the final paddy moisture content at 300 m dryer length decreases for increasing in air inlet velocity.

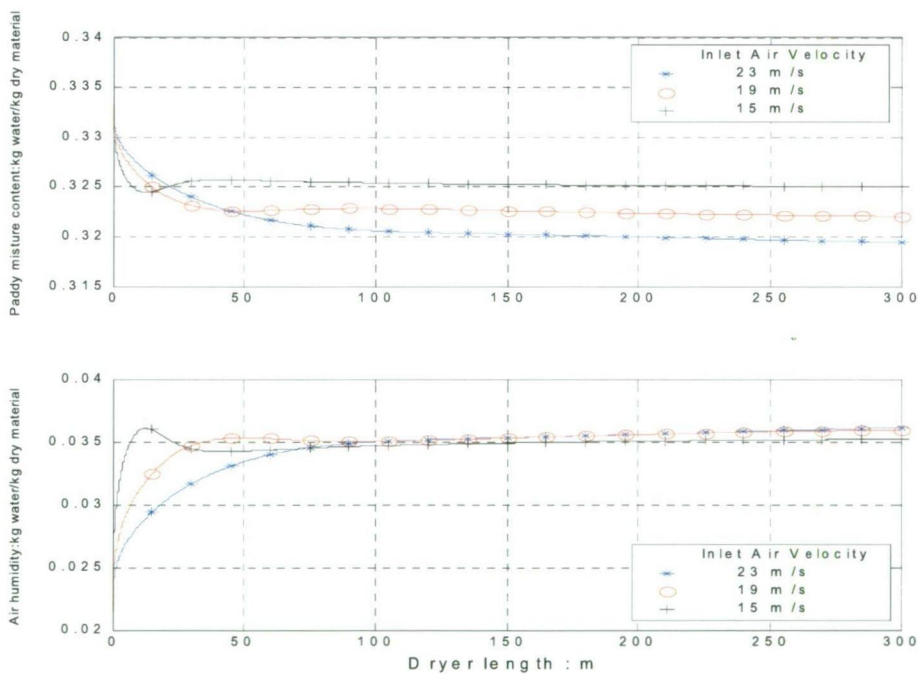
At 15 m/s air inlet velocity the air humidity increases rapidly in the initial stage and then reaches equilibrium. It rises more slowly as the air inlet velocity increases and does not reach equilibrium within the dryer length. The air humidity increases with air velocity at end of the dryer.

3.6 DISCUSSION AND EVALUATION OF THE PNEUMATIC DRYER FOR PADDY DRYING

The final grain temperature must be limited to maintain the quality of paddy after drying in terms of head rice yield and rice whiteness. Head rice yield and rice whiteness depend on the grain temperature, moisture gradients, and exposure time. Gradients produce a dry periphery and wetter centre. The dry periphery tends to constrict, and develop stress inside the kernel. For high grain temperature and longer exposure time the starch granules are partially gelatinised, resulting in accelerated ageing that affects the grain qualities in a way similar to parboiling of rice (Jindal et al., 1986).



(a)



(b)

Figure 3.10 Development of: (a) paddy and air temperatures; and (b) paddy moisture content and air humidity over, the dryer length, with dryer diameter of 0.203 m and paddy feed rate of 0.5 kg/s for three inlet air velocities.

Whiteness of milled rice decreases with increasing grain temperature, drying temperature and exposure time. Chemical and physical transformations induced by heating (Maillard reaction) and translocation of colour from rice husk and bran to endosperm cause discolouration. Longer drying time and higher moisture content during heating also accelerate the Maillard reaction, but do not affect the rate of water removal. For first stage drying, the recommended grain temperature is 64-67°C (Inprasit et al., 2001). The maximum equilibrium temperature of the pneumatic dryer was limited to this range in the current simulation.

For a given paddy feed rate the equilibrium temperature increases with inlet air velocity as shown in Figure 3.11(a). Decreases in equilibrium temperature with increases in paddy feed rate for a fixed dryer diameter are shown in Figure 3.11 (b). The initial drying rate increases due to the water activity, the thermal driving force from the temperature difference between air and grain, and the higher slip velocity. However, after reaching the equilibrium temperature, the driving force tends to zero and the drying rate decreases markedly, thus necessitating a longer residence time for moisture evaporation. As a result, the dryer length required to reach a practical final moisture content of 22 % db is greatly increased.

Figure 3.12 shows the required dryer length to obtained final moisture contents of 32, 31, and 30 % db with values for $T_{fi} = 110\text{ }^{\circ}\text{C}$, $W_i = 0.0215\text{ kg water / kg dry air}$, $T_{pi} = 30\text{ }^{\circ}\text{C}$, $M_i = 0.33\text{ kg water / kg dry material}$, $D = 0.2032\text{ m}$, $F = 0.25\text{ kg/s}$ and $v_f = 23\text{ m/s}$. These conditions gave the highest equilibrium temperature $T_{eq} = 46.6\text{ }^{\circ}\text{C}$. It was found that the required dryer length was inversely proportional to the value of final moisture content. Thus, a longer dryer length and lower paddy feed rate would be necessary to achieve the desired final moisture content of the grain.

3.7 CONCLUSIONS

A one-dimensional mathematical model of a pneumatic dryer, incorporating mass and energy balances and drying kinetics, has been developed to model paddy drying in this device. The model was evaluated for different dryer diameters, paddy feed rates,

and inlet air velocities. The simulation results showed the specific air ratio to increase with dryer diameter and inlet air velocity. In contrast, specific air ratio increased when paddy feed rate decreased. Increasing specific air ratio also increased the equilibrium air temperature (T_{eq}) and yielded a higher moisture diffusion rate inside the paddy grain. Hence, the drying rate increased when the dryer diameter and inlet air velocity increased, while paddy feed rate decreased.

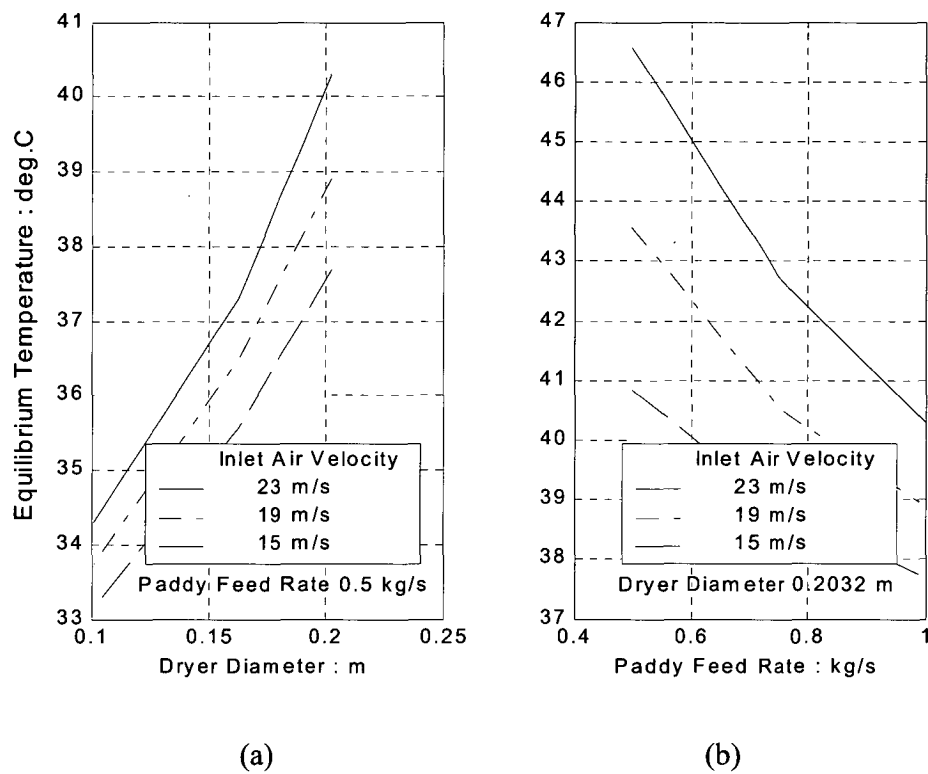


Figure 3.11 Variation of equilibrium temperature with: (a) dryer diameter; and (b) paddy feed rate for, three inlet air velocities.

Due to the huge dryer length and very low paddy feed rate required to achieve a sufficiently low moisture content, it is concluded that the simple pneumatic dryer is not practical to use for first-stage paddy drying. It is more feasible to use the pneumatic dryer as a flash dryer to remove the moisture on free surfaces, as this only requires a short residence time. In order to make a pneumatic dryer useful for hygroscopic materials such as paddy grain, the dryer design would have to be improved to increase the solid residence time and reduce the length of the dryer.

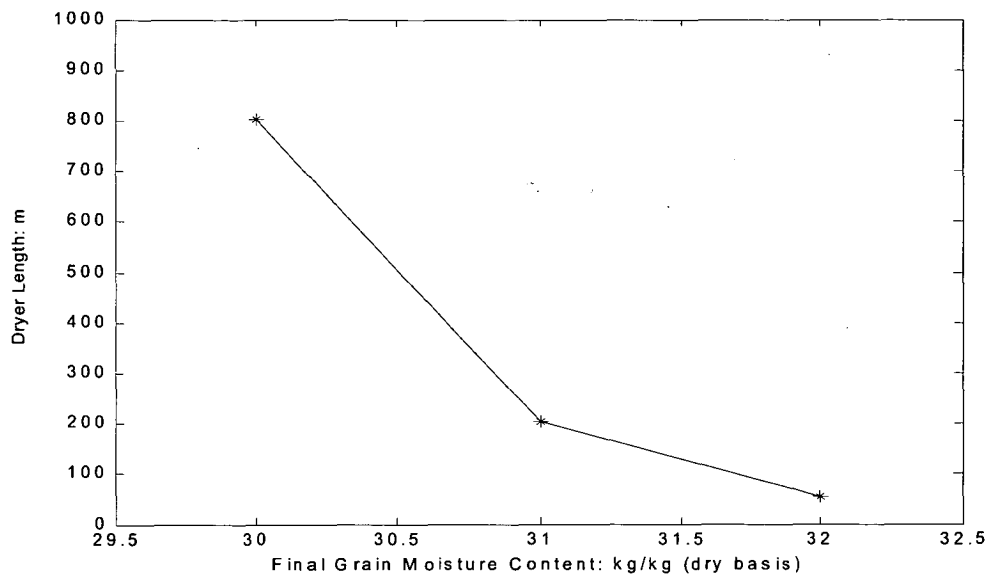


Figure 3.12 Required dryer length to achieve different final moisture contents.

($T_{fi} = 30\text{ }^{\circ}\text{C}$, $M_i = 0.33\text{ kg water / kg dry material}$,

$D = 0.203\text{ m}$, $F = 0.25\text{ kg/s}$, $v_f = 23\text{ m/s}$)

Chapter 4

CYCLONE TECHNOLOGY FOR GRAIN DRYING

4.1 INTRODUCTION

As stated in the previous chapter, the preliminary idea to use a simple pneumatic conveyor as a dryer is not practical due to the fact that a long residence time is required. Simulation results in the previous chapter indicate that a long length of pneumatic transport pipe is required for drying hygroscopic material such as paddy. In the past, various efforts were made to increase the residence time of a pneumatic dryer such as recirculating the solid materials in the dryer and designing a multistage dryer with a delay chamber. However, these efforts were not successful because they increase the complexity of construction and capital cost due to the need for additional parts and the conveying system.

Another approach to the design problem is the cyclonic dryer. This is based on swirl flow or vortex flow which occurs in different types of industrial processing equipment such as the cyclone separator, hydro-cyclone, spray dryer and vortex burner. The advantages of this system are that it increases process intensity and residence time of the solid material. The outcome of this approach was the design of the cyclone dryer. This recently developed pneumatic dryer with one or more delay chambers gives a

longer particle residence time than a simple pneumatic dryer or cyclone separator. It is a medium residence time dryer with solid retained for 5 to 30 minutes. This type of dryer has been used for drying S-PVC and other polymers (Nebra, 2000; Korn, 2001; Heinze, 1984; Ulrich, 2002). A brief description of its design and working principles is given in Section 4.2.

In order to develop the cyclone dryer, it is necessary to review its working principles. The modelling of the flow pattern inside a cyclone separator, particle terminal velocity and particle deposition velocity are all topics relevant to the design of a cyclone dryer. The next section contains short discussions of these topics.

4.2 CYCLONE SEPARATORS

4.2.1 Flow Behaviour

The gas flow pattern in a cyclone separator is fairly well known from experimental evidence collected over a decade. More recently, Computational Fluid Dynamics (CFD) calculations have also shown a fair prediction of the flow field inside a cyclone separator.

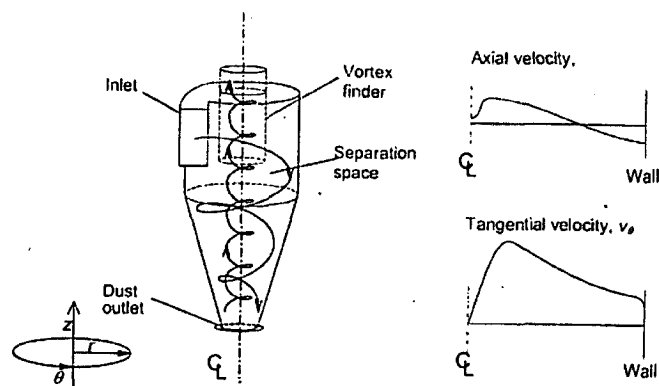


Figure 4.1 Flow pattern inside a tangential inlet cyclone separator
(Hoffmann et al., 2002).

Figure 4.1 shows a sketch of a standard reverse-flow cylinder-on-cone gas cyclone separator with a tangential inlet. The flow pattern is indicated. A swirling motion is created using the tangential gas injection. The gas flow is downward in the outer part

of the swirl and upward in the centre. The downward flow in the outer part of the cyclone is critically important, as it is the dominant mechanism for transporting the solids out at the cyclone bottom. Gravity will assist in vertically oriented cyclones, but its influence is important only for cyclones operating at high solids concentration.

The radial profiles of axial and tangential gas velocity components are sketched on the right of Figure 4.1. The former shows an outer region of downward-directed axial flow and an inner one of upward direction flow. As mentioned, the downward velocity at the wall is the primary mechanism for particle transport through the dust outlet. The axial velocity often shows a dip around the centre line. Sometimes this is so severe that the flow is downward directed. The tangential velocity profile resembles a Rankine vortex: a near loss-free swirl surrounding a core of near solid-body rotation. Various mathematical models have been developed to predict the cyclone velocity distribution and pressure drop across the device.

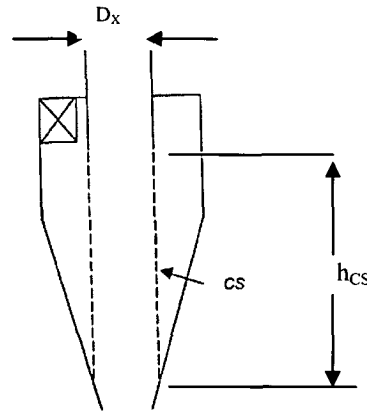


Figure 4.2 Control surface (CS) of cyclone (Hoffmann et al. 2002)

The radial velocity component is computed in a very straight-forward manner. Near the wall the radial velocity is neglected. On the control surface CS shown in Figure 4.2 it is assumed uniform, giving the average radial velocity

$$|v_r(R_x)| \equiv v_{rCS} = \frac{Q}{\pi R_x h_{CS}} \quad (4.1)$$

where Q is the volumetric flow rate through the cyclone, D_x is the diameter of the vortex finder, which is also the diameter of surface CS, and h_{CS} is the height of the surface CS.

In reality, the velocity on CS is not uniform. There occurs a radial, inwardly directed “lip flow” or “lip leakage” just below the vortex tube. Thus some portion of the gas tends to short circuit the imaginary cylinder of height h_{CS} and diameter D_x near the top of the cylinder.

The tangential velocity distribution in real swirl flow is intermediate between two types of ideal swirl flows: the first type is a forced vortex flow, which is a swirl flow with the same tangential velocity distribution as a rotating solid body; the second is a free vortex flow, which is the way a frictionless fluid would swirl. The tangential velocity distribution inside a cyclone is given by

$$\begin{aligned} v_\theta &= c_1 r \quad \text{for } 0 < r < \frac{D_o}{2} \\ v_\theta &= \frac{c_2}{r} \quad \text{for } \frac{D_o}{2} < r < \frac{D}{2} \end{aligned} \quad (4.2)$$

where D_o is the diameter of the forced vortex core, D is the outer diameter of the cyclone, and c_1 and c_2 are constants.

For the axial velocity, the surface CS is assumed to separate the outer region of downward flow from the inner region of upward flow. Axial velocities in each region are assumed to be uniform over the cross section. The upward axial velocity for the inner region of radius R_x is

$$v_{a,u} = \frac{4Q}{\pi R_x^2} \quad (4.3)$$

Mass conservation for incompressible flow gives the average downward axial velocity $v_{a,d}$ for the outer annular region between radii R_x and $R = D/2$ from

$$Q = \pi R_x^2 v_{a,u} = \pi (R^2 - R_x^2) v_{a,d} \quad (4.4)$$

The pressure drop (ΔP) over a cyclone is approximately proportional to the square of the volumetric flow rate. To obtain a characteristic measurement for pressure drop in a given cyclone, the pressure drop is often reported as the dimensionless pressure drop coefficient

$$C_{\Delta P} \equiv \frac{\Delta P}{\frac{1}{2} \rho_f v_{in}^2} \quad (4.5)$$

where v_{in} is the mean velocity at inlet of the cyclone. Equation (4.5) is very useful for estimating the pressure loss through the system at conditions other than design.

4.2.2 Particle Terminal Velocity

A particle falling from the rest in a fluid will initially experience a high acceleration. As the particle accelerates the drag force increases, causing a reduction of the acceleration. Eventually a force balance is achieved where the acceleration is zero and a maximum or terminal relative velocity is reached. This is known as the single particle terminal velocity, v_t . For a spherical particle of diameter d_p the terminal velocity is related to the drag coefficient by (Cheremisinoff et al., 1984)

$$C_D = \frac{4}{3} \frac{g d_p}{v_t^2} \left(\frac{(\rho_p - \rho_f)}{\rho_f} \right) \quad (4.6)$$

Thus in the Stokes law region, with $C_D = 24/Re_p$, the single particle terminal velocity is given by

$$v_t = \frac{d_p^2 (\rho_p - \rho_f) g}{18\mu} \quad (4.7)$$

In the Stokes law region the terminal velocity is proportional to the square of particle diameter. In the Newton drag law region, with $C_D = 0.44$, the terminal velocity is given by (Cheremisinoff et al., 1984)

$$v_t = 5.46 \left(\frac{d_p (\rho_p - \rho_f) g}{\rho_f} \right)^{1/2} \quad (4.8)$$

In this region the terminal velocity is independent of the fluid viscosity and proportional to the square root of the particle diameter. In the intermediate region, with, $C_D = 18.5/Re_p^{0.6}$, the particle terminal velocity is given by (Cheremisinoff et al., 1984)

$$v_t = 0.78 \frac{d_p^{0.43} (\rho_p - \rho_f)^{0.715}}{\rho_f^{0.285} \mu^{0.43}} \quad (4.9)$$

Generally, when calculating the terminal velocity for a given particle or the particle diameter for given velocity, it is not known which region of operation is relevant. One way around this problem is to formulate the dimensionless group $C_D Re_p^2$. To calculate v_t for a given particle size d_p , calculate the group

$$C_D Re_p^2 = \frac{4 d_p^3 \rho_f (\rho_p - \rho_f) g}{3 \mu^2} \quad (4.10)$$

which is independent of v_t , for the given particle and fluid properties. $C_D Re_p^2$ is a constant and will therefore produce a straight line of slope -2 on a logarithmic plot of C_D and Re_p . The intersection of this line with the drag curve gives the value of Re_p and hence v_t .

4.2.3 Particle Deposition Velocity

In the operation of a cyclone or a pneumatic conveyor, it is generally desirable to avoid particles settling out in the horizontal piping or ducting feeding or exiting the cyclones. Thus, it is necessary to know the minimum gas velocity required to prevent solid particles from settling and accumulating on the bottom of piping. Wicks (1971) examines the forces (lift, drag, buoyancy and gravity) acting on a particle (diameter d) resting at the bottom of a horizontal pipe (diameter D) and gives a very useful correlation for computing the minimum superficial pipe velocity v_m which is required to prevent a particle from stagnating on the bottom of the pipe. This correlation is

$$1 = \gamma v_m + \delta v_m^{2.5} \quad (4.11)$$

$$\text{where } \gamma = \frac{10\mu}{(\rho_p - \rho_f) g d_p D} \quad \text{and} \quad \delta = \frac{\rho_p^{1.5}}{100(\rho_p - \rho_f) g \mu^{0.5} D^{0.5}}$$

Equation 4.11 is solved using an iterative method to get the minimum superficial pipe velocity, v_m . To avoid iterative calculation, the following explicit equation

$$v_m = \left(\frac{1}{\delta} - \frac{\gamma}{\delta^{1.4}} \right)^{0.4} \quad (4.12)$$

may be used to provide an approximate answer. In many applications of industrial interest, the $\frac{\gamma}{\delta^{1.4}}$ term is small compared with the $\frac{1}{\delta}$ term. This permits an even greater simplification of Equation 4.12 into

$$v_m = \frac{1}{\delta^{0.4}} \quad (4.13)$$

Where the piping or ducting is not circular, the equivalent or hydraulic mean diameter D_{eq} is used instead of D . This is given by

$$D_{eq} = 4 \frac{A}{WP} \quad (4.14)$$

where A is the cross-sectional area of the duct, and WP is the wetted perimeter.

4.3 THE WORKING PRINCIPLE OF A CYCLONE DRYER

A cyclone dryer is a cylindrical tower, divided by conical orifices into several chambers as shown in Figure 4.3. Hot gas and wet solids are introduced tangentially into the lowest chamber. The conveying air imparts a strong rotational spin to the entry chamber. Subsequently, a ring of recirculating drying material is rotated at high velocity, first at the lowest chamber and later in the upper chambers. The rotational movement continues towards the top of the dryer, slowing as it passes from chamber to chamber. There is a great difference in the velocities of gas and solids inside the cyclone chamber, resulting in high heat and mass transfer coefficients.

The rotational movement in each chamber enables drying material to be successfully separated. It is then re-entrained into the gas jet at the centre of the cyclone after falling down the conical surface to the orifice lip. The residence time of the drying material in the chambers will vary depending on the weight and moisture content of individual particles. Small, light particles move in the direction of the gas direction along the vertical axis, and a short residence time is expected. Large heavy particles, which are more readily separated and redispersed, will have a longer residence time.

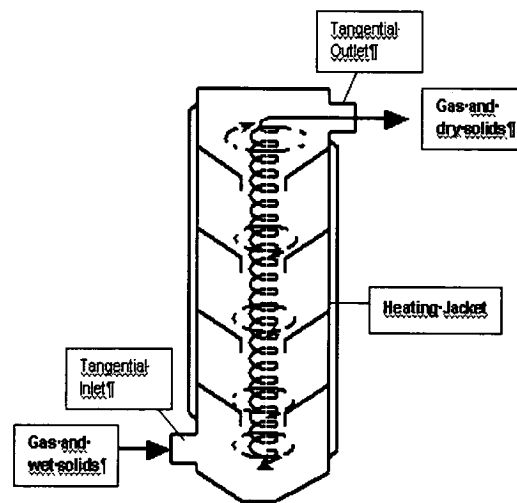


Figure 4.3 Multi-chamber cyclone dryer (Korn, 2001).

4.4 CYCLONE DRYER APPARATUS DESIGN AND DEVELOPMENT

4.4.1 Outline and Basic Assumptions

Figure 4.4 presents a schematic diagram of the laboratory model cyclone dryer used in the present investigation. It consists of five parts: blower, heater, rotary feeder, drying chamber and separation chamber.

The drying chamber is separated into body and orifice parts, for convenient design and set-up. The blower is selected to provide sufficient airflow to develop the necessary total pressure in the air stream to maintain pneumatic conveying and overcome the flow resistance of the system. The heater is sized to deliver sufficient heat to the air to raise its temperature to desirable values. The objective of this chapter is to design all necessary apparatus used in the experimental set-up of the cyclone dryer.

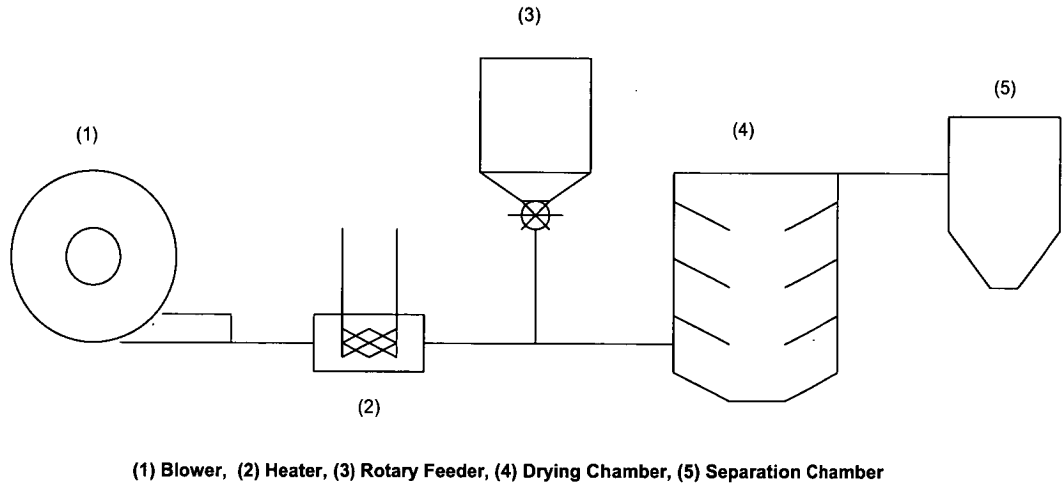


Figure 4.4 Schematic diagram for model cyclone dryer used in this study

The following basic assumptions were made in the cyclone dryer design:

1. Since the angle of repose of paddy grain is 36° , the conical surfaces between the separation chambers slope at 40° to horizontal to ensure that the paddy grain can move down to the orifice lip;
2. At steady state working conditions, the cyclone dryer acts as a pneumatic conveyor which is operated in dilute mode and 5% volume fraction is occupied by paddy;
3. The minimum spouted bed velocity of paddy is 13 m/s (Wetchacama, 1999). To ensure proper working of the cyclone dryer, the axial velocity in the jet through an orifice of the cyclone dryer should exceed the minimum spouted bed velocity;
4. The minimum deposition velocity of paddy is calculated using Equations 4.11 to 4.14. The average velocity at inlet and outlet of the cyclone dryer should be higher than deposition velocity to ensure that paddy can be conveyed through the dryer;
5. Ambient air of 30°C , 80 % RH will be heated to 110°C and used as the heat source for the cyclone dryer.

4.4.2 Drying Chamber

The cyclone dryer is a device whose; the design and performance has been little reported in the open literature. There is therefore little information available about this device for drying of agricultural materials. Korn (2001) presented the relevant geometry and nominal operating data for drying chemical substances in a cyclone dryer. Its sizing was largely dependent on the results of pilot scale tests. The sizing procedure was reported in the same paper. The dimensions of this pilot plant (Korn, 2001) are shown in Table 4.1

Table 4.1 Characteristics of cyclone dryer pilot plant (Korn, 2001).

Quantity	Value
Height of cyclone dryer	1.4 m
Diameter of cyclone dryer	500 mm
Number of chambers	7
Drying air throughput	1200 m ³ /h
Maximum temperature of inlet gas	150 °C

The geometry of the model cyclone dryer chamber used in the present investigation is shown in Figure 4.5. The outer diameter of cyclone dryer is 0.5 m. Other dimensions can be calculated from the specified values of various length ratios. The orifice angle is 40 ° to ensure the paddy grain can slide down the conical surface to the air jet at the orifice lip.

The acceptability of this configuration is checked by evaluating the minimum spouted bed velocity and deposition velocity to ensure that the paddy grain can be conveyed from chamber to chamber with no deposition at the inlet and outlet of cyclone. The minimum spouted bed velocity is used to calculate the velocity in the contracted jet through each orifice. From the continuity equation, the average velocity at inlet and outlet can be calculated and checked against the deposition velocity given by Equations 4.11 to 4.14.

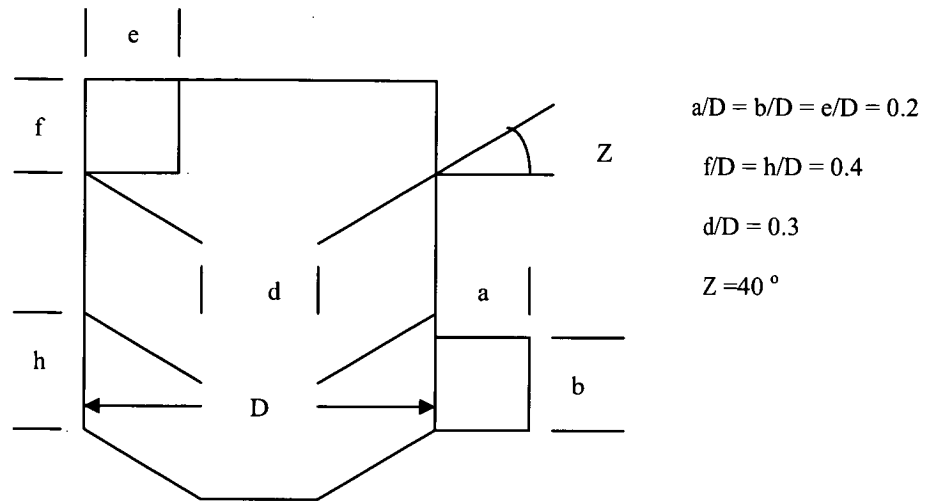


Figure 4.5 Geometry of cyclone dryer chamber used in the present investigation.

Assuming a contraction coefficient of 0.66 for each orifice and a velocity of 13 m/s in the contracted jet, the average velocity values at inlet and outlet are 13.0 and 6.5 m/s, respectively. From Equations 4.11 to 4.14, the deposition velocity for paddy grain at inlet and outlet are 0.25 and 0.27 m/s, respectively. The average velocities at inlet and outlet are higher than the deposition velocity, and thus these configuration ratios are acceptable.

The most important parameter for cyclone dryer design is the total pressure drop. This is not known initially, and must be estimated from experimental data or numerical simulation. The experimental results presented in Section 4.5.2 indicate values of total pressure drop coefficient $C_{\Delta P}$ increasing from 16.0 to 17.5 over the range of cyclone Reynolds number from 2.4×10^5 to 3.9×10^5 for a three-chamber dryer. The single-phase numerical flow simulation reported in Chapter 5 indicates an increase in $C_{\Delta P}$ from 13.1 to 14.4 (or about 10 %) as the number of chambers is increased from three to six. Experimental studies by Yuu et al. (1978) in a conventional single chamber cyclone separator indicated that the total pressure drop coefficient was reduced by an increase in solid loading. Taking all these factors into account, a design value of $C_{\Delta P} = 20$ would appear to be conservative for grain drying applications.

In order to conveniently observe the particle behaviour, the cyclone dryer parts were fabricated from transparent acrylic. They consist of the cyclone body, orifice, bottom, inlet body, outlet body and top lid. Drawings and dimension details are shown in Appendix B.

4.4.3 Blower Selection

The blower is the component in the system that provides energy in the form of total pressure to the air stream to overcome the system resistance. An appropriate blower must develop the necessary pressure to meet the system requirements for the desired airflow. The method of calculation of the required air flow and total pressure drop across the drying system is shown in Appendix C.

4.4.4 Rated Capacity of Heater

The amount of heat required to elevate the air temperature from 30 °C to 110 °C is given by

$$\text{Heat} = \rho_f Q c_{pi} (T_{fi} - T_{\infty})$$

where $T_{fi} = 110^{\circ}\text{C}$, $T_{\infty} = 30^{\circ}\text{C}$

$$c_{pi} = \text{specific heat of air at } (T_{fi} + T_{\infty})/2 = 1.009 \text{ kJ/kg K}$$

$$\rho_f Q = 0.922 * 0.16 = 0.147 \text{ kg/s (calculated at maximum air flow rate)}$$

Hence the required heating rate is

$$\text{Heat} = 0.1474 * 1.009 * (110 - 30) = 11.9 \text{ kW}$$

By assuming a heat loss equal to 20% of the heat input, the capacity of heater should be at least

$$\text{Heat}_{\text{real}} = 11.9 / 0.8 = 14.875 \approx 15 \text{ kW}$$

4.4.5 Separation Chamber

The separation chamber was designed without a top cover. This lets the air out of the dryer and into the atmosphere. In the separation chamber, the grain is separated out by its own weight and falls to the bottom of the chamber. The design and dimension details are given in Appendix B.

Figure 4.6 shows the assembled model cyclone dryer system. The complete drawings with all details, materials of construction and dryer layout are given in Appendix B.

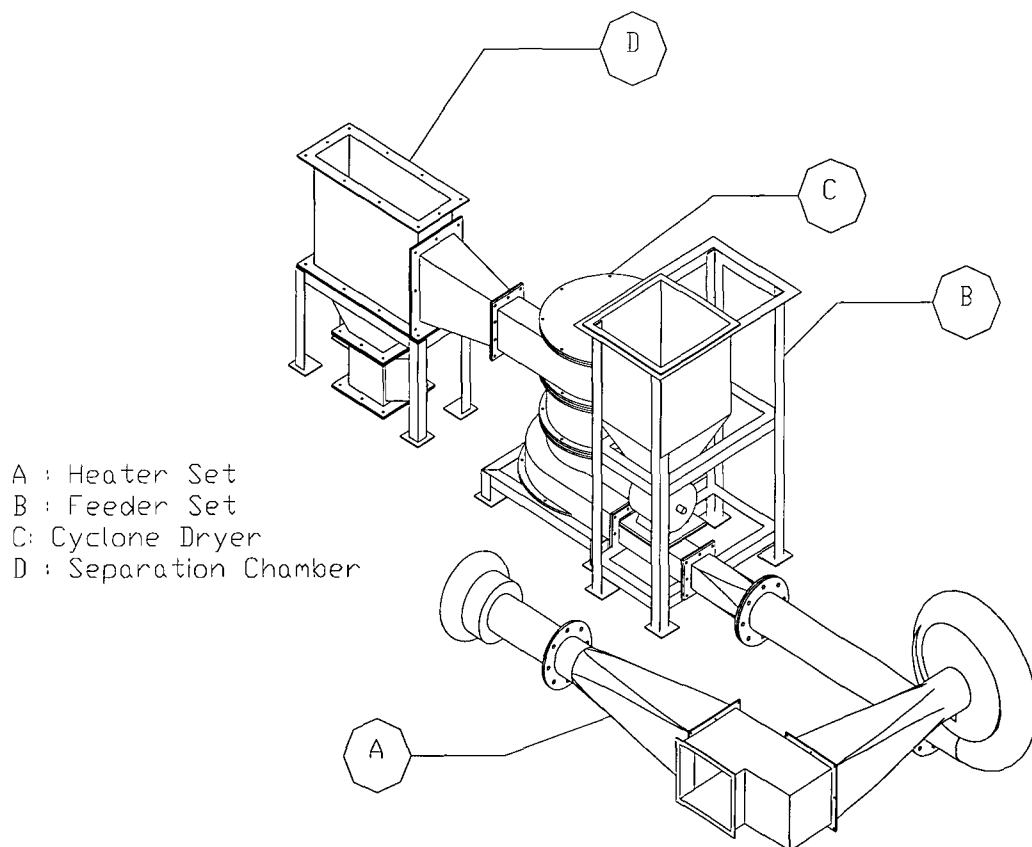


Figure 4.6 Drawing of model cyclone dryer system.

4.5 PRELIMINARY STUDY OF A CYCLONE DRYER

4.5.1 Introduction

Preliminary tests of the model cyclone dryer system were conducted to examine the minimum working air velocity and characteristics of grain flow inside the drying chambers and the pressure drop characteristics of the system. These tests were conducted without any air heating.

4.5.2 Effect of Velocity on Cyclone Dryer Pressure Drop

These measurements were conducted first, to establish the adequacy of the fan and provide data for later validation of numerical simulations. The cyclone dryer was fitted with a centrifugal blower, powered by an AC motor with a variable frequency speed control unit. Four different fan speeds (2925, 2350, 1770 and 1180 rpm) were used to investigate the variation of pressure drop across the cyclone dryer chamber with air flow-rate.

A bellmouth fitted at the fan inlet was used to measure the airflow rate. Pressure tappings were provided at the throat of the bellmouth and other key points through the system. The pressure differentials between individual tapping points and atmosphere were measured with a Furness Controls Model FC012 electronic manometer giving an analog voltage output linear with pressure differential. The selection of pressure sources was performed by a Furness Controls pressure scanner Model FCS421. The fan speed, pressure scanning and data acquisition were controlled by a personal computer.

The total pressure drop across the dryer was calculated by summing the differentials of static and dynamic pressure between inlet and outlet. The results for a 3-chamber configuration are presented in dimensionless form in Figure 4.7, as the total pressure drop coefficient $C_{\Delta P}$ (defined by Equation 4.5) against Reynolds number based on

the cyclone diameter and inlet velocity. There is a slow increase in $C_{\Delta P}$ with Reynolds number, with $C_{\Delta P}$ values between 16.0 to 17.5 over the range tested.

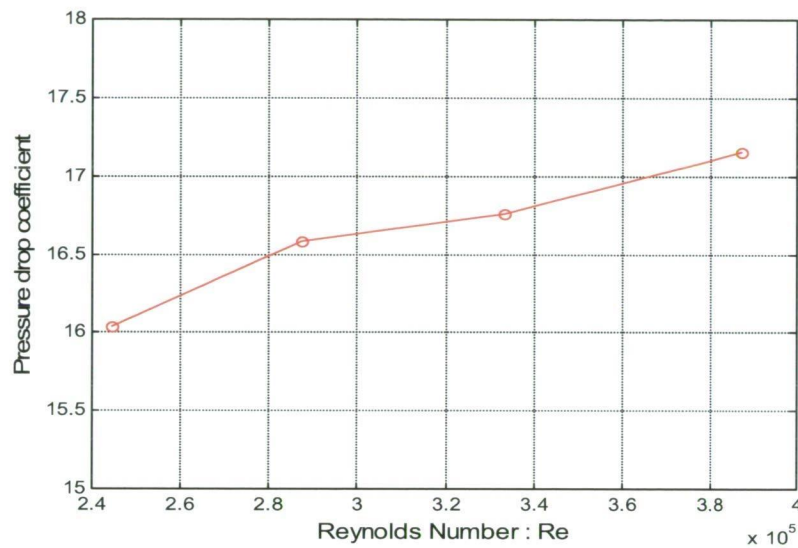


Figure 4.7 Variation of cyclone dryer total pressure drop coefficient with Reynolds number.

4.5.3 Flow Characteristics of Grain Inside the Cyclone Dryer and Minimum Working Velocity

As stated previously, the minimum spouted bed velocity is the key factor to make the cyclone dryer work properly. The cyclone dryer chamber design was based on a value of 13 m/s for paddy grain. Due to the lack of published data, it was considered desirable to check the applicability of this criterion for the multi-chamber cyclone dryer model.

Initial testing was conducted by loading a batch of paddy grain in the base of the model dryer tower. The mode of pneumatic transport of grain inside the chamber was then observed while the airflow rate was gradually increased by adjusting the fan speed until a steady state working condition with satisfactory operation was achieved. At low inlet air velocity, the air simply passed over the solid bed without carrying any paddy grain. Only some of the straw and contaminant material were separated and transported by the air to the exit of the cyclone. Figure 4.8 shows the paddy grain

behaviour at $0.09 \text{ m}^3/\text{s}$ air flow rate, corresponding to an estimated axial jet velocity of 11.5 m/s through the chamber orifices.



Figure 4.8 Paddy grain behaviour at $0.09 \text{ m}^3/\text{s}$ air flow rate.
(Estimated jet velocity 11.5 m/s)

As the air velocity was increased, the bed of grain gradually commenced to rotate inside the lowest chamber and be drawn up into the rotating air stream in the centre of the dryer. A pile of paddy grain grew in the centre of the dryer as air flow was increased. At the critical air flow rate, where the pressure of the air was sufficient to overcome gravity and frictional restraints, the grain was drawn up into the air stream and conveyed from chamber to chamber until reaching the exit. The air stream formed the grain into a rotating fountain through the central orifices, and vigorous recirculation of grain was observed in the central dryer chamber.

Grain was sucked up at the centre of the lowest chamber, while some grain moved in the form of a rotating ring at the wall of lowest chamber. In the next higher chamber, grains separating from the central vortical flow column fell to the conical floor and travelled towards the orifice in the form of a spiral dune flow. This circulation process occurred in every chamber, and slowed down from chamber to chamber until grains were conveyed out of the exit. The pattern of grain movement inside the central cyclone dryer chamber at an air flow rate slightly above the critical value required for

grain transport is shown in Figure 4.9. This flow rate corresponds to an estimated jet velocity of 14 m/s, which is consistent with the minimum spouted bed velocity of 13 m/s for paddy grain proposed by Wetchacama (1999).



Figure 4.9 Paddy grain behaviour at $0.11 \text{ m}^3/\text{s}$ air flow rate.
(Estimated jet velocity 14 m/s)

4.6 CONCLUDING REMARKS

This chapter has reviewed some basic principles of conventional cyclone separator operation and outlined the design of a multi-chamber cyclone suitable for grain drying. The significant feature of this device is the dispersion and recirculation of grain within the individual chambers that increases the residence time of the grain. The feasibility of pneumatically transporting paddy grain through this device has been demonstrated, and the critical air velocity has been found consistent with the minimum spouted bed velocity reported by other workers.

The next chapter will describe detailed measurements of single-phase (clean air) flow through the model dryer and a comparison of these results with numerical simulations.

Chapter 5

CYCLONE DRYER FLOW FIELD: EXPERIMENTAL AND NUMERICAL STUDIES

5.1 INTRODUCTION

As reviewed in Chapter 2, rice grain as harvested in the wet season usually has a high moisture content (24-33 % wb.) which, if not reduced, allows microbial growth causing biochemical deterioration of the grain. Drying of paddy grain (rice) from its fresh harvest moisture content to a more manageable level (18 % wb.) is currently the only practical method to lower the rate of deterioration of grain (Driscoll et al., 1985). Satisfactory drying of newly harvested grains typically requires a residence time of several minutes.

Simulation results in Chapter 3 indicate that an excessively long length of pneumatic transport pipe would be required for drying hygroscopic material such as paddy. The recently developed pneumatic dryer with delay chambers called a “cyclone dryer”, gives a longer residence time of particles than a simple pneumatic dryer. Solid retention times

of 5-30 minutes can be obtained with this dryer (Korn, 2001) making it suitable for large amounts of moisture removal. However, the cyclone dryer reported by Korn (2001) was developed by pilot plant scale testing rather than theoretical predictions.

Computational Fluid Dynamics (CFD) is now widely used to evaluate the working possibility of new process reactors during the conceptual and preliminary design stages. With recent advances in CFD and computer capability it is now possible to simulate the flow field and heat and mass transfer processes in a short enough period of time to have a significant impact on the design cycle. There is, however, still a significant amount of uncertainty about the accuracy of CFD for prediction of the absolute physical characteristics of a newly designed reactor. Due to this lack of confidence, the current practice is to use CFD as a tool for screening a large number of potential designs.

To make further improvements to cyclone dryer designs, a good understanding of the fluid dynamics is required. Analytical techniques do not allow changes in geometry to be readily assessed. Reynolds-Average Navier-Stokes (RANS) based CFD models provide an economical means of understanding the complex fluid dynamics and how it is influenced by changes in design and operating conditions. Validation of the computational results is required to establish confidence in the predictions.

A review of archival literature revealed no research involving simulation of cyclone dryers, but significant advances have been made in simulating cyclone separators. Boysan et al. (1982) who were the early users of the CFD technology, applied the algebraic stress model (ASM) to simulations of a cyclone separator. Later Zhou et al. (1990), Modigell et al. (2000) and Hoekstra et al. (1999) applied CFD to this problem with varying success. But their works dealt only with two-dimensional prediction of single-phase flow in the cyclones, and treated the flow field as axisymmetric and steady.

To get more details of the complicated flow field in cyclone devices it is necessary to perform numerical simulations in three-dimensions. Several researchers have conducted three-dimensional numerical simulations of cyclone separators (Griffiths et al., 1996;

Zhao et al., 2000; Yoshida et al., 1990 & 2001; Montavon et al., 2000; Schimdt et al., 2003; Wang et al., 2003; Derksen et al., 2000; Derksen, 2003; Witt et al., 1999). These authors have tested a number of turbulence models, ranging from the algebraic stress model (Zhao et al., 2000), standard $k-\epsilon$ (Yoshida et al., 1991 & 2001; Witt et al., 1999; Montavon et al., 2000), RNG $k-\epsilon$ (Schimdt et al., 2003), and a Reynolds stress model (Wang et al., 2003; Witt et al., 1999). Their studies have demonstrated that CFD still cannot produce very accurate descriptions of the flow field in cyclones because of difficulties in modelling the phenomena occurring in swirling flow. Calculated results for pressure drop agreed only moderately well with the experimental data. The experimental pressure drop was larger than the calculated pressure drop by 60 %, 15 %, and 16 % for the standard $k-\epsilon$ model (Yoshida et al., 2001), RNG $k-\epsilon$ (Griffiths et al., 1996), and Reynolds stress model (Wang et al., 2003), respectively.

Recently, large eddy simulation (LES) was used to predict the unsteady characteristics and spiral shape of the vortex core in a cyclone separator (Schmidt et al., 2003; Derksen et al., 2000&2003). Good agreement with experimental data was obtained, both in terms of the average velocity and velocity fluctuations, when high spatial and temporal resolution was used. The superiority of the LES approach as compared with the Reynolds-average approach was clearly illustrated, but at greatly increased computational cost.

This chapter presents predictions of the gas-phase flow field and pressure drop inside a laboratory scale cyclone dryer using RANS based CFD. The commercial code CFX 5.7 is run for steady, three-dimensional, single-phase flow conditions. Simulation parameters such as the advection scheme, turbulence model and level of mesh resolution are tested to find the best combination for flows of this type. The computed flow behaviour is compared with experimental results to establish the level of confidence in the numerical predictions. Mean flow field and pressure drop predictions are then presented using the optimised simulation parameters. Finally, the effect of the number of delay chambers on the pressure drop is investigated. This is the first stage in the development of a computational method for cyclone dryer design.

5.2 EXPERIMENTAL INVESTIGATION

5.2.1 Flow Geometry and Physical Model

The geometry of the cyclone dryer used for the initial numerical investigation is shown in Figure 5.1. It is characterised by the principal diameter, D , and the geometric ratios detailed in Figure 5.1. The diameter of the laboratory scale model cyclone dryer tested is 500 mm, similar to the design of Korn (2001). The orifice angle of 40° is greater than the angle of repose of the granular material to ensure that the grains can slide along the surface to the air jet at the orifice. This achieves the necessary recirculation of grain within the dryer chamber for the ultimate drying application. The cylindrical coordinate directions are defined in Figure 5.1. The origin of the coordinate system is located at the level of the interface between the conical bottom and the cylindrical body.

In order to judge the quality of numerical simulations, experimental data were required. These were obtained from the laboratory scale cyclone dryer, which was constructed from 10 mm thick acrylic. Air was drawn from the atmosphere through a horizontal duct to a centrifugal blower with a flow straightening honeycomb at exit. It then fed tangentially to the lower cyclone chamber and finally discharged freely to atmosphere from the upper chamber. The centrifugal blower was powered by an AC motor with variable frequency speed control. A bellmouth nozzle was fitted at the fan inlet in order to measure the air flow-rate across the system. Static pressure tapings were provided at the nozzle throat and the cyclone inlet.

As shown in Figure 5.1 (a), axial and tangential velocity profiles were measured at two elevations (at $z = 0.055$ and 0.255 m) by means of a 3-hole probe. At each axial location, the measurement probe was traversed from either wall along a diameter orientated 11° from the normal to the inlet duct. The traverse locations in the x-y plane are shown in Figure 5.1 (b). The measuring devices and data acquisition systems will be described in the following sub-section.

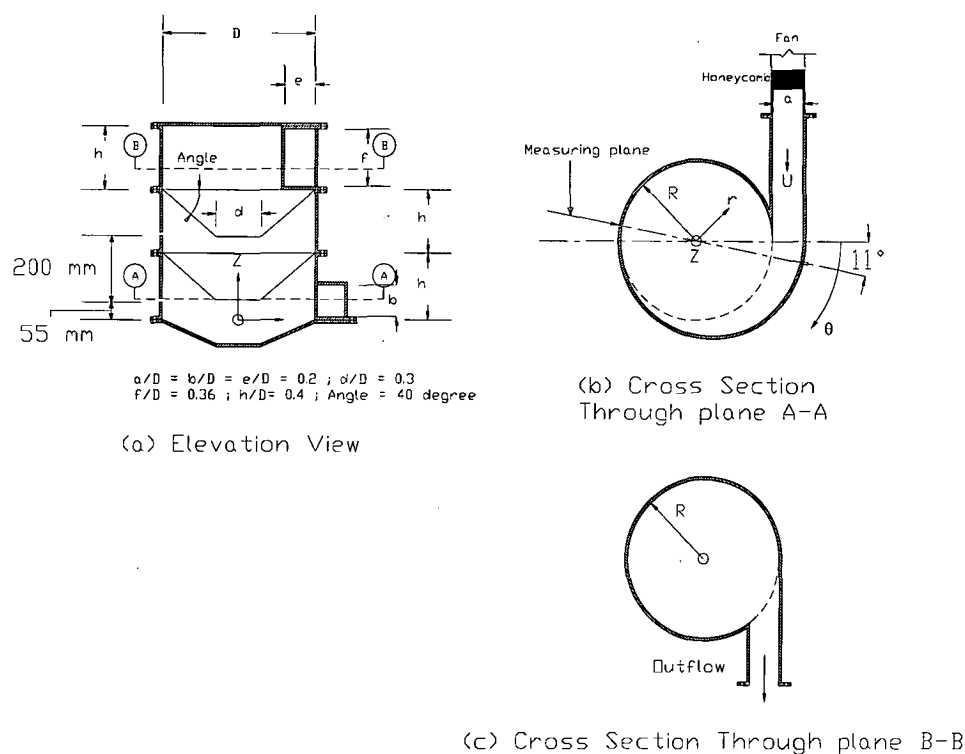


Figure 5.1 Model cyclone dryer geometry in x-z and x-y planes. The configuration geometric ratios and measuring positions are also shown.

5.2.2 Measurement Techniques

For all the velocity traverses presented graphically in this chapter, the fan motor was operated at 30 Hz frequency, giving an inlet velocity of about 9 m/s. Two pressure taps were used to measure the static pressure at the bellmouth and cyclone dryer inlet. The air flow rate was calculated from the static pressure differential across bellmouth inlet. The total pressure drop across the cyclone dryer was calculated from summation of the static and dynamic pressure differentials between the inlet and outlet. The dynamic pressures were based on the mean velocities determined from the measured flow rate.

A three-hole modified wedge probe was used to measure the radial profiles of axial and tangential velocity. Figure 5.2 shows the detail of the probe head and hole numbering. In the cyclone dryer chamber, where the direction and the magnitude of velocity are not known, this device indicates the flow direction in one plane only. The axial and tangential velocity components are determined from the direction and magnitude of velocity. The three-hole probe was calibrated in uniform flow in a wind tunnel. Details of the calibration procedure are given in Appendix D. The calibration results showed that the uncertainties of the local angle and velocity measurement in two-dimensional flow were both less than 1% over the range of calibration. A MATLAB program (Ucpct.m) was written to reduce the probe pressure measurements into angle and magnitude of velocity at the probe head. These values were then used to calculate the local axial and tangential velocity components.

Five pressures were measured: P_0 at the bellmouth; P_{in} at the cyclone inlet; and P_1 , P_2 and P_3 at the front, top and bottom sides of three-hole probe head. A pressure scanner (Furness FCS421) was used to select different pairs of pressure sources as shown in Table 5.1. The pressure scanner was linked to a 0-100 mm H₂O range micromanometer (Furness FC012), which gave an analog voltage output proportional to the observed pressure differential. A LabVIEW program was used to control the automatic data acquisition. This program operated the channel selection and recording of measured voltages at the desired sampling rate. The estimated uncertainties in these measurements were $\pm 6\%$ for total pressure and $\pm 2\%$ for velocity. The radial velocity component was not measured.

While the non-zero pitch angle produced by radial velocity components within the model dryer would have caused deviations from the 2-D probe calibration, these effects are thought to have been acceptably small in the outer vortex region $|r/R| > 0.4$. Here the CFD predictions indicated the pitch angles to be generally less than 2° ; the likely measurement errors from this source are less than 1° in angle and 2% in flow speed. Larger errors would have occurred for velocity measurements in the inner core region

$|r/R| < 0.4$ at $z = 0.055$ m, where pitch angles of up to 10° were predicted. The inner core measurements at $z = 0.255$ m must be considered unreliable due to predicted pitch angles averaging 20° , with higher peaks. Additional measurement error is likely in regions of high shear at the edge of the vortex core due to flow non-uniformity over the probe head.

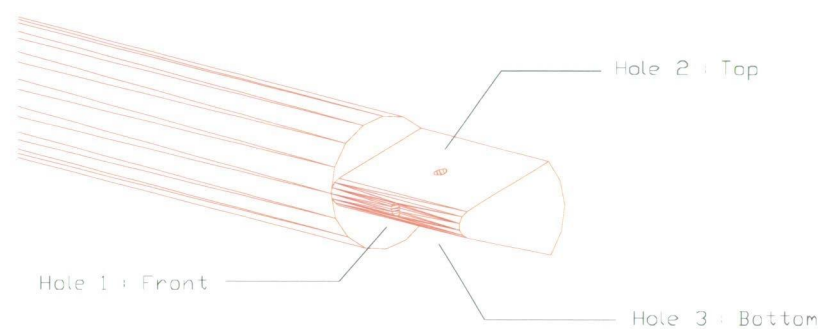


Figure 5.2 Three-hole modified wedge probe.
(support diameter 6.35 mm)

Axial and tangential velocities inside the cyclone chamber were normalised with the mean inlet air velocity. The pressure drop was expressed in terms of a pressure coefficient, using a dynamic pressure based on the mean inlet velocities. These values were used to validate the quality of the flow field simulated by the flow solver CFX 5.7. The validation procedure and development of an optimised CFD model will be discussed in section 5.3.3.

Table 5.1 Pressure scanner channel set-up during flow field measurement of the cyclone dryer

Channel	1	2	3	4
+ side	P_0	P_{in}	P_1	P_2
- side	P_{atm}	P_{atm}	P_3	P_3

5.2.3 Experimental Results

Figure 5.3 presents typical measurements of radial profiles of tangential and axial velocity components at elevations, $z = 0.055$ m and 0.255 m, as indicated in Figure 5.1.

The tangential velocity profiles in Figure 5.4 (b) show the expected Rankine (or combined) type vortex, consisting of an outer potential vortex with a region of near solid rotation at the core. This flow pattern has been reported in flow field measurements of cyclone separators by several researchers (e.g. Stirmand, 1952; Ter linden, 1949; Shepherd et al., 1939). The maximum tangential velocity rises to 2.5 and 1.5 times the inlet air velocity at the first and second measurement stations, respectively.

For measurements taken at $z = 0.055$ m, the tangential velocity maxima occur at $R/R_{\text{cyclone}} = \pm 0.2$, indicating symmetrical swirl flow in the lowest chamber of the cyclone dryer. At $z = 0.255$ m, the tangential velocity maxima are not symmetric about the orifice centre, indicating an eccentric swirl flow pattern in the higher chamber. However, the flow pattern still represents a Rankine type vortex.

The axial velocity profiles in Figure 5.4 (a), show maxima in similar locations to this of the tangential velocity profiles for both measurement stations. In the outer core, the magnitude of axial velocity is nearly constant except in the near wall region, which shows a variation depending on the direction of the local air-flow. The magnitudes of the tangential and axial velocity maxima decrease from chamber to chamber due to turbulent diffusion inside the cyclone dryer. Energy losses cause a general decay in the level of tangential velocity from the first to the second chamber of the dryer.

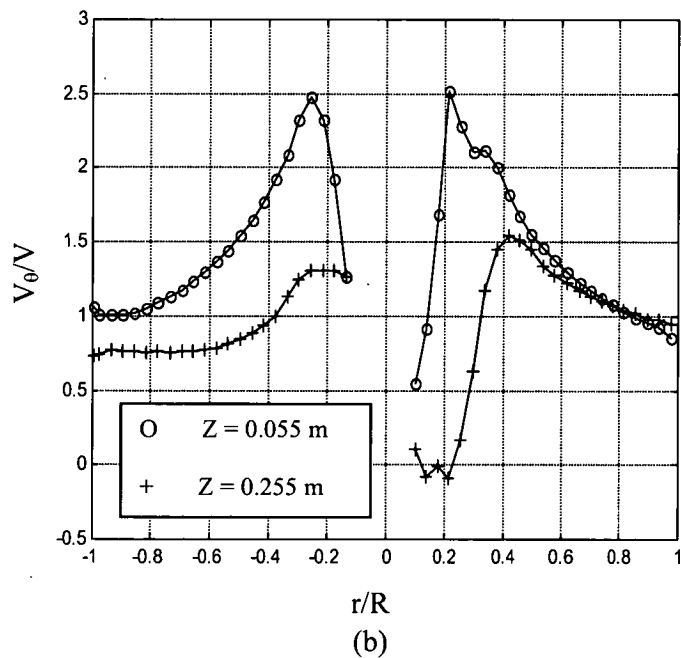
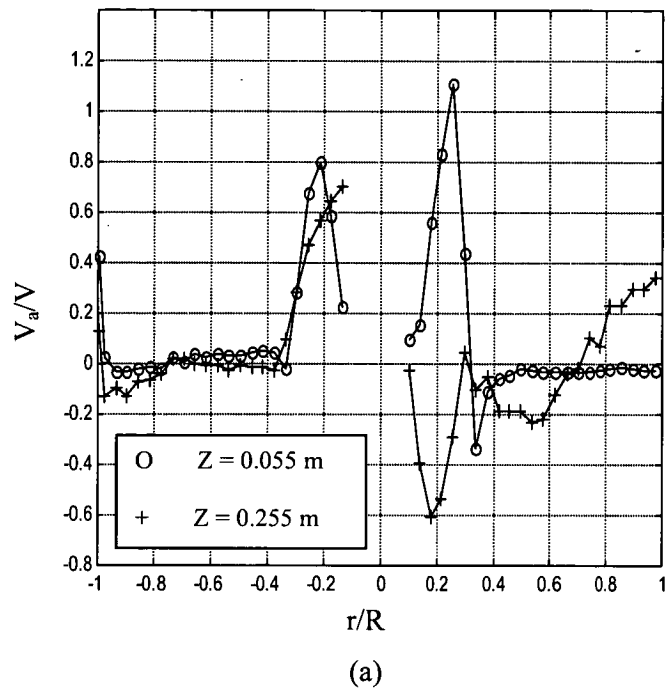


Figure 5.3 Radial profiles of velocity components at elevations $z = 0.055$ m and 0.255 m: (a) axial velocity; (b) tangential velocity.

The velocity distribution was found to retain a high degree of similarity over a range of inlet velocities. Another measurement at 11 m/s inlet velocity showed a slight reduction in the dimensionless value of peak tangential velocity, but no change in its position; there appeared to be nearly perfect similarity in the distributions. Thus, the results for 9 m/s inlet velocity were used to validate the numerical simulations in the following section.

5.3 NUMERICAL SIMULATION AND VALIDATION

5.3.1 Basic Governing Equations

Turbulent flow can be described by the Reynolds-averaged Navier-Stokes equations. The Reynolds averaged equation for conservation of mass is written:

$$\nabla \cdot (\rho_f \mathbf{u}) = 0 \quad (5.1)$$

while the Reynolds averaged equation for conservation of momentum is written:

$$\nabla \cdot (\rho_f \mathbf{u} \otimes \mathbf{u}) = -\nabla P + \nabla \cdot (\mu_{\text{eff}} (\nabla \mathbf{u} + (\nabla \mathbf{u})^T)) - \rho_f \overline{\mathbf{u}' \otimes \mathbf{u}'} \quad (5.2)$$

where μ_T is the turbulent eddy viscosity obtained from:

$$\mu_T = C_\mu \rho_f \frac{k^2}{\varepsilon} \quad (5.3)$$

Here \mathbf{u} is the Reynolds averaged flow velocity while \mathbf{u}' is the turbulent fluctuation. An effective viscosity can be defined by $\mu_{\text{eff}} = \mu + \mu_T$. μ is molecular viscosity and μ_T is turbulence eddy viscosity. The over-bar represents the Reynolds-averaging operator. Solution of the above equations by analytical techniques is only possible for very simple cases. Numerical solution methods have been developed, but are complicated by the

additional Reynolds stress terms $(-\rho_f \overline{\mathbf{u}' \otimes \mathbf{u}'})$ on the right hand side of Equation (5.2). To obtain values for the Reynolds stress terms a suitable turbulence model must be used. The models used in this study are the RNG $k-\varepsilon$ and SSG Reynolds stress turbulence models.

5.3.1.1 Two-equation turbulence model

A widely used turbulence model is the $k-\varepsilon$ model, which is based on the eddy viscosity hypothesis. In the $k-\varepsilon$ turbulence model the Reynolds stress terms are approximated by:

$$\rho_f \overline{\mathbf{u}' \otimes \mathbf{u}'} = -\frac{2}{3} \rho_f k \mathbf{I} - \frac{2}{3} \mu_T \nabla \cdot \mathbf{u} \mathbf{I} + \mu_T (\nabla \mathbf{u} + (\nabla \mathbf{u})^T) \quad (5.4)$$

The equations below are solved to obtain k and ε , which are the turbulence kinetic energy and dissipation rate, respectively.

$$\nabla \cdot (\rho_f \mathbf{u} k) - \nabla \cdot \left(\mu + \frac{\mu_T}{\sigma_k} \right) \nabla k = P_k - \rho_f \varepsilon \quad (5.5)$$

$$\nabla \cdot (\rho_f \mathbf{u} \varepsilon) - \nabla \cdot \left(\mu + \frac{\mu_T}{\sigma_\varepsilon} \right) \nabla \varepsilon = C_1 \frac{\varepsilon}{k} P_k - C_2 \rho_f \frac{\varepsilon^2}{k} \quad (5.6)$$

Shear production is defined as:

$$P_k = \mu_T \nabla \mathbf{u} \cdot (\nabla \mathbf{u} + (\nabla \mathbf{u})^T) - \frac{2}{3} \nabla \cdot \mathbf{u} (3\mu_T \nabla \cdot \mathbf{u} + \rho_f k) \quad (5.7)$$

For the standard $k-\varepsilon$ turbulence model, the constants are $\sigma_k=1$, $\sigma_\varepsilon=1.3$, $C_1=1.44$, $C_2=1.92$. The RNG $k-\varepsilon$ turbulence model is based on renormalisation group analysis

of the Navier-Stokes equations. The transport equations for turbulence generation and dissipation are the same as those for the standard $k-\varepsilon$ turbulence model, but the model constants differ and the constant C_1 is replaced by the function $C_{\varepsilon 1RNG}$. The transport equation for turbulence dissipation becomes:

$$\nabla \cdot (\rho_f \mathbf{u} \varepsilon) - \nabla \cdot \left[\left(\mu + \frac{\mu_T}{\sigma_{\varepsilon RNG}} \right) \nabla \varepsilon \right] = C_{\varepsilon 1RNG} \frac{\varepsilon}{k} P_k - C_{\varepsilon 2RNG} \rho_f \frac{\varepsilon^2}{k} \quad (5.8)$$

where

$$C_{\varepsilon 1RNG} = 1.42 - f_\eta \quad (5.9)$$

$$f_\eta = \frac{\eta \left(1 - \frac{\eta}{4.38} \right)}{(1 + \beta_{RNG} \eta^3)} \quad (5.10)$$

$$\eta = \sqrt{\frac{P_k}{\rho_f C_{\mu RNG} \varepsilon}} \quad (5.11)$$

The values of constants for the RNG $k-\varepsilon$ model are: $C_{\varepsilon 2RNG} = 1.68$, $\sigma_{\varepsilon RNG} = 0.7179$, $\beta_{RNG} = 0.012$ and $C_{\mu RNG} = 0.085$.

5.3.1.2 Reynolds stress turbulence model

Another choice of turbulence model is the Reynolds stress turbulence model (RSM). Transport equations have been developed for each component of Reynolds stresses as shown below. These differential equations can be solved to obtain each stress component.

$$\nabla \cdot (\rho_f \mathbf{u} \otimes \overline{\mathbf{u}' \otimes \mathbf{u}'}) - \nabla \cdot \left(\left(\mu + \frac{2}{3} C_S \rho_f \frac{k^2}{\varepsilon} \right) \nabla \mathbf{u} \otimes \mathbf{u} \right) = P_s + \Pi - \frac{2}{3} \rho_f \varepsilon \mathbf{I} \quad (5.12)$$

$$\nabla \cdot (\rho_f \mathbf{u} \varepsilon) - \nabla \cdot \left[\left(\mu + \frac{\mu_T}{\sigma_k} \right) \nabla \cdot \varepsilon \right] = C_{\varepsilon 1} \frac{\varepsilon}{k} P_k - C_{\varepsilon 2} \rho_f \frac{\varepsilon^2}{k} \quad (5.13)$$

The shear production term, P_s is defined as:

$$P_s = -\rho_f (\overline{\mathbf{u}' \otimes \mathbf{u}'} (\nabla \mathbf{u})^T + (\nabla \mathbf{u}) \overline{\mathbf{u}' \otimes \mathbf{u}'}) \quad (5.14)$$

The pressure strain term, Π is given by the following equations:

$$\Pi = \Pi_1 + \Pi_2 \quad (5.15)$$

$$\Pi_1 = -\rho_f \varepsilon \left(C_{S1} \mathbf{a} + C_{S2} \left(\mathbf{a} \mathbf{a} - \frac{1}{3} \mathbf{a} \cdot \mathbf{a} \mathbf{I} \right) \right) \quad (5.16)$$

$$\begin{aligned} \Pi_2 = & -C_{r1} P \mathbf{a} + C_{r2} \rho k \mathbf{S} - C_{r3} \rho_f k \mathbf{S} \sqrt{\mathbf{a} \cdot \mathbf{a}} \\ & + C_{r4} \rho_f k \left(\mathbf{a} \mathbf{S}^T + \mathbf{S} \mathbf{a}^T - \frac{2}{3} \mathbf{a} \cdot \mathbf{S} \mathbf{I} \right) + C_{r5} \rho_f k (\mathbf{a} \boldsymbol{\omega}^T + \boldsymbol{\omega} \mathbf{a}^T) \end{aligned} \quad (5.17)$$

where

$$\mathbf{a} = \frac{\overline{\mathbf{u}' \otimes \mathbf{u}'}}{k} - \frac{2}{3} \mathbf{I} \quad (5.18)$$

$$\mathbf{S} = \frac{1}{2} (\nabla \mathbf{u} + (\nabla \mathbf{u})^T) \quad (5.19)$$

$$\boldsymbol{\omega} = -\frac{1}{2} (\nabla \mathbf{u} - (\nabla \mathbf{u})^T) \quad (5.20)$$

\mathbf{I} is the Kronecker delta, \mathbf{a} the anisotropy tensor, \mathbf{S} the strain rate and $\boldsymbol{\omega}$ the vorticity. Constants for the SSG Reynolds stress model are $C_S=0.22$, $C_\varepsilon=0.18$, $C_{\varepsilon 1}=1.45$, $C_{\varepsilon 2}=1.9$, $C_{S1}=1.7$, $C_{S2}=-1.05$, $C_{r1}=0.9$, $C_{r2}=0.8$, $C_{r3}=0.65$, $C_{r4}=0.625$ and $C_{r5}=0.2$.

5.3.2 Numerical Set-up and Solution Technique

The commercial CFD software package CFX uses a finite volume method to find a steady-state solution of the above set of partial differential equations. For each iteration, the full set of equations is solved using an algebraic multigrid method (AMG). The hydrodynamic equations are solved simultaneously as a single system. This solution approach uses a fully implicit discretisation of the equations at any given iteration. Transport equations for the turbulence properties are then solved. The solution procedure is repeated until the specified convergence criteria are met.

A series of definition files was created to obtain simulation results from CFX5.7. The simulation assumes isothermal (25 °C) flow of a generic ideal gas with a reference pressure of 1 atm. Fluid enters the domain with uniform velocity of 10 m/s normal to the inlet surface. The outlet boundary was specified with an average static pressure of 0 Pa. This is compatible with the experimental set-up, in which air was discharged freely to the atmosphere. Scalable wall functions were applied to describe the velocity distribution near the wall.

Boundary conditions for k and ε at the inlet were determined by assuming a turbulence intensity of 5%. A high turbulence intensity was expected due to the combined effects of the fan discharge and honeycomb mesh. A simulation using a turbulence intensity of 1% at the inlet was also run. This change was found to have only a small effect on the results.

The values of k and ε at inlet were calculated using $k = \frac{3}{2} I^2 v_{in}^2$ and $\varepsilon = k^{3/2} / 0.3D$.

All simulations were started from the automatic initial condition. Hexahedral meshes of various fineness were used in this study. Mesh concentration was applied in the near wall regions to capture flow gradients in boundary layer. Figures 5.4 (a), (b), (c) and (d) show the series of meshes having 864,185, 419,928, 190,057 and 86,555 nodes, that were used for mesh sensitivity studies. These are required for quality assurance purpose, as

specified for example in the statement on the control of numerical accuracy by the ASME Journal of Fluids Engineering. (<http://journaltools.asme.org/Templates/JFENumAccuracy.pdf>).

The predicted distributions of normalised axial and tangential velocity components v_z and v_θ , as well as the total pressure drop coefficient $C_{\Delta P} = \Delta P / \frac{1}{2} \rho v_{in}^2$, were compared with the experimental results to validate the numerical solutions.

5.3.3 Simulation Results and Validation

To investigate the effect of different modelling parameters and approaches, the following tests were performed:

1) Advection scheme test: Calculations were made with a series of differencing schemes of first order accuracy (upwind), high resolution, and second order accuracy (specific blend factor = 1) using the low resolution mesh of 86,555 nodes and the RNG k- ϵ turbulence model. The advection scheme that gave closest agreement with experimental results was used for further modelling tests.

2) Grid sensitivity test: Based on the optimum advection scheme identified, a series of calculations for mesh resolutions of 864,185 nodes, 419,928 nodes, 190,057 nodes, and 86,555 nodes were made. The predicted axial and tangential velocity distributions, as well as the total pressure drop coefficient, were compared to identify an adequate mesh resolution.

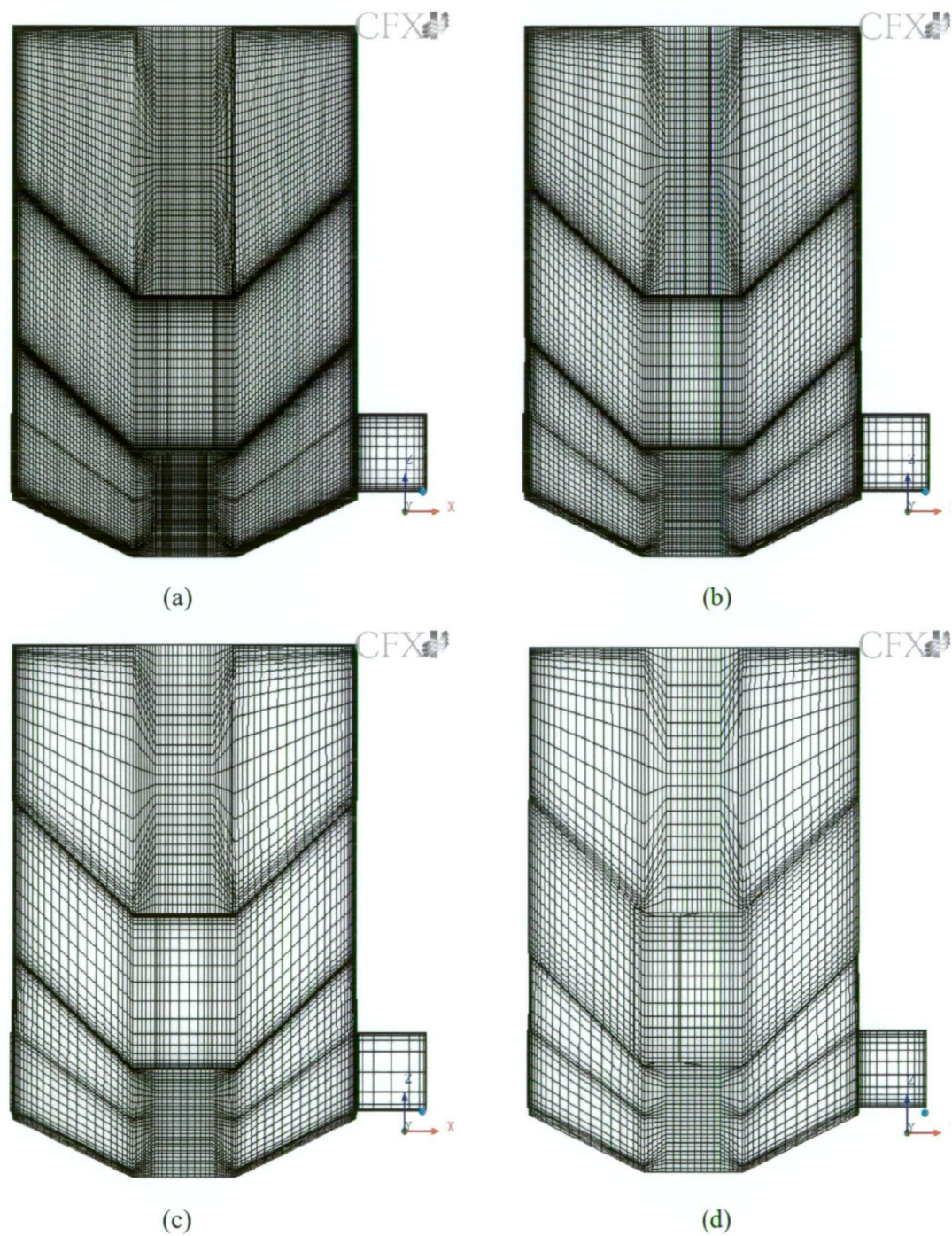


Figure 5.4 Series of meshes of different fineness used for grid sensitivity studies: (a) 864,185 nodes; (b) 419,928 nodes; (c) 190,057 nodes; (d) 86,555 nodes.

3) Turbulence model test: the RNG k- ϵ and SSG Reynolds stress turbulence models were tested using the optimum advection scheme and level of mesh resolution identified as described above. The predicted axial and tangential velocity distributions, as well as the total pressure drop coefficient, were compared with experimental data to choose the best performing turbulence model for the cyclone dryer problem.

The optimised numerical model based on the optimum advection scheme, mesh resolution and turbulence model was then used to predict the effect of inlet air velocity variation and number of dryer chambers on the velocity distributions and overall pressure drop coefficient for the cyclone dryer.

5.3.3.1 Advection (differencing) scheme

Simulations were run using first order (upwind), high resolution and second order differencing schemes, on a hexahedral mesh of 86,555 nodes with the RNG k- ϵ turbulence model. For all differencing schemes, a tight convergence of RMS level 10^{-6} was achieved. Figures 5.5 and 5.6 compare the predicted non-dimensional velocity distributions at the two elevations indicated in Figure 5.1 (a). The results are presented at a circumferential location 11° from the point where the inlet duct is attached.

With the upwind differencing scheme the tangential velocity was seriously under-predicted compared to the experimental data at both locations $z = 0.055$ m and $z = 0.255$ m. The adverse gradient of axial velocity in the core region was not captured due to the smearing effect of this differencing scheme. The high resolution and second-order differencing schemes produced significant improvements in predictions of the non-dimensional tangential and axial velocity distributions. They give good agreement for locations of the axial and tangential velocity maxima.

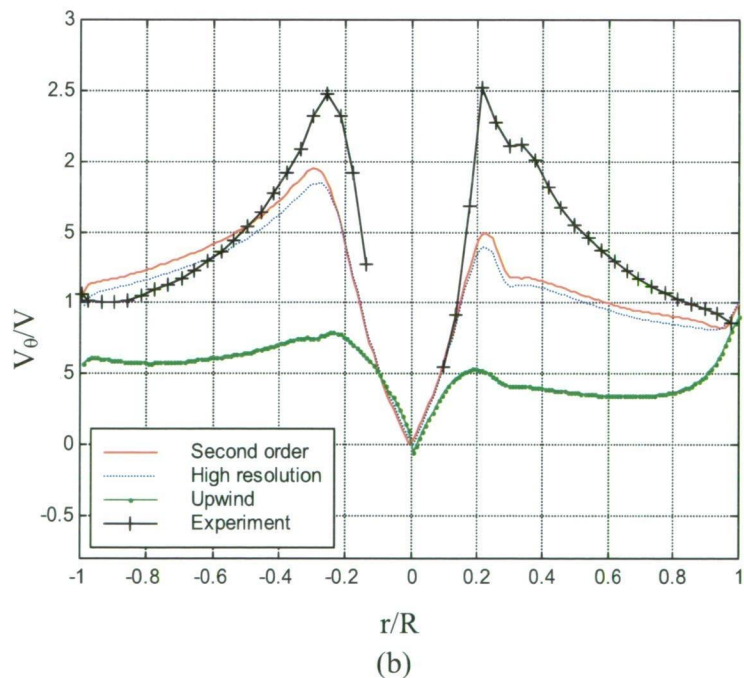
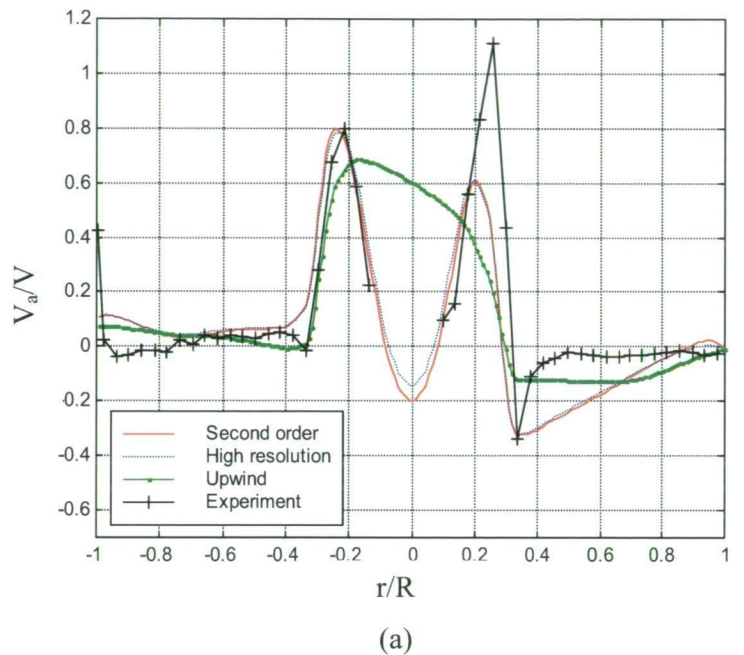


Figure 5.5 Influence of differencing scheme on predicted velocity distributions at $z = 0.055$ m: (a) axial velocity; (b) tangential velocity.

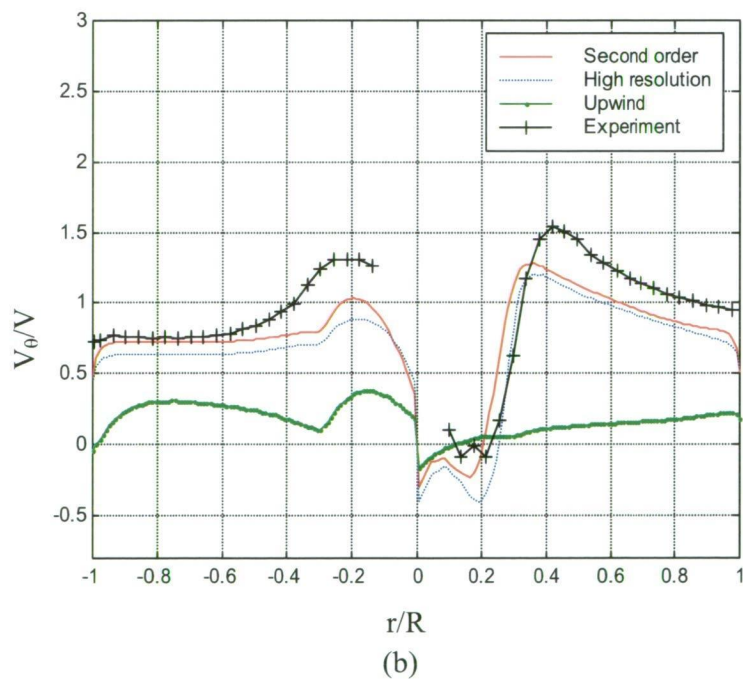
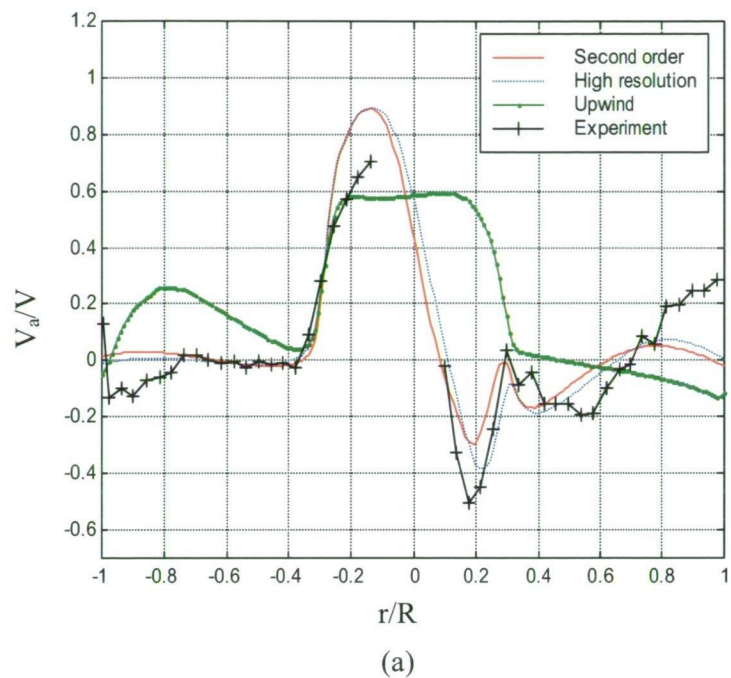


Figure 5.6 Influence of differencing scheme on predicted velocity distributions at $z = 0.255$ m: (a) axial velocity; (b) tangential velocity.

The optimum differencing scheme was determined by comparing the calculated total pressure drop coefficients with the experimental results as shown in Table 5.2. Based on these results, the second-order differencing scheme was chosen as the most appropriate scheme for modelling of the cyclone dryer flow.

Table 5.2 Effect of differencing scheme on predicted total pressure drop coefficient using mesh of 86,555 nodes and RNG k-ε turbulence model.

Source of value	Total pressure drop coefficient
Experimental result	16-17
Simulation	
- First order (Upwind)	4.9
- High resolution	11.4
- Second order	12.0

5.3.3.2 Grid sensitivity

The hexahedral mesh used to model the flow field inside the cyclone dryer was generated at four levels of resolution as shown in Figure 5.4. Mesh concentration was applied at all solid surface to assist in capturing the boundary layer flows. The mesh of 86,555 nodes was used in the previous testing. Similar refined meshes of 190,057, 419,928 and 864,185 nodes were created to test the sensitivity of the results to domain discretisation. As the CFX solver modelling manual states that RMS residual levels of 10^{-6} are the most appropriate for design investigations, the RMS levels of convergence were evaluated to ensure that sufficiently accurate results were obtained at each level of mesh resolution.

The RNG k-ε turbulence model with a second order differencing scheme was used throughout the grid sensitivity testing. The predicted tangential and axial velocity distributions for different mesh resolutions are plotted and compared with experimental data in Figures 5.7 and 5.8.

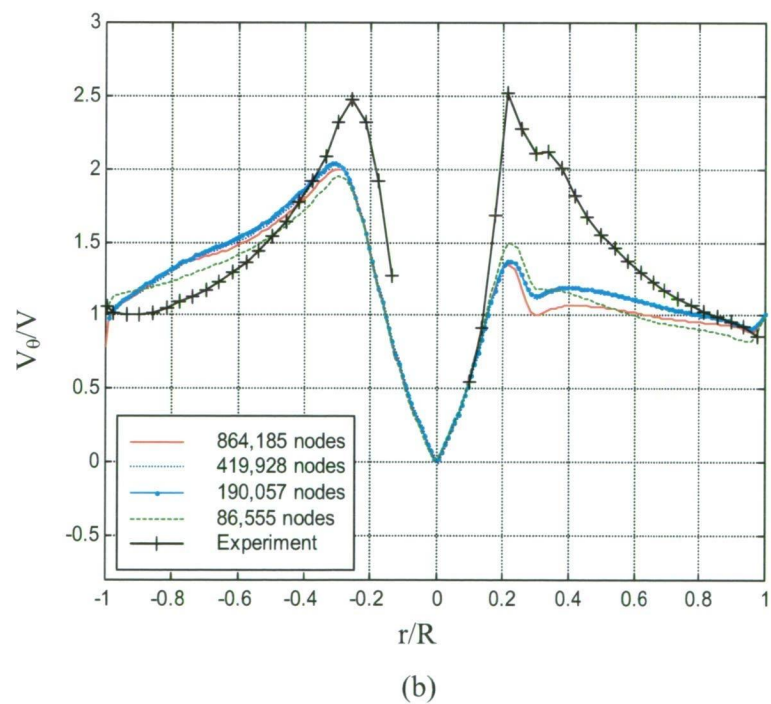
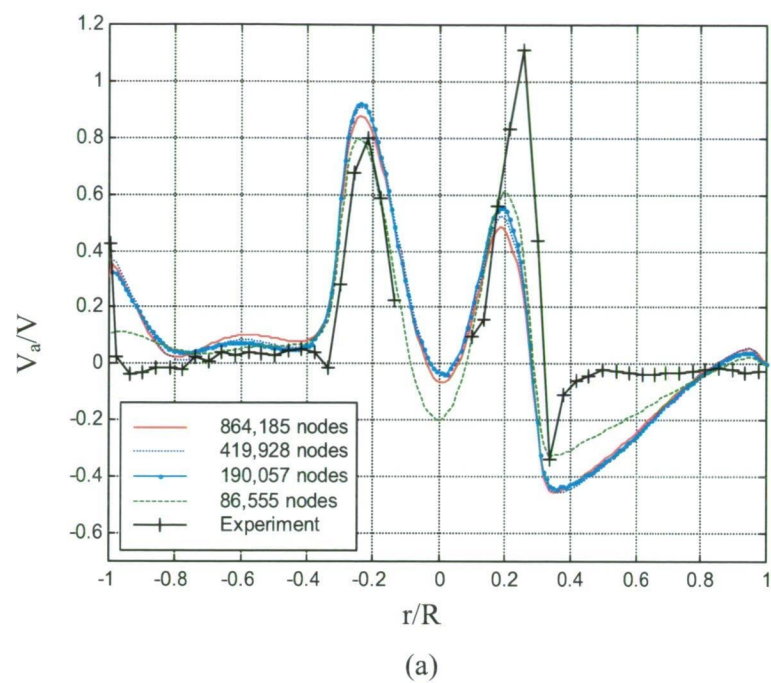


Figure 5.7 Influence of mesh resolution on velocity distributions at $z = 0.055$ m for RNG $k-\epsilon$ turbulence model: (a) axial velocity; (b) tangential velocity.

As the mesh was refined, the velocity distributions changed only slightly for the last three resolutions (190,057, 419,928 and 864,185 nodes). It was thus not clear from the velocity distribution alone which is the best resolution. Additional information is provided by the total pressure drop predictions for different mesh resolutions shown in Table 5.3. The predicted pressure drop coefficient for a mesh of 190,067 nodes is significantly more accurate than that for the coarsest mesh. There is little difference for the mesh of 419,928 nodes. For the finest mesh of 864,185 nodes the accuracy of the predicted pressure drop noticeably deteriorates.

An excellent convergence level of 10^{-6} RMS was obtained for mesh resolutions of 86,555, 190,057 and 419,928 nodes. For the finest mesh of 864,185 nodes the RMS residual fluctuated, and the best convergence that could be obtained was 5×10^{-5} as shown in Table 5.3. The reasons for this deterioration in convergence are not clear, but poorer mesh quality may possibly have been a factor.

Figures 5.9 shows the predicted distributions of tangential velocity at computational nodes within 10 % of the cyclone dryer radius from the cyclone wall for different mesh resolutions at an elevation of $z = 0.255$ m (in the intermediate chamber). The velocity was sampled along a line normal to the inlet duct on the inlet and outlet sides of the dryer. The results for meshes of 419,928 and 864,185 nodes are closely similar. The predicted velocity distributions show increasing deviation as the mesh is coarsened to 190,057 and 86,555 nodes.

Taking all the above mentioned considerations into account, the mesh of 419,928 nodes was chosen as the most appropriate for all further work. It gave the best agreement with the measured velocity distributions and a good level of convergence with the RNG $k-\epsilon$ turbulence model. The predicted total pressure drop coefficient for this mesh differs only slightly from the best approximation obtained with the mesh of 190,057 nodes; but the predicted velocity distributions for that mesh were noticeably worse.

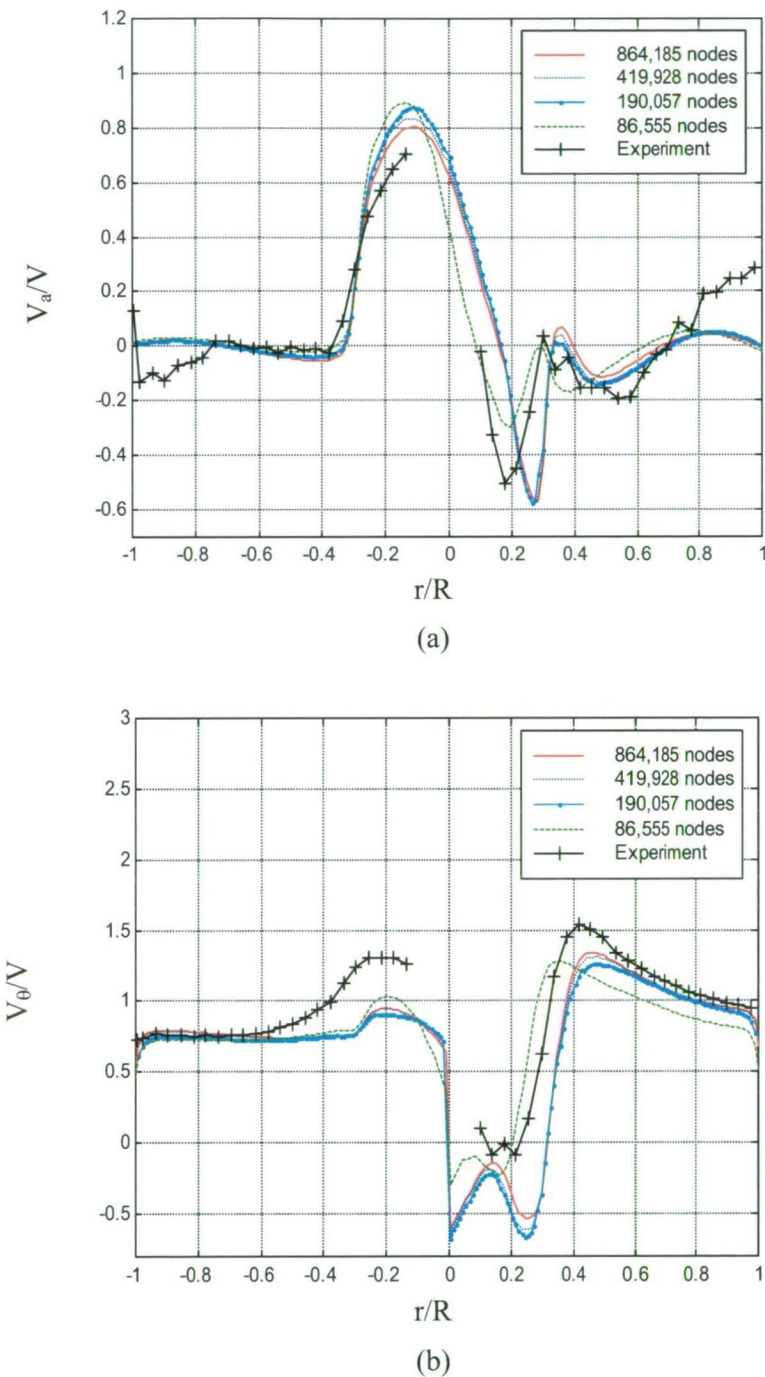
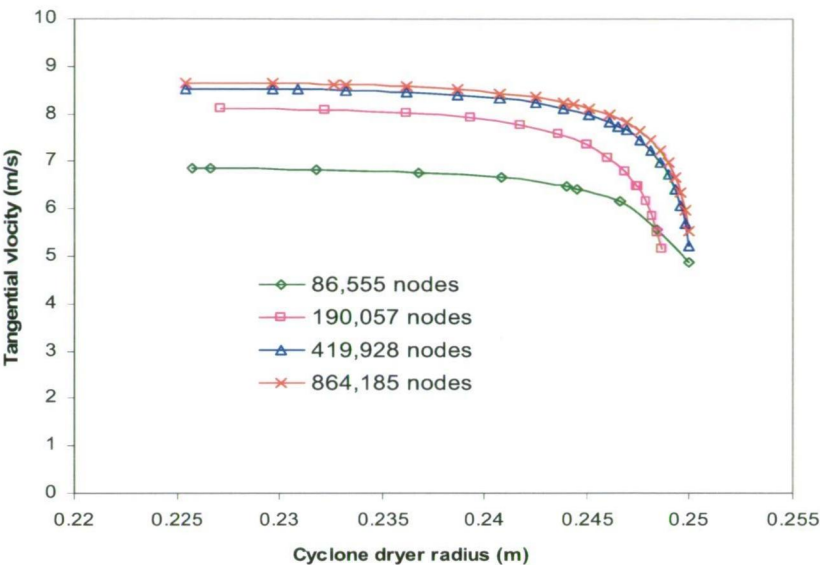
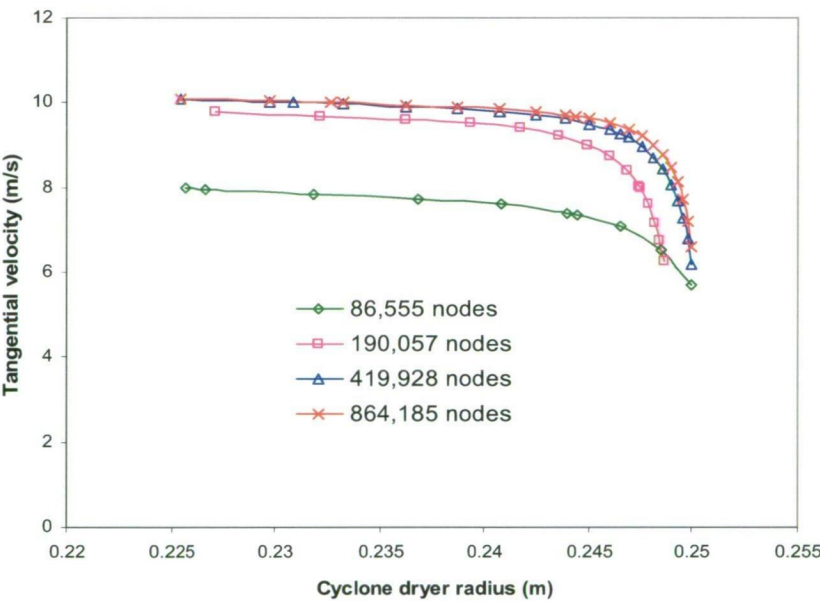


Figure 5.8 Influence of mesh resolution on velocity distributions at $z = 0.255$ m for RNG $k-\epsilon$ turbulence model: (a) axial velocity; (b) tangential velocity.



(a)



(b)

Figure 5.9 Predicted near-wall tangential velocity distributions for different mesh resolutions using the RNG k- ϵ turbulence model: (a) inlet pipe side; (b) outlet pipe side. Values plotted at computational nodes.

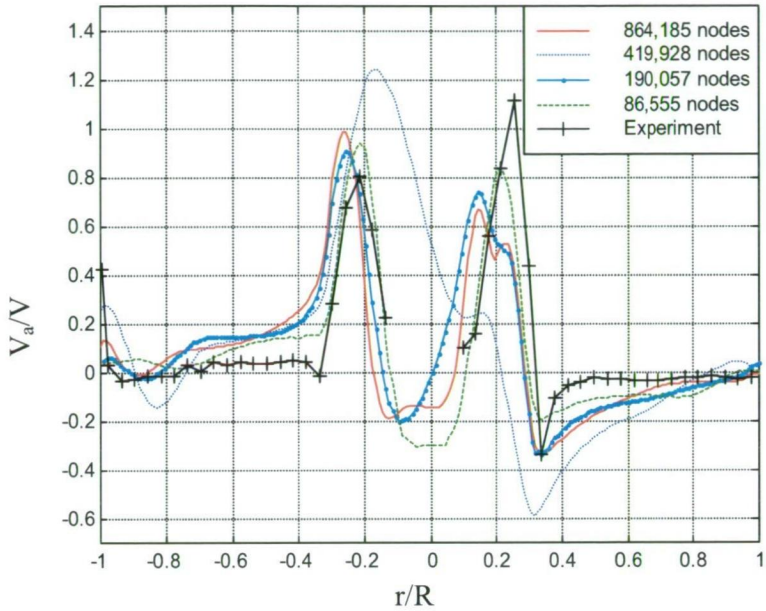
Table 5.3 Comparison of predicted total pressure drop coefficient and RMS residual value for different mesh resolutions using RNG k-ε turbulence model with second-order differencing scheme.

Mesh resolution	Predicted total pressure drop coefficient		RMS residual
	Value	Difference from experiment (%)	
864,185 nodes	12.65	- 23.3	5×10^{-5}
419,928 nodes	13.08	- 20.7	1×10^{-6}
190,057 nodes	13.20	- 20.0	1×10^{-6}
86,555 nodes	11.99	- 27.3	1×10^{-6}

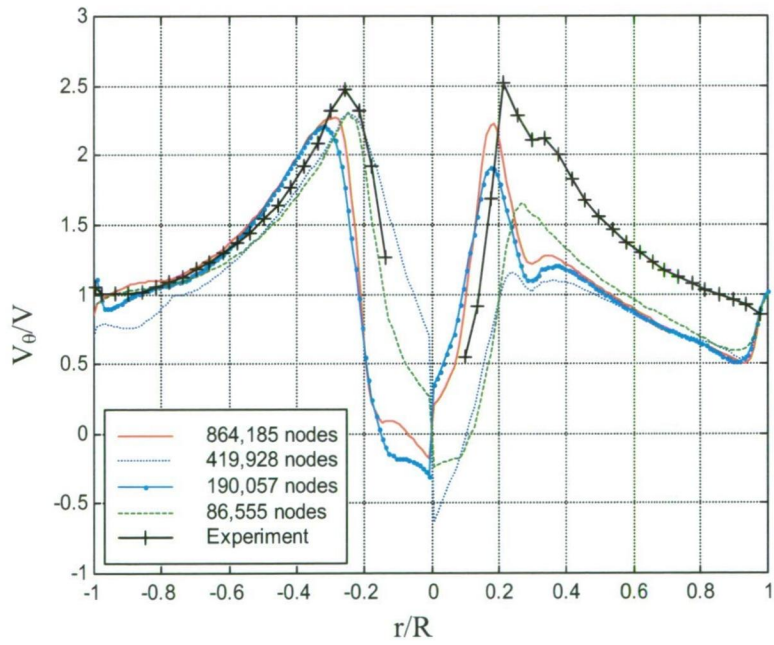
With the 419,928 nodes mesh the value of dimensionless distance y^+ at nodes nearest the solid boundaries was generally less than 20 except for small isolated regions in the centre of the roof and floor of the cyclone and the corners of the inlet and outlet ducts. As seen from Figure 5.9, there were generally about 10 computational nodes in the boundary layer regions. This complies with recommendations of the CFX 5 user guide, and should have adequately captured the boundary layer flow.

5.3.3.3 Turbulence model

This section discusses computations of the model cyclone dryer flow using the SSG Reynolds stress turbulence model and compares the results obtained with these for the RNG k-ε model. Reynolds stress models are physically more realistic, and generally give more accurate predictions than k-ε model for complex flows. Simulations were conducted for the four different mesh resolutions shown in Figure 5.4 using a second-order differencing scheme. Simulation results for the velocity distributions and the pressure drop coefficient were compared with the experimental data. The levels of convergence achieved for with different mesh resolutions were also examined.



(a)



(b)

Figure 5.10 Influence of mesh resolution on predicted velocity distributions at elevation $z = 0.055$ m for SSG Reynolds stress turbulence model: (a) axial velocity; (b) tangential velocity.

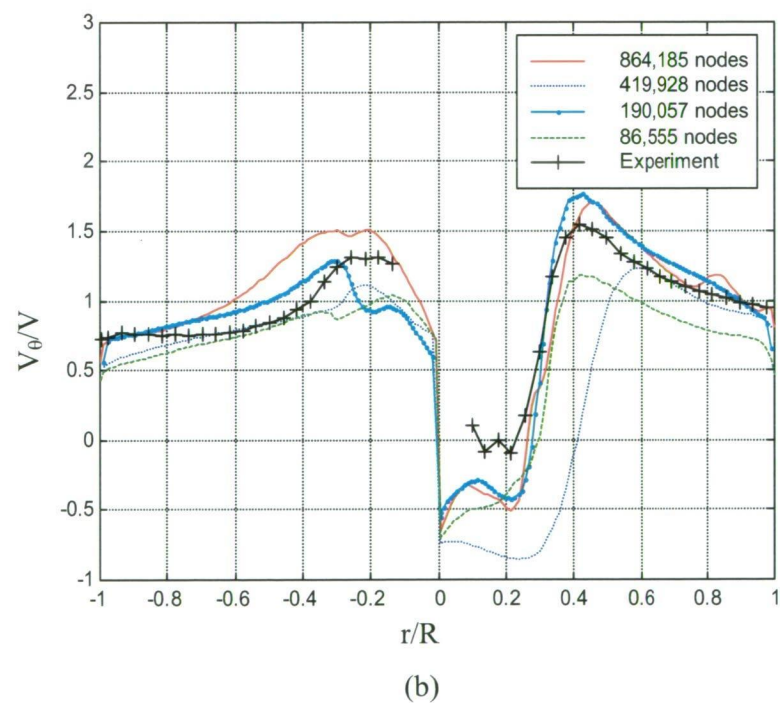
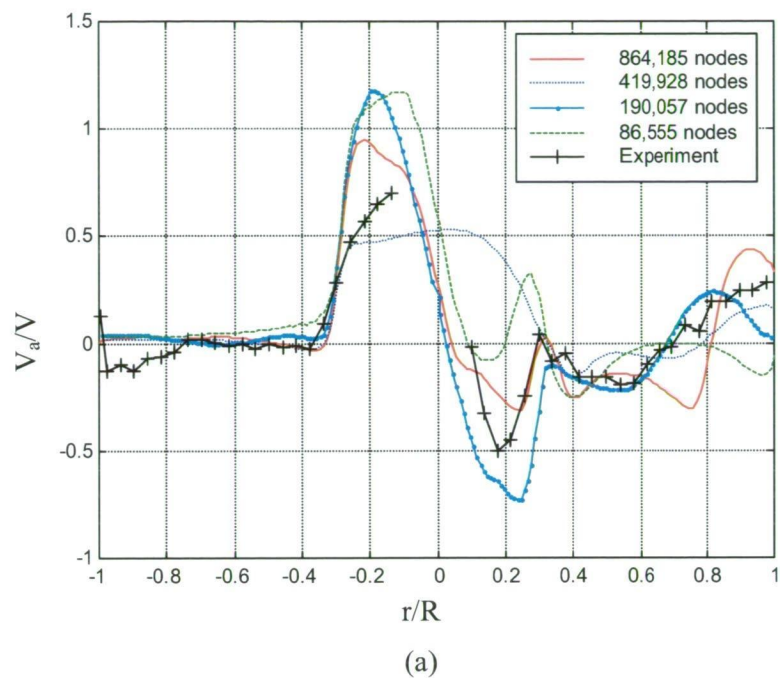


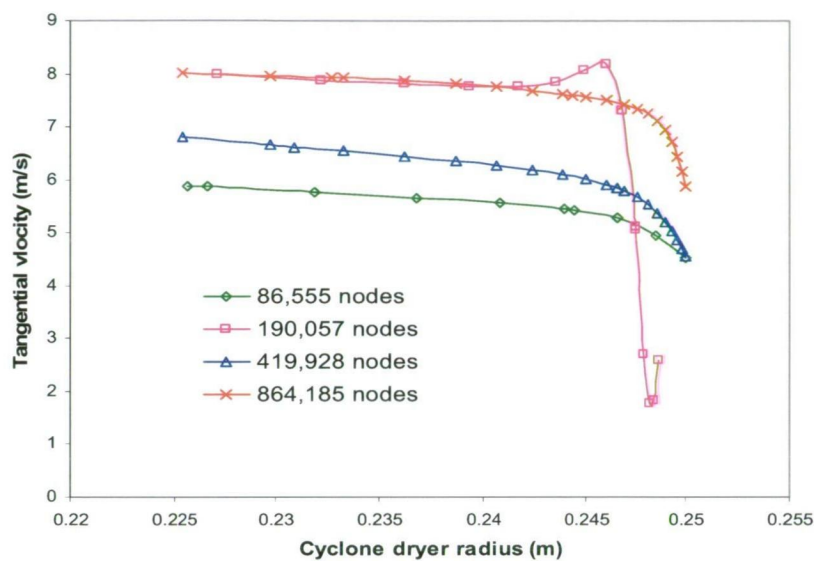
Figure 5.11 Influence of mesh resolution on predicted velocity distributions at $z = 0.255$ m for SSG Reynolds stress turbulence model: (a) axial velocity; (b) tangential velocity.

The tangential and axial velocity distributions obtained with the SSG Reynolds stress turbulence model for four different mesh resolutions are plotted and compared with the experimental data in Figures 5.10 and 5.11. The general trend of the velocity distributions is correctly predicted at the mesh resolutions of 864,185, 190,057 and 86,555 nodes, but a significantly discrepancy is observed for the mesh resolution of 419,928 nodes. The convergence level of RMS residual achieved with the SSG Reynolds stress model was generally poor. As seen from Table 5.4, the RMS residual values were all of order 10^{-3} .

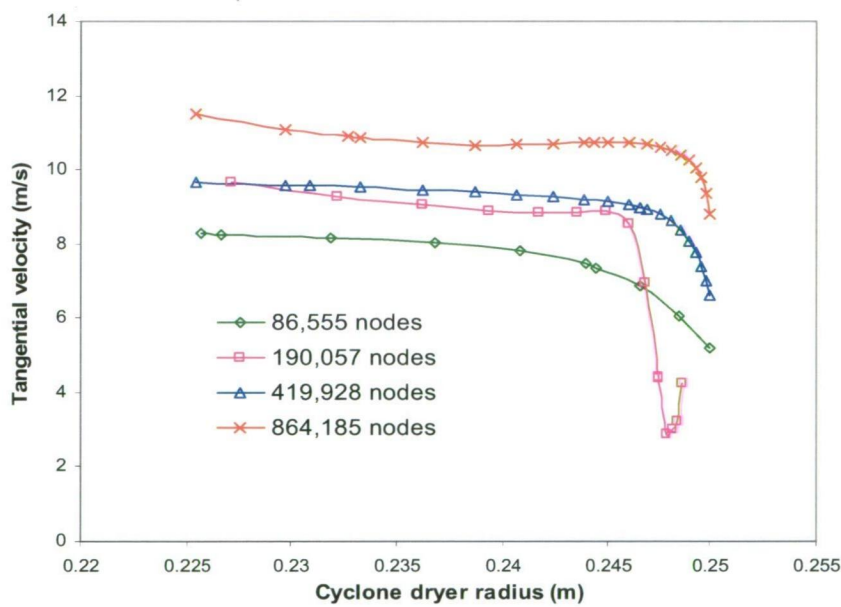
Table 5.4 Comparison of predicted total pressure drop coefficient and RMS residual value for different mesh resolutions using SSG Reynolds stress turbulence model with second-order differencing scheme.

Mesh resolution	Predicted total pressure drop coefficient		RMS residual
	Value	Difference from experiment (%)	
864,185 nodes	13.3	- 19.2	7.5×10^{-4}
419,928 nodes	9.2	- 44.0	1.5×10^{-3}
190,057 nodes	12.4	- 24.7	8.8×10^{-4}
86,555 nodes	10.5	- 36.2	3.5×10^{-3}

The values of total pressure drop coefficient predicted by the SSG Reynolds stress model are presented in Table 5.4. They generally differ more from experiment than the predictions of the RNG k- ϵ model. There is a very rough (but not entirely consistent) correlation between the accuracy of the pressure drop prediction and the trend of near-wall convergence achieved. Similar trends can be seen in the near-wall distributions of tangential velocity presented in Figure 5.12. These distributions do not exhibit convergence with increasing mesh resolution, as was observed with the RNG k- ϵ model results presented in Figure 5.9.



(a)



(b)

Figure 5.12 Predicted near-wall tangential velocity distributions for different mesh resolution using the SSG Reynolds stress turbulence model: (a) inlet pipe side; (b) outlet pipe side.

Figures 5.13 and 5.14 compare the distributions of tangential and axial velocity predicted by the RNG k- ϵ and SSG Reynolds stress turbulence models at elevations $z = 0.055$ m and 0.255 m. The curves presented are those for the best converged solutions obtained with each turbulence model. The SSG Reynolds stress turbulence model does not perform significantly better overall than the RNG k- ϵ turbulence model.

It was decided on the basis of these results to use the RNG k- ϵ turbulence model for all further work. The SSG Reynolds stress model results were considered unreliable due to the inability of this model to produce acceptable levels of solution convergence.

5.3.3.4 Optimised numerical model

On the basis of the foregoing results, the RNG k- ϵ turbulence model using a second-order differencing scheme with a mesh resolution of 419,928 nodes was selected for all further cyclone dryer investigations. This procedure produced good solution convergence with an RMS residual level of 10^{-6} . The SSG Reynolds stress turbulence model was considered unreliable, due to its inability to produce adequate levels of solution convergence. The selected computation procedure gave values of predicted total pressure drop coefficient about 20 % lower than experiment; this is comparable with the accuracy of computational pressure drop predictions for simple cyclone separators reported in the literature.

5.4 NUMERICAL PREDICTIONS

5.4.1 Effect of Inlet Air Velocity

The optimised numerical model described in Section 5.3.3.4 was subsequently applied to predict the influence of inlet air velocity variation on the velocity field and pressure drop

characteristics of the cyclone dryer. The uniform inlet velocity was varied from 8 to 13 m/s.

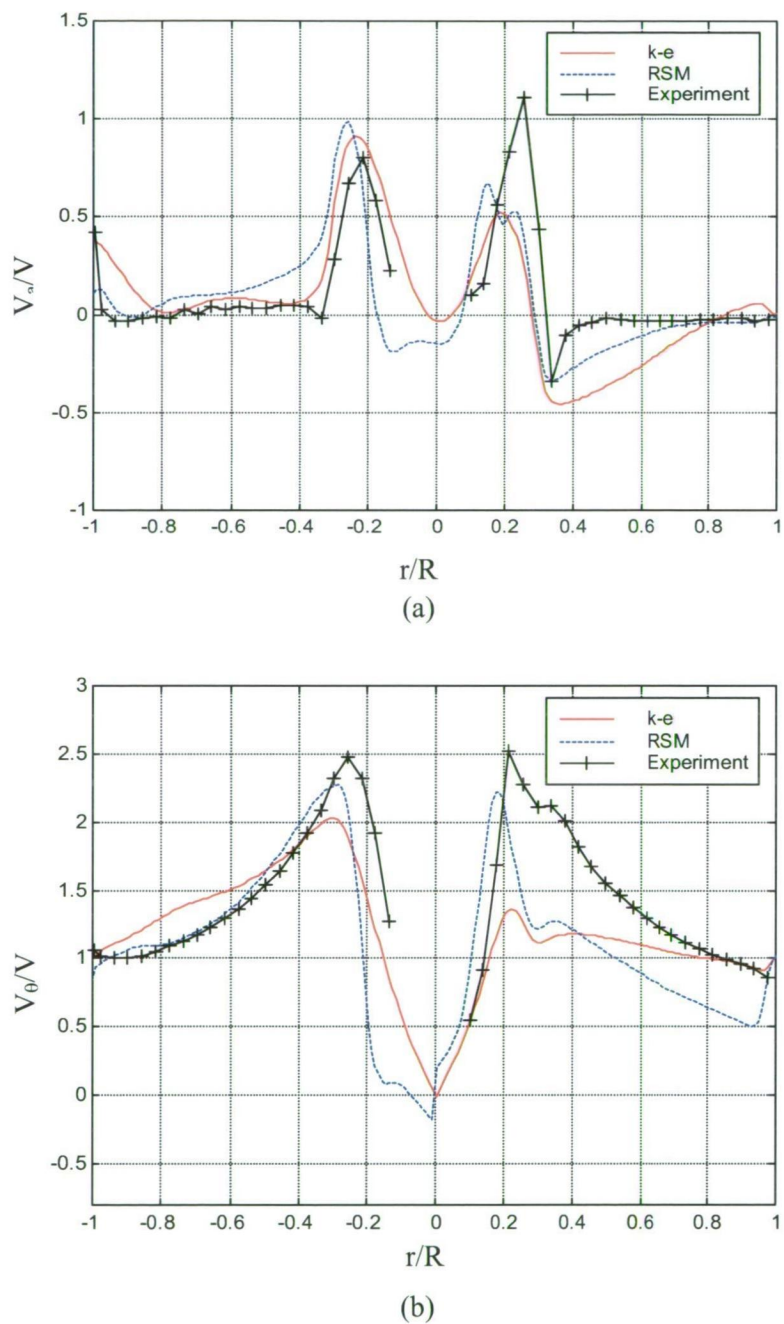


Figure 5.13 Influence of different turbulence models on the predicted velocity distributions at elevation $z = 0.055$ m: (a) axial velocity; (b) tangential velocity.

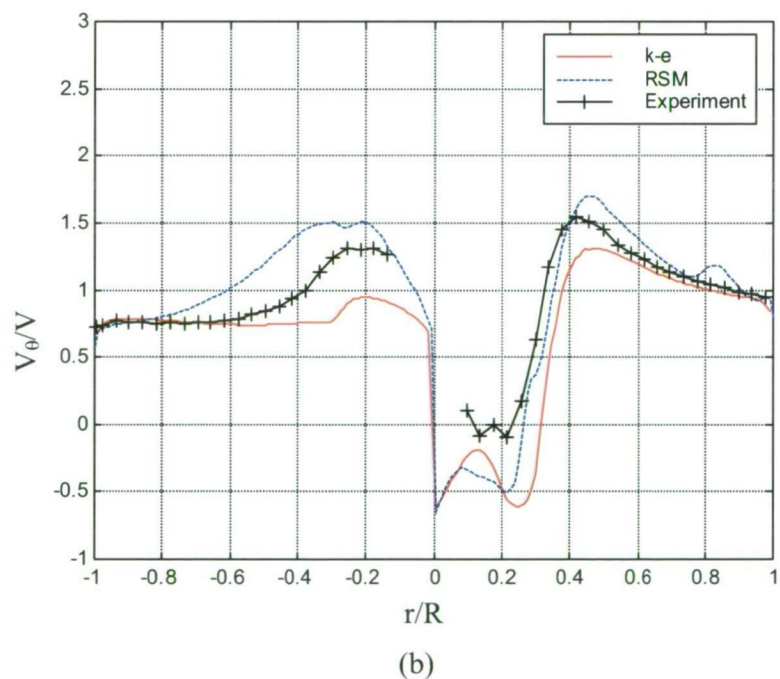
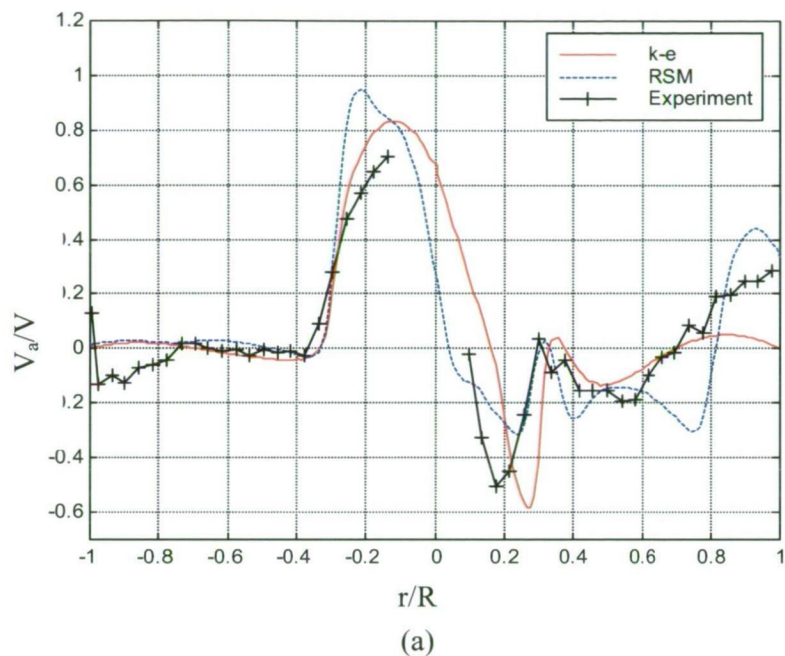


Figure 5.14 Influence of different turbulence models on the predicted velocity distributions at $z = 0.255$ m: (a) axial velocity; (b) tangential velocity.

Figure 5.15 shows the predicted total pressure drop coefficient plotted against the cyclone dryer Reynolds number. The results are compared to the experimental data presented earlier in Section 4.5.2. The predicted variation of pressure drop coefficient with Reynolds number is closely similar to that observed experimentally. However, as indicated in Table 5.3, the predicted values of total pressure drop coefficient are about 20 % below the experimental values.

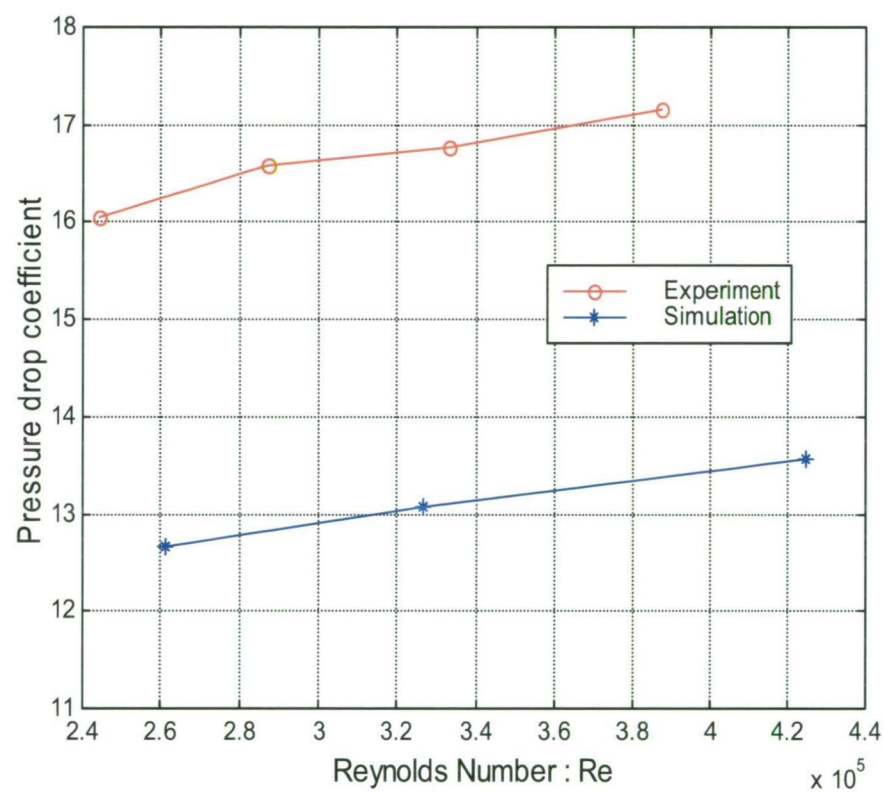


Figure 5.15 Pressure drop characteristics from simulation and experiment.

The predicted radial profiles of dimensionless axial and tangential velocity at 8, 10 and 13 m/s inlet velocity are closely similar, as shown in Figure 5.16. This indicates that a similar flow pattern is obtained in the cyclone dryer over its practical operating range for grain drying.

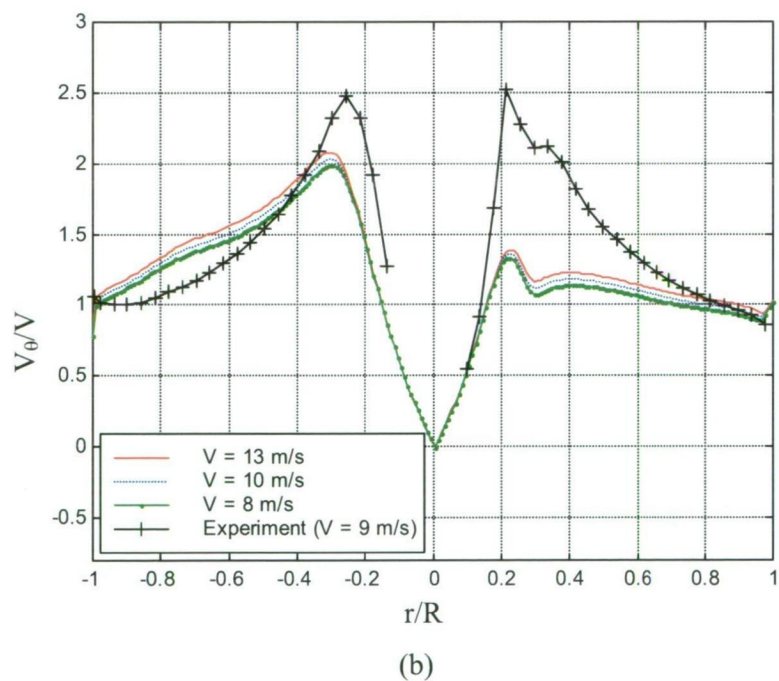
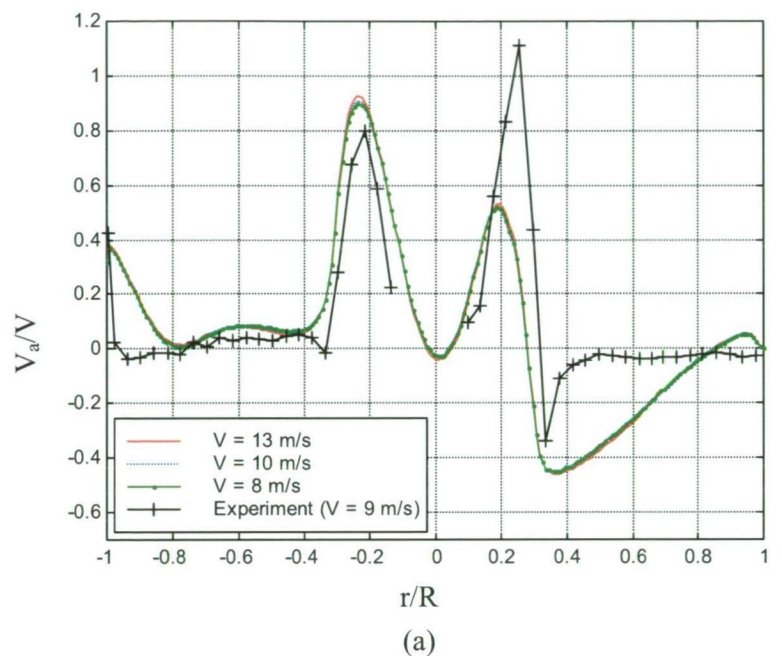


Figure 5.16 Comparison of axial and tangential velocity profiles predicted by RNG $k-\varepsilon$ turbulence model at different inlet velocities (8, 10 and 13 m/s): (a) axial velocity; (b) tangential velocity.

5.4.2 Effect of Number of Chambers

The number of internal separation chambers in a cyclone dryer may need to be altered to change the residence time of the material being dried. The effect of additional chambers on the velocity distribution and pressure drop across the model cyclone dryer was also investigated by means of the optimised numerical simulation. Calculations for the 3-chamber dryer were repeated for dryers with 4, 5 and 6 chambers by adding further internal chambers. The meshing scheme for the additional chambers was identical to that used for the central chamber in the 3-chamber dryer flow computation. A uniform inlet velocity of 10 m/s was used in all cases.

Figure 5.17 shows velocity vector plots together with pressure contours on an x-z plane and x-y planes at various elevations in a 3-chamber dryer. Velocity vector plots and pressure contours in a 4-chamber cyclone dryer are shown in Figure 5.18. The velocity and pressure distributions for the 5- and 6-chamber cyclone dryer calculations are not shown here, but the predicted total pressure drop coefficients are presented in Table 5.5.

For the 3-chamber cyclone dryer, the simulation results in Figure 5.17 (a) indicate the complicated structure of the axial velocity field inside the cyclone dryer chambers. In the lowest chamber, air-flow separates at the wall into upward and downward streams at a point close to the middle of the inlet pipe. Upward flow is present along the wall surface above the middle of inlet pipe, and it causes a downward flow along the surface of the orifice plate and a short circuit through to the higher chamber at the orifice. Below the middle of inlet pipe, there is a downward flow along the conical bottom surface leading to an upward flow at the axis of the cyclone dryer.

The upward velocity components near the axis of the cyclone dryer are small and widely distributed in the lowest chamber, but larger and more concentrated at the higher chambers. This air core has an asymmetric pattern in the second chamber, but becomes more symmetrical with a higher number of chambers, as seen from the velocity vector plot for the 4-chamber dryer in Figure 5.18 (a).

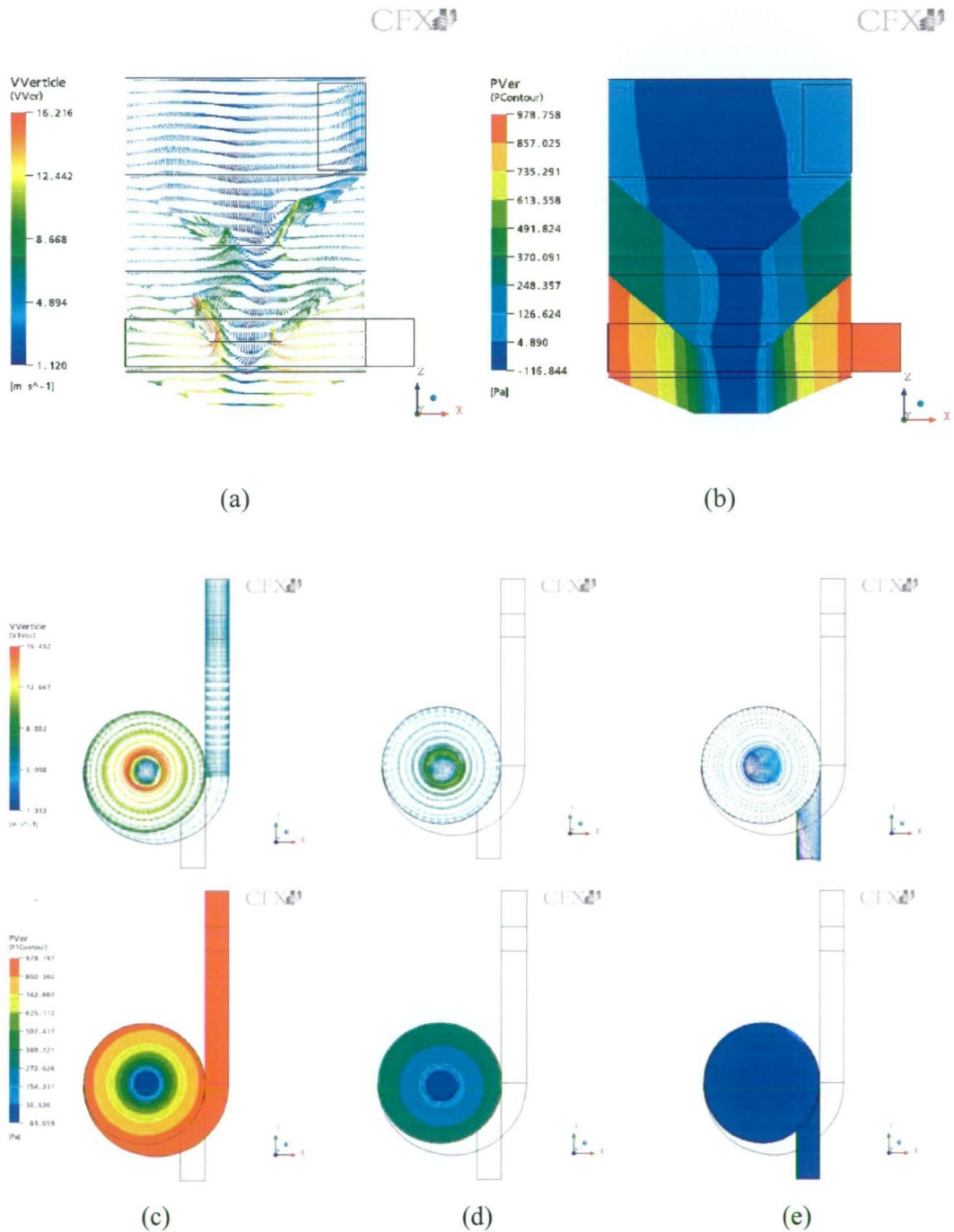


Figure 5.17 Velocity vector plot and pressure contours for three-chamber cyclone dryer: (a) velocity vector plot in x-z plane at $y = 0$ m; (b) pressure contour plot in x-z plane at $y = 0$ m; (c), (d) and (e) velocity vector and pressure contour plots in x-y plane at $z = 0.055$ m, 0.255 m and 0.455 m.

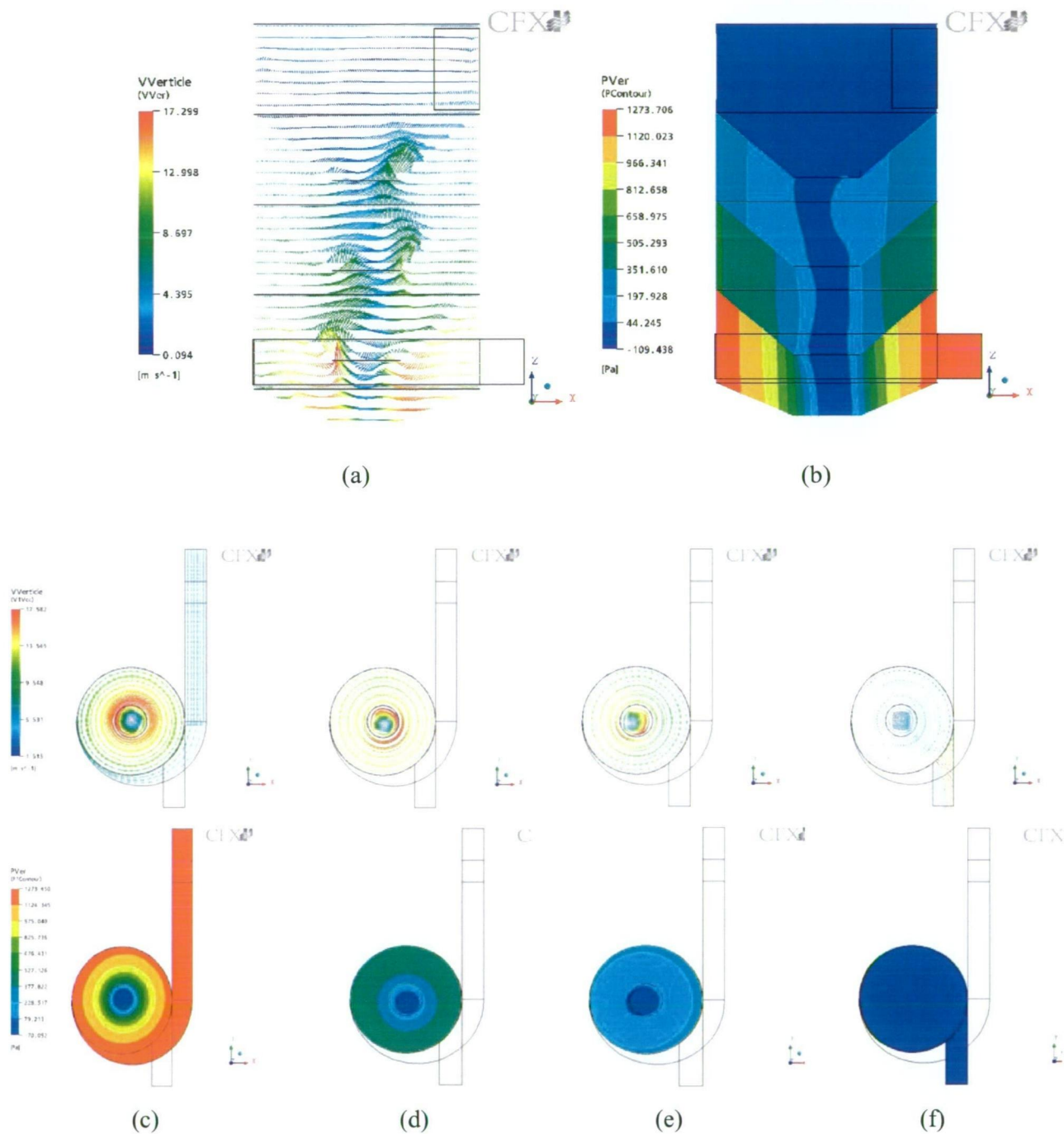


Figure 5.18 Velocity vector plot and pressure contours for four-chamber cyclone dryer: (a) velocity vector plot in x-z plane at $y = 0$ m; (b) pressure contour plot in x-z plane at $y = 0$ m; (c), (d), (e) and (f) velocity vector and pressure contour plots in x-y plane at $z = 0.055$ m, 0.255 m, 0.455 m and 0.655 m.

The swirl velocity becomes weaker as it passes through successive chambers, while the axial velocity becomes stronger for additional chambers of cyclone dryer. This is seen in the comparison of vector plots for 3- and 4-chamber dryers shown in Figures 5.17 (a) and 5.18 (a). These flow patterns indicate that the drying material should first move downward along the surface of the conical bottom and then upward from chamber to chamber due to the high upward velocity component in the orifice flow near the axis of the cyclone dryer.

In the highest or exit chamber, the flow pattern is different from that in the internal chambers as the upward core air flow vanishes. The vortex core is deflected from the cyclone axis and changes its direction to the exit pipe. This causes a large scale recirculation inside the highest chamber which continues into the exit pipe in the y direction. This flow pattern is clearly seen in the velocity vector plots for x-y planes at $z = 0.455$ m, $z = 0.655$ m and $z = 0.855$ m for the 3- and 4-chamber cyclone dryers, which exhibited similar behaviour (Figures 5.17(e) and 5.18(f)).

The static pressure decreases radially from the wall to the centre of cyclone dryer chamber, and a negative pressure zone appears in the forced vortex region in the centre of the vortex core. This is indicated by the dark blue colour on the pressure contour plot.

The pressure gradient is largest in the radial direction of the lowest dryer chamber, where the swirl velocity is highest. Another significant pressure gradient occurs along the exit pipe, as a flow deflection exists at this part of the cyclone dryer. Negative static pressure can be seen in the pressure contour plots for x-y planes at $z = 0.455$ m, and $z = 0.655$ m for the 3- and 4-chamber cyclone dryers (Figures 5.17(e) and 5.18(f)).

The predicted influence of the number of chambers on the overall total pressure drop coefficient for the model cyclone dryer is shown in Table 5.5. The computed pressure drop coefficient increases only slowly with number of chambers. There is certainly no direct proportionality between these two quantities.

Table 5.5 Predicted influence of number of chambers on total pressure drop coefficient for model cyclone dryer.

Number of chambers	3	4	5	6
Total pressure drop coefficient	13.1	13.4	14.0	14.4

5.5 CONCLUSIONS

This chapter has reviewed the development of an optimised numerical model, based on the commercial CFD software package CFX 5.7, for prediction of the single-phase flow field in the model cyclone dryer. Experimental data for internal velocity distributions and overall pressure drop were used to validate the computations and assist in choosing the optimal procedure.

Grid independence was demonstrated with a hexahedral mesh of about 420,000 nodes for the 3-chamber dryer case. The best results were obtained using second-order differencing with the RNG k-ε turbulence model, which gave good solution convergence to an RMS residual level of 10⁻⁶. The SSG Reynolds stress turbulence model, which is physically more accurate, was not adopted because it did not produce acceptable solution convergence.

The optimised numerical model gave predictions of the internal velocity distributions that agreed fairly well with experiment. The predicted variation of the overall total pressure drop coefficient with Reynolds number agreed well with experiment, but the predicted pressure drop levels were about 20% lower. This is comparable with the accuracy of

computational pressure drop predictions for simple cyclone separators reported in the literature.

The optimised model predicted closely similar internal flow patterns over the range of inlet velocities practical for grain drying. The additional of more internal chambers, which might be required to obtain longer residence time for solid particles in the dryer, was predicted to produce only a slight increase in the overall pressure drop coefficient.

The next chapter will discuss two-phase isothermal solid-gas flow in the model cyclone dryer. The residence time characteristics of both paddy grain and spherical silica gel particles will be examined experimentally and compared with numerical predictions.

Chapter 6

SOLID-GAS FLOW BEHAVIOUR AND PARTICLE RESIDENCE TIME DISTRIBUTION OF A CYCLONE DRYER

6.1 INTRODUCTION

Drying of paddy grain in a pneumatic dryer was studied in Chapter 3. The simulation results showed that this type of dryer could not achieve the large residence time required to reduce the moisture content of paddy to a safe storage level. Particle residence time is

an extremely important variable in paddy grain drying. Cyclone dryer technology offers the prospect of more suitable residence times for paddy grain drying. However, the development of this technology in the chemical industry appears to have been largely empirical, and no detailed studies of particle residence time and drying behaviour have been reported in the open literature.

The dynamic behaviour of traditional gas-cleaning cyclone separators has been extensively studied. Most of these investigations were related to separation efficiency and pressure drop. Several recent studies have examined possible cyclone applications for heat transfer equipment (Szekely et al., 1966; Yen et al., 1990) and heat and mass transfer equipment (Silva et al., 1991; Benta et al., 1997) because of the good contact between gas and solid phase. Particle residence time was not examined by these workers, but is obviously an important variable as the results they obtained were strongly process dependent.

The application of CFD for the numerical calculation of particle-gas flow in a cyclone has become popular in recent decades. Two different modelling approaches can be employed: the Eulerian-Lagrangian and the Eulerian-Eulerian multiphase models. In the Eulerian-Lagrangian multiphase model, the flow of gas is treated as a continuum carrying numerous discrete particles. The trajectory of each particle within the air flow is predicted by solving the Lagrangian equations of mass and momentum. In the Eulerian-Eulerian multiphase model, the air flow and particle phases are both treated as interpenetrating interactive continua. The governing equations for each phase are similar to the Navier-Stokes equations, with extra source terms in the momentum equation to account for the turbulent dispersion of particles.

One of the first CFD simulations of the cyclone separator was done by Boysen et al. (1982). They used an Eulerian-Lagrangian multiphase model with an algebraic turbulence model to provide the details of gas flow and particle motion occurring in this device. Grade-efficiency was obtained by means of a stochastic particle tracking technique. Several researchers have undertaken numerical simulations, attempting to

predict the pressure drop and grade-efficiency of cyclone separators by Lagrangian-Eulerian multiphase models (Griffiths et al., 1996; Yoshida et al., 1991 and 2001; Derksen 2003 and Wang et al., 2003). Silva and Nebra et al. (1991, 1994, and 1997) used an Eulerian-Eulerian multiphase model to model particle-gas flow in cyclone separators. These studies determined design specifications and performance characteristics for various types of cyclone separator, but the particle residence time was not studied or reported.

Kemp et al. (1998) have studied particle residence time and drying in a cyclone separator. They concluded that particle residence time increased with cyclone diameter, particle diameter, and particle density but decreased when solid-gas loading increased. They also observed that drying in a cyclone increased with cyclone diameter, gas temperature, and gas flow rate, but it decreased with solid-gas loading. Other authors have observed this influence in cyclone separators. Correa et al.(2001) and Dibb et al. (1997) used software developed by Silva et al. (1991), in which the particle-gas flow was described by an Eulerian-Eulerian multiphase model to examine the influence of cyclone geometry. It was concluded that the cyclone diameter had the most significant influence on particle residence time. A Lagrangian-Eulerian multiphase model provided by the commercial CFD code CFX4.4 was used by Correa et al. (2004a and 2004b) to study the influence of cyclone dimensions on particle residence time. Experimental and theoretical results showed the solid volumetric concentration to have the greatest influence on particle residence time, but the qualitative agreement between simulated and experimental residence times was poor.

This chapter describes studies of the residence time of spherical silica gel particles and paddy grain in various builds of the model cyclone dryer designed previously in Chapter 4. Experimental studies of the influence of the number of chambers and operating conditions of the cyclone dryer on particle residence time were performed. Computational fluid dynamics studies were undertaken using the commercial code CFX 5.7. A Lagrangian-Eulerian multiphase model was used to simulate particle transport with one-way coupling. Due to the irregular shape of paddy grain, additional experiments

were conducted with spherical shaped material (silica gel). This provides a more valid comparison between numerical and experimental results, as the particle drag model in CFX assumes particles of spherical shape.

6.2 RESIDENCE TIME DISTRIBUTION (RTD) OF PARTICLES IN A CYCLONE DRYER

This chapter deals in large part with the residence time distribution (or RTD) approach to particle transport through a cyclone dryer. There are two idealised flow models: plug and mixed flows (Levenspiel, 1972). The first of the two ideal steady-state flow models is plug flow, which occurs in a plug flow reactor (PFR). It is characterised by orderly flow of fluid through the reactor with no element of fluid overtaking or mixing with any other element ahead or behind. There may actually be lateral mixing of fluid in a plug flow reactor; however, there must be no mixing or diffusion along the flow path. The necessary and sufficient condition for plug flow is for the residence time in the reactor to be the same for all elements of fluid. The other ideal flow model is called mixed flow, and occurs in a constant flow stirred tank reactor (CFSTR). It is a flow in which the contents are well stirred and uniform through out. Thus the exit stream has the same composition as the fluid within the reactor. Figure 6.1 shows diagrams of these two ideal types of reactor.

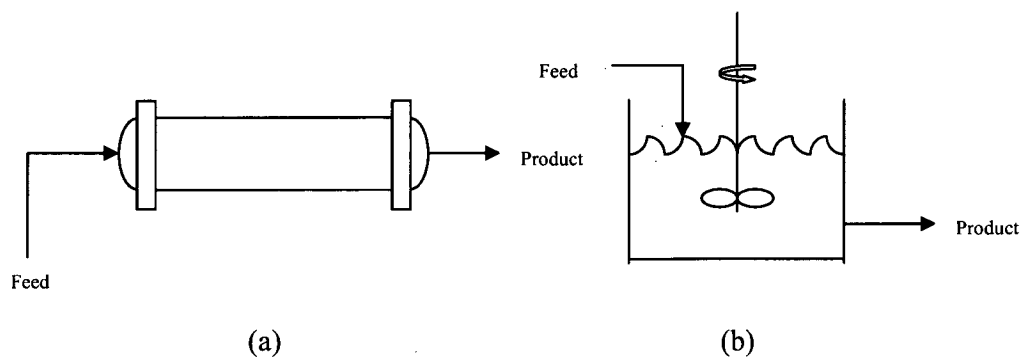


Figure 6.1 The two ideal types of reactor: (a) plug flow; (b) mixed flow.

In order to characterise the dynamic behaviour of a real dryer, the particle residence time must be determined. The particle flow patterns and residence time distributions used for characterisation of the real (non-ideal) device will be discussed in the following section.

6.2.1 RTD Theory

It is evident that particles in a dryer taking different routes will require different lengths of time to pass through the dryer (Levenspiel, 1972). Some particles might leave the dryer after a shorter time than the mean residence time. These would still be wet, while other particles might remain in the dryer much longer than mean residence time and leave the dryer over-dried. Figure 6.2 shows the cumulative age distribution of tracer particles recorded in the exit stream from the dryer. This is called the $F(t)$ curve, and it represents the proportion of tracer having left the dryer at time t relative to the initial amount of tracer. It always rises from 0 to 1.

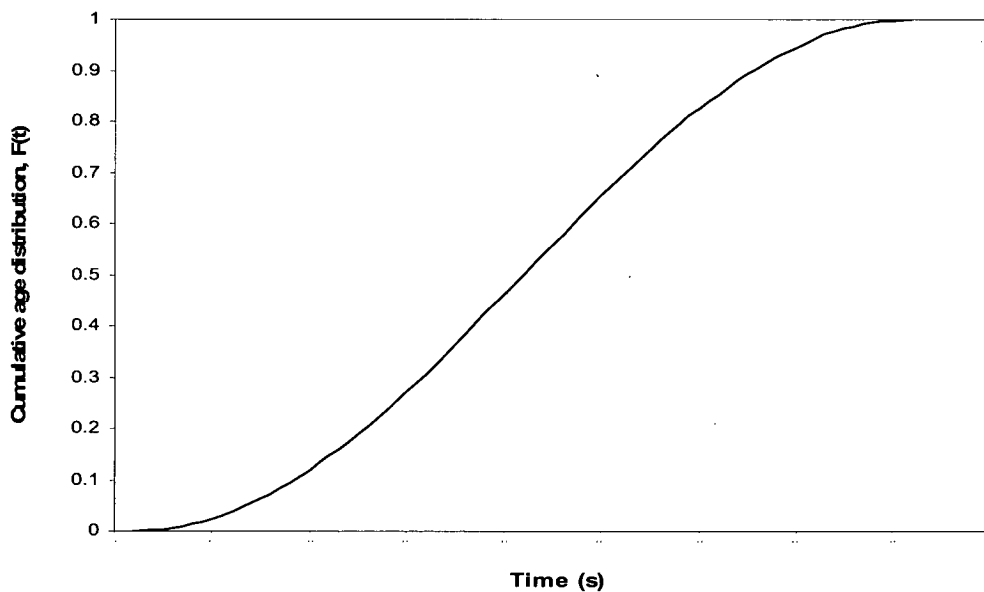


Figure 6.2 Cumulative age distribution, or $F(t)$ curve.

The RTD depends on the flow pattern: in particular, whether it tends towards well-mixed or ideal plug flow. The distribution of residence times of each particle is called the exit age distribution, E , or the residence time distribution (RTD) of particles. It is the differential of the cumulative age distribution (F curve) with time as shown in Equation 6.1:

$$\frac{dF(t)}{dt} = E(t) \quad (6.1)$$

The RTD can be represented in such a way that the area under the curve is unity, i.e.

$$\int_0^{\infty} E(t) dt = 1 \quad (6.2)$$

This procedure is called distribution normalisation and is shown in Figure 6.3. The fraction of particles exiting between $t + dt$ and t is $E(t)dt$. The fraction of particles with residence time less than t_1 is $\int_0^{t_1} E(t) dt$. The fraction of exit particles staying in the dryer

longer than t_1 , shown as the shaded area in Figure 6.3, is

$$\int_{t_1}^{\infty} E(t) dt = 1 - \int_0^{t_1} E(t) dt \quad (6.3)$$

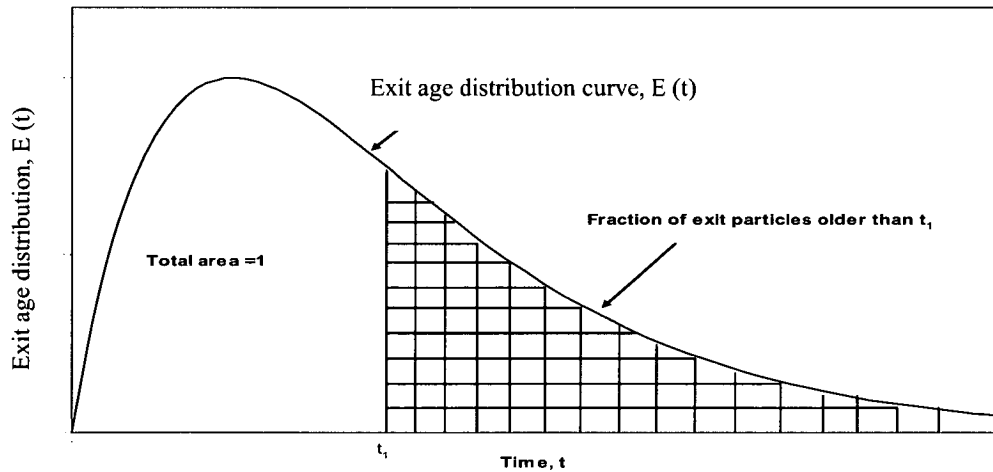


Figure 6.3 The exit age distribution curve, $E(t)$ for particle flow through a dryer, also called the residence time distribution or RTD (Levenspiel, 1972).

6.2.2 Experimental Evaluation of RTD

The following methods of experimentation have been widely used to characterise the exit age distribution function or residence time distribution. They might be classified as stimulus-response techniques, in which the system is disturbed and subsequently observed to examine the system response. In the present experiments, the stimulus was a tracer input into the inlet of the dryer; the response was a time record of the tracer particles leaving the dryer. When injecting tracers into the dryer, the tracer pulse was made as short as possible. The residence time distribution (RTD) function was determined experimentally from the following relation (Seker, 2005; Levenspiel, 1972):

$$E(t) \cong c_i / (\sum_{i=0}^{\infty} c_i \Delta t) \quad (6.4)$$

where c_i = the tracer concentration at time t = mass of tracer in sample at time t / mass of sample at time t . The accumulated quantity of tracer at the exit, represented by the $F(t)$ curve, is given by the following equation:

$$F(t) \cong (\sum_{i=0}^t c_i \Delta t) / (\sum_{i=0}^{\infty} c_i \Delta t) \quad (6.5)$$

The mean residence time (τ), or centroid of the RTD, is

$$\tau \equiv \int_0^{\infty} t E(t) dt \cong (\sum_{i=0}^{\infty} t_i c_i \Delta t) / (\sum_{i=0}^{\infty} c_i \Delta t) \quad (6.6)$$

The variance (σ^2), which measures the spread of the residence time distribution, is given by

$$\sigma^2 \cong ((\sum_{i=0}^{\infty} t_i^2 c_i \Delta t) / (\sum_{i=0}^{\infty} c_i \Delta t)) - \tau^2 \quad (6.7)$$

The dimensionless parameter θ used for comparison of residence time distribution curves is defined by:

$$\theta = t / \tau \quad (6.8)$$

The dimensionless RTD and cumulative age distribution curves are $E(\theta)$ and $F(\theta)$, respectively.

6.2.3 RTD Modelling for Non-Ideal Flow

As stated earlier in this section, the flow in a real reactor does not conform to the ideal situations of a plug flow reactor (PFR) or constant flow stirred tank reactor (CFSTR). These differences result from a certain degree of back mixing, which may be due to channelling, axial mixing caused by vortices and turbulence, and bypass or short-circuiting.

In order to consider deviations from these ideal flow behaviours, more complex models are needed. Two well-known models were applied in this work to describe the behaviour of particles in the cyclone dryer. These models are now briefly described.

6.2.3.1 Dispersion model

The dispersion model is often used to characterise the behaviour of tubular reactors. It considers mass transport in the axial direction (z) as a diffusion-like process in terms of an axial dispersion coefficient, D_p , which is superimposed on the plug flow. For steady-state flow through the dryer (but unsteady with respect to the tracer concentration C) (Tang et al., 2004). The differential mass balance is given in a dimensionless form by Levinspiel (1972) as

$$\frac{\partial C}{\partial \theta} = \frac{D_p}{uL} \frac{\partial^2 C}{\partial z^2} - \frac{\partial C}{\partial z} \quad (6.9)$$

where u is the velocity and L is the characteristic length of the reactor. According to this model, the reactor performance changes from that of a PFR for $D_p/uL = 0$ to that CSFTR for $D_p/uL = \infty$. The dimensionless group D_p/uL is called the dispersion number. The effect of dispersion number on the RTD curve, which corresponds to degree of mixing, is shown in Figure 6.4 (a). The solution of Equation (6.9) for large dispersion in an open vessel is given by

$$E(\theta) = \frac{1}{2\sqrt{\pi\theta(D_p/uL)}} \exp\left[-\frac{(1-\theta)^2}{4\theta(D_p/uL)}\right] \quad (6.10)$$

The variance of this distribution is found to be

$$\sigma_\theta^2 = \frac{\sigma^2}{\bar{t}^2} = 2\frac{D_p}{uL} + 8\left(\frac{D_p}{uL}\right)^2 \quad (6.11)$$

6.2.3.2 Tank-in-series model

The tank-in-series model is an alternative to the dispersion model for dealing with deviations from plug flow. In this model, it is assumed that the actual reactor can be “replaced” by n identical stirred tank reactors, whose total volume is the same as that of the actual reactor. The only parameter of this model is the number of tanks (n). The $E(t)$ curve of this model is obtained in the form

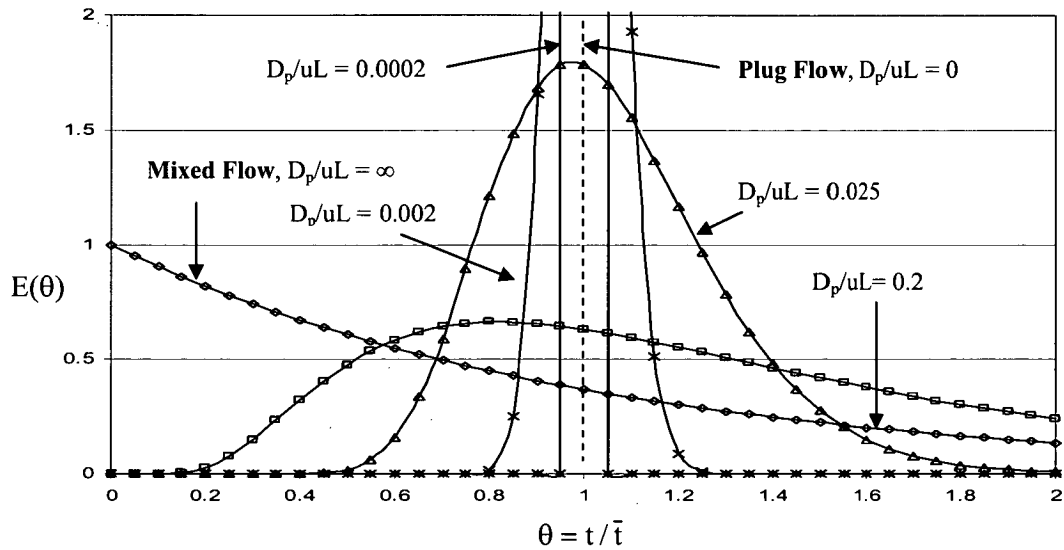
$$\bar{t}_i E(t) = \left(\frac{t}{\bar{t}_i}\right)^{n-1} \frac{1}{(n-1)!} e^{-t/\bar{t}_i} \quad (6.12)$$

Here \bar{t}_i = mean residence time of each tank, $\bar{t} = n\bar{t}_i$ = mean residence time in the N tank system. The effect of number of tanks (n) on the RTD curve, which corresponds to degree of mixing, is shown in Figure 6.4 (b).

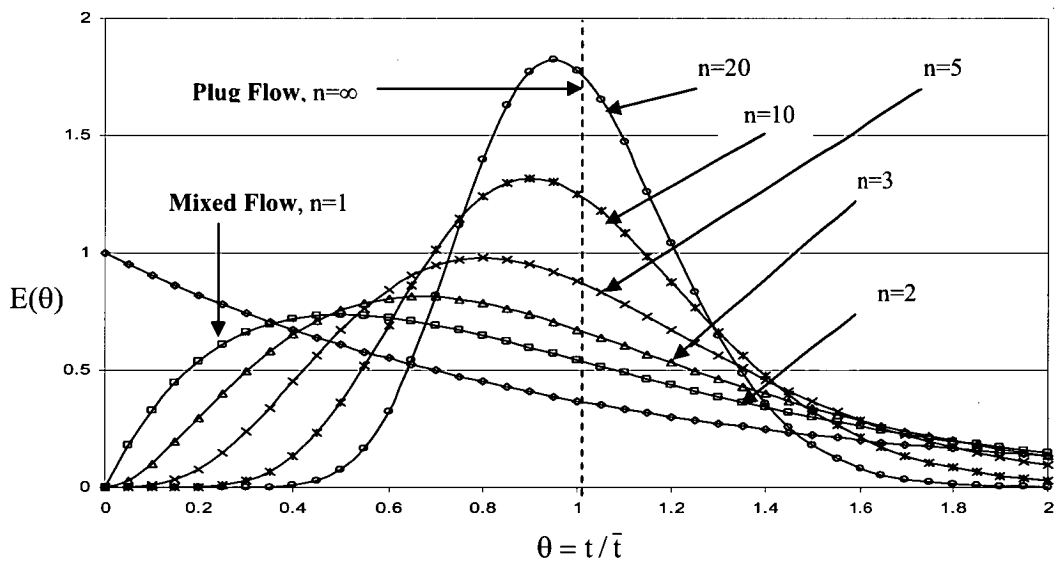
6.3 EXPERIMENTAL INVESTIGATION

A series of experiments was conducted to observe the dynamic behaviour of the model cyclone dryer. Spherical silica gel particles with 3.25 mm mean diameter (33 % moisture content) and paddy grain with 3.5 mm mean diameter (14% moisture content) were used as test particles. The average particle diameter was measured using grading sieves. The moisture content of these particles was measured by the oven-dry method. In this method, an 11 g sample of silica gel was dried at 200 °C for 24 hours (Ashworth et al., 1980), while a 3 g sample of whole paddy grain was dried at 105 °C for 72 hours (Chen, 2003). The influence of inlet air velocity, particle feed rate and number of chambers on the RTD

was observed. The applicability of the dispersion and tank-in-series model for describing particle flow in the cyclone dryer was examined.



(a)



(b)

Figure 6.4 Effect of model parameters on the RTD curve, indicating various degrees of mixing: (a) Dispersion model: influence of dispersion number, D/uL ; (b) Tank-in-series model: influence of number of tanks, n . (Levenspiel, 1972)

6.3.1 Experimental Set-up

The test rig used to determine the RTD of the cyclone dryer is shown in the schematic diagram of Figure 4.5. Details of the configuration and the measuring devices used are briefly given below.

6.3.1.1 Intake system

This part consists of a bellmouth nozzle, heater and blower. Ambient air was drawn into the system by a centrifugal blower (1). The air flow rate was measured using the throat pressure tapping at the bellmouth nozzle intake. Readings were corrected for variations of atmospheric conditions (temperature and pressure).

For the residence time experiments, it was not necessary to use hot air. Therefore the heater (2) was not operated at this stage. Inlet air velocity was about 17-21 m/s and 19-23 m/s for the paddy and silica gel tests, respectively.

6.3.1.2 Particle feeder

A rectangular conical hopper with an adjustable sliding plate at exit was used as a particle feeder. The particle feed rate was controlled by adjusting the position of sliding plate to calibrated positions. A rotary feeder was used to prevent the air blowing back through the open sliding plate. The mean relative deviation (Er_m) of particle feed rate was calculated by the following equation (Narimatsu et al., 2001):

$$Er_m = \frac{1}{\bar{F}} \left(\frac{1}{n} \sum_{i=1}^n |F_i - \bar{F}| \right) \quad (6.13)$$

where F_i = measured particle feed rate (kg/s); \bar{F} = average particle feed rate (kg/s). Figures 6.5 and 6.6 show typical calibration curves for the solid flow rate of paddy and

silica gel at different levels of fan motor frequency (Hz) and sliding plate opening. The particle flow rate provided by the feeder did not change with the fan speed over the range tested, but it varied significantly with the sliding plate opening.

Er_m was less than 0.5% for both paddy grain and silica gel. The experiments showed good reproducibility. Particle feed rates used were 0.0339-0.0697 kg/s and 0.0340-0.0778 kg/s for paddy and silica gel, respectively.

6.3.1.3 Cyclone dryer chamber

Design details and dimensions of the cyclone dryer used for these experiments are given in Appendix B. The outer diameter of cyclone dryer chamber was 500 mm. Experiments were conducted using three- and four-chamber configurations of the dryer. The static pressure drop across the dryer was measured between a pressure tap at the dryer inlet and atmosphere at outlet.

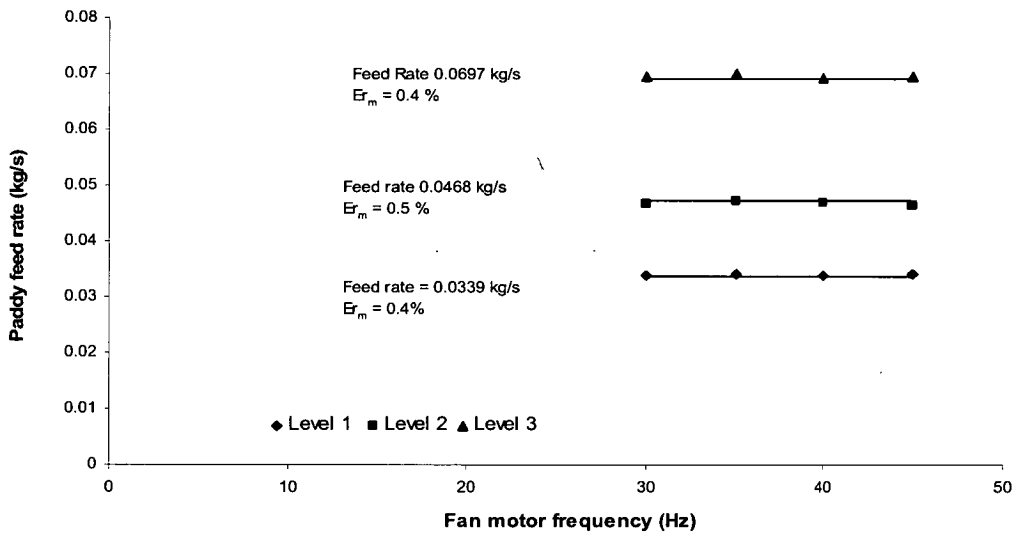


Figure 6.5 Paddy flow rates versus motor fan frequency at different sliding plate openings.

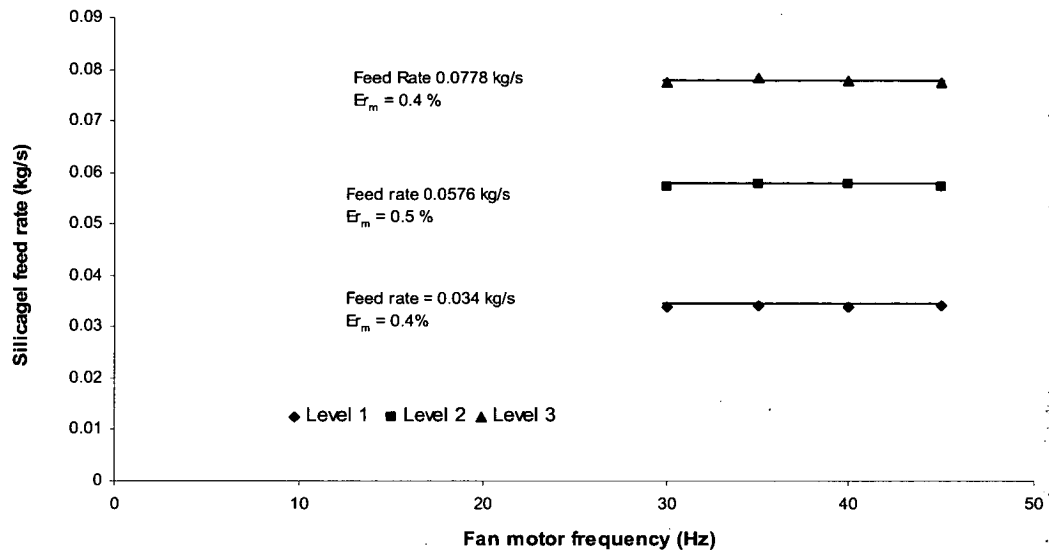


Figure 6.6 Silica gel flow rates versus fan motor frequency at different sliding plate openings.

6.3.1.4 Separation chamber

Test particles were collected at the cyclone exit by means of gravitational separation, while the air was being exhausted to atmosphere. The separation chamber design and dimensions are shown in Appendix B. By using the pulsing technique (Levenspiel, 1972) the extent of non-ideal flow can be characterised.

The exhausted particles were collected in a succession of cups at the outlet of the separation chamber and the tracer particles were counted. The RTD curves for tracer particles for different operating conditions and number of chambers were established from the tracer concentrations in successive collecting cups.

6.3.2 Experimental Procedure

The test particles were loaded into the hopper, located at cyclone inlet. The sliding plate was adjusted to the desired position to control particle feed rate. The centrifugal fan and rotary feeder were then operated and the test particles were continuously blown through the cyclone dryer chamber. This operation was continued until a steady flow of particles was attained, and the pressure differentials across the cyclone and the bellmouth intake was recorded. The dyed tracer particles were then injected to obtain the residence time distribution (RTD).

A total mass of 100-200 g of tracer particles was injected into the cyclone dryer chamber via a specially designed injector located at the cyclone inlet. The test particles were collected from the outlet of separation chamber every 10 seconds until 450 seconds had elapsed to ensure no tracers remained in the dryer chamber. The exhausted particles collected in each time interval were analysed by separating the dyed particles and weighing them using an electronic balance with an accuracy of 0.001 g. This procedure was then repeated for three different particle feed rates and three different inlet velocities, for both three- and four-chamber dryer configurations. The RTD curves for different operating conditions were determined following the method in Section 6.2.2.

The first experiments were with 3.25 mm average diameter silica gel particles at feed rates of 0.0340, 0.0576, and 0.0778 kg/s, and inlet velocities of 23, 21, and 19 m/s for three- and four-chamber configurations of the cyclone dryer. Experiments with paddy grain at feed rates of 0.0339, 0.0468, and 0.0697 kg/s, and inlet velocities of 17, 19, and 21 m/s for three- and four-chamber cyclone dryers were subsequently conducted.

6.3.3 Experimental Results

The experimental results at twenty operating conditions using silica gel and paddy as testing materials are shown in Table 6.1. The first and second moments of residence time

were first calculated from the measured distributions. The mean and variance were then computed following Equations (6.6) and (6.7). The measured cumulative age distributions, $F(t)$, for the complete of tests on silica gel particles and paddy grain are shown in Figures 6.7 and 6.8, respectively.

The measured effects of particle feed rate and inlet air velocity on the mean and variance of residence time are first discussed. The experimental observations are then compared with the two ideal reactor models outlined in Section 6.2.3. This matching was performed by using the functions available in Microsoft Excel. The sum of squares of the residuals was minimised with respect to the mean residence time and the relevant model parameter: D/uL for the dispersion model; and n for the tank-in-series model.

Table 6.1 Influence of cyclone geometry and operating conditions on experimental residence time distributions for silica gel particles and paddy grain.

Case	Test particle	Number of Chambers	Inlet Air Velocity (m/s)	Particle Feed Rate (kg/s)	Mean Residence Time, τ (s)	Standard Deviation	
						σ (s)	σ/τ
1	Paddy	3	21	0.0339	154	108	0.700
2	Paddy	3	21	0.0468	138	102	0.740
3	Paddy	3	21	0.0697	115	95	0.825
4	Paddy	3	19	0.0697	122	90	0.740
5	Paddy	3	17	0.0697	130	140	1.080
6	Paddy	4	21	0.0339	191	119	0.622
7	Paddy	4	21	0.0468	152	104	0.687
8	Paddy	4	21	0.0697	106	81	0.761
9	Paddy	4	19	0.0697	111	83	0.752
10	Paddy	4	17	0.0697	124	94	0.755
11	Silica gel	3	19	0.0778	134	102	0.761
12	Silica gel	3	21	0.0778	132	96	0.727
13	Silica gel	3	23	0.0778	148	116	0.784
14	Silica gel	3	21	0.0576	135	103	0.763
15	Silica gel	3	21	0.0340	184	119	0.645
16	Silica gel	4	19	0.0778	136	102	0.750
17	Silica gel	4	21	0.0778	138	101	0.735
18	Silica gel	4	23	0.0778	132	100	0.758
19	Silica gel	4	21	0.0576	161	190	0.678
20	Silica gel	4	21	0.0340	194	122	0.629

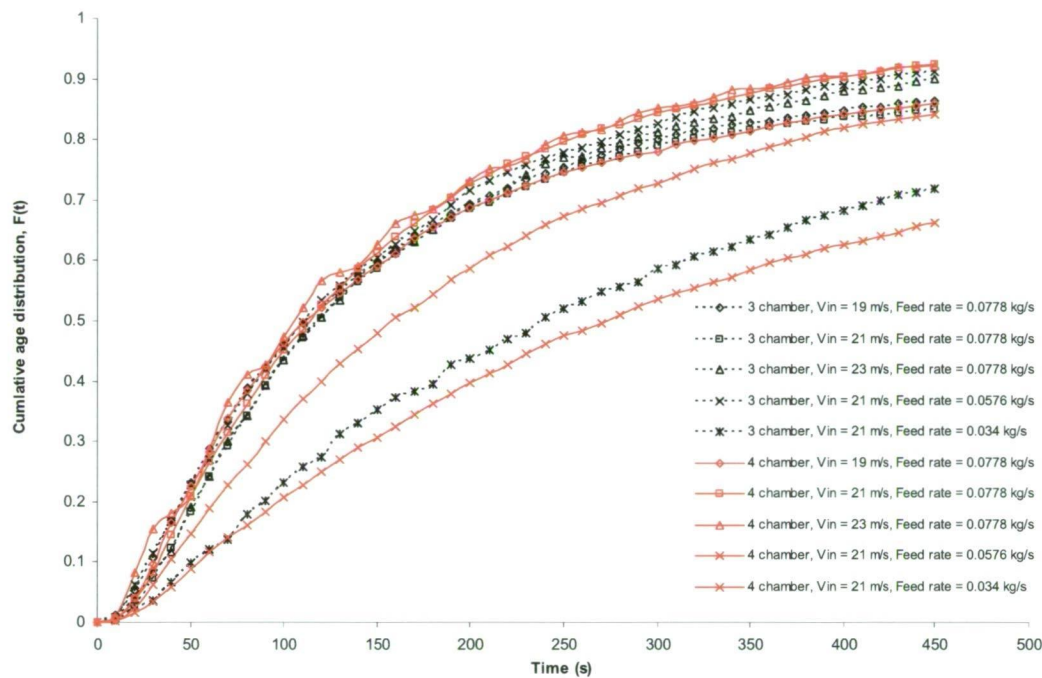


Fig 6.7 Cumulative age distribution, $F(t)$, of silica gel particles.

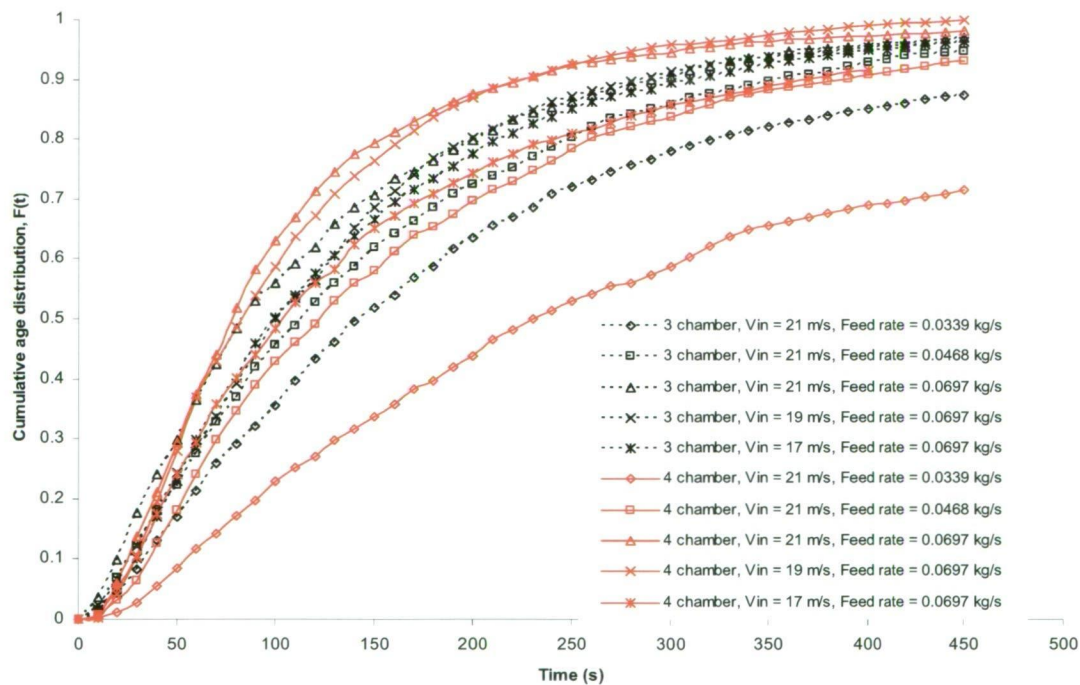


Fig 6.8 Cumulative age distribution, $F(t)$, of paddy grain.

6.3.3.1 Effect of inlet air velocity

The cumulative age distributions, $F(t)$, at different inlet air velocities with the same feed rate of silica gel particles and paddy grain in the three- and four-chamber cyclone dryers are shown in Figures 6.9 and 6.10. The shape of the distributions does not change greatly with the number of chambers. Figures 6.9 and 6.10 also show that the inlet velocity had a slight effect on the cumulative age distribution.

For paddy grain, a higher inlet air velocity consistently gives a lower residence time, as might be expected from kinematic similarity. (See cases 3, 4 and 5 for the three-chamber dryer, and cases 8, 9 and 10 for the four-chamber dryer, as shown in Table 6.1.) For silica gel particles, however, the trend of mean residence time with inlet air velocity is inconsistent. (See cases 11, 12 and 13 for three-chamber dryer, and cases 16, 17 and 18 for the four-chamber dryer.)

6.3.3.2 Effect of particle feed rate

Figures 6.11 and 6.12 for silica gel particles and paddy grain, respectively, show how the cumulative age distribution curves varied with particle feed rate for a given inlet air velocity for both three- and four-chamber cyclone dryers.

For paddy grain, the mean residence time increased significantly when the particle feed rate decreased. (See cases 1, 2 and 3 for the three-chamber dryer and cases 6, 7 and 8 for the four-chamber dryer.) For silica gel particles this trend was less consistent. (See cases 12, 14 and 15 for the three-chamber dryer and cases 17, 19 and 20 for the four-chamber dryer.)

The relative deviation of the residence time distributions, σ/τ , tended to increase with the particle feed rate. But again this trend was less consistent for the silica gel particles tests.

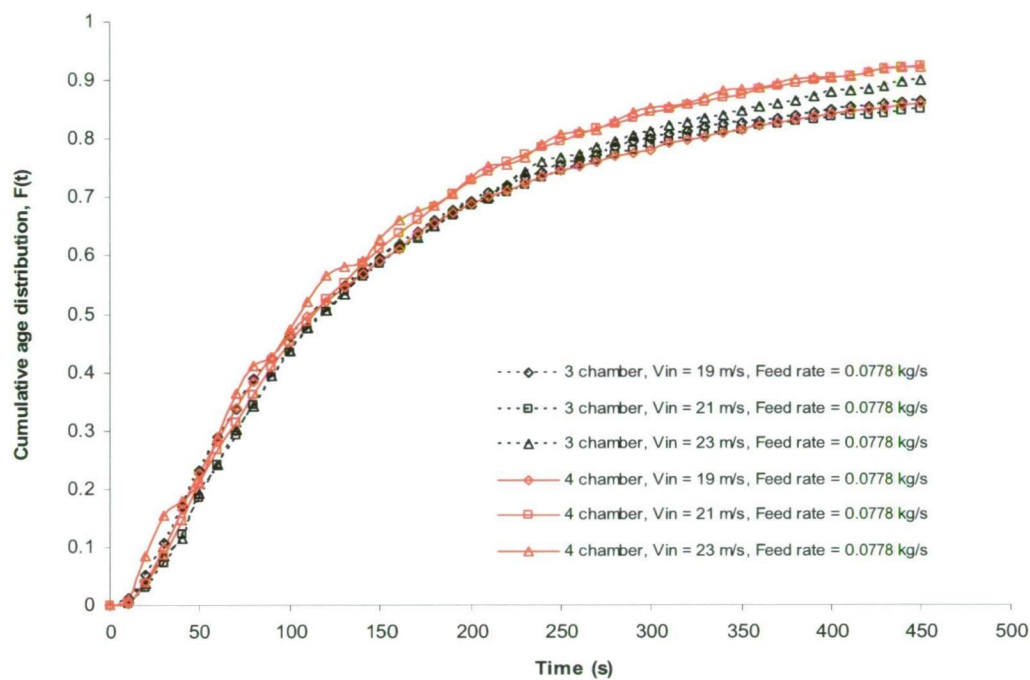


Figure 6.9 Influence of inlet air velocity on cumulative age distribution of silica gel particles.

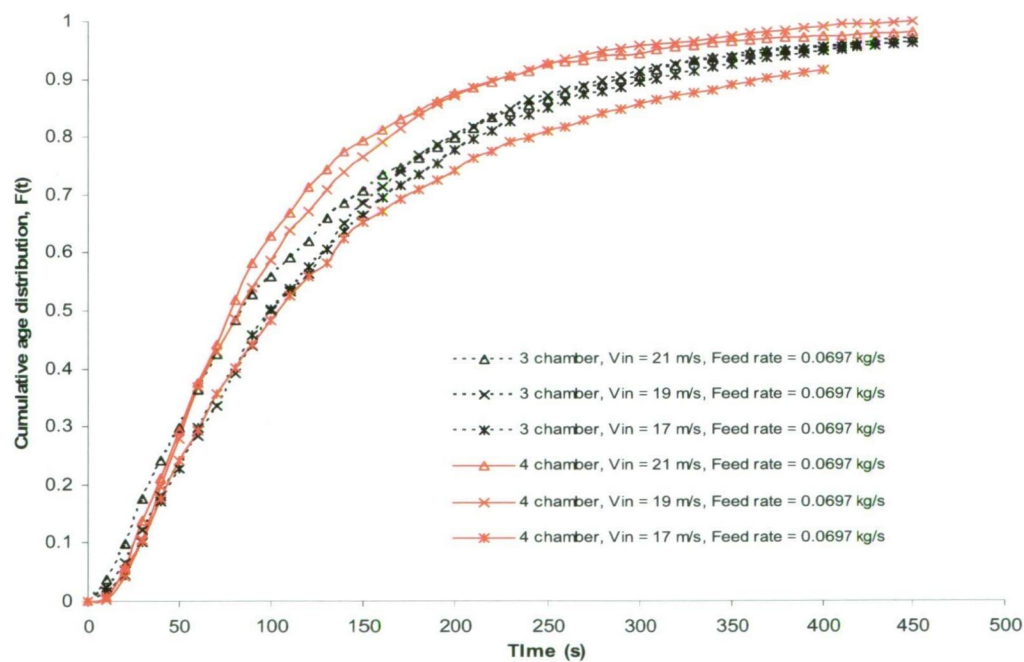


Figure 6.10 Influence of inlet air velocity on cumulative age distribution of paddy grain.

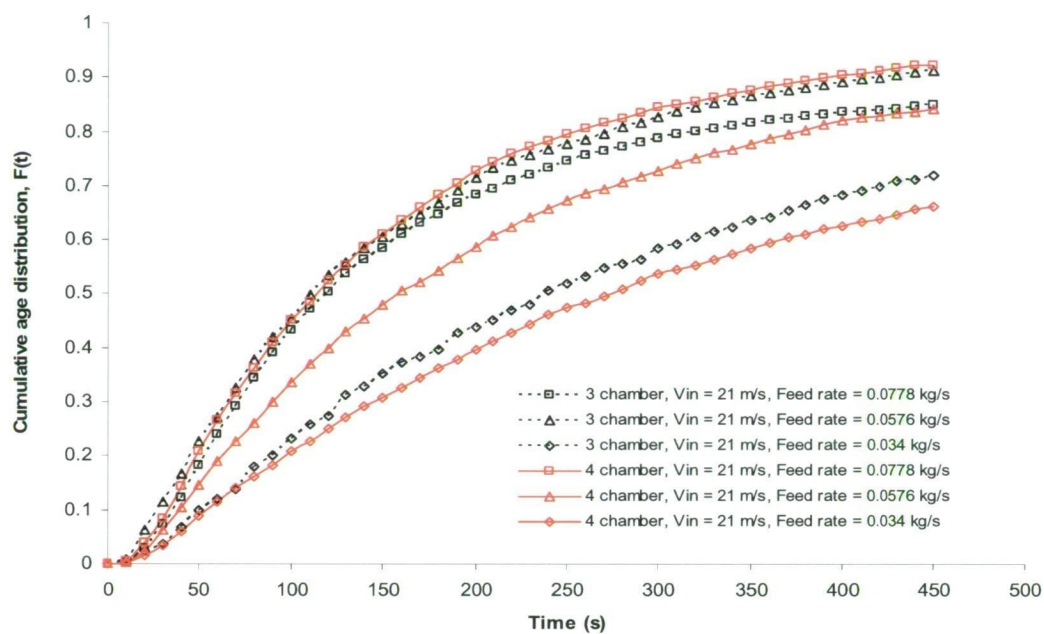


Figure 6.11 Influence of particle feed rate on cumulative age distribution of silica gel particles.

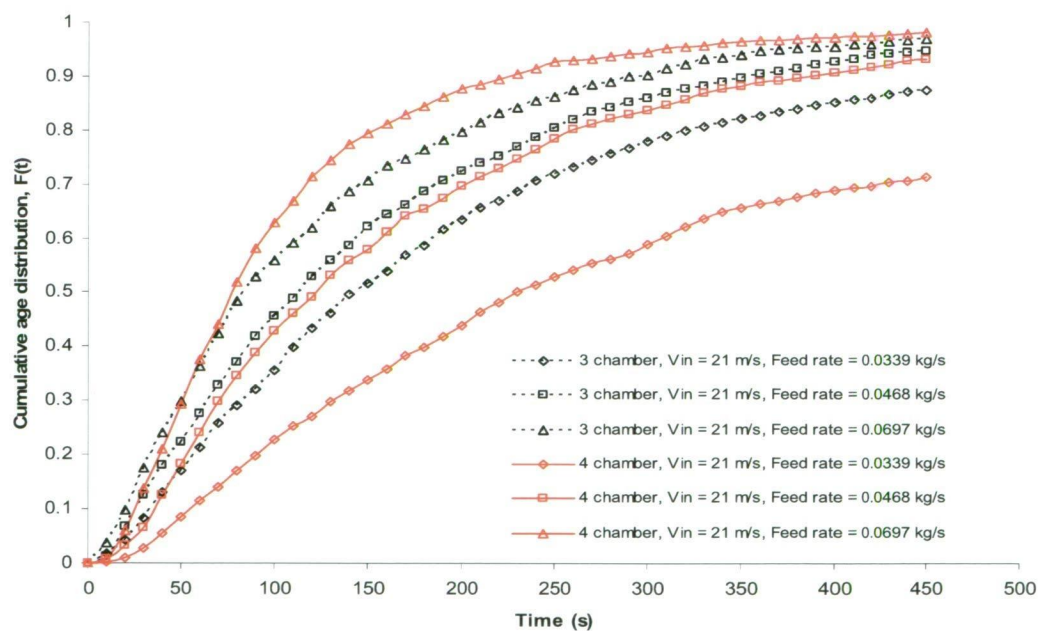


Figure 6.12 Influence of particle feed rate on cumulative age distribution of paddy grain.

6.3.3.3 Effect of number of chambers

In previous work on sugar cane bagasse drying in a cyclone separator, Correa et al. (2004a) tried to obtain a general correlation for the average particle residence time (APRT) as a function of variables like volumetric concentration, inlet gas velocity, particle diameter, particle density and dimensions such as cyclone height and diameter. It was concluded that none of the variables always had the same influence, except for volumetric concentration, which always had an inverse influence on APRT. This was also true in the present work, where the number of chamber had a variable influence on the mean residence time. The relative deviation of the residence time distribution, σ/τ , was more consistently influenced by the number of chambers. As seen from Table 6.1, σ/τ mostly decreases when the number of chamber is increased from three to four.

The inlet air velocity and solid feed rate jointly determine the mass concentration. The effect of mass concentration on mean residence time for three- and four-chamber cyclone dryers is plotted in Figures 6.13 and 6.14 for paddy and silica gel, respectively. The mean residence time varies quadratically with mass concentration. The fitted quadratic curves shown in the figures describe the mean residence times with standard deviations of 8 and 10 % for paddy grain and silica gel particles, respectively.

6.3.3.4 Effect of particle density

The effect of particle type on average residence time is summarised in Table 6.1. The data show that a higher particle residence time is obtained for silica gel with closely similar feed rates at the same inlet air velocity. (See cases 3&4 vs 11&12; cases 8&9 vs 16&17.)

As mentioned in Chapter 4, heavier particles (larger diameter and higher density) will spend more time in the swirl flow field of a cyclone dryer because of the action of

entrainment and re-dispersion. Therefore silica gel, which has nearly the same diameter but higher density than paddy grain, exhibits the higher residence time in this experiment.

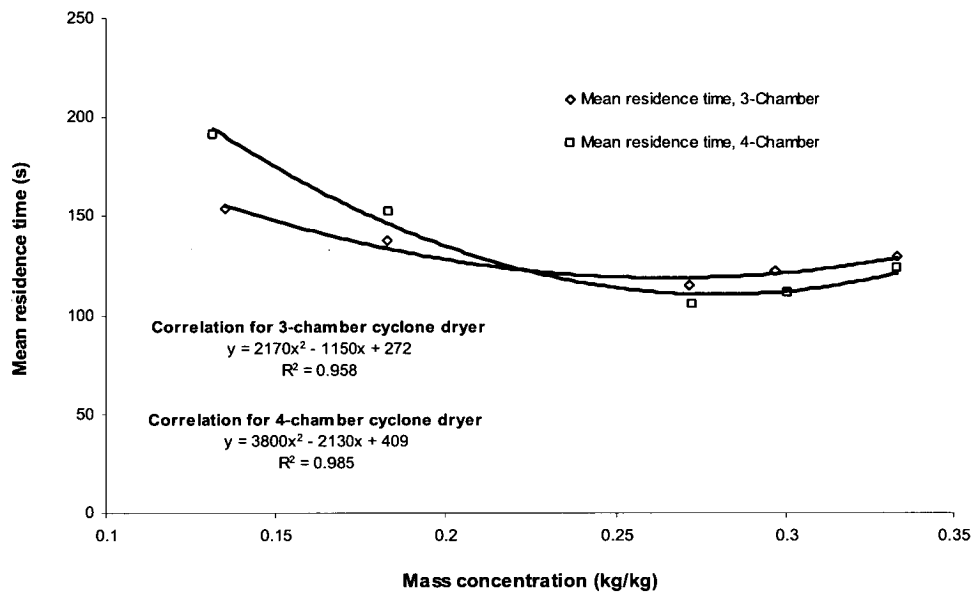


Figure 6.13 Influence of mass concentration on mean residence time of paddy grain for three-and four-chamber cyclone dryers.

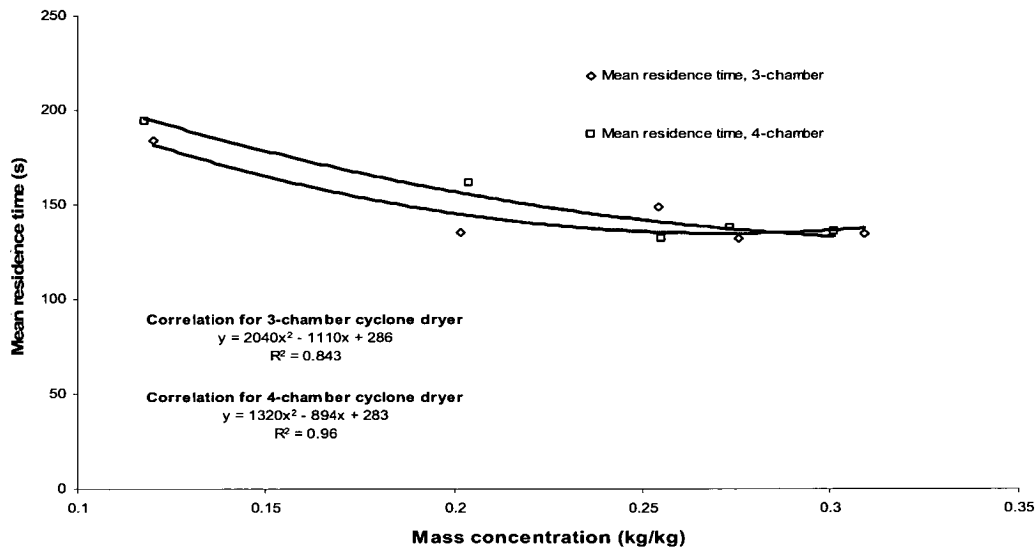


Figure 6.14 Influence of mass concentration on mean residence time of silica gel particles for three-and four-chamber cyclone dryers.

6.3.3.5 Comparison with non-ideal flow models

The comparison of experimental data with ideal theoretical models is a useful means of defining the behaviour and performance characteristics of the model cyclone dryer. The best fit of the ideal dispersion model given by Equation 6.10 was first studied, using the experimental RTD data from test cases 1 to 10 (for paddy grain) and 11 to 20 (for silica gel particles). The square of the correlation coefficient (R^2) was minimised with respect to the value of dispersion number. The tank-in-series model given by Equation 6.13 was subsequently fitted to this experimental data, and the model parameter, n (number of tanks in series) for best fit was obtained.

The best fit dispersion and tank-in-series models are compared with the experimental data from test cases 1 and 11 in Figures 6.15 and 6.16 for paddy grain and silica gel particles, respectively. The agreement is fairly good for the tank-in-series model, but a large deviation is observed for dispersion model. The tank-in-series model is, therefore, more acceptable for describing the RTD of a cyclone dryer.

The model parameters and R^2 values for all operating conditions shown tabulated in Table 6.2. The tank-in-series model clearly gives much lower deviations from the experimental RTD curves than the dispersion model. This indicates that the cyclone dryer produces a well-mixed flow behaviour. The number of tanks, n , for best fit of the experimental data in this study varies between 2 and 3, and is generally less than the number of chambers in the dryer. This is consistent with the smaller amount of solid recirculation in the exit chamber seen in both visual and numerical particle tracking results. Typical numerically predicted particle tracks are shown in Figure 7.17.

For the tests with paddy grain (cases 1-10) the average value n for best fit to the tank-in-series model is lower for the three-chamber cases than for the four-chamber cases. This tendency is not evident for the tests with silica gel particles (cases 11-20), where most of the cases are best fitted by $n=3$.

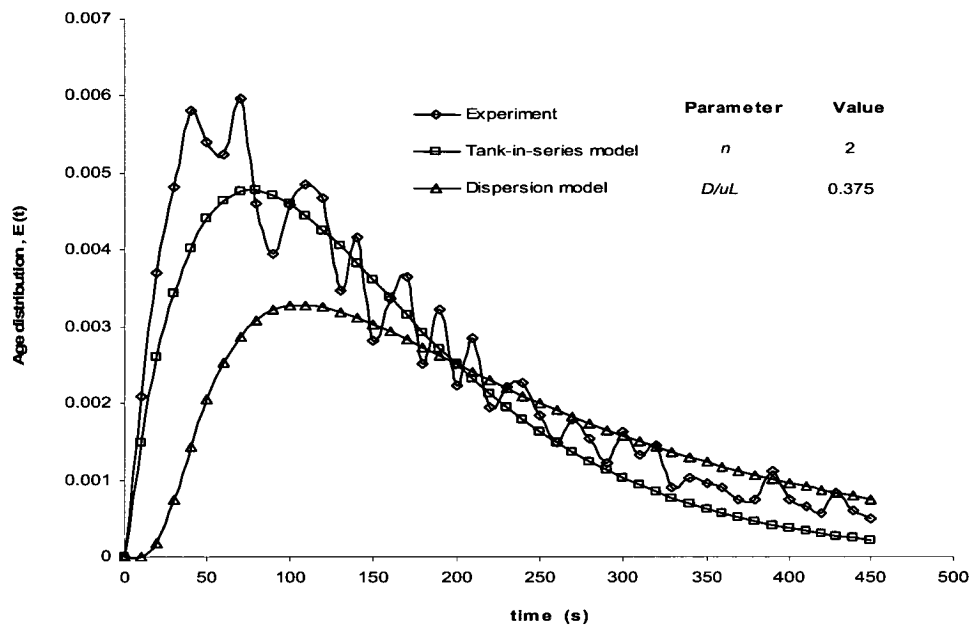


Figure 6.15 Comparison of best fit tank-in-series and dispersion models with experimental RTD for paddy grain. Test case 1.

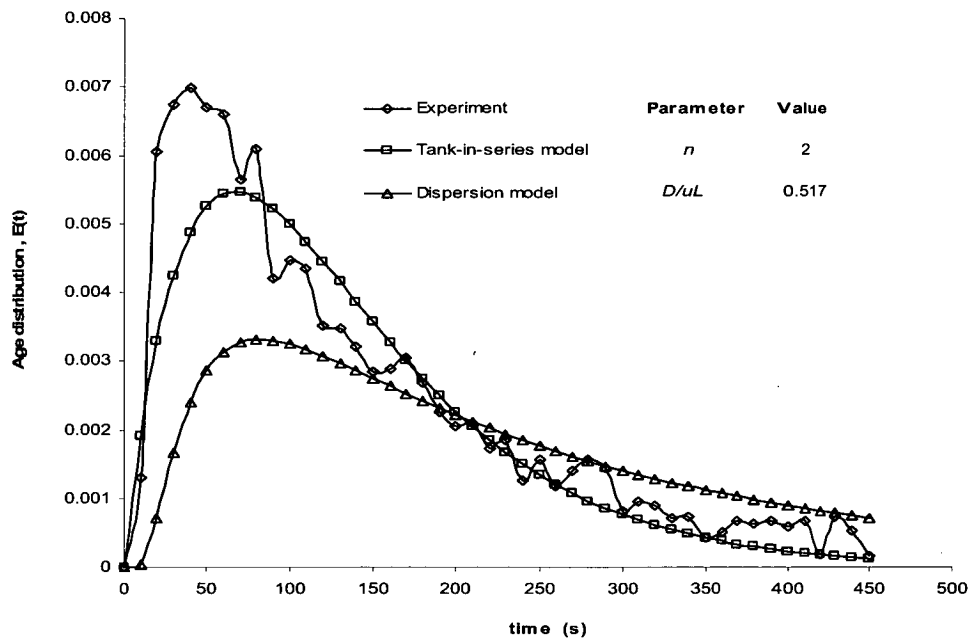


Figure 6.16 Comparison of best fit tank-in-series and dispersion models with experimental RTD for silica gel. Test case 11.

Table 6.2 Best fit to experimental residence time distribution for tank-in-series and dispersion models for cases specified in Table 6.1.

Case	Number Of Chambers	Tank-in-series Model		Dispersion Model	
		Number of tanks, n	R ²	Dispersion number, D/uL	R ²
1	3	2*	0.968	0.375	0.456
		3	0.807		
2	3	2	0.86	0.481	0.32
		3*	0.926		
3	3	2	0.814	0.499	0.253
		3*	0.996		
4	3	2*	0.916	0.463	0.302
		3	0.876		
5	3	2	0.827	0.48	0.283
		3*	0.962		
6	4	2	0.819	0.257	0.779
		3*	0.998		
7	4	2	0.808	0.354	0.406
		3*	0.968		
8	4	2	0.768	0.524	0.223
		3*	0.936		
9	4	2	0.758	0.491	0.232
		3*	0.932		
10	4	2	0.782	0.472	0.235
		3*	0.989		
11	3	2	0.836	0.517	0.29
		3*	0.951		
12	3	2	0.751	0.433	0.277
		3*	0.946		
13	3	2	0.742	0.585	0.336
		3*	0.943		
14	3	2	0.803	0.521	0.286
		3*	0.987		
15	3	2*	0.794	0.289	0.951
		3	0.636		
16	4	2	0.733	0.491	0.276
		3*	0.952		
17	4	2	0.776	0.456	0.265
		3*	0.982		
18	4	2	0.886	0.51	0.301
		3*	0.896		
19	4	2	0.869	0.336	0.511
		3*	0.902		
20	4	2*	0.654	0.226	0.671
		3	0.535		

* Indicates the number of tanks giving the best fit to the experimental data for the tank-in-series model

6.4 NUMERICAL SIMULATION

This section describes the numerical simulations used to study the gas-solid flow in the model cyclone dryer. The simulations were performed using a Lagrangian-Eulerian multiphase model with an RNG k - ϵ turbulence model.

6.4.1 Mathematical Modelling

Chapter 5 described the three-dimensional Navier-Stokes and mass conservation equations and presented numerical solutions for the gas phase. Details of the numerical set-up for turbulence modelling, mesh type, advection scheme, mesh resolution, and convergence criteria were also discussed in the previous chapter. The numerical results for the gas phase are now used as initial conditions for particle transport modelling in the model cyclone dryer.

In the particle transport model the gas phase is treated as a continuum, while the particulate phase is treated as discrete elements. This approach is called a Lagrangian-Eulerian multiphase model. The flow of the particulate phase is modelled by tracking a small number of representative particles as they move through the fluid continuum.

Particle-particle interactions and the influence of the particle phase on the gas phase are not taken into account. Only the gravity force and the gas drag force on the particles are calculated. The interactions when particles hit the cyclone wall are described in terms of parallel and perpendicular restitution coefficients.

The BBO equation presented in Chapter 3 is used to describe particle transport in the Lagrangian-Eulerian multiphase model. The virtual mass force (or Basset force), Magnus force, and Saffman force are not considered. The implemented model has a large number of parameters that can be used to improve the RTD data fit. As mentioned by Crowe et al. (1997), the response time of particles to changes in flow velocity or temperature are

important in establishing non-dimensional parameters to characterise the flow. The momentum response time (τ_v) relates to the time required for a particle to respond to turbulent velocity fluctuations. It is related to the fluid and the particle properties by

$$\tau_v = \rho_p d_p^2 / 18\mu_a \quad (6.14)$$

A quantitative estimate of the effect of turbulence on particle response time is given in term of the Stokes number (St_v), which is defined by the ratio of the momentum response time to a characteristic time for the flow field (τ_T):

$$St_v = \tau_v / \tau_T \quad (6.15)$$

If $St_v \ll 1$, the particle will have ample time to respond to velocity fluctuations. On the other hand, if $St_v \gg 1$, then the particle velocity will be little affected during passage through the flow field.

The CFX simulations for the model cyclone dryer were run with and without turbulence dispersion for the particle phase. The predicted cumulative age distributions of the solid particles with and without turbulence dispersion effects were then compared with the experimental results.

6.4.2 Numerical Procedure

The grid used for the multiphase flow was the hexahedral element grid of 419,928 nodes shown in Figure 5.4. The gas phase was assumed to enter the domain with a uniform inlet velocity through the tangential inlet to the bottom chamber. One thousand particles were injected into the calculation domain through the solid feeder inlet at different positions equally spaced over the inlet. Restitution coefficients of unity were assigned for the simulations, i.e., it was assumed that the particles were perfectly elastic.

In order to compare the predicted results with experimental results described in the previous section, the following data were used. Equivalent diameters of 3.25 mm and 3.5 mm were used for the silica gel particles and paddy grain, respectively. The moisture content and density of the particulate phase were taken from the experimental results. The

densities of the paddy grain at 14 % dry-basis and silica gel particles at 33% dry-basis were 1132 and 1523 kg/m³, respectively.

A series of simulations was performed in which important design parameters were varied. Simulations using silica gel particles were run with feed rates of 0.0340, 0.0576 and 0.0778 kg/s and inlet velocities of 23, 21 and 19 m/s for three- and four-chamber cyclone dryer configurations. These feed rates and inlet air velocities are the same as those used experimentally. Simulations of paddy grain behaviour at feed rates of 0.0379, 0.0468, and 0.0697 kg/s and inlet velocities of 17, 19 and 21 m/s for three- and four-chamber dryer configurations were subsequently conducted. The particle residence time distributions were calculated by the following method. The particle mass fraction was defined by a new probability parameter c_i , which is given by

$$c_i = NP_i / n_o \quad (6.16)$$

Here NP_i is the number of particles left in the chamber at time t_i , and n_o is the number of particles initially injected into the computational domain. This particle mass fraction was then used to calculate the cumulative age distribution of particles $F(t)$ following the method described in Section 6.2.2.

6.4.3 Numerical Results

6.4.3.1 Effect of turbulent dispersion model

Figures 6.17 and 6.18 show the cumulative age distributions of silica gel particles at different inlet air velocities calculated with and without turbulence dispersion for three- and four-chamber cyclone dryers. The predicted cumulative age distributions of paddy grain at different air velocities for three- and four-chamber cyclone dryers are shown in Figures 6.19 and 6.20. The corresponding experimental results are also presented in these figures.

The cumulative age distributions calculated with turbulence dispersion exhibit an abrupt early break, after which the particles exit very slowly and there is an almost constant accumulation of solids in the dryer. These curves differ greatly in shape from the experimental results. For particle tracking without turbulence dispersion, the predicted cumulative age distributions are similar in form to the experimental curves, but indicate a more rapid exit of particles from the dryer than is actually observed. The predicted variations in the cumulative age distributions with changes in air velocity are, however, quite similar to those observed experimentally.

The above observations indicate that particle trajectories were little affected by turbulent velocity fluctuations in the real flow situation. The influence of turbulent velocity fluctuations was further examined by evaluating typical Stokes numbers for silica gel particles and paddy grain in the cyclone dryer flow. The characteristic time of the cyclone dryer adopted was a convective time scale obtained by dividing the cyclone dryer diameter by the velocity of air at the orifice assuming uniform flow conditions.

As shown in Table 6.3, the Stokes numbers for both silica gel particles and paddy grain range from 500 to 800 when the cyclone diameter is used as the characteristic length scale. However, the length scale of turbulent eddies in the cyclone orifice flow that are primarily responsible for the dispersion and re-entrainment of solid particles would be at least an order of magnitude smaller than the cyclone diameter. Hence the relevant Stokes number for the paddy grain and silica gel particles should be of order 10^4 . This provides a possible explanation for the apparent lack of turbulent dispersion effects. Further justification is provided by the experimental results of Modigell et al. (2000) who observed that particles larger than 50% cut off diameter (equal to $4\text{ }\mu\text{m}$) were unaffected by turbulent dispersion in a cyclone separator flow.

Following the above observations, all further numerical computations were conducted without turbulent dispersion effects applied by the CFX solver.

Table 6.3 Stokes number of paddy grain and silica gel particles at different inlet air velocity

Inlet air velocity (m/s)	Stokes number (St_v)	
	Paddy grain	Silica gel particles
17	506	-
19	565	656
21	625	725
23	-	794

6.4.3.2 Comparison of numerical residence time predictions with experimental results

Table 6.4 compares the experimental mean particle residence times with the numerical predictions obtained by neglecting turbulent dispersion. The case numbers in Table 6.4 correspond to those in Table 6.1.

The mean residence time predicted by the simulations was roughly doubled by increasing the number of cyclone dryer chambers from 3 to 4; but changing this parameter had relatively little effect on the experimental results. An inconsistent trend of mean residence time variations for both experimental and numerical results was obtained when the inlet air velocity was changed. The simulation results for different particle feed rates have the same particle trajectories and mean residence time.

The predicted mean residence times are generally more accurate for four-chamber dryer cases than for three-chamber cases (as indicated by the higher ratio of numerical to experimental values shown in Table 6.4). The predicted mean residence times for paddy grain are more accurate than those for silica gel particles.

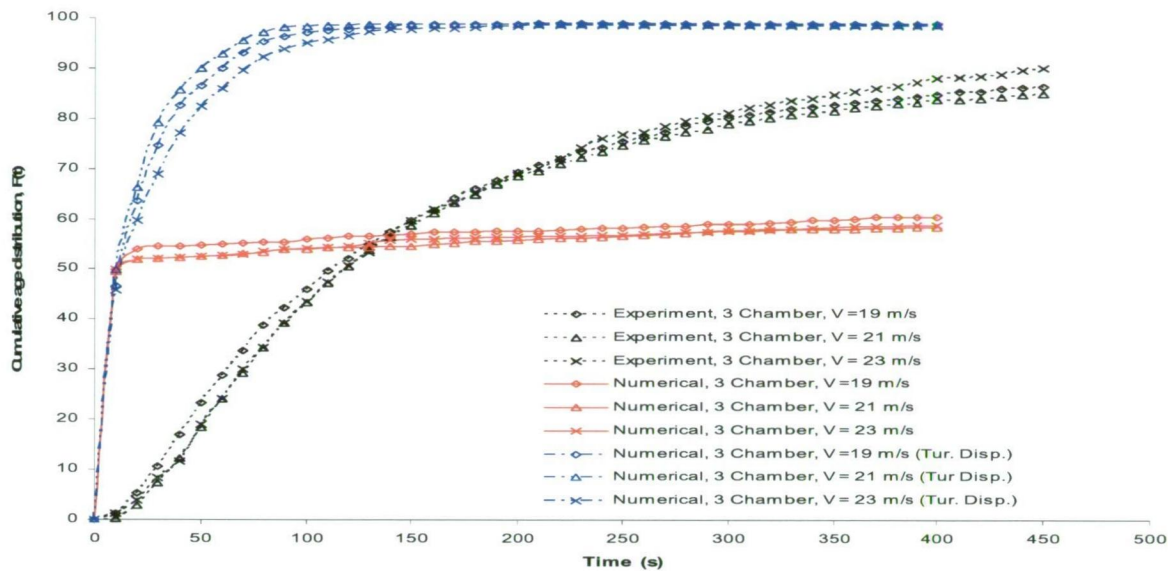


Figure 6.17 Comparison of experimental and numerical cumulative age distributions of silica gel particles in a three-chamber cyclone dryer. (Silica gel feed rate = 0.0778 kg/s)

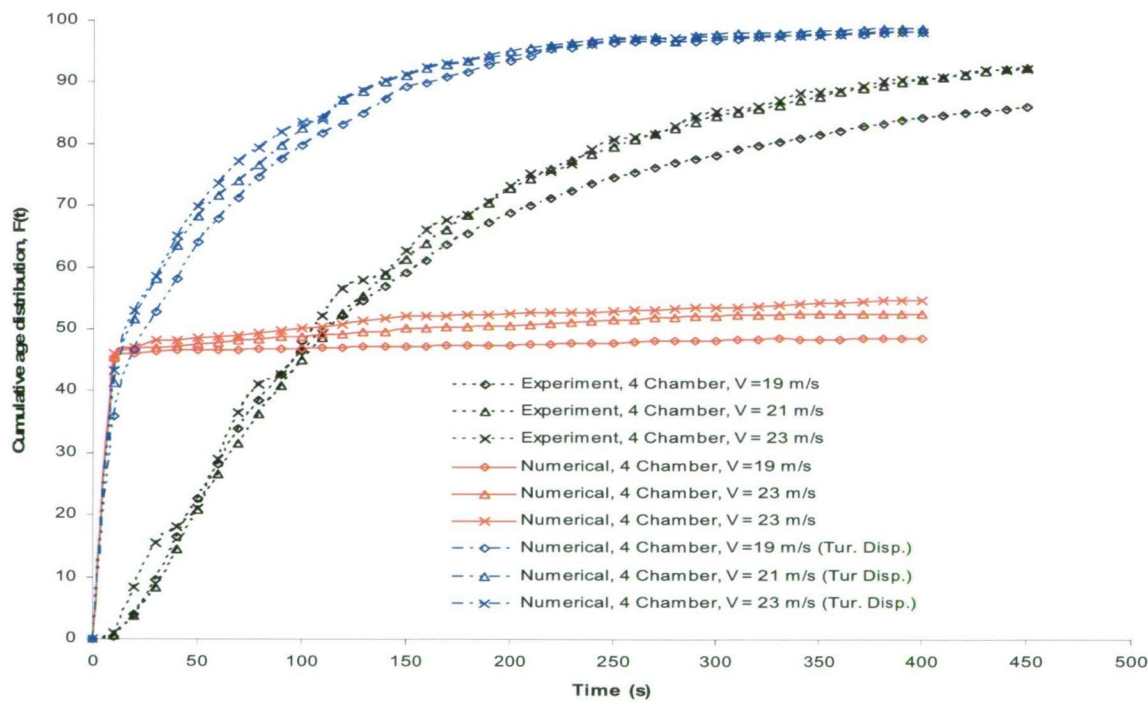


Figure 6.18 Comparison of experimental and numerical cumulative age distributions of silica gel particles in a four-chamber cyclone dryer. (Silica gel feed rate = 0.0778 kg/s)

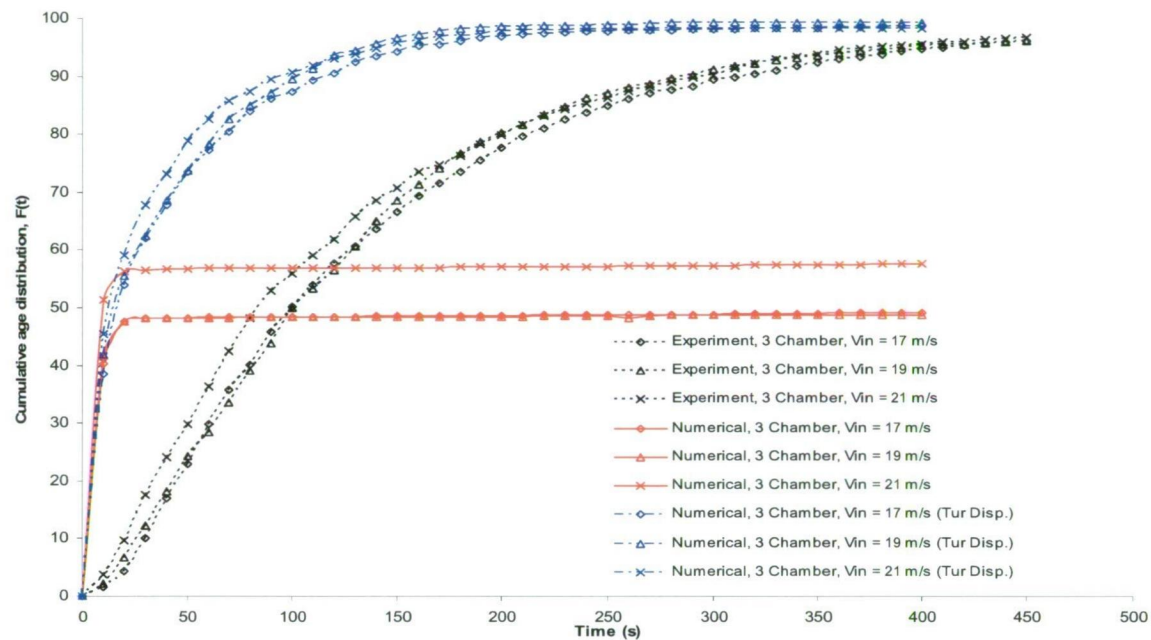


Figure 6.19 Comparison of experimental and numerical cumulative age distributions of paddy grain in a three-chamber cyclone dryer. (Paddy feed rate = 0.0697 kg/s)

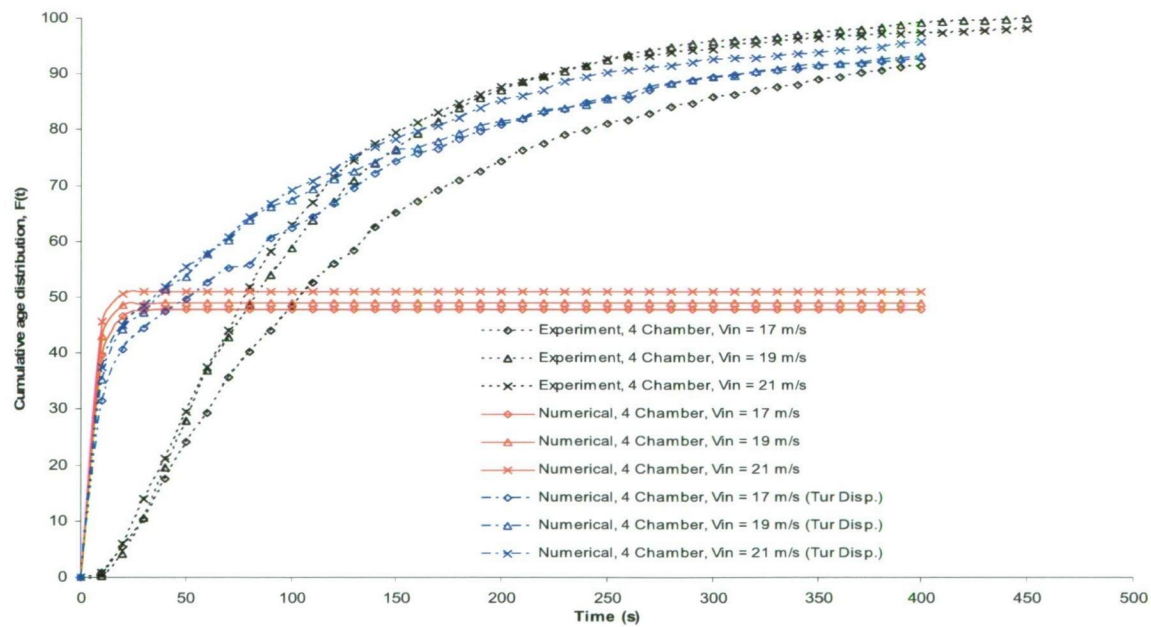


Figure 6.20 Comparison of experimental and numerical cumulative age distributions of paddy grain in a four-chamber cyclone dryer. (Paddy feed rate = 0.0697 kg/s)

Table 6.4 Comparison of experimental and numerically simulated mean particle residence times.

Case	Test particle	Number of Chambers	Inlet air velocity (m/s)	Particle feed rate (kg/s)	Mean residence time		
					Experimental τ_{exp} (s)	Numerical τ_{num} (s)	Ratio τ_{num}/τ_{exp}
3	Paddy	3	21	0.0697	115	36	0.313
4	Paddy	3	19	0.0697	122	40	0.328
5	Paddy	3	17	0.0697	130	44	0.338
8	Paddy	4	21	0.0697	106	78	0.736
9	Paddy	4	19	0.0697	111	80	0.721
10	Paddy	4	17	0.0697	124	86	0.694
11	Silica gel	3	23	0.0778	134	31	0.231
12	Silica gel	3	21	0.0778	132	24	0.182
13	Silica gel	3	19	0.0778	148	27	0.182
16	Silica gel	4	23	0.0778	136	49	0.360
17	Silica gel	4	21	0.0778	138	53	0.384
18	Silica gel	4	19	0.0778	132	58	0.439

The numerically predicted and experimental age distributions, $E(t)$, for silica gel particles and paddy grain in three- and four-chamber cyclone dryers are compared in Figures 6.21 to 6.24. The model and experimental results differ significantly, with the model curves showing significantly higher peak values occurring at earlier times. The tails of the model and experimental curves both exhibit an exponential decay, but the decay rate is much higher for the numerical predictions.

Solid particles clearly leave the cyclone chamber much faster than reality in the numerical simulation. These deviations may be due to a number of factors, including:

- (a) The experimental mean residence time is strongly dependent on particle feed rate, as shown in Table 6.1. This fact was not taken into account in the Lagrangian particle transport modeling, which used one-way coupling between the particle and gas phases. The model also neglected interactions between particles and the influence of the particle phase on the gas phase;
- (b) Differences in the fluid phase velocity distribution will influence the particle

residence time. As discussed in Chapter 5, although the simulated velocity distributions represent the experimental results fairly well there are some significant deviations in the outer region due to the diffusive nature of RNG $k - \varepsilon$ turbulence model;

(c) Deviations from perfect elastic behaviour in particle-particle and particle-wall collisions will affect particle trajectories and speed.

In summary, the simulated residence time distributions deviate significantly from the experimental data. The predicted mean residence times are consistently too low. However, the quantitative results are of the same order of magnitude and there is qualitative agreement for the trends in residence time associated with changes in some operating conditions.

6.5 CONCLUSIONS

The influence of cyclone dryer operating parameters and geometry on the particle residence time of paddy grain and silica gel particles were investigated by means of experimental and numerical simulation studies. In numerical simulation studies, it was found that the mean residence time of paddy grain and silica gel particles increased with the number of chambers. The experimental results indicated a variable influence of the number of chambers on the mean residence time, but there was a noticeable tendency for the relative deviation of the RTD, σ/τ , to be reduced with a higher number of chambers. In experimental studies, the parameter most influencing the mean residence time was the particle feed rate; in numerical studies, the inlet air velocity was found to have the most influence.

Numerical simulations without a turbulence dispersion model gave better predictions of the cumulative age distribution for both paddy grain and silica gel particles. The apparent lack of turbulent dispersion effect was explained by the relatively high value of Stokes number for the solid particles in the model dryer.

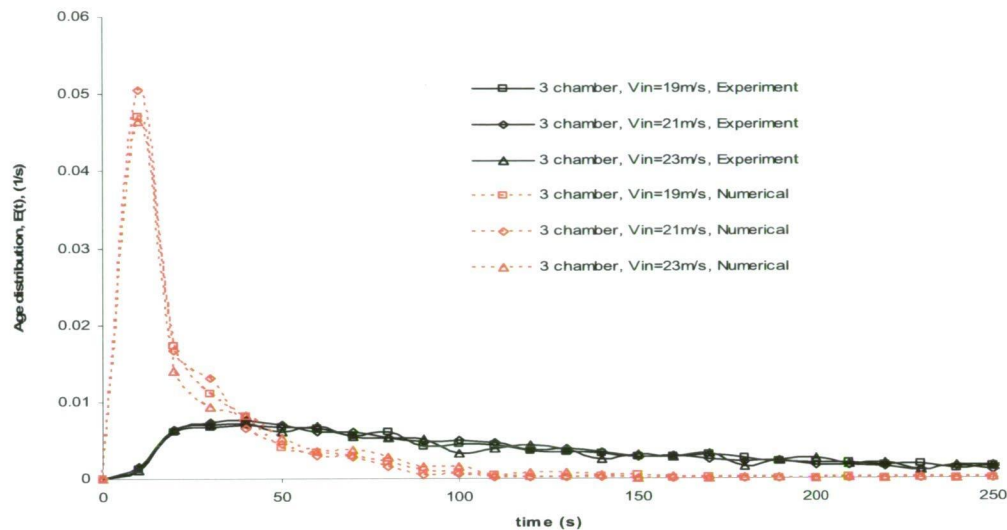


Figure 6.21 Comparison of numerical and experimental age distributions, $E(t)$, for silica gel particles in a three-chamber cyclone dryer, showing influence of inlet air velocity.

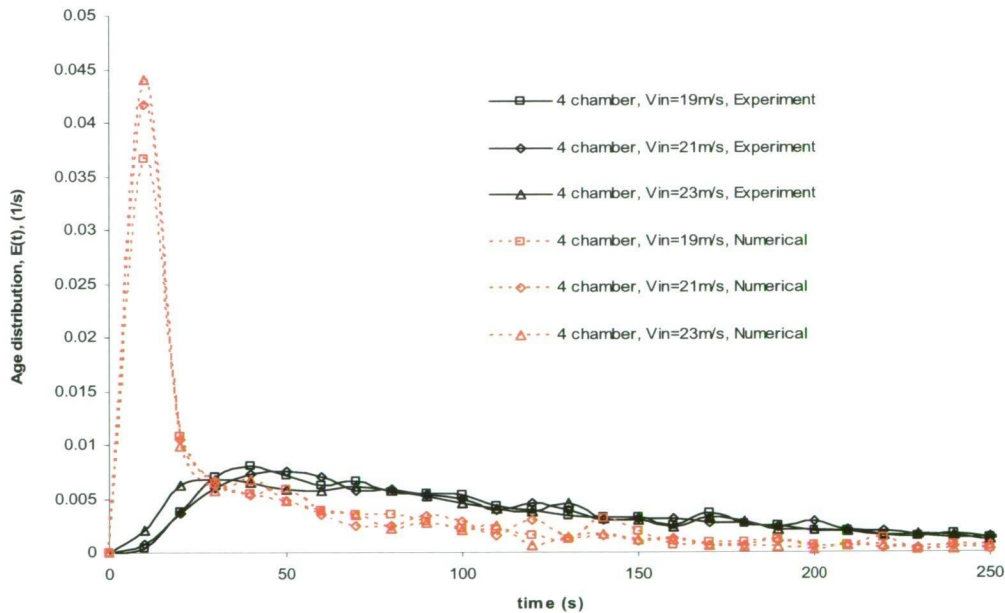


Figure 6.22 Comparison of numerical and experimental age distributions, $E(t)$, for silica gel particles in a four-chamber cyclone dryer, showing influence of inlet air velocity.

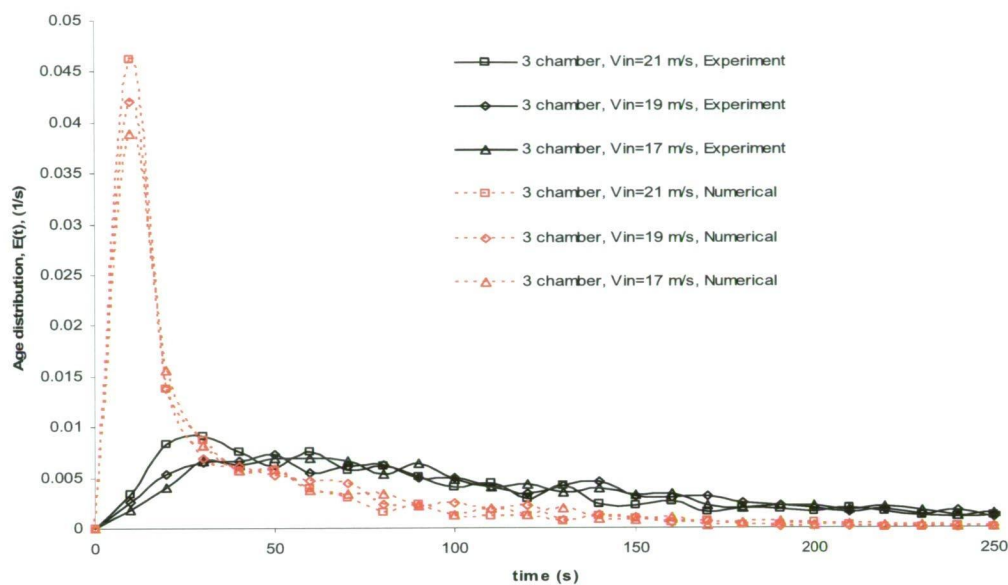


Figure 6.23 Comparison of numerical and experimental age distributions, $E(t)$, for paddy grain in a three-chamber cyclone dryer, showing influence of inlet air velocity.

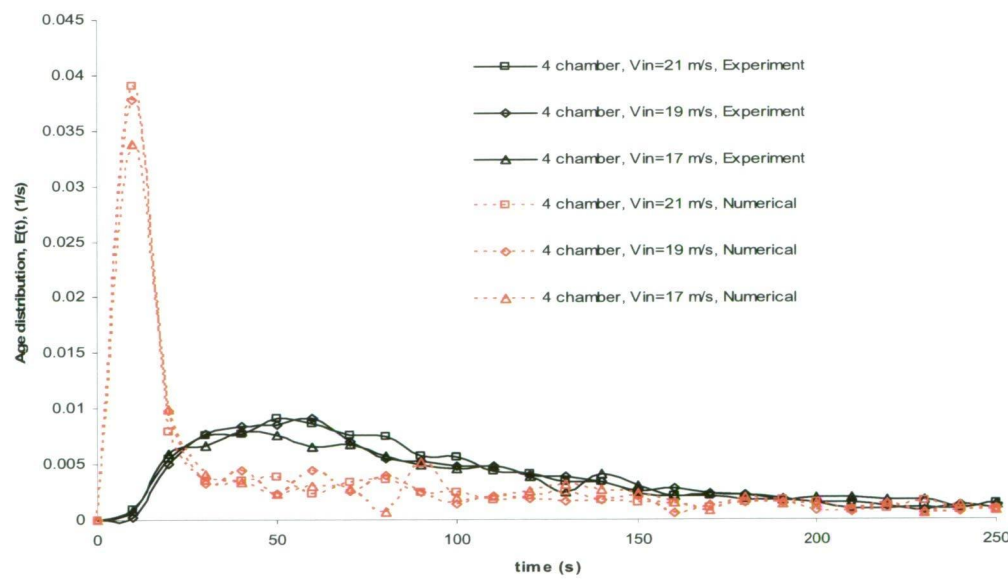


Figure 6.24 Comparison of numerical and experimental age distributions, $E(t)$, for paddy grain in a four-chamber cyclone dryer, showing influence of inlet air velocity.

The numerical simulations without turbulence dispersion gave reasonable qualitative predictions of the observed behaviour but large quantitative discrepancies in the residence time distributions and mean particle residence times. The Lagrangian-Eulerian multiphase model used did not take into account the effect of interactions between particles and the influence of the particle phase on the gas phase. This is believed to be the main reason why the numerical simulation results were so different from the experimental data. Further work is needed to examine and improve the usefulness of CFD predictions for the cyclone dryer.

A more advanced numerical model using two-way particle-fluid coupling will be used in the next chapter to investigate heat and mass transfer during the drying process inside the model cyclone dryer.

Chapter 7

EXPERIMENTAL AND NUMERICAL STUDIES OF CYCLONE DRYER PERFORMANCE

7.1 INTRODUCTION

In Thailand, most of the paddy harvested during the second season usually has a moisture content higher than 25% of dry basis. It needs to be dried to an acceptable moisture level for safe storage. The drying process needs good mixing and effective gas-solid contact to provide efficient heat utilisation due to the irregular shape and large size of paddy grain. Drying of large varieties of particulate materials in cyclone separators has been reported during the last decade (Silva, 1992; Kemp., 1998; Benta, 1997; Correa, 2004a). Those studies indicated that a cyclone is a very efficient heat exchanger between gas and solid particles, and also plays an important role in pneumatic drying. A swirling flow is

induced in this device, within which the particles experience centrifugal forces. High relative velocities between particles and air are obtained, resulting in high heat and mass transfer intensity. However, most drying tasks for hygroscopic materials require a long residence time. Therefore, due to the short residence time of the particles, a cyclone separator is only used as a dryer for heat sensitive materials or pre-drying (Benta, 1997).

Drying of solids in a swirling flow field was studied by Jinscue (1992) who reported experimental results showing that helicoidal motion of the solid particles varied with their weight and diameter. The heavier particles stayed at a lower level of the chamber while drying advanced, until the particle weight reduced and they moved on to higher levels of the chamber until evacuated by pneumatic transport. These effects were responsible for the excellent results obtained with the swirling flow dryer, as the particle residence time increased with particle weight. Consequently, the second stage of drying (falling rate period) was obtained in this kind of dryer. Furthermore, a relatively uniform moisture content of the final product was expected for drying material with different initial moisture contents. This characteristic demonstrated the potential for obtaining diffusion controlled drying of hygroscopic material such as paddy grain.

Since the 1980s, a type of swirling flow dryer known commercially as the “Cyclone Dryer” has been industrially applied in drying powder (Hienze, 1984). Korn (2001) has reported the drying of chemical substances with this device. A cyclone dryer consists of a cylindrical tower containing a series of inverted conical baffles with central orifices, which divide the tower into chambers. The moist particulate matter is fed into a stream of hot, dry air, which enters the dryer tangentially at the base of the tower, creating a rotating flow within the dryer. This rotating flow is considerably more complex than that seen in cyclonic separators. A precessing central vortex forms within the open region at the centre of the tower, while recirculation zones form within each of the chambers. The central vortex and through flow jet transports the particles upwards from chamber to chamber. Most of the drying occurs within the chambers where the particles spend time trapped in the recirculating air flow. This system ensures adequate residence time and excellent mixing between the hot dry gas and the moist particles, which enables rapid

transfer of moisture from the particles to the gas. Very little performance data for this device has been published in the open literature and the design of cyclone dryers has to date relied predominantly on pilot plant testing. No previous reports of agricultural material being dried drying by this technique have been located by the present study.

The major purpose of the present work is to investigate the working performance of a cyclone dryer in paddy drying. Another purpose is to test the ability of a currently available commercial CFD code to predict the performance of this kind of dryer. The performance of the laboratory model dryer described in Chapter 4 was investigated experimentally using paddy grain and silica gel particles as drying materials. While paddy grain was the target material of this research it was difficult to get direct comparisons of experimental and numerical results due to the irregularities in shape of the paddy grain particles. The boundary conditions for wall impacts are particularly complex for paddy grain. Therefore, additional experiments with spherical silica gel particles were undertaken to provide closer agreement between the experimental and numerical models, because the silica gel particles approximate the spherical shape assumed in the CFX modeling. Details of the experimental conditions and the methods for performance investigation will first be described. The influences of key drying parameters such as inlet air temperature, particle feed rate, number of cyclone chambers, and material tested will then be reported.

The performance of a cyclone dryer is directly related to the changes of temperature and moisture content of air and solid particles during drying. These changes depend on both the air-flow pattern and the particle trajectories inside the drying chambers. Using the commercial CFD code CFX 5.7, the air-flow pattern as well as particle trajectories were calculated. This commercial code was first used to predict the single-phase air-flow pattern inside the cyclone dryer chambers as discussed in Chapter 5. The optimal single-phase model was then used to predict the particle trajectories from a one-way coupling procedure as detailed in Chapter 6. In the present chapter, the model will be further applied to predict the changes in temperature and humidity of both air and solid particles during drying by including the exchanges of mass, energy, and momentum in a two-way

coupling model. The mathematical details of this approach are given in Section 7.3.1. The mathematical model is used to investigate the effects of changes in various operating parameters such as the inlet air conditions, the particle feed rate and the number of chambers in the dryer. Finally, the results of numerical simulation are compared with experimental results.

In conclusion, the numerical and experimental results will be applied to estimate the performance of commercial scale cyclone dryers and make comparisons with the performance of other types of commercial paddy drying equipment.

7.2 EXPERIMENTAL STUDIES

7.2.1 Experimental Apparatus and Instrumentation

A schematic diagram of the cyclone dryer is shown in Figure 4.5. As described previously, it consisted of a centrifugal blower, an electrical heater, solid material hopper, rotary feeder, drying chambers, and separation chamber. The configuration was changed from three to four chambers by adding extra chamber. The hopper was used to hold solid material for the rotary feeder supply. The feed rates of material were controlled by a sliding plate installed between hopper and rotary feeder. The centrifugal blower was used to supply ambient air to an electrical heater. The heated air from electrical heater was used to both convey and dry the solid material.

The temperatures of drying air and paddy were measured by k-type thermocouples with an accuracy of $\pm 1^\circ\text{C}$. Thermocouples were positioned at the heater outlet and inlet, and outlet of the drying chamber to measure changes of air temperature during drying. One additional thermocouple was embedded at the cyclone outlet to measure the temperature of dried material in the separation chamber. Inlet and outlet air humidity were monitored by humidity probes (Testo 635 at inlet with an accuracy of $\pm 2\%$ RH, and Elektronik EE29 at outlet with an accuracy of $\pm 1\%$ RH). These were calibrated periodically with

wet/dry bulb thermometers in a wind tunnel. Air-flow rate was measured by observing the pressure drop across the inlet nozzle with a Furness FCO12-micromanometer accurate to $\pm 1\%$.

All measuring sensors were connected to a National Instruments data acquisition board (NI-4351) to record the data via LabView program on a personal computer. The data were recorded in text file format for further processing. The electrical power consumption of the heater was measured by a clamp-on current meter (Lutron DM 1000) with an accuracy of $\pm 1.2\%$. Drying material moisture content was determined by oven drying, and weighing of samples in an electronic balance with an accuracy of ± 0.0001 g. (as previously discussed in Chapter 6).

7.2.2 Experimental Procedure

The gas flow was set at a steady state value, usually by setting up fan motor converter frequencies of 42.5, 44.5 and 46.5 Hz. The current to the heater was then adjusted. The testing materials were then introduced into the gas stream by opening the sliding plate under the rotary feeder to predetermined levels from the calibration given in Chapter 6.

Once a steady state had been established, the air-flow rate was measured with a pressure tap at the bellmouth nozzle. The signals from all sensors connected to the NI 4351 data acquisition board were recorded at one-minute intervals for five minutes. The testing material at the inlet hopper and separation chamber outlet were sampled at the same time and subsequently dried in a hot air oven for moisture content determination. The experimental results at three levels of particle feed rate, fan motor converter frequency, and inlet air temperature for paddy and silica gel were then collected.

The data obtained enabled the calculation of heat and mass transfer rates as shown in subsequent sections. However, for calculation of heat and mass transfer coefficients, an average residence time of particles in the cyclone dryer was also required. Due to the difficulties of obtaining the residence time distributions during drying tests, the particle

residence time was estimated using correlations obtained from experiments described in Chapter 6. The residence times are principally a function of mass concentration.

7.2.3 Experimental Heat and Mass Transfer

The macroscopic heat transfer was calculated by measuring the gas and solid temperatures at both inlet and outlet of the cyclone dryer using method outlined by Silva et al. (1991). For solid particles of diameter d_p and density ρ_p with total contact area as between gas and solid particles in the cyclone dryer, the integral energy balance is expressed as

$$\dot{Q} = m_f (c_f + c_v W_i) \cdot \Delta T_f = h a_p (\Delta T)_m \quad (7.1)$$

where \dot{Q} is the heat transfer rate; m_f and m_p are the mass flow rates of air and particles; ΔT_f is the air temperature differential between inlet and outlet of the cyclone dryer given by $(T_{fi} - T_{fo})$; c_f and c_v are the specific heats of air and water vapour given by Eqs. (3.50) and (3.53); and h is the heat transfer coefficient between gas and solid particles. $(\Delta T)_m$ is the log-mean temperature differential, given by

$$(\Delta T)_m = \frac{(T_{fi} - T_{pi}) - (T_{fo} - T_{po})}{\ln \frac{T_{fi} - T_{pi}}{T_{fo} - T_{po}}} \quad (7.2)$$

where T_{fi} and T_{fo} are the air temperatures at inlet and outlet; T_{pi} and T_{po} are the particle temperatures at inlet and outlet. Assuming that the particles are spherical in shape, the contact area a_p can be expressed as (Silva et al., 1991)

$$a_p = \frac{m_p \cdot \tau}{\frac{\pi}{6} \rho_p d_p^3} \cdot \pi d_p^2 = \frac{6m_p \cdot \tau}{\rho_p d_p} \quad (7.3)$$

where τ is the average residence time of particles in the dryer. By substitution of Eq. (7.3) into Eq. (7.1), the heat transfer coefficient is formulated as

$$h = \frac{1}{6} \rho_p d_p (c_f + c_v W_i) \frac{\Delta T_f m_f}{\tau (\Delta T)_m m_p} \quad (7.4)$$

The moisture mass transfer rate between gas and solid can be expressed as

$$\dot{Q}_m = m_f (W_o - W_i) = m_p (M_i - M_o) = K_m a_p (\Delta W)_m \quad (7.5)$$

where M_i and M_o are the moisture contents of particles at inlet and outlet, W_i and W_o are the air humidities at inlet and outlet of the cyclone dryer, and K_m is the mean mass transfer coefficient. The log-mean humidity differential between the saturated particle surface and air, $(\Delta W)_m$, is defined by

$$(\Delta W)_m = \frac{(W_{sat} - W_i) - (W_{sat} - W_o)}{\ln \frac{W_{sat} - W_i}{W_{sat} - W_o}} \quad (7.6)$$

where W_{sat} is the humidity of air in the saturated state. By substituting Eq. (7.3) into Eq. (7.5), the mass transfer coefficient can be expressed as

$$K_m = \frac{1}{6} \rho_p d_p \frac{M_i - M_o}{\tau (\Delta W)_m} \quad (7.7)$$

The dimensionless forms of heat and mass transfer coefficients are defined as

$$Nu = \frac{h d_p}{\lambda} \quad \text{Nusselt number} \quad (7.8)$$

$$\text{and} \quad Sh = \frac{K_m d_p}{\rho_f D_{v-a}} \quad \text{Sherwood number} \quad (7.9)$$

where λ is the thermal conductivity of air given by Eq. (3.51) and D_{v-a} is the diffusivity of water in air calculated using the correlation given by Pakowski (1991). The heat and mass transfer coefficients can be calculated from the foregoing relations if the inlet and outlet temperatures and moisture contents of gas and solid particles in cyclone dryer are measured. The moisture reduction in the solid particles (MR) is calculated from

$$MR = M_i - M_o \quad (7.10)$$

The following section is devoted to detailed discussion of the experimental results. The moisture reduction will be evaluated and the dimensionless heat and mass transfer for three- and four-chamber cyclone dryer operation will be discussed.

7.2.4 Results and Discussion

Tables E.1 to E.4 of Appendix E show the experimental results for paddy and silica gel drying using three- and four-chamber cyclone dryer configurations. The results were obtained for different particle feed rates and inlet air temperatures. Three different particle feed rates were employed for each set of tests. The feed rates were 0.0289, 0.0411 and 0.0611 kg of dry paddy grain per second, and 0.0256, 0.0433 and 0.0585 kg of dry silica gel particles per second. The feed rate was adjusted using the sliding mechanism described in Chapter 6. The inlet air temperature was varied between 57 to 90°C. The initial moisture content was varied between 20.7 to 42.9 % of dry basis for paddy grain and 17.3 to 26.4 % of dry basis for silica gel particles. The moisture reduction, heat and mass transfer, and specific energy consumption figures deduced from the experimental observations will now be discussed.

7.2.4.1 Moisture reduction

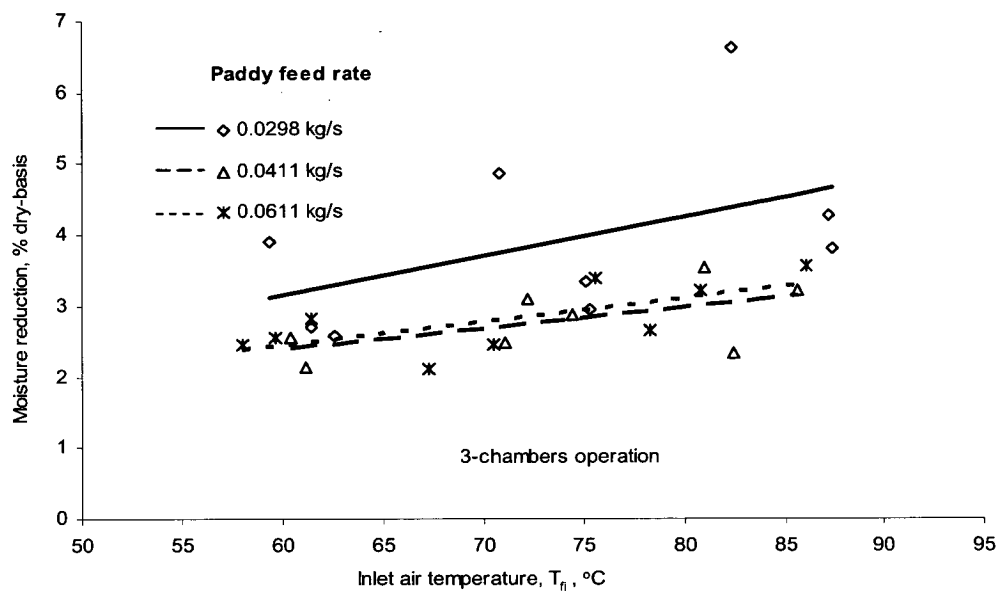
Figures 7.1 (a) and (b) show the variation of moisture reduction (MR) of paddy grain with inlet air temperature for different feed rates in three- and four-chamber cyclone dryer configurations, respectively. MR increases with inlet air temperature increase in all cases. A lower feed rate of material enables longer mean residence time of particles as discussed in Chapter 6, and hence more heat and mass exchange between the particles and air is obtained. Therefore, the MR generally decreases as the particle feed rate is increased at constant inlet air temperature. However, at medium and high feed rates with three-chamber operation, the moisture reduction does not differ significantly. Similar trends are observed for the silica gel particle drying results shown in Figures 7.2 (a) and (b).

A comparison of drying performance for three- and four-chamber operation is shown in Figures 7.3 (a), (b) and (c). MR increases with inlet air temperature, as discussed previously, but only a small, variable effect of the number of cyclone chambers on the MR is indicated. The experimental data are scattered around the same range. In Chapter 6, the mean particle residence time was found to be variably influenced by changing from three- to four-chamber operation. The drying results presented here are consistent with those observations.

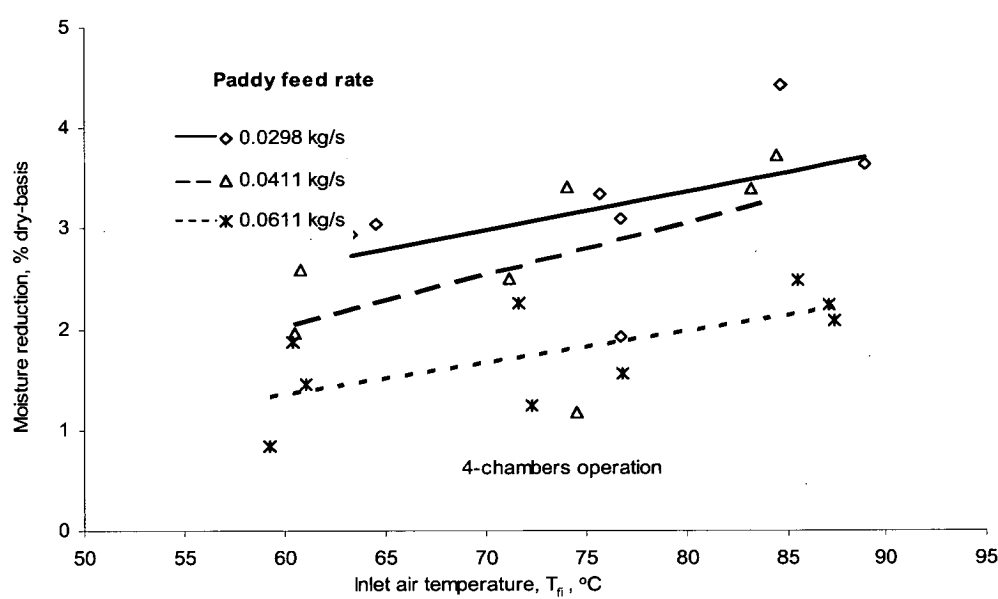
For approximately identical feed rates, the moisture reduction for silica gel particles exceeded that for paddy grain over the whole range of inlet air temperature. As indicated in Chapter 4, the heavier silica gel particles (larger diameter and higher density) spent more time in the cyclone dryer due to the dispersion and re-entrainment effects. The lighter paddy grain particles follow the air stream more closely, resulting in a lower residence time. The paddy grain and silica gel particles had almost the same mean particle diameter (3.25 mm for silica gel, 3.5 mm for paddy) but the higher density of silica gel particles results in longer residence times. This would give greater moisture reduction in the initial drying stage; but internal diffusivity would become an additional factor in the second (falling rate) drying stage.

7.2.4.2 Heat transfer

Figures 7.4 (a) and (b) summarise the experimental heat transfer data obtained at three levels of paddy feed rate for three- and four-chamber cyclone dryer operation, respectively. The dimensionless heat transfer (Nusselt number, Nu) is plotted against inlet air temperature (T_{in}). The results indicate consistent tendencies for Nu to decrease with increasing inlet air temperature. The same trends are observed for the silica gel drying results presented in Figures 7.5 (a) and (b). Nu decreases consistently with increases in particle feed rate for three-chamber operation. However, there is no clear trend for the influence of feed rate on Nu for four-chamber operation.



(a)



(b)

Figure 7.1 Variation of percentage of moisture reduction (MR) with inlet air temperature (T_{fi}) at different paddy feed rates: (a) three-chamber cyclone dryer; (b) four-chamber cyclone dryer.

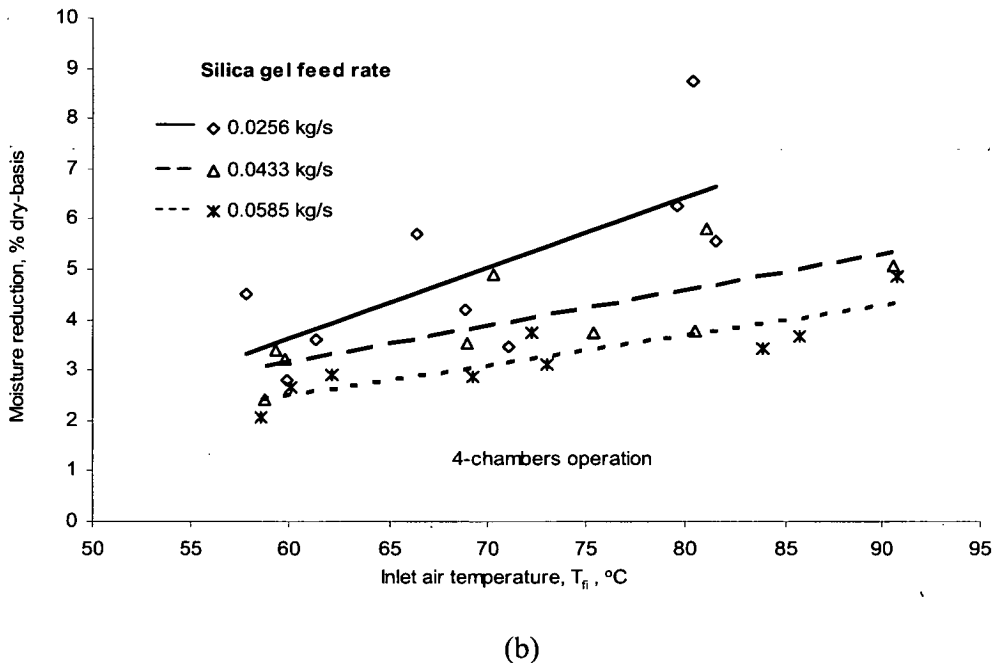
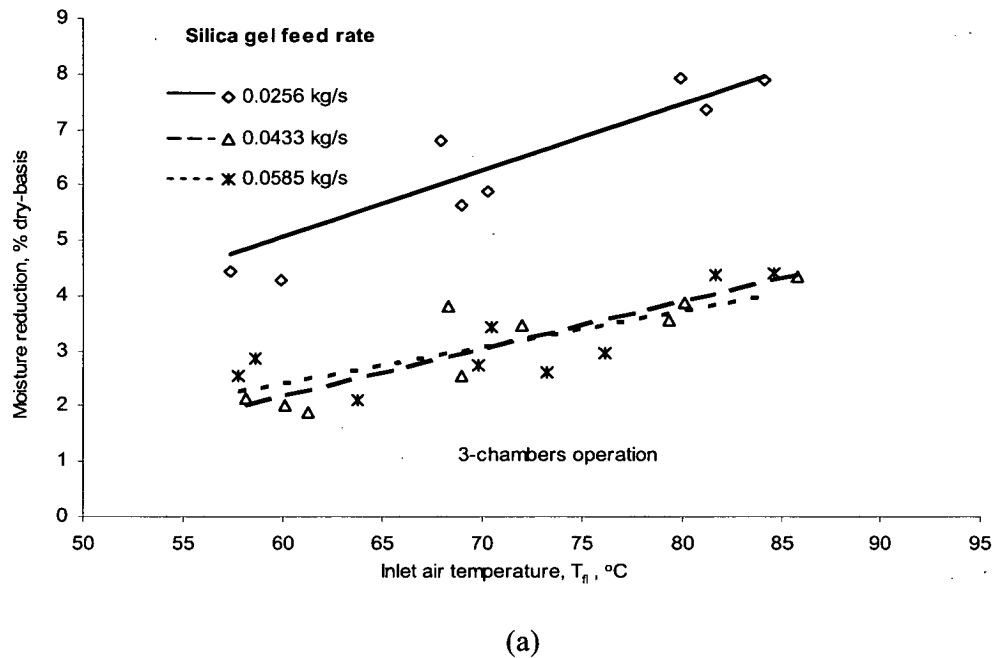
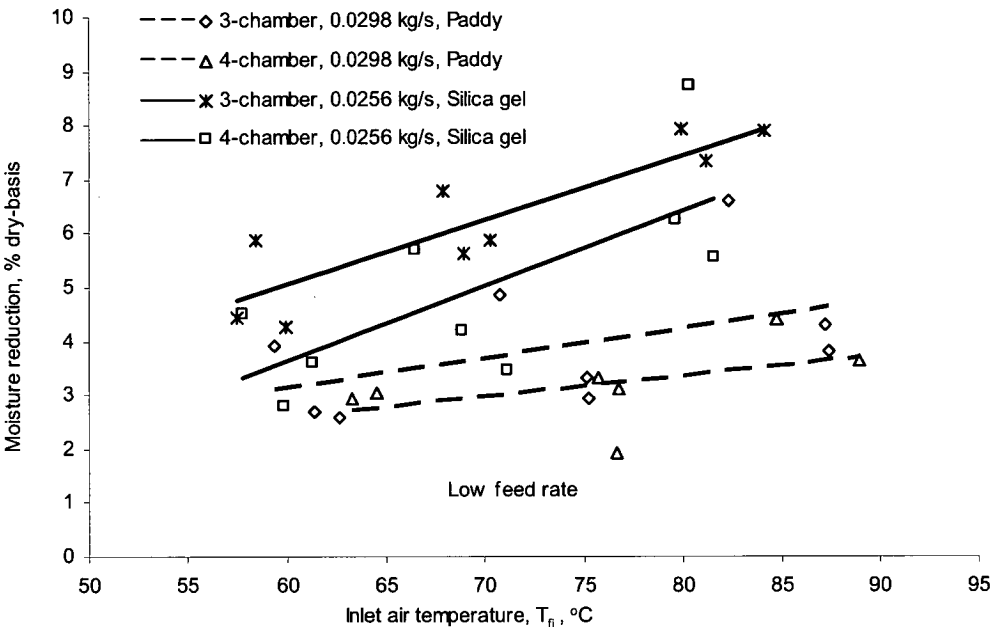
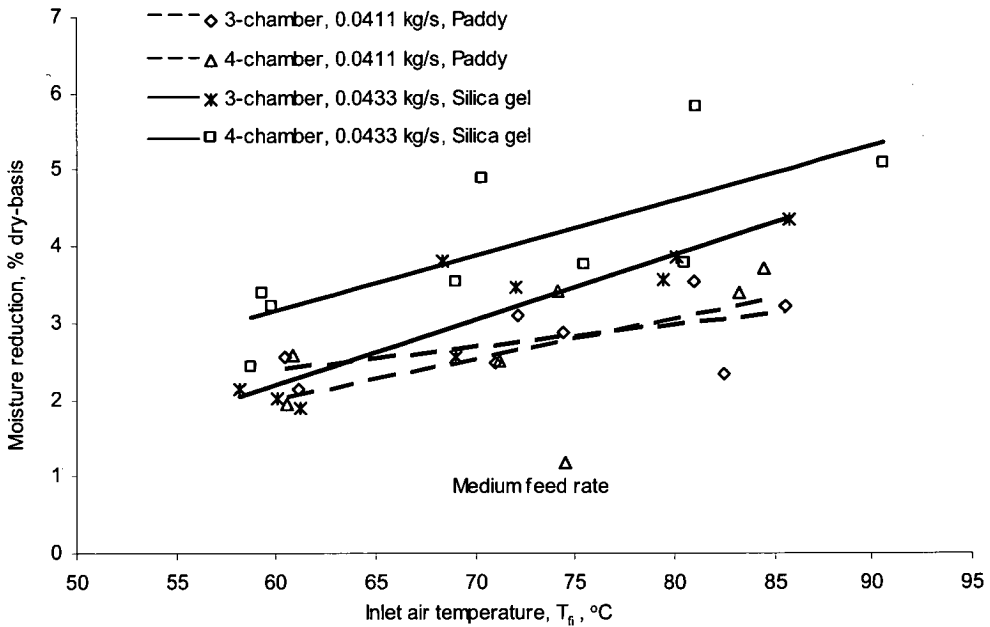


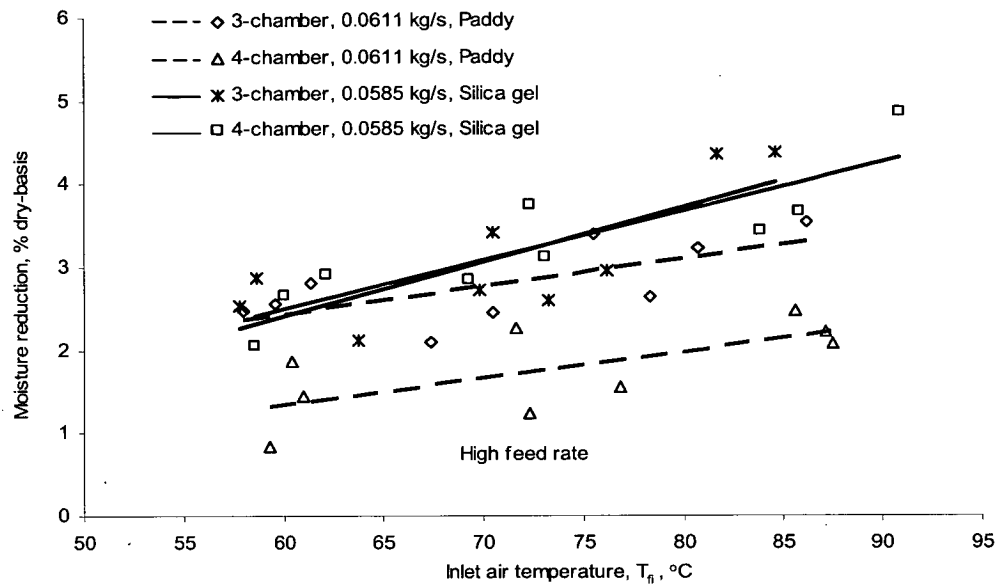
Figure 7.2 Variation of percentage of moisture reduction (MR) with inlet air temperature (T_{fi}) at different silica gel feed rates: (a) three-chamber cyclone dryer; (b) four-chamber cyclone dryer.



(a)



(b)

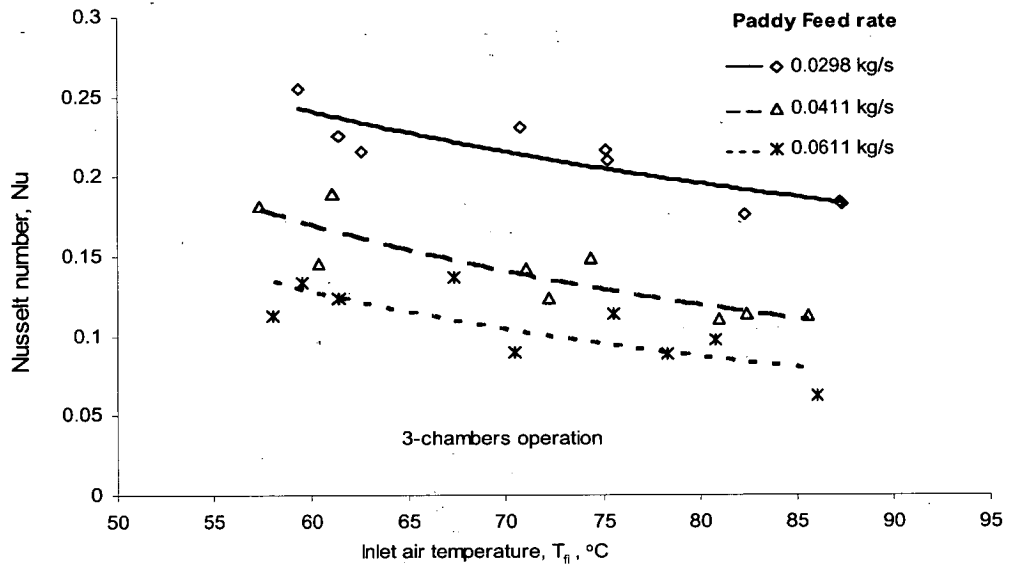


(c)

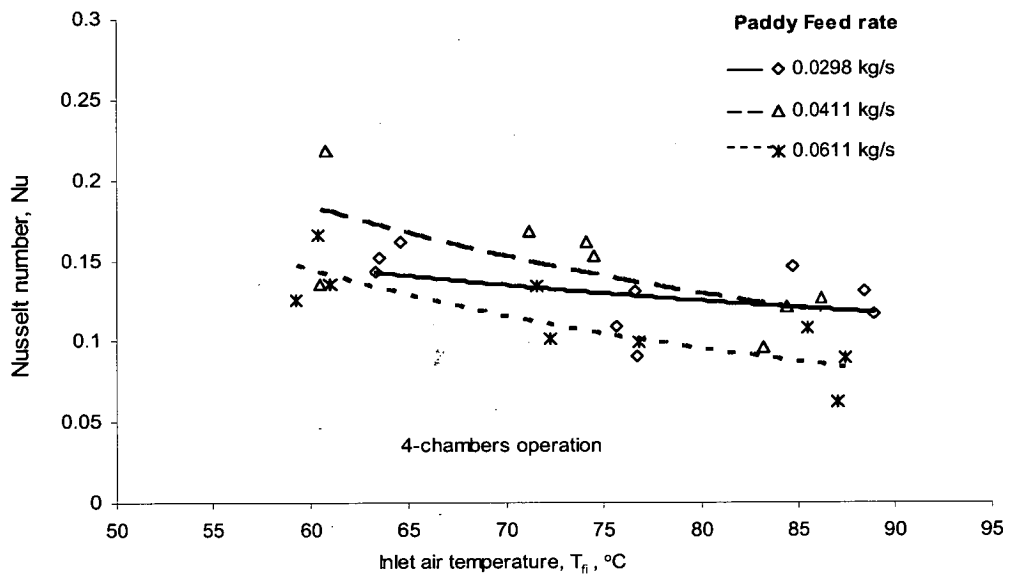
Figure 7.3 Comparison of moisture reduction (MR) for three- and four-chamber cyclone dryers at different feed rates: (a) low feed rate; (b) medium feed rate; (c) high feed rate.

The effects of particle feed rate on flow patterns in cyclone separators were studied by Yuu et al. (1978). The tangential velocity decreased noticeably when the particle feed rate increased, compared with single-phase air measurements. The turbulence intensity was lower for higher particle feed rates, thus giving lower gas-particle relative velocity and degree of mixing. Another reason for decreasing Nu with increasing feed rate is the greater heat transfer area (a_p). As seen from Eq. (7.4) the Nusselt number will decrease with increasing particle feed rate, provided that the temperature differential remains constant.

A comparison of heat transfer data for both paddy grain and silica gel particle drying is shown in Figure 7.6. This figure again shows the consistent trend for Nu to decrease with increasing inlet air temperature for both three- and four-chamber cyclone dryer operation. However, at the medium and high feed rates there is almost no effect of the number of cyclone dryer chambers on the Nusselt number.

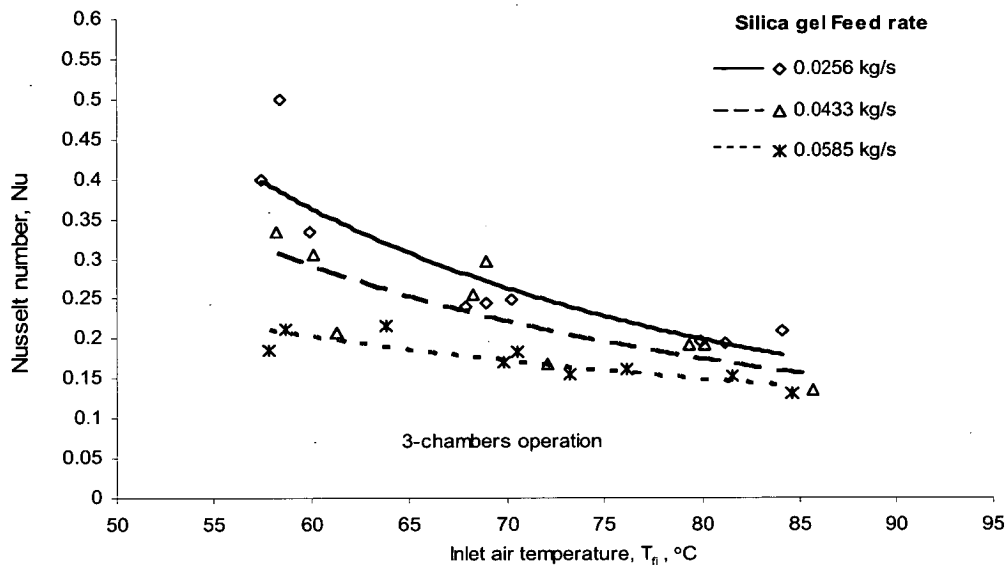


(a)

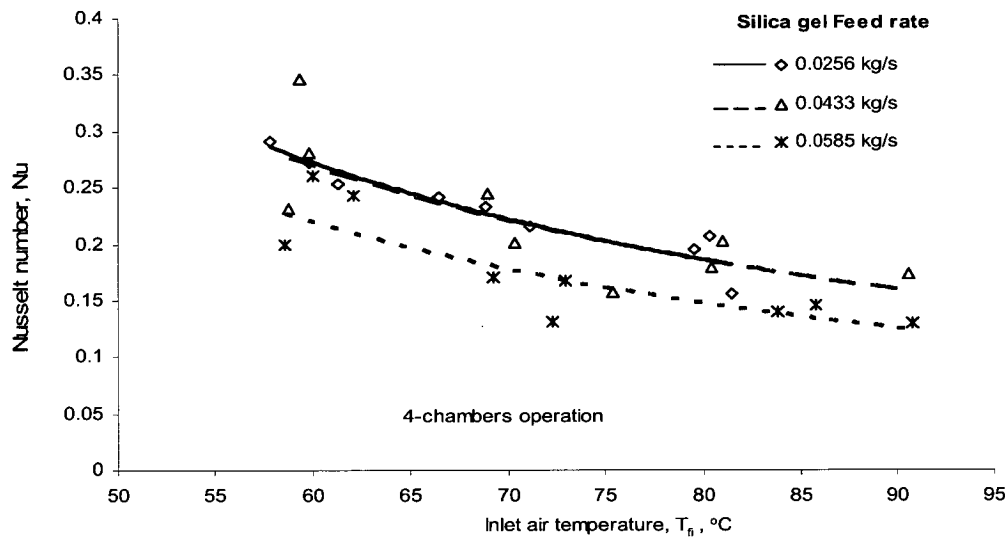


(b)

Figure 7.4 Variation of dimensionless heat transfer coefficient (Nu) with inlet air temperature for different paddy feed rates; (a) three-chamber cyclone dryer; (b) four-chamber cyclone dryer.

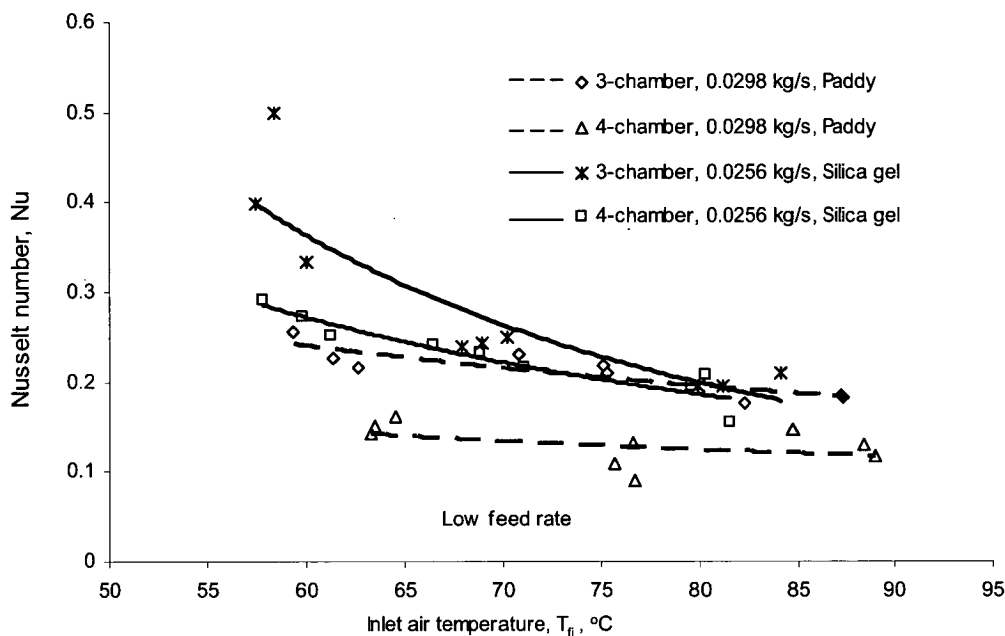


(a)

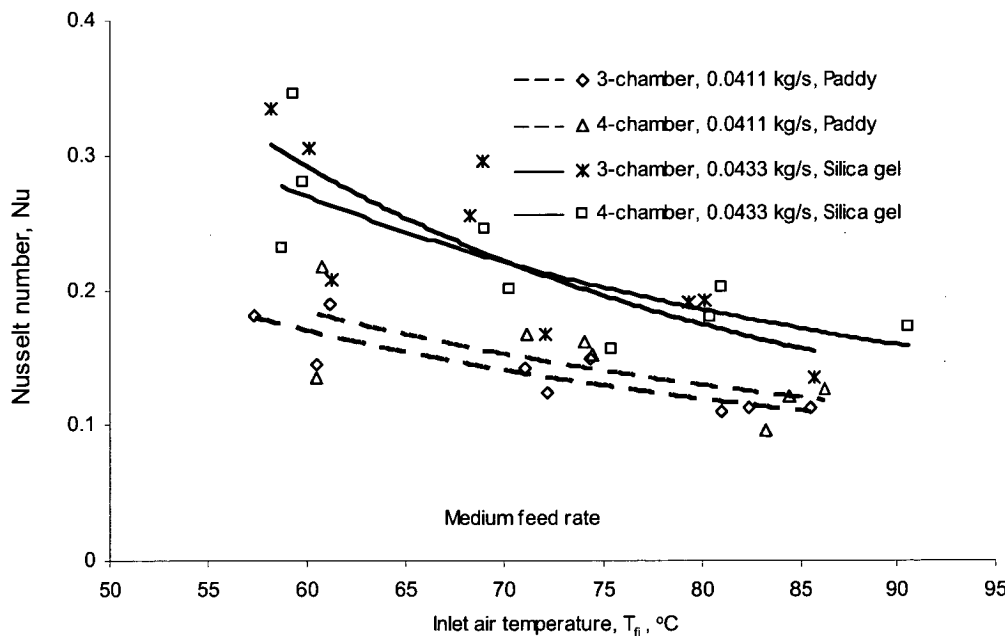


(b)

Figure 7.5 Variation of dimensionless heat transfer coefficient (Nu) with inlet air temperature for different silica gel feed rates: (a) three-chamber cyclone dryer; (b) four-chamber cyclone dryer.



(a)



(b)

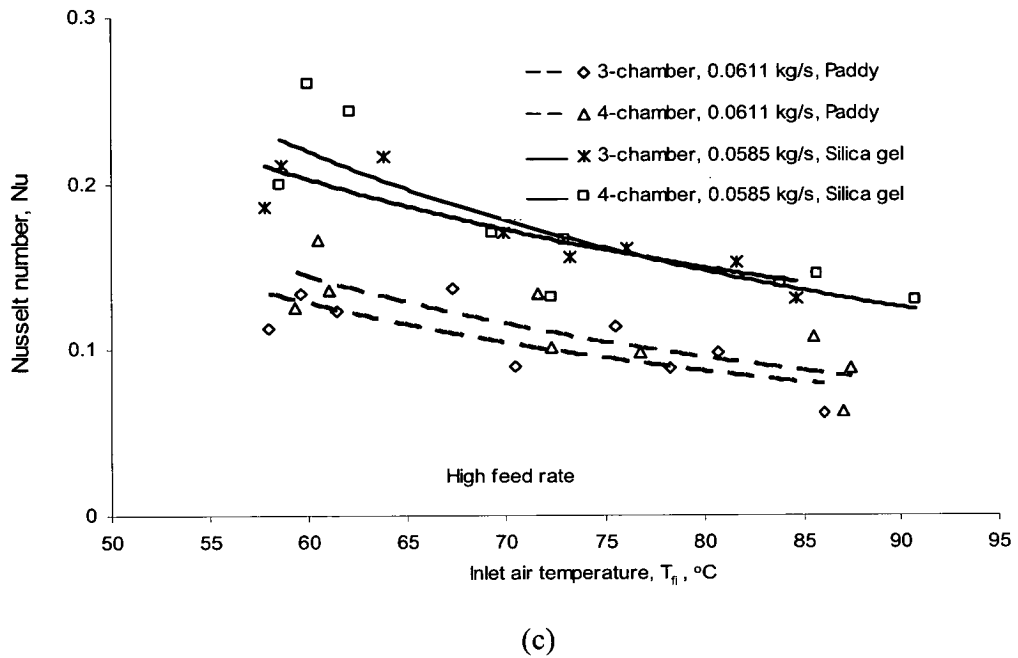
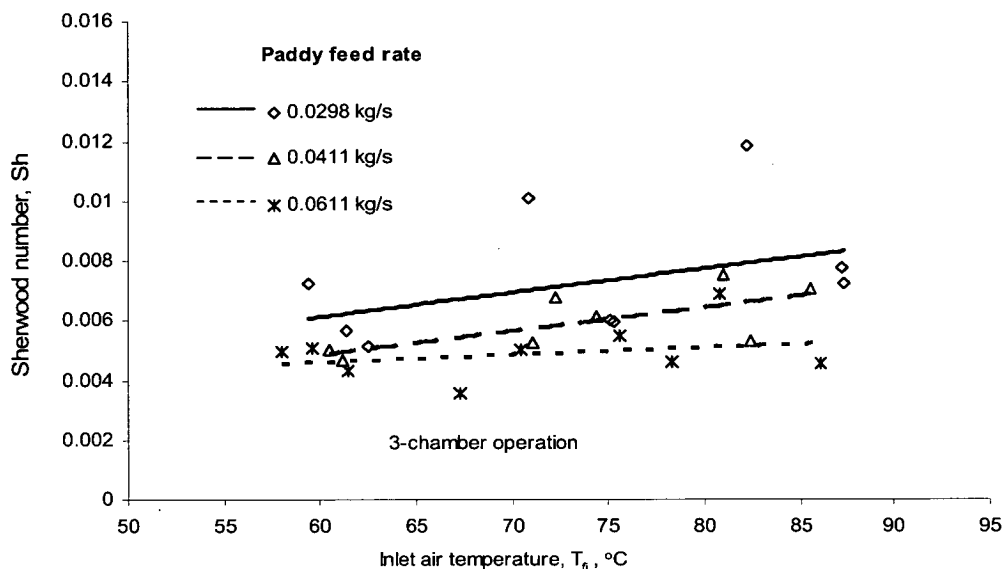


Figure 7.6 Comparison of dimensionless heat transfer coefficient (Nu) validation with inlet air temperature for three- and four-chamber cyclone dryer operation at different feed rates: (a) low feed rate; (b) medium feed rate; (c) high feed rate.

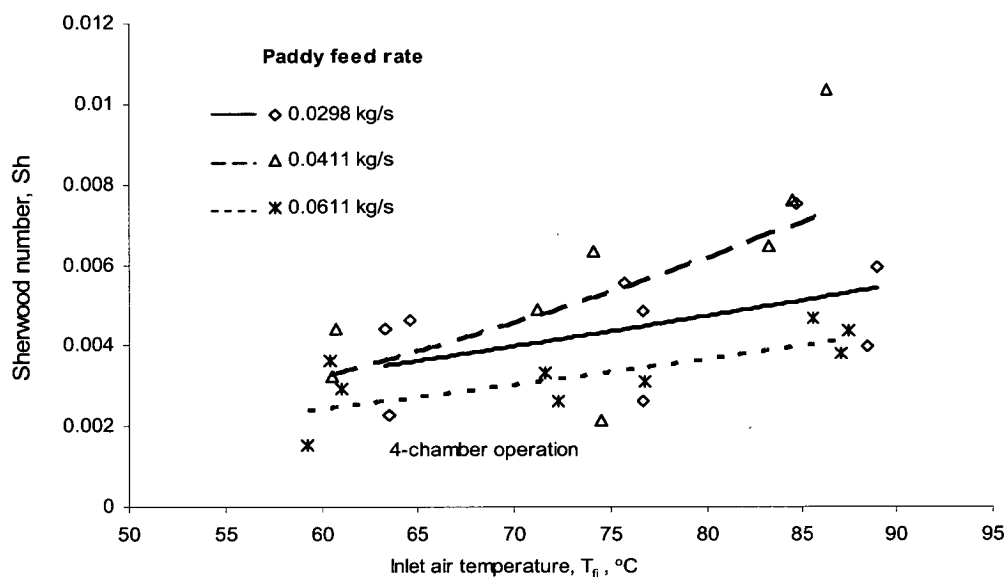
Nu values are scattered around the same range for these feed rates for both paddy grain and silica gel particle experiments. This may possibly be due to the suppression of turbulence at high particle feed rates as discussed above. Figure 7.6 also shows that at approximately identical feed rates, the values of Nu for silica gel particles were higher than for paddy grain over the whole temperature range tested.

7.2.4.3 Mass transfer

The variation of dimensionless mass transfer coefficient (Sherwood number, Sh) for paddy grain and silica gel particle drying is shown in Figures 7.7 and 7.8, respectively. These figures show the expected trend for mass transfer to increase with inlet air temperature at constant particle feed rate.

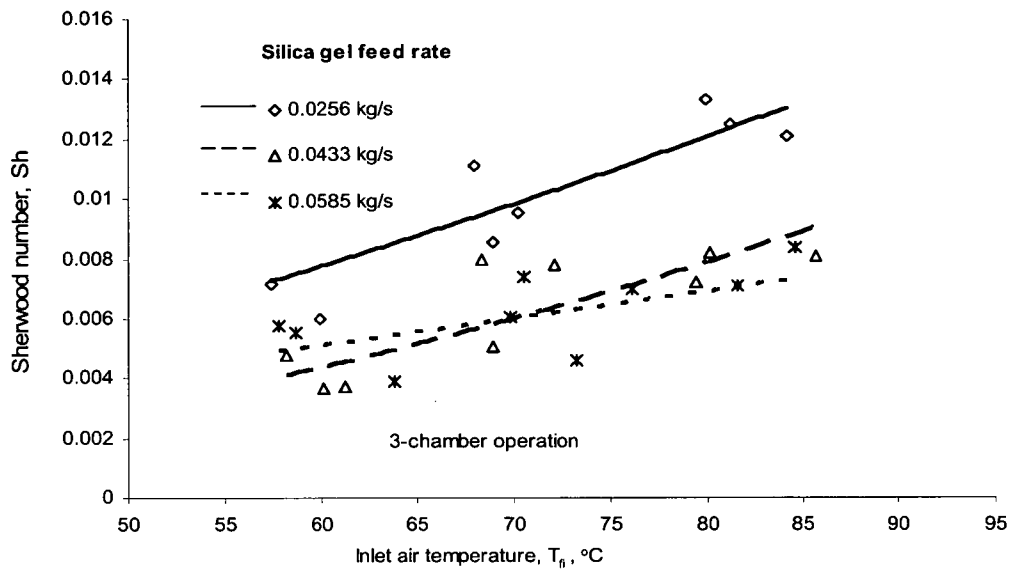


(a)

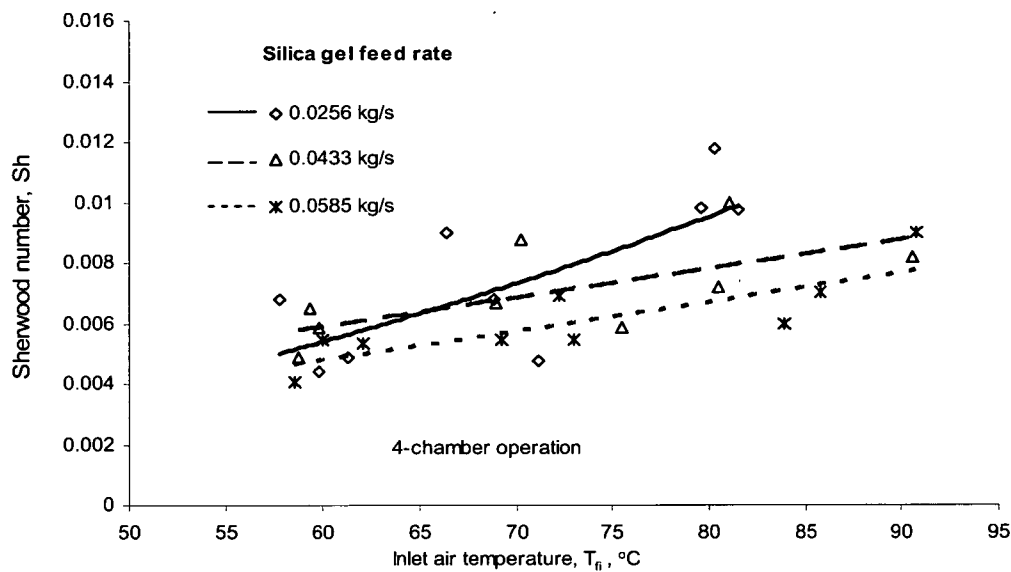


(b)

Figure 7.7 Variation of dimensionless mass transfer coefficient (Sh) with inlet air temperature for different paddy feed rates: (a) three-chamber cyclone dryer; (b) four-chamber cyclone dryer.

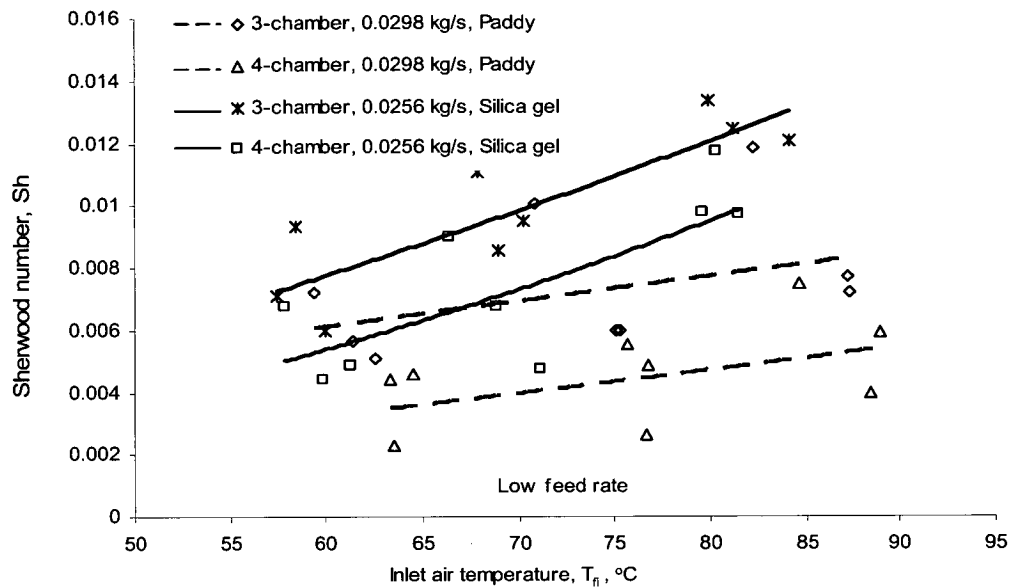


(a)

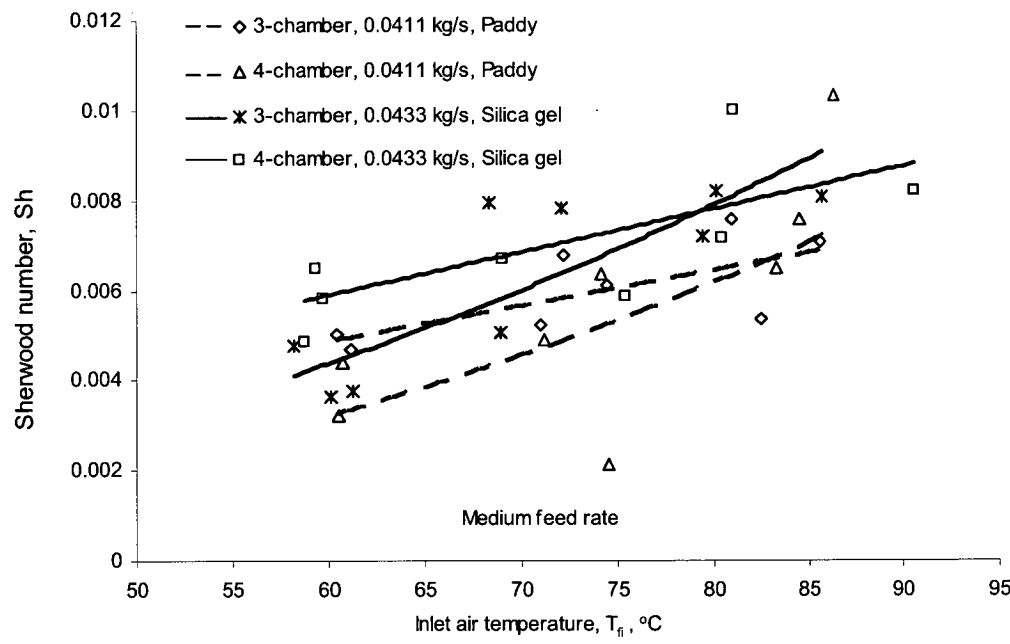


(b)

Figure 7.8 Variation of dimensionless mass transfer coefficient (Sh) with inlet air temperature for different silica gel feed rates: (a) three-chamber cyclone dryer; (b) four-chamber cyclone dryer.



(a)



(b)

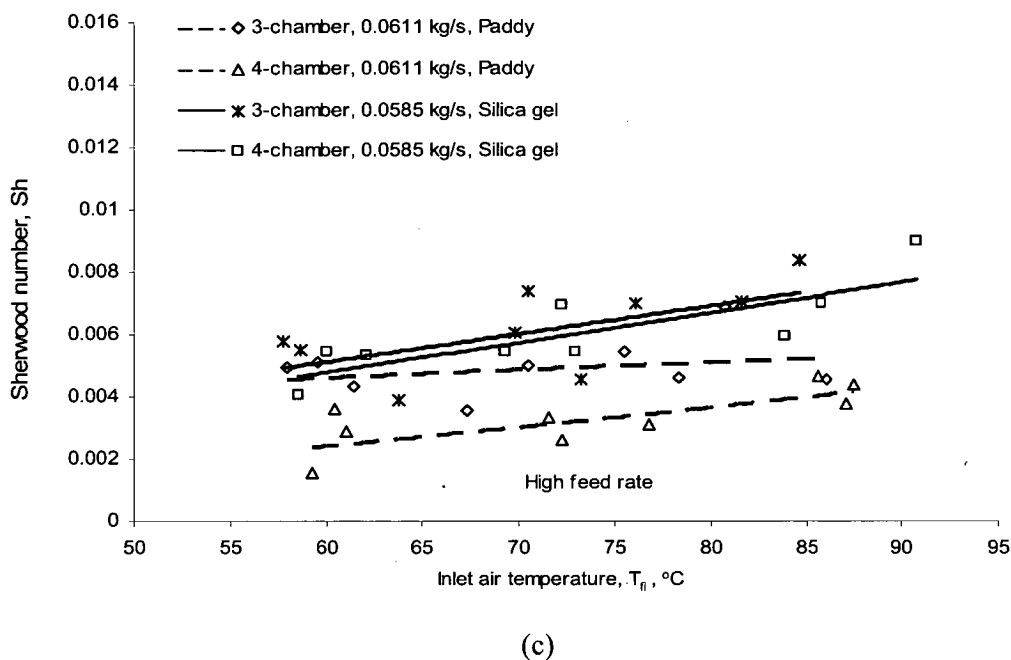
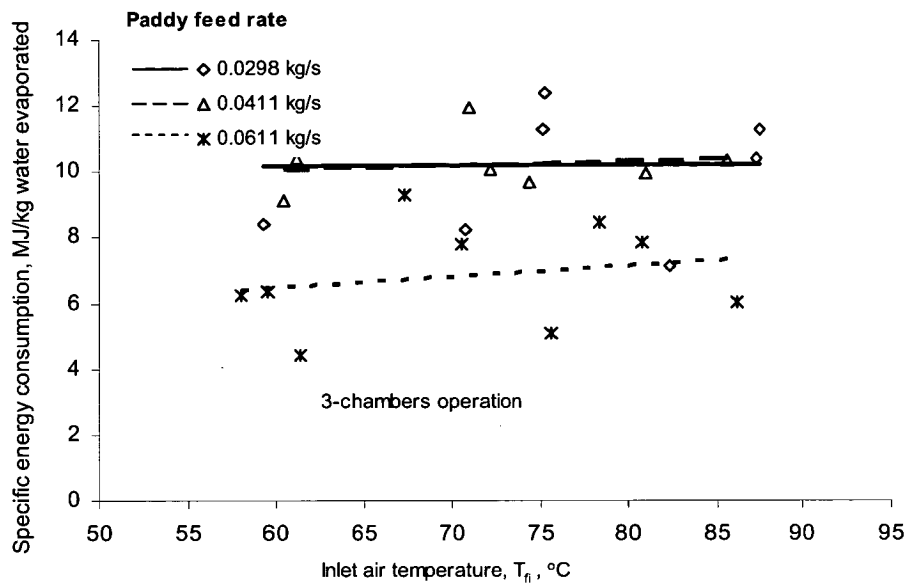


Figure 7.9 Comparison of dimensionless mass transfer coefficients (Sh) for paddy grain and silica gel particle drying: (a) low feed rate; (b) medium feed rate; (c) high feed rate.

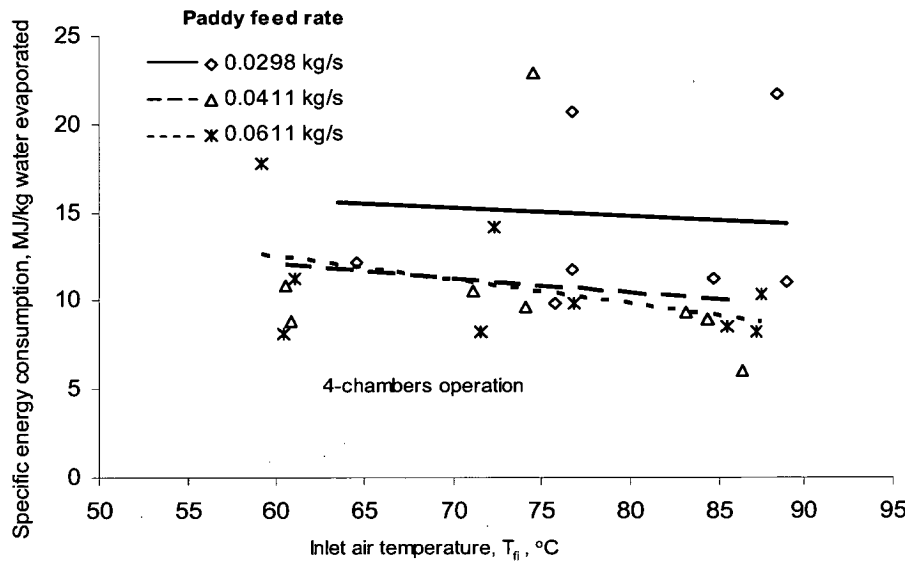
Increasing the particle feed rate decreases Sh at constant inlet air temperature. As shown in Figure 7.9, the values of Sh for silica gel particle drying are higher than for paddy grain over the entire range of particle feed rates. As with the heat transfer coefficient, the number of cyclone dryer chambers appears to have a rather variable influence on the mass transfer coefficient.

7.2.4.4 Specific energy consumption

The effects of inlet air temperature and particle feed rate on specific energy consumption for paddy grain and silica gel particle drying are shown in Figures 7.10 and 7.11, respectively. The specific energy consumption (SPEC) is defined as the total electrical energy consumption in the dryer system divided by amount of water evaporated. Values of SPEC are given in MJ/kg water evaporated.

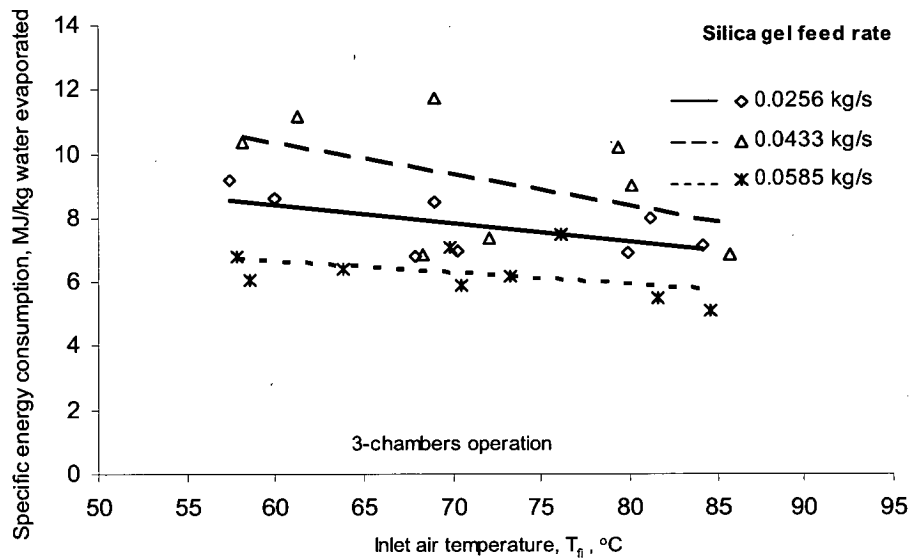


(a)

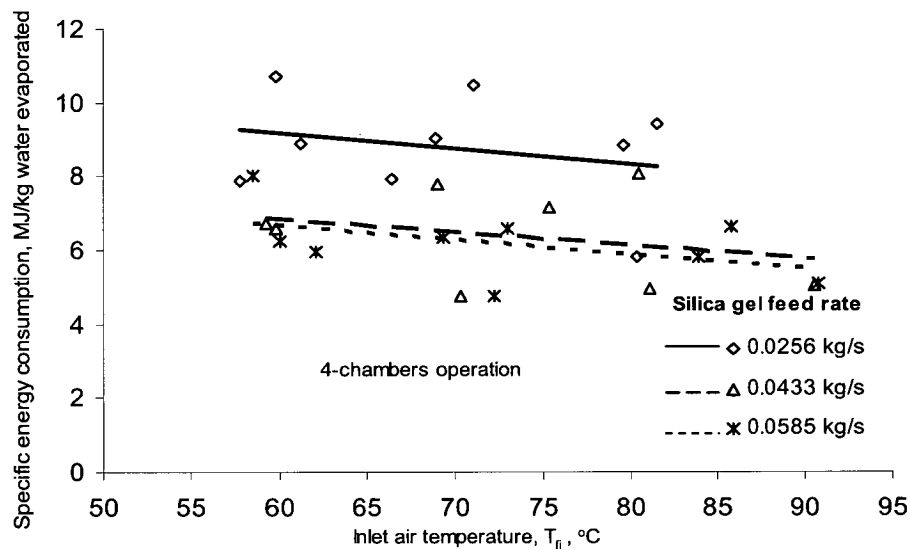


(b)

Figure 7.10 Variation of specific energy consumption (SPEC) with inlet air temperature at different paddy feed rates: (a) three-chamber cyclone dryer; (b) four-chamber cyclone dryer.

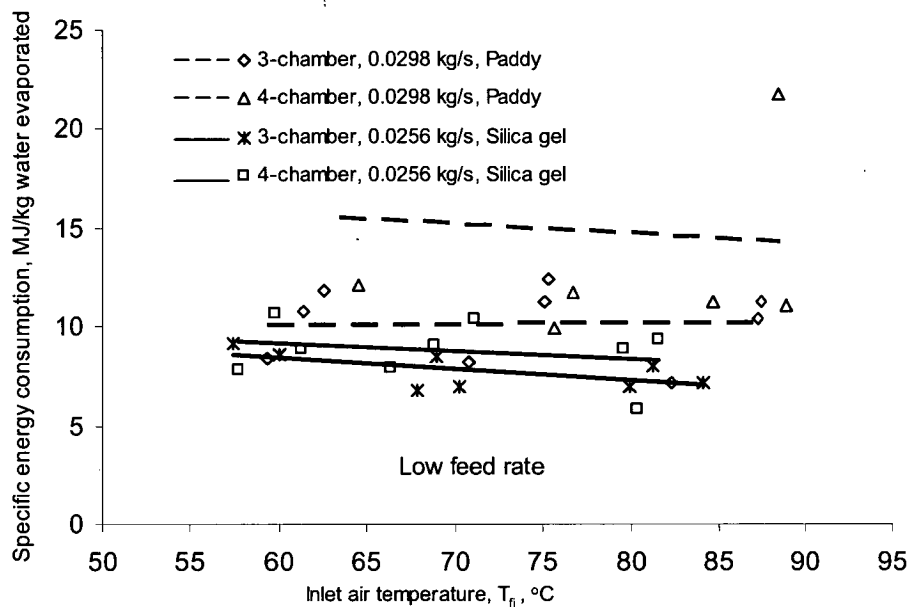


(a)

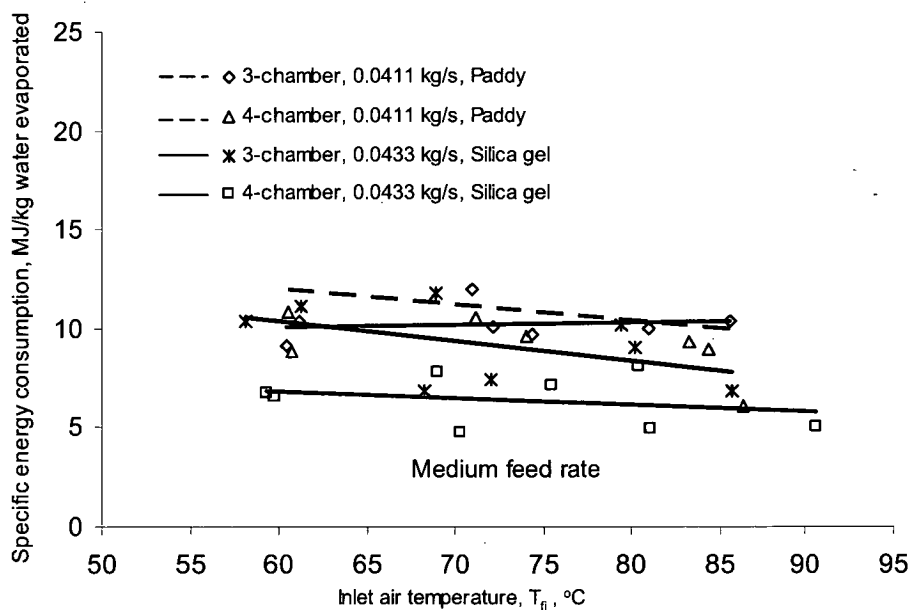


(b)

Figure 7.11 Variation of specific energy consumption (SPEC) with inlet air temperature at different silica gel feed rates: (a) three-chamber cyclone dryer; (b) four-chamber cyclone dryer.



(a)



(b)

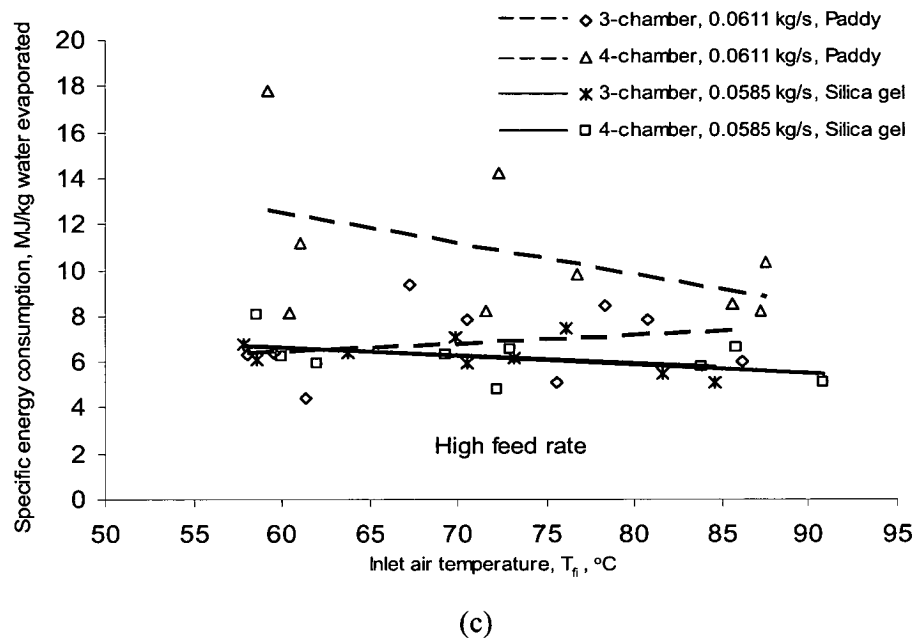


Figure 7.12 Comparison of specific energy consumption (SPEC) for paddy grain and silica gel particle drying: (a) low feed rate; (b) medium feed rate; (c) high feed rate.

Figure 7.10 indicates the SPEC for paddy grain drying to be essentially invariant with air temperature, but to decrease with increasing particle feed rate. There is a relatively large scatter in the SPEC results, especially for four-chamber operation. The SPEC for paddy grain drying is higher than for silica gel particles for all inlet temperatures with approximately identical particle feed rates, as shown in Figure 7.12.

For silica gel particle drying, the SPEC tends to decrease when inlet air temperature is increased at all feed rates, as shown in Figure 7.11. This is because the increased drying rate at higher air temperatures causes the energy consumed per unit of evaporated water to decrease.

Effects of initial moisture content of the drying material on SPEC are shown in Figure 7.13. This figure confirms the result that there were no conclusive effects of either particle feed rate or number of cyclone dryer chambers on the SPEC. SPEC tends to increase when the initial moisture content decreases for both silica gel and paddy drying

operations. Figure 7.13 indicates the SPEC for paddy drying to be consistently higher than for silica gel at a given initial particle moisture content over the whole range tested.

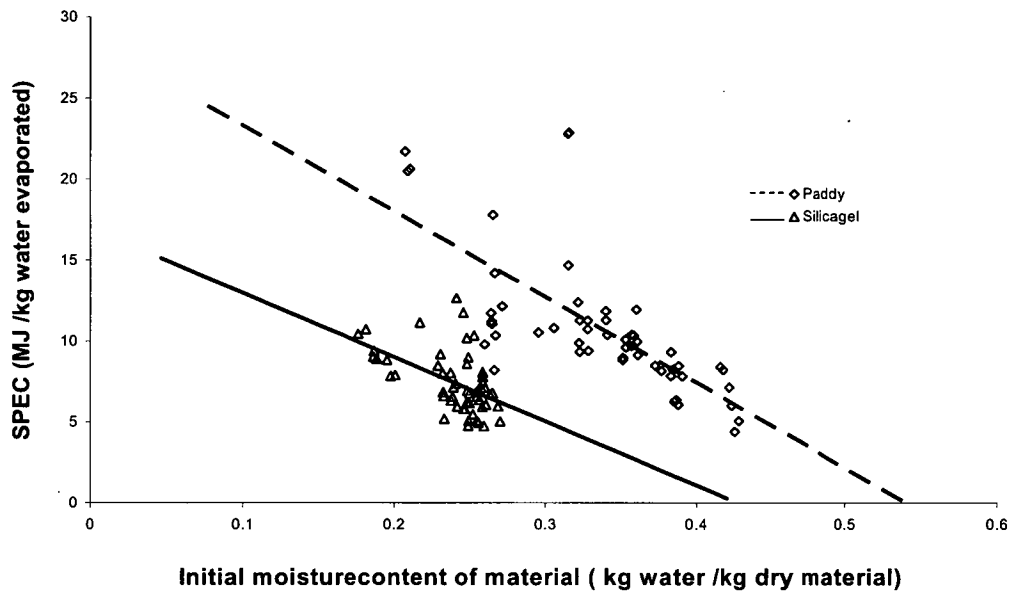


Figure 7.13 Influence of initial moisture content of particles on the SPEC.

7.2.4.5 Summary of experimental results for single pass drying and comparison with other paddy dryers

The present experimental results show that the moisture reduction increases with inlet air temperature at the same particle feed rate; and at the same inlet air temperature, the moisture reduction decreases when particle feed rate is increased. There is no clear trend for the influence of the number of cyclone chambers on moisture reduction. Higher moisture reductions are observed for silica gel particles due to their higher density, which results in higher particle residence times.

The dimensionless heat transfer coefficient (Nu) decreases when inlet air temperature and particle feed rate is increased. The presence of solids reduces the heat transfer between gas and solid due to depression of turbulence intensity and solid mixing inside

cyclone dryer. Values of Nu for three- and four-chamber cyclone dryers are almost the same in all cases.

The specific energy consumption decreases at higher inlet air temperatures for silica gel particle drying, but is not significantly affected by inlet air temperature for paddy grain drying. Higher inlet air temperatures give lower specific energy consumption. No definitive conclusions on specific energy consumption can be drawn concerning the effect of particle feed rate and the number of cyclone chambers.

Drying of paddy grain in these tests was conducted with three- and four-chamber cyclone dryer configurations with inlet air temperatures of 60-90 °C and paddy feed rates of 0.0298-0.0611 kg/s. The percentage of moisture reduction increases when the inlet air temperature is increased or the paddy feed rate is decreased. The maximum moisture reduction achieved was 2.6-6.5% dry-basis at inlet air temperatures of 82-89 °C and a paddy feed rate of 0.0298 kg/s. The specific energy consumption did not seem to differ with inlet air temperature or particle feed rate, but increased with the initial moisture content of the paddy grain as previously discussed.

Table 7.1 compares the working performance of the model cyclone dryer and other paddy dryers at approximately the same initial moisture content of paddy. This comparison shows that the moisture reduction of the model cyclone dryer is less than that of a commercial fluidised bed dryer. The specific energy consumption of the model cyclone dryer is also higher than industrial fluidised bed paddy dryers. Similar comparisons are obtained with commercial spouted bed dryers. The model cyclone dryer has a lower moisture reduction and higher specific energy consumption at about the same initial moisture content of paddy. The lower specific energy consumption for commercial fluidised bed and spouted bed paddy dryers is due to their larger scale, and their use of 50-70% of air recycling and higher inlet air temperatures. The model cyclone dryer has approximately the same moisture reduction and specific energy consumption as a commercial cross-flow dryer without air recycling at about the same inlet air temperature.

The experimental results indicate that single-pass drying of paddy in the model cyclone dryer did not achieve the target moisture reduction from 33% of dry-basis to 22% of dry-basis. This raises the question of how to achieve results of practical use with the multi-chamber cyclone dryer that are sufficiently energy efficient. The inlet air temperature can be further raised to increase the moisture reduction of paddy, but the experimental data indicate that this will have no effect on SPEC. In any case, the allowable inlet air temperature is severely limited by problems of adversely affecting grain quality. Increasing the number of cyclone chambers does not significantly increase the particle residence time, and only slightly increases the moisture reduction on a single pass drying.

Table 7.1 Comparison of working performance of the model cyclone dryer and commercial paddy dryers

No.	Dryer Type	Capacity Ton/h	T _{ai} °C	M _i % db.	M _o % db.	SPEC MJ/kg	Air Recycle (%)	Reference
1	Fluidised bed dryer	1.00	60.0	27.0	23.2	4.24	66	
	Cyclone dryer	0.20	59.3	26.6	24.5	17.75	0	Table E.2, test 22
2	Fluidised bed dryer	1.00	106.0	45.3	24.2	1.43	66	
	Cyclone dryer	0.10	8.3	42.2	35.6	7.14	0	Table E.2, test 9
3	Fluidised bed dryer	9.50	120.0	28.7	22.5	2.83	69	
	Cyclone dryer	0.15	71.2	29.6	27	10.52	0	Table E.2, test 11
4	Fluidised bed dryer	9.50	116.0	26.0	22.5	3.56	69	
	Cyclone dryer	0.20	76.8	26.0	24.5	9.80	0	Table E.2, test 20
5	Fluidised bed dryer	9.50	115.0	22.0	20.1	8.63	69	
	Cyclone dryer	0.10	76.7	21.0	19.1	20.64	0	Table E.2, test 8
6	Fluidised bed dryer	9.50	130.0	30.6	23	2.33	69	
	Cyclone dryer	0.15	60.5	30.5	28.6	10.81	0	Table E.2, test 10
7	Fluidised bed dryer	4.80	150.0	27.0	21	4.05	53	
	Cyclone dryer	0.10	88.9	26.5	22.8	11.06	0	Table E.2, test 6
8	Spouted bed dryer	3.20	154.0	29.4	25	3.96	60-70	
	Cyclone dryer	0.15	83.3	32.3	28.9	9.43	0	Table E.2, test 12
9	Spouted bed dryer	3.55	160.0	22.8	19	3.55	60-70	
	Cyclone dryer	0.10	76.7	21.0	19.1	20.46	0	Table E.2, test 8
10	Spouted bed dryer	2.40	159.0	25.0	19.7	5.70	60-70	
	Cyclone dryer	0.20	87.1	26.0	24.5	8.20	0	Table E.2, test 21
11	Cross flow dryer	7.00	71.0	21.8	17	22.46	0	
	Cyclone dryer	0.10	76.7	21.0	19.1	20.46	0	Table E.2, test 8

Thus, the only feasible option to remove large amounts of water in the model scale dryer is by multi-pass operation. Decrease of SPEC will require a high fraction of exhaust air

recycling, as employed in commercial fluidised bed and spouted bed dryers. Suitable strategies for paddy drying to remove large amounts of water with higher energy efficiency will be explored in detail in the next section.

7.2.5 Strategy for Paddy Drying with the Model Cyclone Dryer

A possible strategy for achieving a large amount of water removal with high energy efficiency in the model cyclone dryer is to use multi-pass drying and suitable arrangements for air recycling. Thus multi-pass drying of paddy grain in three- and four-chamber cyclone dryers was subsequently investigated in a final series of tests. The effect of air recycling on SPEC was investigated theoretically assuming adiabatic processes of drying and air mixing.

7.2.5.1 Characteristics of multi-pass drying in the model dryer

The multi-pass experiments for paddy grain drying were conducted at 46 Hz motor converter frequency, a high inlet air temperature of 75-85°C, 0.0298-0.0411 kg/s feed rate, and 26-29 % of dry-basis initial moisture content of paddy. The paddy was dried in three separate passes of the model dryer.

The results in terms of moisture reduction and specific energy consumption for each pass are shown in Tables 7.2 and 7.3 for three- and four-chamber cyclone dryers, respectively. Test data for initial and final moisture content, average inlet air temperature, average moisture content difference between inlet and outlet, and average specific energy consumption are shown in Table 7.4.

As shown in Tables 7.2 and 7.3, the paddy moisture content difference between inlet and outlet and specific energy consumption were almost the same for each drying pass for both three- and four-chamber operation. Moisture content was reduced by approximately 2.9% and 2.3% dry-basis in each drying pass for three-chamber operation with 0.0298 and 0.0411 kg dry paddy per second feed rates, respectively. Higher moisture reductions

of 3.9 % and 2.5% dry-basis per pass were obtained in four-chamber cyclone drying with 0.0298 and 0.0411 kg dry paddy per second feed rates.

Table 7.2 Results of multi-pass drying of paddy grain in a three-chamber cyclone dryer.

Test	Pass No.	m_p kg dry/s	T_{fi} °C	M_i % dry-basis	M_o % dry-basis	MR % dry-basis	SPEC MJ/kg-water
1	1	0.0298	77.9	28.1	25.1	2.97	15.3
	2	0.0298	83.0	25.1	22.0	3.15	15.1
	3	0.0298	84.2	22.0	19.2	2.71	19.1
2	1	0.0411	84.5	26.4	24.3	2.10	16.2
	2	0.0411	87.0	24.3	22.2	2.15	16.5
	3	0.0411	87.4	22.2	19.7	2.53	14.0

Table 7.3 Results of multi-pass drying of paddy grain in a four-chamber cyclone dryer.

Test	Pass No.	m_p kg dry/s	T_{fi} °C	M_i % dry-basis	M_o % dry-basis	MR % dry-basis	SPEC MJ/kg-water
3	1	0.0298	84.5	29.0	25.3	3.67	13.3
	2	0.0298	86.8	25.3	20.7	4.67	10.3
	3	0.0298	85.2	20.7	17.4	3.28	14.6
4	1	0.0411	80.0	27.9	25.5	2.37	14.4
	2	0.0411	84.4	25.5	23.0	2.45	14.3
	3	0.0411	84.8	23.0	20.3	2.76	12.7

Table 7.4 Overall average values for multi-pass paddy drying tests.

Test	m_p kg dry/s	T_{fi} °C	$M_{initial}$ % dry-basis	M_{final} % dry-basis	MR % dry-basis	SPEC MJ/kg-water
1	0.0298	81.7	28.1	19.2	2.94	16.5
2	0.0411	86.3	26.4	19.7	2.26	15.6
3	0.0298	85.5	29.0	17.4	3.87	12.7
4	0.0411	83.0	27.9	20.3	2.52	13.8

Average SPEC decreased when the number of chambers was increased. During the three-chamber cyclone dryer tests, the average SPEC values were 16.5 and 15.6 MJ/kg of water evaporated using 0.0298 and 0.0411 kg dry paddy per second feed rates, respectively.

Lower SPEC values of 12.8 and 13.8 MJ/kg of water evaporated were obtained for the four-chamber cyclone dryer using 0.0298 and 0.0411 kg dry paddy per second feed rates.

It is concluded from these tests that the desired moisture reduction of approximately 11% dry-basis from 33% to 22% dry-basis could be achieved in the model dryer by three passes of drying in a four-chamber cyclone dryer using approximately 80°C inlet air temperature and 0.0298 kg dry paddy per second of feed rate (Test condition 3).

7.2.5.2 Predicted effect of air recycling

Although sufficient moisture removal could be achieved by three-pass drying using the model four-chamber cyclone dryer, the energy efficiency is the most important factor in practical dryer performance. The single-pass and multi-pass drying tests show the SPEC of the model cyclone dryer to be higher than that of industrial fluidised bed and spouted bed dryers with approximately the same initial moisture content of paddy grain. This is due to the air recycling of 50-70% used in industrial dryers. Hence the effects of exhaust air recycling on SPEC need to be explored to improve the energy efficiency of the model cyclone dryer.

To investigate the effects of air recycling on SPEC, the results of first-pass drying in each multi-pass test are used as case studies. The following assumptions are made:

1. Drying and air mixing processes are assumed to be adiabatic.
2. The temperature and mass flow rates at the cyclone inlet are assumed to be the same, to maintain the thermal and fluid dynamic similarity of the cyclone dryer operation.
3. The influence of moisture content of air on the flow field inside the cyclone dryer is neglected.
4. No heat loss to the surroundings.
5. Effects of the blower on the inlet air conditions are neglected.

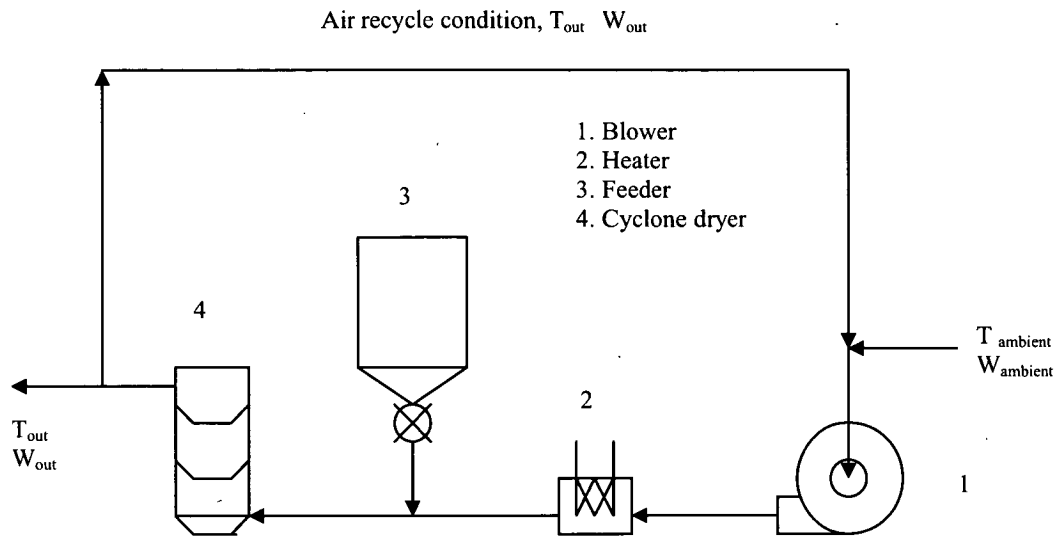


Figure 7.14 Schematic diagram of cyclone dryer with air recycling system.

Figure 7.14 shows a schematic diagram of a cyclone dryer with air recycling. The moisture content is the same at the inlet of the heater and the cyclone dryer. The amount of water evaporated is the same as in operation without recycling. The total enthalpy of solid and gas phases at inlet and outlet of cyclone dryer is the same due to the adiabatic assumption. The moisture content of air at outlet is the summation of moisture content at inlet and water evaporated inside the dryer. An initial value of moisture content of air after mixing is assigned. Then the fraction of air recycled to give the same value of moisture content at the heater inlet is calculated from the adiabatic air mixing process between ambient and outlet air from cyclone dryer. The value of moisture content at the mixing condition is varied corresponding to fractions of recycled air from 10% to 90%. The amount of energy required to heat up the incoming air is calculated from the difference between the enthalpies of enthalpy of air at the mixing point and the cyclone dryer inlet. Finally, the SPEC values are obtained.

Figure 7.15 shows the computed influence of moisture content at the mixing condition on the variation of SPEC and fraction of air recycling required. The results indicate that SPEC should increase, while the fraction of recycled air should decrease with increasing mixing moisture content until they are not significantly changed at 0.045-0.05 kg

water/kg dry air of mixing moisture content. This corresponds to a 90% fraction of air recycled. Further increase in the fraction of air recycled greatly increases the required mixing moisture content and produces little further reduction of SPEC. Therefore, the mixing moisture content should be limited at this value, which gives a maximum effective air recycling fraction of 90%.

Figure 7.16 shows the predicted variation of SPEC with the fraction of air recycled. The SPEC decreases linearly as the fraction of air recycled is increased. At 90% fraction of air recycled, the percentage of reduction of SPEC for all cases studies (data from the first-pass drying of each multi-pass drying test) is between 70-75% of the non-recycled air drying SPEC. It varies between 3.5-4 MJ/kg water evaporated. This is comparable to the fluidised bed paddy dryer performance at approximately the same initial moisture content of paddy grain (as shown in comparison no. 1, 4 and 7 of Table 7.1).

7.2.5.3 Summary of paddy drying strategy in the model scale cyclone dryer

The strategy for practical paddy drying using the model cyclone dryer has been examined. The aim was to remove a sufficient large amount of water from paddy grain (around 11% dry-basis difference) with high energy efficiency. The inlet air temperature could not be further increased due to adversely effects on paddy grain quality. The only feasible strategy was to use multi-pass drying to achieve the require amount of water removal. To maximize energy efficiency exhaust air recirculation is required, as employed in commercial fluidised bed and spouted bed dryers. The effect of air recycling on SPEC was investigated theoretically. The most efficient paddy drying strategy in the model scale cyclone dryer was determined to be follows:

1. Use of three-pass drying in a four-chamber cyclone dryer at inlet air temperatures of about 80°C with 0.0298 kg/s paddy grain feed rate. This can reduce the moisture content of paddy grain by approximately 11% dry-basis, with SPEC of 13 MJ/kg water evaporated with no air recycling.

2. Implement 90% air recycling to give 70-75% reduction of SPEC compared to non-recycled air operation. The SPEC should then vary between 3.5-4 MJ/kg water evaporated. This range of SPEC is comparable to commercial fluidised bed paddy dryer operation at approximately the same initial moisture content of paddy grain.

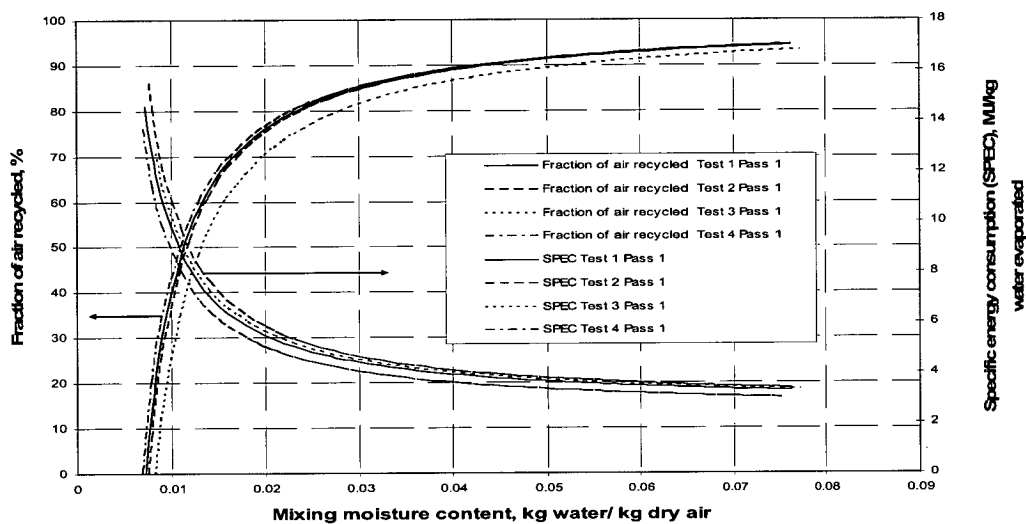


Figure 7.15 Influence of mixing moisture content on fraction of air recycled and SPEC.

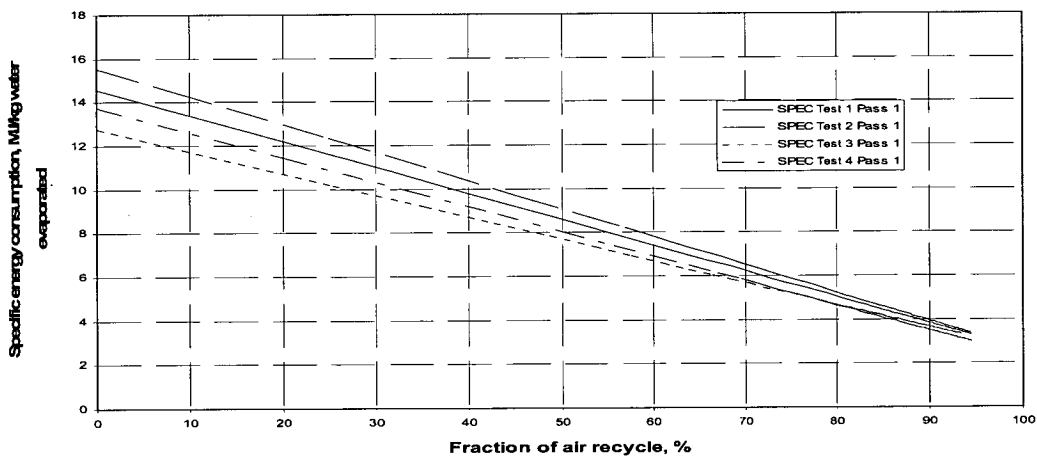


Figure 7.16 Variation of SPEC with fraction of air recycled.

7.3 NUMERICAL STUDIES

The numerical study described in this section aims to evaluate the usefulness of a commercial CFD code for predicting the drying process inside a cyclone dryer. In Chapter 5, CFX 5.7 was used to predict the single-phase flow field inside the cyclone dryer. The RNG $k-\varepsilon$ turbulence model combined with a second order accurate differencing scheme gave an acceptable result for the flow field simulation without particles present. In Chapter 6, the particle phase was added and the model was used to predict the residence time of the particles. As discussed in Chapter 6, better agreement between the shapes of residence time distribution obtained from numerical and experimental results was obtained by using a numerical model without turbulence dispersion for both silica gel particles and paddy grain. This model provided a reasonable qualitative prediction of trends, and a quantitative prediction of mean particle residence time with the correct order of magnitude. However, as seen from Table 6.4, the predicted mean residence times varied between 18 and 74% of those observed experimentally. The lack of particle-particle and particle-fluid interactions in this earlier modelling undoubtedly contributed to the quantitative discrepancies observed.

The following treatment uses a more advanced Lagrangian/Eulerian approach that takes into account mass, momentum and energy transfer between the particulate and continuous phases to describe the drying process in the cyclone dryer. The computational fluid dynamics study was carried out to compare the gas flow, temperature and humidity patterns, as well as the trajectories of silica gel particles in three- and four-chamber cyclone dryers. Although the complex transport phenomena occurring in the cyclone dryer cannot yet be modelled with high accuracy, the CFD results are nevertheless a useful guide to further improve the design and operation of cyclone dryers.

In the next section, the conservation equations of the particulate and continuous phases are modified to include the two-way coupling effects. The numerical results obtained using the commercial code CFX 5.7 for some experimental conditions are presented in

the subsequent section. The final section compares the numerical and experimental results.

7.3.1 Mathematical Model

7.3.1.1 Governing conservation equations for the continuous phase

The flow patterns were calculated by solving the steady state three-dimensional equations for continuity, momentum and energy. The continuity and momentum equations in Chapter 5 were rewritten to add a source term for the mass and momentum of the particulate phase. The resulting equations for continuity, momentum and energy are:

$$\nabla \bullet (\rho_f \mathbf{u}) = S_{MS} \quad (7.11)$$

$$\nabla \bullet (\rho_f \mathbf{u} \otimes \mathbf{u}) = -\nabla P + \nabla \bullet (\mu_{\text{eff}} (\nabla \mathbf{u} + (\nabla \mathbf{u})^T)) + S_M \quad (7.12)$$

$$\nabla \bullet (\rho_f \mathbf{u} h'_{\text{tot}}) = \nabla \bullet (\lambda \nabla T) + S_E \quad (7.13)$$

where S_{MS} is a mass source term, S_M is a momentum source and S_E is an energy source. Turbulent flux terms, $(-\rho_f \overline{\mathbf{u}' \otimes \mathbf{u}'})$ and $(-\rho_f \overline{\mathbf{u}' h'})$ are added to the right hand side of the Equations (5.2) and (5.3), respectively. These terms are modelled by using an eddy viscosity (μ_t) and eddy diffusivity (Γ_t) as follows:

$$-\rho_f \overline{\mathbf{u}' \otimes \mathbf{u}'} = \mu_t (\nabla \mathbf{u} + (\nabla \mathbf{u})^T) - \frac{2}{3} \rho_f k \mathbf{I} - \frac{2}{3} \mu_t \nabla \cdot \mathbf{u} \mathbf{I} \quad (7.14)$$

$$-\rho_f \overline{\mathbf{u}' h'} = \Gamma_t \nabla h' \quad (7.15)$$

where the eddy diffusivity can be defined as function of eddy viscosity

$$\Gamma_t = \frac{\mu_t}{Pr_t} \quad (7.16)$$

Here k is the turbulence kinetic energy, \mathbf{I} is the Kronecker delta, and Pr_t is the turbulent Prandtl number. The eddy viscosity is obtained using the RNG $k - \varepsilon$ turbulence model as described in Chapter 5.

7.3.1.2 Governing equations for the dispersed phase

Based on the solution obtained for the continuous phase, the Lagrangian/Eulerian approach was used to calculate the particle trajectories. The governing equation for the dispersed phase is the BBO equation described in Chapter 3. Interactions between particles were neglected. The BBO equation describes the force balance on a particle by considering only the dispersed phase inertia, the aerodynamic drag force, and the gravity force. Details of the BBO equation, inertia force evaluation, aerodynamic force evaluation, and numerical integration procedure were discussed previously in Chapter 3. The particle sources in the fluid phase momentum equations were obtained by solving a transport equation for the sources. From the BBO equation, the equation for the momentum source is expressed as

$$\frac{dS_M}{dt} = \frac{1}{8} \pi \rho_f d_p^2 C_D |v_f - v_p| (v_f - v_p) \quad (7.17)$$

7.3.1.3 Heat and mass transfer

In general, the moisture transfer between the continuous and particulate phases during the constant drying rate period is assumed to satisfy the equation (CFX 5.7 manual: Solver theory)

$$\frac{dm_w}{dt} = \pi d_p \rho_f D Sh(r_p - r_f) \quad (7.18)$$

where m_w is the mass of water in the particle, r_p and r_f are the fractions of mass in the particulate and continuous phases, $\rho_f D$ is the diffusivity of the mass fraction in the continuous phase, and Sh is the Sherwood number given by

$$Sh = 2 + 0.6 Re^{0.5} \left(\frac{\mu}{\rho_f D_{v-a}} \right)^{\frac{1}{3}} \quad (7.19)$$

The rate of temperature change is governed by two physical processes: sensible heat transfer and latent heat transfer associated with mass transfer of water. The equation of energy balance is given by

$$m_p c_p \frac{dT_p}{dt} = \pi d_p \lambda Nu (T_f - T_p) + h_{fg} \frac{dm_w}{dt} \quad (7.20)$$

where T_f is the gas temperature, m_p and c_p are respectively the mass and heat capacity of the particles, λ is the thermal conductivity of the gas, and h_{fg} is the latent heat of vaporisation of the liquid water. The Nusselt number (Nu) is calculated from

$$Nu = 2 + 0.6 Re^{0.5} \left(\frac{\mu c_p}{\lambda} \right)^{\frac{1}{3}} \quad (7.21)$$

7.3.2 Modelling Set up

The simulations presented in this chapter were performed using CFX 5.7. The structured mesh was generated using ICEM 5. As discussed in Chapter 5, reasonable accuracy and computational time were obtained using the RNG $k - \varepsilon$ turbulence model with a second order accurate differencing scheme and a 419,928 node mesh. Parcels of the particulate phase were tracked using the Lagrangian particle-tracking feature of CFX 5.7. The evaporation of water in the particles was simulated by employing the evaporation model

incorporated within CFX 5.7, which models heat and mass transfer between the discrete and gas phases as described above. The density of the continuous phase was computed as a function of temperature according to the ideal gas law, while its viscosity, thermal conductivity, and specific heat were defined as polynomial functions of temperature.

The mean diameter of a silica gel particle was taken as 3.25 mm. In the simulations presented in this chapter a restitution coefficient of unity was used to determine the behaviour of particles impacting at the wall of the cyclone dryer, i.e. the particles were allowed to rebound elastically from the wall. Particle agglomeration was neglected within the dryer due to unavailability of this model in CFX.

In each simulation, 1000 particle tracks were used to represent the flow of particles within the dryer. Limited simulations were conducted by setting up the inlet air and particle mass flow rates, (and the inlet temperature and moisture content according to some experimental results, as shown in Tables E.3 and E.4 of Appendix E. Additional simulations were conducted at different particle feed rates, inlet air temperatures and initial particle moisture contents to investigate the effects of these parameters on the humidity, velocity, temperature field, and particle trajectories inside the cyclone dryer. The inlet conditions of air and particles for the additional simulations are shown in Tables E.5 and E.6.

7.3.3 Simulation Results

In this section, simulations of silica gel particle drying in three- and four-chamber cyclone dryers are presented. Four sets of experimental results were selected for each of the three- and four-chamber configurations. These sets of data were used for the initial validation of the numerical model. Another seven simulations were then conducted at different particle feed rates, inlet air temperatures, and initial particle moisture contents to evaluate the influence of these parameters on the humidity, velocity and temperature distributions inside the cyclone dryer.

7.3.3.1 Particle trajectories

Typical calculated particle trajectories for the three-and four-chamber cyclone dryers are shown in Figures 7.17 (a) and (b), respectively. The results show 5 of the particle tracks for simulations corresponding to the experimental results of Test numbers 4 and 10 of Tables E.3 and E.4. The colour of the trajectory in each plot indicates the length of time that particles represented by the particle track spend within the dryer.

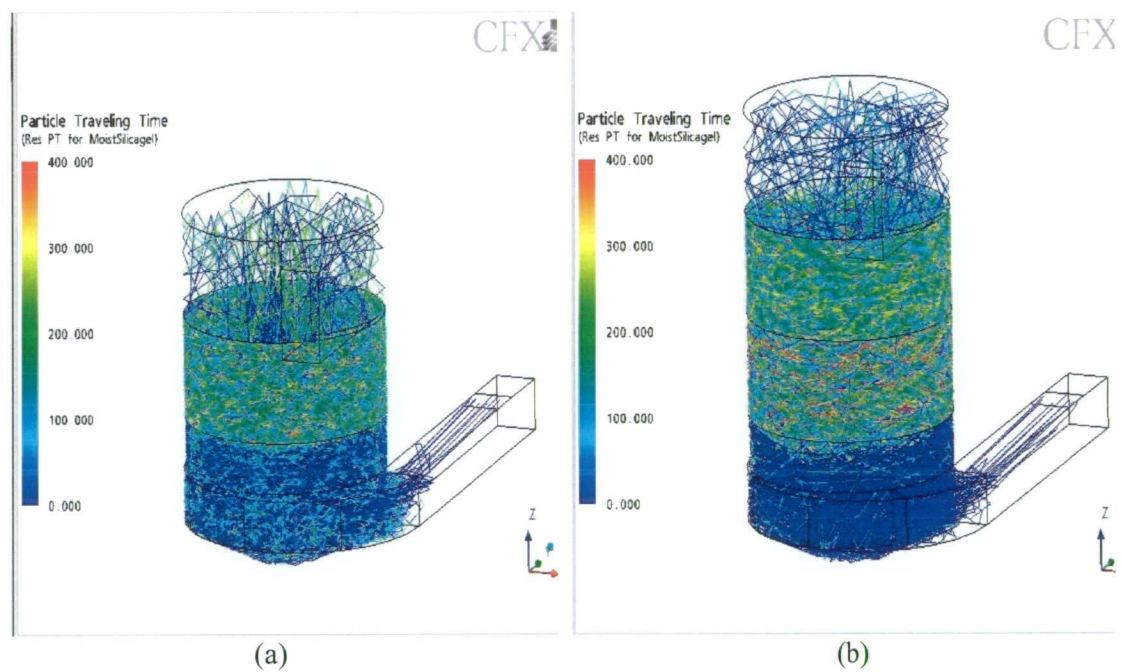


Figure 7.17 Typical particle trajectories: (a) three-chamber cyclone dryer; (b) four-chamber cyclone dryer. Colour contours indicate residence time in seconds.

As shown in Figure 7.17, the particles move upward to the higher chamber and then keep moving around the wall of the dryer. The particle trajectories show almost circular motion for a certain period of time in the intermediate chamber. The residence times of particles become longer in this chamber as indicated by the different track colour. There

is no significant change in track colour in the inlet and outlet chambers, where particles stay for a relatively short time.

7.3.3.2 Velocity distribution

Figures 7.18 to 7.20 show the predicted tangential velocity distributions for different silica gel particle feed rates, inlet air temperatures, and initial moisture content, respectively. As shown in Figure 7.18, the tangential velocity decreases when silica gel feed rate increases. This verifies that the presence of a particulate phase has a great influence on the gas velocity distribution, and provides a partial explanation for the influence of solid loading on the experimentally observed particle residence time distributions. The change in the gas axial velocity is negligible compared with the very large change in the tangential velocity.

The effect of different inlet air temperatures is shown in Figure 7.19. Changing the inlet air temperature causes only small changes in the tangential velocity distribution. The tangential velocity decreases by a negligible amount when the initial moisture content of silica gel particles increases, as shown in Figure 7.20. Similar results were obtained for the tangential velocity distribution in the four-chamber cyclone dryer configuration (results not shown here).

7.3.3.3 Temperature and humidity distributions

Figures 7.21 (a) and (b) show the predicted temperature distributions in the first and second chambers of the three-chamber cyclone dryer at different silica gel feed rates. The corresponding humidity distributions are depicted in Figures 7.24 (a) and (b). From Figures 7.21 (a) and 7.24 (a), it can be seen that the first part of the drying takes place in the fast flowing core of the first chamber, where the air temperature decreases and humidity increases. The second part of the drying process takes place in an outer core of the second chamber where the air temperature further decreases and humidity increases as shown in Figures 7.21 (b) and 7.24 (b). These phenomena can be explained from the

previous discussion of particle trajectories. It appears that most of the particles are trapped in the outer region of the intermediate chamber for a long time. Drying takes place in this region at a high particle concentration, which encourages a high intensity of particle and gas mixing. This pattern of temperature and humidity distributions was also predicted for the four-chamber cyclone dryers (results not shown).

The effects of particle feed rate on the distributions of humidity and air temperature are shown in Figures 7.21 and 7.24. The predicted humidity and air temperature distributions in the outer region of the second chamber are almost constant, while significantly different distributions occur in the first chamber and the central core of the second chamber. This is because of the effect of different particle feed rates on the velocity distribution in these regions. The tangential velocity distribution plays an important role in the degree of mixing in these cases, and is considered a major factor in the predicted differences in humidity and temperature distributions.

The inlet air temperature plays an important role in the humidity and temperature distributions shown in Figures 7.22 and 7.25. A higher inlet air temperature gives a higher driving force for water evaporation, and therefore the humidity of the air increases when inlet air temperature increases. There is little difference in the humidity and temperature of the air at different initial moisture contents of silica gel, as shown in Figures 7.23 and 7.26. A similar trend was predicted for the humidity and air temperature distributions in a four-chamber cyclone dryer (results not shown).

7.3.4 Numerical Validations

Due to the lack of experimental data on velocity, temperature and humidity distributions of air inside the cyclone dryer with solid loading, only the predicted overall humidity and temperature differentials of air between inlet and outlet could be used to validate the numerical model. These values were calculated and compared with the experimental data for the same operating conditions.

Table 7.5 presents a comparison between numerical and experimental results for drying of silica gel particles in the three- and four-chamber cyclone dryers. Studies of the particle residence time distributions in Chapter 6 showed that the numerical model predicted lower mean residence times than were observed experimentally. This would be expected to reduce the air humidity and temperature differentials predicted in drying simulations. However, the numerical predictions for air humidity and temperature differentials are somewhat higher than the experimental results, as seen from the ratios of numerical and experimental values in Table 7.5. This indicates that the heat and mass transfer model used in this study gives significant overprediction of the mass and energy transfer rates. It plays a more important role than residence time prediction in the accuracy of drying process predictions.

Table 7.5 Comparison of numerical and experimental results for overall air temperature and humidity changes in silica gel drying.

No.	$\Delta T = T_f - T_{fo}, ^\circ\text{C}$			$\Delta W = W_o - W_i, \text{kg/kg}$			Remark
	$(\Delta T)_{\text{exp}}$	$(\Delta T)_{\text{num}}$	$(\Delta T)_{\text{num}}/(\Delta T)_{\text{exp}}$	$(\Delta W)_{\text{exp}}$	$(\Delta W)_{\text{num}}$	$(\Delta W)_{\text{num}}/(\Delta W)_{\text{exp}}$	
1	20.39	30.63	1.50	0.0082	0.0145	1.77	Test 27, Table E.3
2	16.26	30.61	1.88	0.0059	0.0112	1.90	Test 26, Table E.3
3	11.42	24.05	2.11	0.0042	0.0076	1.81	Test 25, Table E.3
4	17.26	27.65	1.60	0.0061	0.0095	1.56	Test 4, Table E.3
5	12.21	26.58	2.17	0.0032	0.0109	3.41	Test 22, Table E.4
6	16.71	34.70	2.08	0.005	0.0125	2.50	Test 23, Table E.4
7	32.58	37.16	1.14	0.0072	0.0137	1.90	Test 24, Table E.4
8	15.54	30.68	1.97	0.0048	0.0074	1.52	Test 10, Table E.4

The model employed to simulate heat and mass transfer between the particles and air is based on the concept of droplet evaporation, which assumes that the vapour at the surface of the particles is always saturated. This model does not accurately describe the heat and mass transfer during the falling rate drying period in which the rate of water evaporation is controlled by moisture diffusion inside the particle. Throughout the numerical simulations, the ratio between the numerical and experimental air temperature differential is within the range 1.1-2.2, while a higher deviation ratio of 1.5-3.4 is obtained for the air humidity differentials. Larger deviations are obtained for a dryer with a higher number of

chambers, as seen by comparing results for the four-chamber configuration (Numbers 5, 6, 7 and 8) with results for the three-chamber configuration (Numbers 1, 2, 3 and 4).

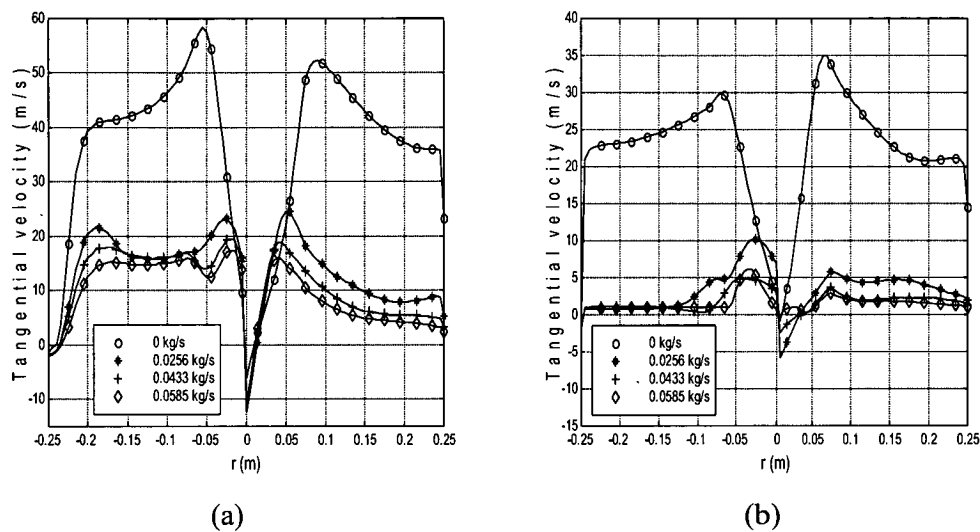


Figure 7.18 Influence of silica gel feed rate on predicted tangential velocity profiles for three-chamber cyclone dryer at: (a) 0.055 m elevation ;(b) 0.255 m elevation. (Inlet air temperature 57.43 °C; initial moisture content of silica gel 21% db.)

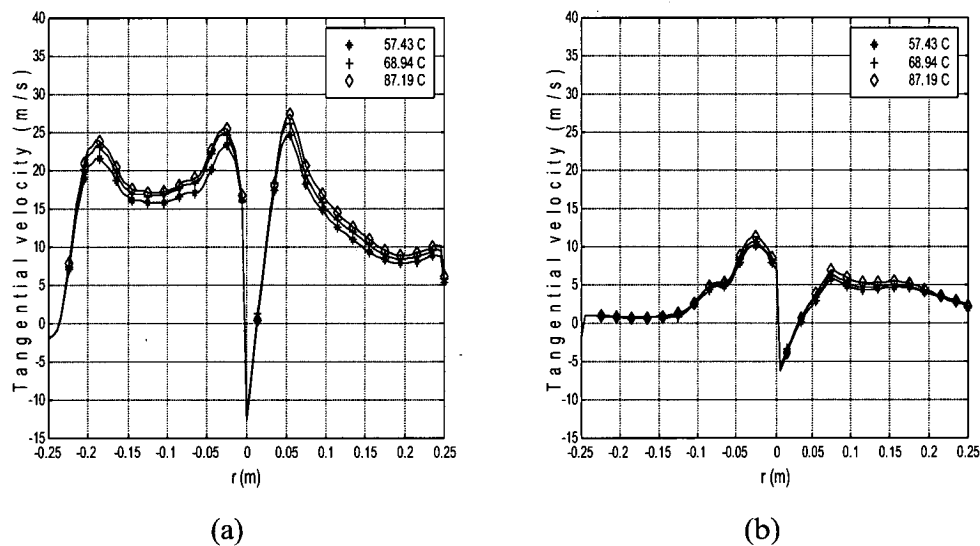


Figure 7.19 Influence of inlet air temperature on predicted tangential velocity profiles for three-chamber cyclone dryer: (a) 0.055 m elevation; (b) 0.255 m elevation. (Silica gel feed rate 0.0256 kg/s; initial moisture content of silica gel 21% db.)

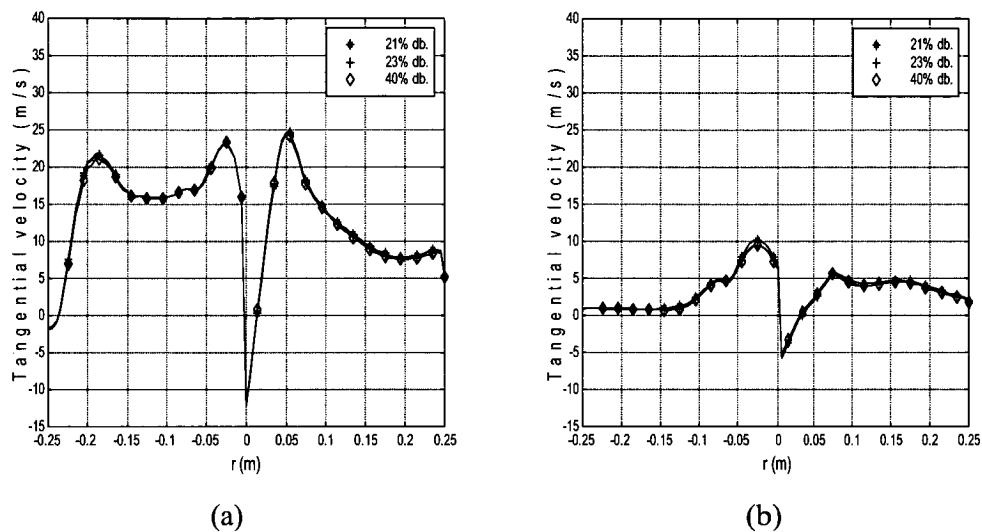


Figure 7.20 Influence of initial moisture content of silica gel on predicted tangential velocity profiles for three-chamber cyclone dryer: (a) 0.055 m elevation; (b) 0.255 m elevation. (Inlet air temperature 57.43 °C; silica gel feed rate 0.0256 kg/s.)

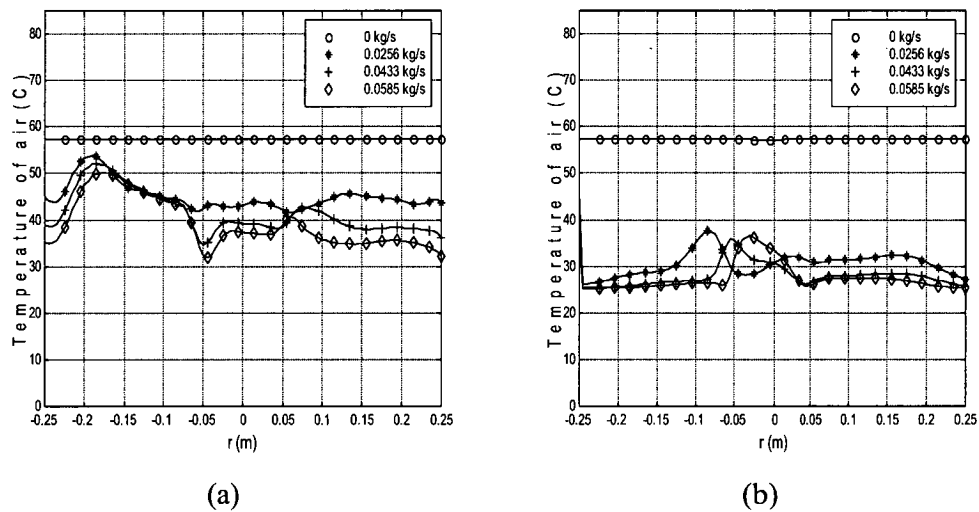


Figure 7.21 Influence of silica gel feed rate on predicted temperature profiles for three-chamber cyclone dryer: (a) 0.055 m elevation; (b) 0.255 m elevation (Inlet air temperature 57.43 °C; initial moisture content of silica gel 21% db.)

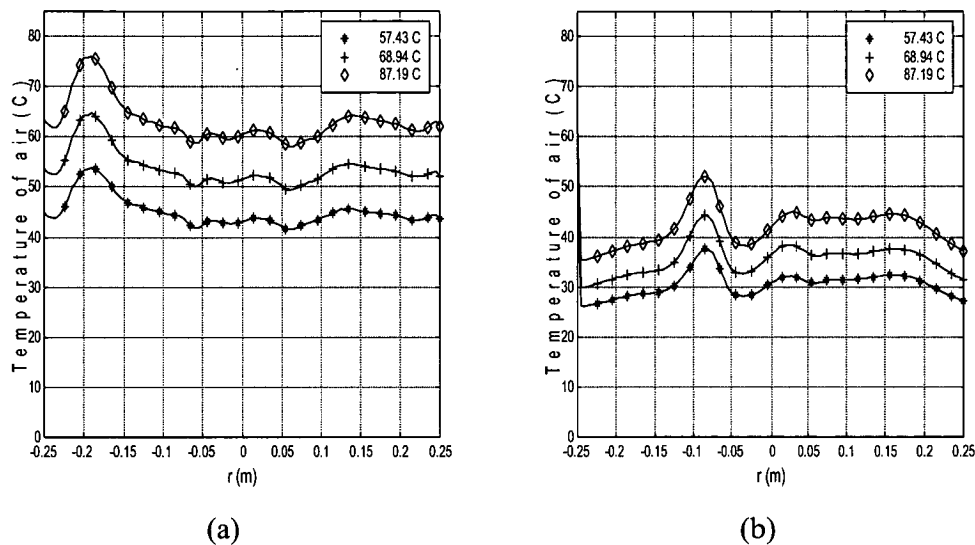


Figure 7.22 Influence of inlet air temperature on predicted temperature profiles for three-chamber cyclone dryer: (a) 0.055 m elevation; (b) 0.255 m elevation
(Silica gel feed rate 0.0256 kg/s; initial moisture content of silica gel 21% db.)

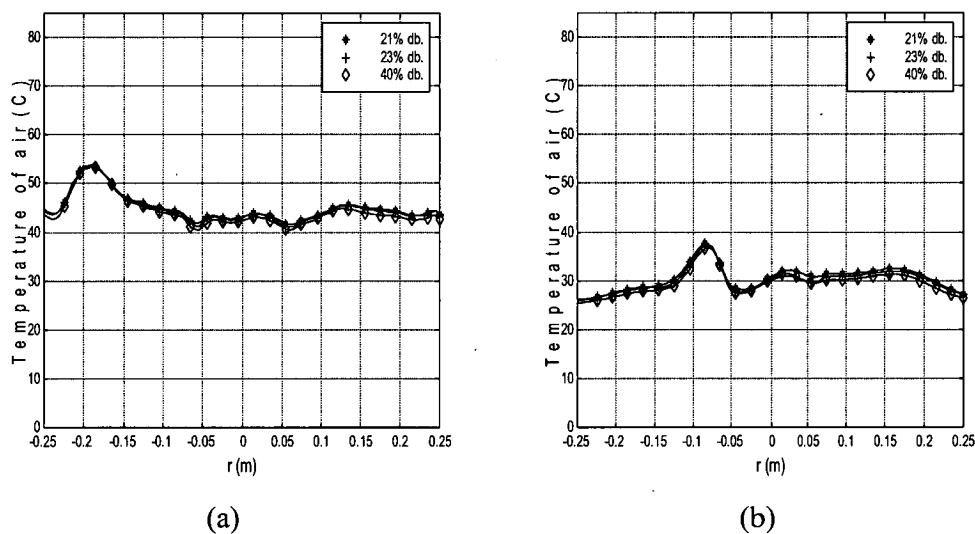


Figure 7.23 Influence of initial moisture content of silica gel on predicted temperature profiles for three-chamber cyclone dryer: (a) 0.055 m elevation; (b) 0.255 m elevation.
(Inlet air temperature 57.43 °C; silica gel feed rate 0.0256 kg/s)

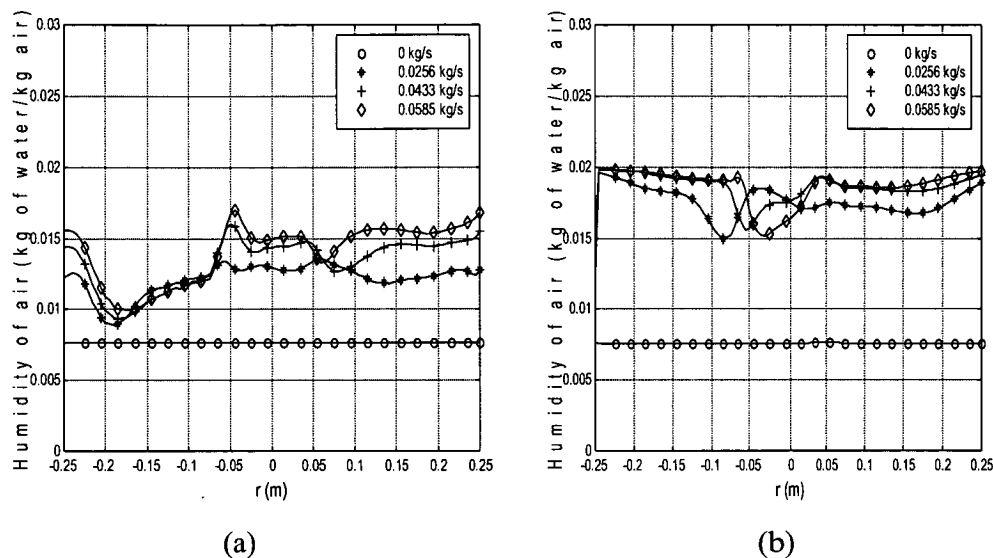


Figure 7.24 Influence of silica gel feed rate on predicted humidity profiles for three-chamber cyclone dryer: (a) 0.055 m elevation; (b) 0.255 m elevation. (Inlet air temperature 57.43 °C; initial moisture content of silica gel 21% db.)

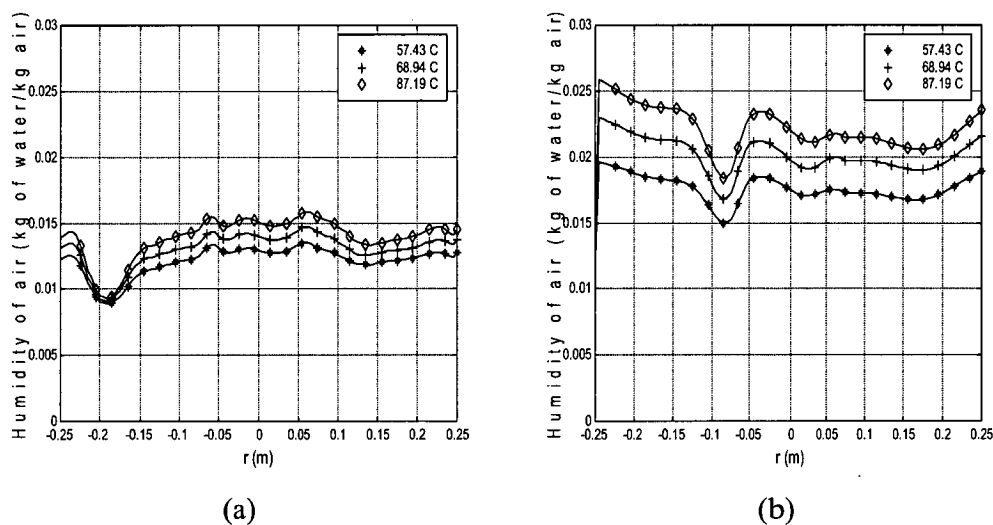


Figure 7.25 Influence of inlet air temperature on predicted humidity profiles for three-chamber cyclone dryer: (a) 0.055 m elevation; (b) 0.255 m elevation. (Silica gel feed rate 0.0256 kg/s; initial moisture content of silica gel 21% db.)

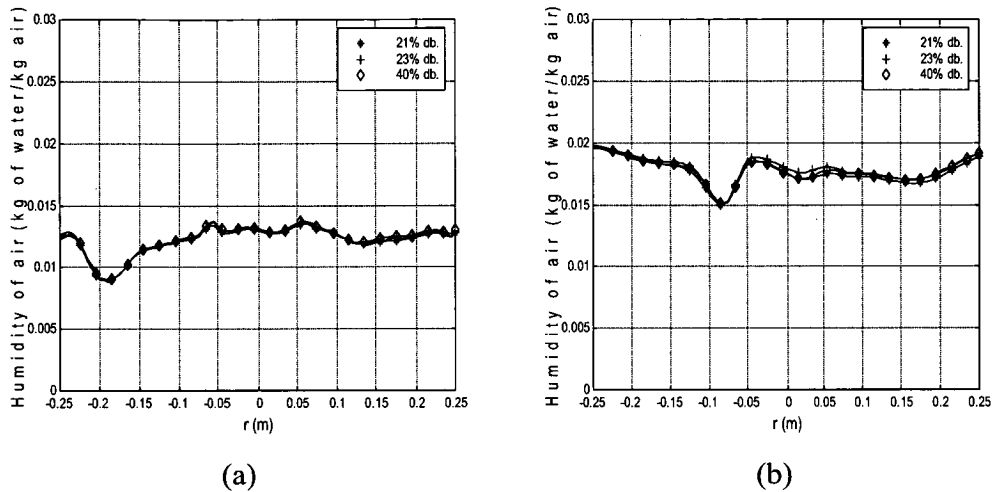


Figure 7.26 Influence of initial moisture content of silica gel on predicted humidity profiles for three-chamber cyclone dryer: (a) 0.055 m elevation; (b) 0.255 m elevation. (Inlet air temperature 57.43 °C; silica gel feed rate 0.0256 kg/s.)

7.4 PROJECTED COMMERCIAL SCALE PROTOTYPE PERFORMANCE

Both experimental and numerical modelling of the laboratory scale cyclone dryer gave positive results: faster drying time, and reasonable energy consumption for multi-pass operation with air recycling compared to commercial paddy dryers. The model cyclone dryer results can be used to predict performance for a larger commercial scale dryer with higher capacity and able to evaporate the excessive moisture within a single pass operation. However, much consideration is required before a suitable cyclone dryer commercial scale prototype can be constructed. The principal concerns in designing a cyclone dryer chamber are to ensure sufficient residence time. Hence particle residence time is the key parameter for successful scaling up of the cyclone dryer.

Theoretical considerations of cyclone dryer scaling effects based on CFD predictions will now be investigated. The most appropriate strategies for cyclone dryer scale-up will be

identified. As discussed previously, CFD simulations of the complex transport phenomena occurring in a cyclone dryer are subject to considerable uncertainty. However, the computations can still give a useful indication of trends and help to limit the number of pilot plant tests needed to achieve effective large-scale dryer operation.

7.4.1 Scale up Considerations

One of the primary factors influencing the cyclone dryer scale-up is the particle residence time. This parameter directly influences the final moisture content of the drying material. It is particularly important in the drying of thermally sensitive material such as cereal grain, where product deterioration or degradation could occur if the particle remains in a gas stream for too long or too short a time. From the laboratory scale cyclone dryer studies, it is apparent that the desired production capacity and final moisture content of paddy grain could not be achieved with a single-pass operation. The objective of scaling up the dryer size is to achieve this goal. With a sufficiently high residence time some reduction in air temperature might also be possible, with a beneficial effect on product quality and specific energy consumption.

Previous experimental studies on cyclone separators (Dibb et al. 1997; Nebbra et al., 2000) suggest that particle residence time is significantly increased when the diameter and height of a cyclone separator are increased. Jinscua (1992) also reported an increase in particle residence time when the height of a swirl flow dryer was increased. The influence of diameter and height of the present cyclone dryer chambers on particle residence time will now be studied using numerical modelling. The cyclone dryer chamber geometries used here are derived from the laboratory scale model previously studied, which is shown in Figure 4.6. Scale factors of 1.25 and 1.5 are applied to all of the model cyclone dryer dimensions, i.e. geometric similarity is assumed. These selected values are only representative and not optimal in any way. The main aim was obtain an indication of the functional relationship between the predicted mean residence time and the geometric scale factor. Care should be taken in interpretation, and especially in extrapolating the results obtained from this study.

CFD based Lagrangian-Eulerian multiphase flow modelling was used with one-way coupling to examine the influence of scale-up factor on the particle residence time. Boundary conditions for the fluid and particle phases were set up as described in Chapter 6. Note that the inlet air velocity was held constant to keep the grain particles entrained. According to this assumption, the capacity of the cyclone dryer in terms of the solid feed rate should increase as the square of the geometric scale factor. One thousand silica gel particles were tracked through the computational domain to obtain the residence time of particles for geometric scale factors of 1.25 and 1.5. The numerical simulation results are discussed in the following section.

7.4.2 Numerical Results and Discussion

To compare the numerical results of different chamber geometries, the inlet air conditions (velocity and temperature) are set to be the same. Air inlet velocity and temperature are 19 m/s and 25 °C, respectively. The predicted cumulative age distributions of silica gel particles with different scale-up factors of 1, 1.25 and 1.5 are compared in Figure 7.27. The geometric scale factor clearly has a significant influence on the cumulative age distribution.

Table 7.6 shows the predicted effect of the geometric scale up factor on the mean residence time of silica gel particles. A logarithmic plot of mean residence time against geometric scale factor is shown in Figure 7.28. This indicates that the variation of mean residence time with geometric scale factor is highly non-linear. The mean residence time is predicted to increase at more than the cube of the geometric scale factor over the range investigated. This behaviour shows that the cyclone geometry could easily be modified to meet the required residence time for single pass drying of paddy. If the solid particles moved with the fluid, then kinematic similarity would require a linear increase in residence time with geometric scale factor if the inlet air velocity were held constant. The predicted results indicate significant non-linearity due to gravitational effects and aerodynamic forces arising from relative air-particle motion.

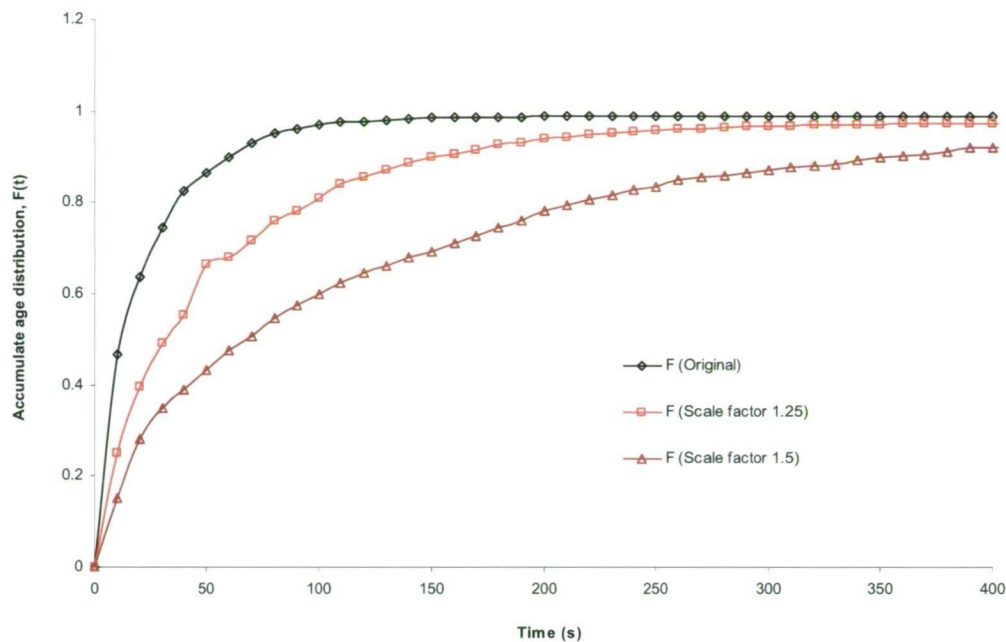


Figure 7.27 Influence of geometric scale factor on RTDs of silica gel particles.

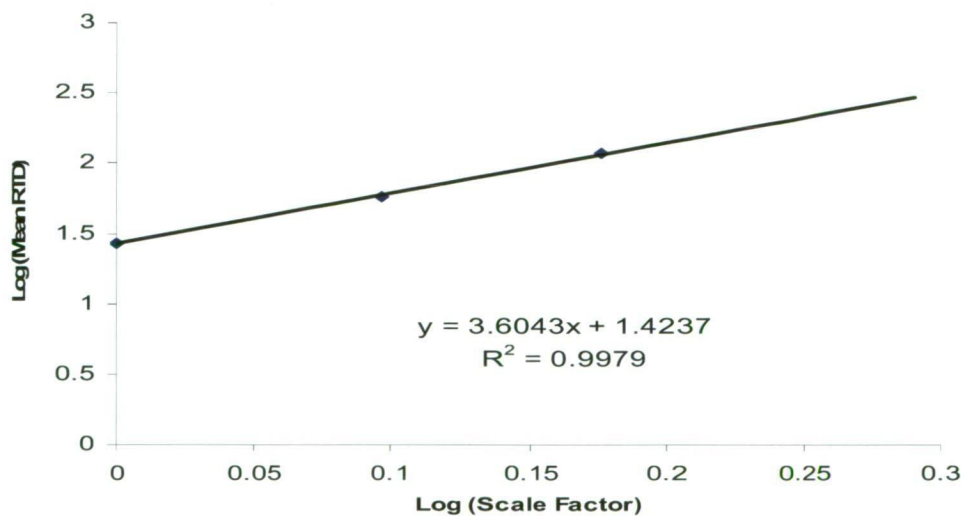


Figure 7.28 Predicted variation of mean residence time with geometric scale factor.

Table 7.6 Influence of geometric scale-up factor on mean residence time.

Scale factor	Mean residence time (s)
1 (original case)	27
1.25	57
1.5	117

7.4.3 Cyclone Dryer Scale-up Strategy

A heat and mass transfer analysis incorporating moisture diffusion as discussed in Chapter 3 indicates that a residence time of 180 seconds would be required for drying of paddy grain in air at 80 °C. Assuming the paddy grain to have similar aerodynamic properties to silica gel particles the geometric scale factor of 1.7 would be required to give this mean residence time, as indicated by the correlation in Figure 7.28. The corresponding cyclone diameter is 0.85 m. This prediction shows that the cyclone geometry could easily be modified to meet the required residence time for single pass drying of paddy. The modified dryer should still be small enough to be easily portable in the field.

Due to the complexity of the processes taking place and the imprecision of residence time and mass transfer predictions, current CFD practice cannot completely replace pilot-scale testing and the partly empirical nature of the design process. Traditional techniques will continue to be used for routine design, but CFD is invaluable for supporting this work and for investigating the most promising dryer geometry to minimise pilot scale testing.

7.5 CONCLUSIONS

The performance of a laboratory scale multi-chamber cyclone dryer has been evaluated experimentally. The effect of operating parameters such as particle feed rate and inlet air temperature on the moisture reduction, heat and mass transfer, and specific energy

consumption were investigated. It was found that particle feed rate and inlet air temperature significantly affected the moisture reduction. When particle feed rate decreased or inlet air temperature increased, the moisture reduction increased. Nusselt number (Nu) decreased when either the particle feed rate or inlet air temperature was increased. At higher inlet air temperatures, specific energy consumption (SPEC) decreased. The particle feed rate did not significantly affect the SPEC.

In these experiments, the maximum moisture reduction for paddy grain was obtained at the highest inlet air temperature and at the lowest paddy feed rate. This was due to the larger thermal driving force and particle residence time at higher inlet air temperature and lower particle feed rate, respectively. However, the target moisture reduction of paddy grain (33% to 22% dry-basis, or about 11% dry-basis reduction) was not achieved within a single pass of the model dryer. Therefore, an appropriate paddy drying strategy to remove the required amount of water with high energy efficiency in the model scale dryer was designed based on multi-pass drying and exhaust air recycling.

A multi-pass drying experiment showed that sufficient moisture reduction in the model dryer could be achieved by this means. The moisture content of paddy with a feed rate of 0.0298 kg per second was reduced from 29 to 17% dry-basis with three-pass operation of a four-chamber cyclone dryer. Average moisture difference was 3.87% dry-basis per pass, and an overall SPEC of 12.76 MJ per kg of water evaporated was achieved.

The use of exhaust air recycling to improve energy efficiency was examined theoretically. The calculations indicated that 90% air recycling should give a 70-75% reduction of SPEC compared to non-recycled air operation. This gave an SPEC of 3.5-4 MJ/kg water evaporated, which is comparable to commercial fluidised bed paddy dryer operation at approximately the same initial moisture content of paddy grain.

The commercial CFD code CFX5.7 was used to model silica gel drying in the cyclone dryer. The influence of changes in particle feed rate, inlet air temperature, and initial particle moisture content on the humidity, velocity and temperature distributions were

examined. A large decrease in tangential velocity was predicted when the particle feed rate increased. There was little change in the tangential velocity distribution with either the initial moisture content of the paddy grain or the inlet air temperature.

The simulation results showed the inlet air temperature to have the greatest influence on the humidity and temperature distributions. This was due to a higher thermal driving force between the air and the particle. A higher particle feed rate yielded an increase in humidity and a decrease in temperature, especially in the bottom chamber and the central core of higher chambers. This was considered largely due to the effect of the particles on the tangential velocity distribution in that region, which resulted in changes to the heat and mass transfer rates. The effect of initial moisture content of the particles on humidity and temperature distributions was found to be insignificant compared to the effect of inlet air temperature.

Numerical predictions of the overall humidity and temperature differentials of the air between inlet and outlet were compared to the experimental results. The CFD predictions gave ratios of numerical and experimental air temperature and humidity differentials within the ranges of 1.5-3.4 and 1.1-2.2, respectively. This indicates that the heat and mass transfer models used did not accurately describe heat and mass transfer during the falling rate drying period, because they used a droplet evaporation model in which the vapour at the surface of particle is always saturated; this is incorrect for falling rate drying. Nevertheless, the model gave a reasonable prediction of trends in the humidity and temperature changes at the outlet. The CFD model could be improved and used for further cyclone dryer simulations.

In order to investigate the performance of a commercial scale cyclone dryer, a CFD based Lagrangian-Eulerian particle transport model was used to conduct exploratory studies on the effect of changes in chamber geometry. From numerical modelling of three geometrically similar cyclone dryers, the mean residence time of silica gel particles was predicted to increase non-linearly with dryer size. By suitable increase in geometric scale, both silica gel particles and paddy grain could be dried to achieve the desired final

moisture content in a single pass operation without excessive particle degradation due to the resulting longer residence time; a lower inlet air temperature could also be applied. Further investigations of cyclone dryer performance at pilot scale are still necessary because of the limited accuracy of current CFD models in predicting particle residence time and the heat and mass transfer between gas and particles. However, the CFD predictions can still be used as a design guide to suggest the most appropriate strategy for dryer scale up and to indicate the influence of changes in geometry and operating parameters.

Chapter 8

SUMMARY AND RECOMMENDATIONS

8.1 INTRODUCTION

The primary objectives of this research have been:

- 1) to design, construct and test a model of a cyclone dryer suitable for use in paddy drying;
- 2) to investigate the residence time distribution (RTD) behaviour for paddy grain during continuous operation of the cyclone dryer and propose a simple model for the RTD;
- 3) to evaluate the drying characteristics of the cyclone dryer in continuous operation;
- 4) to investigate an applicability of computational fluid dynamics (CFD) for the design and performance prediction of this type of dryer.

The following conclusions regarding each objective may be drawn from the experimental results and CFD calculations. The apparatus design criteria are covered first, followed by

experimental results for the RTDs and the drying characteristics of the model cyclone dryer. The applicability of CFD for predicting the pressure, humidity, velocity, and temperature distributions and particle RTDs in a cyclone dryer are then reviewed. Finally, some estimates for commercial scale dryer performance are produced and recommendations for further research are addressed.

8.2 SUMMARY

8.2.1 Apparatus Design and Preliminary Investigation

The principal components of the model cyclone dryer are the drying chamber, duct work, feeding unit, blower, and heater. The model cyclone dryer design was based on a capacity of 200 kg/h. The dryer chamber geometry was developed from the design of Korn (2000) used in the pharmaceutical industry. Due to the complexity of flow phenomena inside the cyclone chambers, simple one-dimensional flow calculations were unable to determine the flow-field and pressure drop characteristics. The commercial CFD code ANSYS CFX 5.7 was therefore used to investigate the flow field and pressure drop across the model cyclone dryer for various cases.

The predicted pressure drop coefficient was used to determine the system resistance curve for blower selection. The blower flow rate was chosen high enough to keep the particles moving through the dryer chambers; this depended on both the internal orifice geometry and the terminal velocity of the solid particles to be conveyed. Finally, a heater was selected based on the amount of energy required to heat up this volumetric rate of airflow and generate the required rate of evaporation of moisture from the transported solids.

Preliminary trials were conducted to test the design. The flow pattern of paddy grain was observed to be uniform inside cyclone dryer chambers. The paddy was conveyed from inlet to outlet continuously without any sign of blower overload. There was no serious

damage of paddy at the outlet of cyclone dryer. The cyclone dryer seemed to have reasonable potential at this stage..

8.2.2 RTD of Solid Particles in the Model Cyclone Dryer

The residence time distributions for paddy grain and silica gel particles in the model dryer were measured experimentally by the stimulus-response technique at three levels of particle feed rate and inlet air velocity, with three-and four-chamber geometries.

The ideal single-parameter Tank-In-Series (TIS) model generally fitted the experimental data much better than the ideal dispersion model. The overall flow pattern of particles in dryer was between a plug flow and a perfectly mixed flow. The level of mixing was relatively high, as indicated by value of the parameter n (number of tanks) in the TIS model ranging from 2-3.

The mean particle residence times of paddy grain and silica gel particles observed in the model dryer varied between 105-192 seconds and 132-195 seconds, respectively. Higher mean residence times were obtained with lower mass concentrations of solid particles. The mean residence time increased slightly with the number of recirculation chambers and the specific gravity of particles at low solid concentrations. A quadratic function was found to describe the relation between the mean residence time of particles and their concentration with a deviation of less than 10 % of mean residence time.

8.2.3 Performance of the Model Cyclone Dryer During Continuous Operation

The experimental studies with paddy grain and silica gel particles in the model cyclone dryer showed that higher percentage moisture reductions were obtained with low particle feed rates and high inlet air temperatures and a greater number of cyclone chambers. The

lowest specific energy consumption (SPEC) for silica gel drying was achieved by using the highest available inlet air temperature. However, the SPEC for paddy grain drying did not change significantly with inlet air temperature. The SPEC increased when the initial moisture content of paddy grain was decreased.

No serious damage of paddy grain was observed during the single pass drying experiments. Maximum moisture reductions of 2.5-6.5 % dry-basis were obtained at inlet air temperatures of 82-89°C and a paddy feed rate of 0.0298 kg dry paddy per second. The corresponding SPEC varied between 7-20.5 MJ/kg water evaporated, depending on the initial paddy moisture content. These values are high compared to SPECs achieved in commercial fluidised bed spouted bed dryers employing 50-70% exhaust air recycling. As the target paddy moisture reduction from 33% to 22% dry-basis was not achieved by single pass drying in the model cyclone dryer, a multi-pass drying strategy was subsequently investigated; the use of air recycling to improve energy efficiency was predicted. Three-pass drying at 75-85°C and 0.0298 kg dry paddy per second showed that the model four-chamber cyclone dryer could reduce the moisture content of paddy from 29% to 17.4% dry-basis with an SPEC of 13 MJ/kg of water evaporated without air recycling. This is still high compared to other commercial paddy dryers. However, a competitive SPEC could be obtained by using 90% recycling of exhaust air. Calculations showed that an SPEC between 4-3.5 MJ/kg of water evaporated could be achieved. This lies in the same range of SPEC as a fluidised bed dryer operating with about the same initial moisture content of paddy grain.

8.2.4 Applicability of CFD for Cyclone Dryer Design

Single-phase simulation of the flow field inside a laboratory scale three-chamber cyclone dryer was carried out using ANSYS CFX 5.7, a RANS-based commercial computational fluid dynamics (CFD) code. The RNG k- ϵ turbulence model using a second-order differencing scheme with a mesh resolution of 419,928 nodes gave satisfactory results. It produced good solution convergence with an RMS residual level of 10^{-6} . The SSG

Reynolds stress turbulence model was considered unreliable, due to its inability to produce adequate levels of solution convergence. The optimal numerical model using RNG k- ϵ turbulence model with a second-order differencing scheme at a mesh resolution of 419,928 nodes gave useful descriptions of the axial and tangential velocity distributions were obtained, and the predicted pressure drop across the cyclone dryer was about 20 % lower than experiment. This is comparable with the accuracy of pressure drop predictions for cyclone separators reported in the literature.

To estimate the particle residence time inside the laboratory scale cyclone dryer, a numerical study was conducted using the Lagrangian/Eulerian approach with one-way solid-fluid coupling in CFX 5.7. The numerical simulations without turbulence dispersion gave reasonable qualitative predictions of the observed behaviour but large quantitative discrepancies in the residence time distributions and mean particle residence times. The apparent lack of turbulent dispersion effect was explained by the relatively high value of Stokes number for the solid particles in the model dryer. The predicted cumulative age distribution curve altered with inlet air velocity, but was not influenced significantly by changes in particle feed rate. The mean particle residence times were not accurately predicted. Evidently the one-way coupling did not sufficiently account for particle-particle and particle-fluid interactions. Nevertheless, these numerical calculations gave useful qualitative predictions of the influence of operating conditions on mean residence time. The predicted mean residence times are generally more accurate for four-chamber dryer cases than for three-chamber cases. The predicted mean residence times for paddy grain are more accurate than those for silica gel particles.

A full simulation of some silica gel drying tests in the laboratory scale cyclone dryer was conducted using CFX5.7 with a Lagrangian/Eulerian approach and two-way coupling that accounted for mass, momentum and energy transfer between the solid particles and gas phase. The simulation results showed the particle feed rate to have the greater influence on the tangential velocity distribution. The CFD model used over estimated both mass and energy transfer. The ratio between the numerical and experimental air temperature was within range 1.1-2.2, while a higher ratio of 1.5-3.4 was obtained for the

air humidity. Larger deviations were also obtained for dryers with a higher number of chambers. The results indicate that the heat and mass transfer model used in this study played a more important role than the residence time prediction in the accuracy of drying process prediction. Nevertheless, the model gave a reasonable prediction of trends in the humidity and temperature changes at the outlet. The CFD model could be improved and used for further cyclone dryer simulations.

An examination of the influence of cyclone dryer size on the mean particle residence time conducted numerically. CFD predictions for geometrically similar dryers indicated a highly non-linear relation between the mean residence time and the geometric scale. Hence by suitably increasing the chamber dimensions, it should be possible to achieve the desired final moisture content of grain within a single-pass operation in a unit small enough to be easily field portable.

8.2 RECOMMENDATIONS

1. Experimental studies at commercial pilot plant scale should be undertaken with a view to increasing particle residence time and achieving single-pass drying of paddy at reduced air temperature. The effects of drying parameters (inlet air temperature, particle feed rate and initial particle moisture content) on the final product qualities of paddy, such as percentage of head rice yield and whiteness of rice grain after milling process, should be examined.
2. Improvements of the CFD water evaporation model to incorporate the drying characteristics of the solid particles during the falling rate drying period need to be developed.
3. Experimental studies of the effects of exhaust air recycling on SPEC need to be conducted.

References

ASHRAE, 1971, (American Society of Heating, Refrigeration and Air Conditioning Engineers), *Duct Design*, In Fundamental Handbook, ASHRAE, Atlanta, USA, pp 33.1-33.43.

ANSYS, 2004, *Turbulence and wall function theory and initial condition modelling*, In CFX-5. Solver theory, ANSYS Canada Ltd, Waterloo.

ASME, *Statement on the control of numerical accuracy by the ASME Journal of Fluids Engineering*, <http://journaltools.asme.org/Templates/JFENumAccuracy.pdf>, ASME Journal of Fluid Engineering.

Ashworth, J.C. and Carter, J.W., 1980, *Experimental study of drying behavior of silica-gel granules by continuous weighing in an air stream*, Drying'80, Vol. 1, Hemisphere Publishing Corporation, New York, pp. 151-159.

Benta E.S., and Silva, M.A., 1997, *Cyclone drying of milled corncob*, Proceedings of the Inter-American Drying Conference (IADC), Itu-SP, Brazil, pp. 288-295.

Boonthumjinda, S., Exell, R.H.B., Rongtawng, S. and Kaewnikom, M., 1983, *Field tests of solar rice drier in Thailand*, Proceedings of ISES Solar World Forum, Perth, Australia, pp.1258-1263.

Boysan, F., Ayers, W. H., Swithenbank, J., 1982, *A fundamental mathematical modeling approach to cyclone design*, Trans. IChem E., 16, pp. 222-230.

Brooker, D.B., Bakker-Arkema, F.W., and Hall, C.W., 1992, *Drying and storage of grains and oilseeds*, AVI Publication, New York.

Chamsingl, A. and G. Singh, 2000, *Rice mechanization and processing in Thailand*, Agricultural Mechanization in Asia, Africa and Latin America, 31, pp. 21-30.

Chen, C., 2003, *Evaluation of air oven moisture content determination methods for rough rice*, Biosystems Engineering, 86, pp. 447-457.

Cheremisinoff, N.P. and Cheremisinoff, P.N., 1984, *Hydrodynamics of gas-solid fluidisation*, Gulf Publication Co., Houston, Texas, USA.

Correa, J. G. L., Chamma, M.O., Godoy, A.L., Silva, M.A., and Nebra, S.A., 2001, *Experimental study of drying and residence time of sugar cane bagasse in cyclonic devices*, Proceedings of 2nd Inter-American Drying Conference, Boca del Rio, Veracruz, Mexico, pp. 407-414.

Correa, J. G. L., Graminho, D.R., Silva, M.A. and Nebra, S.A., 2004a, *Cyclone as a sugar cane bagasse dryer*, Chinese Journal of Chemical Engineering, 12, pp. 826-830.

Correa, J. G. L., Graminho, D.R., Silva, M.A. and Nebra, S.A., 2004b, *The cyclone dryers - a numerical and experimental analysis of the influence of geometry on average particle residence time*, Brazilian Journal of Chemical Engineering, 21, pp. 103-112.

Crowe, C., Sommerfield, M, and Tsuji, Y., 1997, *Multiphase flows with droplets and particles*, CRC Press, New York.

Debrand, S., 1974, *Heat transfer during a flash drying process*, I&EC Process Design Development, 13, pp. 396-404.

De Padua, D.B., 1985, *Requirements for drying high moisture content grain in Southeast Asia*, Preserving Grain Quality by Aeration and In-Store Drying, AICAR Proceeding no. 15, Kuala Lumpur, Malaysia, pp. 45-49.

Department of Agricultural Economy, 2002, *Agricultural statistics crop year 2000-01*, Ministry of Agriculture and Co-operative, Thailand.

Derksen, J.J., 2003, *Separation performance predictions of a Stairmand high-efficiency cyclone*, AIChE Journal, 49, pp. 1359-1371.

Derksen, J.J., Van den Akker, H.E.A. 2000, *Simulation of vortex core precession in a reverse-flow cyclone*, AIChE Journal, 46, pp. 1317-1331.

Dibb, A. and Silva, M.A., 1997, *Cyclone as dryer - the optimum geometry*, Proceedings of Inter-American Drying Conference (IADC), Itu-SP, Brazil, pp. 396-403.

Driscoll, R.H., and Adanezak., T., 1985, *Drying systems for the humid tropics*, Preserving grain quality by aeration and in-store drying, AICAR Proceedings no.15, Kuala Lumpur, Malaysia, pp. 58-68.

Exell, R.H.B., Kornsakool, S. and Triratrakoolchai, 1979, S., *A low cost solar rice drier for farmers in South-East Asia*, Agricultural Mechanization in Asia, Africa and Latin America, Authum, pp. 75-78.

Fredericks, L.J., and Mercader, J.P., 1985, *Cost implication of implementation of grain quality systems*, Preserving Grain Quality by Aeration and In-Store Drying, AICAR Proceedings no.15, Kuala Lumpur, Malaysia, pp. 152-160.

Griffiths, W.D., and Boysan, F., 1996, *Computational Fluid Dynamics (CFD) and empirical modeling of the performance of a number of cyclone samples*, J. Aerosol Sci., 27, pp. 281-304.

Heinze, C., 1984, *New cyclone dryer for solid particles*, Ger. Chem. Eng, 7, pp. 274-279.

Hoekstra, A.J., Derksen, J.J., 1999, Van Der Akker, H.E.A., *An experimental and numerical study of turbulent swirling flow in gas cyclones*, Chemical Engineering Science, 54, pp.2055-2065.

Hoffmann, A. C., and Stein, L. E., 2002, *Gas Cyclones and Swirl Tube*, Springer, Heildenberg, Germany.

Idelchik, I.E.; editor, Steinberg, M.E.; translated by Malyaskaya, G.R.; translation editor, Martynenko, O.G., 1994, *Handbook of hydraulic resistance*, 3rd edition, CRC Press.

Inprasit, C. and Noomhorm, A., 2001, *Effect of drying air temperature and grain temperature of different types of dryer operation on rice quality*, Drying Technology, 19, pp. 389-404.

Jindal, V.K. and Obaldo, L.G., 1986, *Rice husk-fired drier for infestations and rapid drying for paddy*, 9th Annual ASEAN grains post-harvest technology seminar (Singapore), Paper no. 86202, ASEAN crops post-harvest programme, Manila, Philippines.

Jinescu, G., Vasilescu, P., and Dumitru, V., 1992, *Drying of solid in the centrifugal field*, Drying'92, A.S. Mujumdar Editor, Elsevier Science Publishers B.V., USA, pp. 1624-1650.

Kemp, I.C., Frankum, D.P., Abrahamson, J., and Saruchera, T., 1998, *Solids residence time and drying in cyclones*, Drying'98, Hikidiki, Greece, pp. 581-588.

Klenin, N.I., I.F. Popov and V.A. Sakan, 1986, *Agricultural mechanics: theory of operation, computation of controlling parameters and the conditions of operation*, Russian Translations Series 31, Gidson Printing Works, New Delhi, India.

Korn, O., 2001, *Cyclone Dryer: A pneumatic dryer with increased solid residence time*, Drying Technology, 19, pp.1925-1937.

Kunze, O.R. and David L. Calderwood, 1980, *Systems for drying rice*, Drying and Storage of Agricultural Crops, AVI Pub Co. Ltd., Connecticut, USA.

Laithong, C., 1987, *The study of thermo physical properties of rough rice*, Master Thesis, King Mongkut's Institute of Technology Thonburi.

Levy, A. and Borde, J., 1999, *Steady state one-dimensional flow for a pneumatic dryer*, Chemical Engineering and Process, 38, pp. 121-130.

Levenspiel, O., 1972, *Chemical reaction engineering*, 2nd edition, John Wiley and Sons, New York.

Madhiyanon, T., Soponronnarit, S. and Tia, W., 2001, *Industrial-scale prototype of continuous spouted bed paddy drier*, Drying Technology, 19, pp. 207-216.

Modigell, M., and Weng, M., 2000, *Pressure loss and separation characteristics calculation of a uniflow cyclone with a CFD method*, Chem. Eng. Technol., 23, pp.753-758.

Montavon, C.A., Grotjans, H., Hamill, I.S., Phillips, H.W., and Jones, I.P., 2000, *Mathematical modelling and experimental validation of flow in a cyclone*, 5th International Conference on Cyclone Technologies, Warwick, UK, 31 May-2 Jun, 2000; BHR Group, pp.175-186.

Morita, T and R.P. Singh, 1979, *Physical and thermal properties of short grain rough rice*, Transactions of ASAE, 22, pp. 630-636.

Mujumdar, A. S., 1995, *Handbook of Industrial Drying*, 2nd Edition, Marcel Dekker Inc., New York, USA.

Narimatsu, C.P., and Feeeira, M.C., 2001, *Vertical pneumatic conveying in dilute and dense phase flow: experimental study of the influence of particle density and diameter on fluid dynamic behavior*, Brazilian Journal of Chemical Engineering, 18.

Nebra, S.A., Silva M.A., Mujumdar. A.S., 2000, *Drying in cyclones - A review*, Drying Technology, 18, pp. 791-832.

Pakowski, Z., Bartczak, Z., Strumillo, C., and Stenstrom, S., 1991, *Evaluation of equations approximating thermodynamic and transport properties of water, steam and air from used in CAD of drying processes*, Drying Technology, 9, pp. 753-773.

Prachayawarakorn, S., 1997, *Drying of high moisture paddy by fluidization technique*, Master Thesis, King's Mongkut's Institute of Technology, Bangkok. (In Thai)

Puechkamutr, Y., 1985, *Design and development of natural convection rotary dryer for paddy*, Master Thesis, Asian Institute of Technology, Thailand.

Reyes, V.G., Jr. and V.K. Jindal, 1988, *Effect of heat treatment on the head rice yields of high moisture rough rice*, Journal of Food Science, 53, pp. 482-487.

Rordprapat, W., Soponronnarit, S. and Wangji, M., 1999, *Paddy drying systems in rice mills*, Kasetsart Journal (National Science), 33, pp. 126-133. (In Thai)

Saastanoinen, J., 1992, *Model of flash drying*, Drying'92, Amsterdam, the Netherlands, pp. 434-443.

-
- Schmidt, S., Blackburn, H. M., 2003, *Simulation of turbulent flow in a cyclonic separator*, Third International Conference on CFD in the Minerals and Process Industries, Melbourne, Australia, Dec 10-12 2003; CSIRO, pp. 365-369.
- Seker, M., 2005, *Residence time distribution of starch with high moisture content in a single-screw extruder*, Journal of Food Science, 67, pp. 317-324.
- Singhagajen S., 1981, *Farm grain dryer - Thailand*, Food Drying, Proceeding of a workshop, Edmonton, Alberta, pp. 89-93.
- Silva, M.A. and Nebra, S.A., 1991, *Drying in cyclone - an experimental study*, Drying'91 edited by Mujumda, A.S., Elsevier Science Publishers, Amsterdam, pp. 281-291.
- Silva, M.A. and Nebra, S.A., 1994, *Numerical calculations of gas-solid flow in a cyclone*, Drying'94, Vol. b, Gold Coast, Australia, pp. 1319-1326.
- Silva, M.A. and Nebra, S.A., 1997, *Numerical simulation of drying in a cyclone*, Drying Technology, 15, pp. 1731-1741.
- Silva, M.A., and Nebra, S.A., 1992, *Experimental and theoretical study of drying in a cyclone*, Drying'92, edited by Mujumda, A.S., Elsevier Science Publishers, Amsterdam, pp. 1651-1663.
- Soponronnarit, S., 1985, *Paddy drying in Thailand*, AICAR Proceedings no.15: Preserving Grain Quality by Aeration and In-Store Drying, Kuala Lumpur, Malaysia, pp.192-199.
- Soponronnarit, S. and Prachayawarakorn, S., 1994, *Optimum strategy for fluidized bed paddy drying*, Drying Technology, 12, 1667-1686.

-
- Soponronnarit, S., Prachayawarakorn, S. and Sripawatakul, O., 1996a., *Development of cross-flow fluidized bed paddy drier*, *Drying Technology*, 14, 2397-2410.
- Soponronnarit, S., Rordprapat, W. and Wetchacama, S., 1998, *Mobile fluidized bed paddy drier*, *Drying Technology*, 16, 1501-1513.
- Soponronnarit, S., Wetchacama, S., Trutassanawin, S. and Jariyatontivait, W., 2001, *Design, testing and optimization of vibro-fluidized bed paddy drier*, *Drying Technology*, 19, 1891-1908.
- Sopomronnarit, S., Prachayawarakorn, S., and Wangji, M., 1996b., *Commercial fluidized bed paddy drying*, *Drying' 96*, Vol a., Krakow, Poland, pp. 638-644.
- Stanford, H. W. and Englewood Cliffs, N.J., 1988, *Analysis and design of heating, ventilating, and air-conditioning systems*, Prentice-Hall, New York.
- Steffe, J.F. and R.P. Singh, 1982, *Diffusion coefficients for predicting rice drying behavior*, *Journal of Agricultural Engineering Research*, 27, pp. 489-493.
- Stirmand, C. J., 1952, *The design and performance of modern gas cleaning equipment*, *Journal Institution Fuel*, 29, pp. 58-76.
- Strumillo, C. and T. Kudra, 1986, *Drying: principles, application and design*, Gordon and Breach Science Publishers, New York.
- Szekely, J., and Carr, R., 1966, *Heat transfer in a cyclone*, *Chemical Engineering Science*, 21, pp. 1119-1132.
- Tang, D, Jess, A., Ren, X., Bluemich, B. and Stapf, S., 2004, *Axial dispersion and wall effect s in narrow fixed bed reactors: A comparative study based on RTD and NMR measurements*, *Chemical Engineering Technology*, 27, pp 866-873.

-
- Taweerattanapanish, A., S. Soponronnarit, S. Wetchakama, N. Kongseri and S. Wongpiyachon, 1999, *Effect of drying on head rice yield using fluidized technique*, Drying Technology, 17, pp. 345-353.
- Ter Linden, 1949, *Investigations into cyclone dust collectors*, Proceeding International Mechanical Engineering, London, pp. 160.
- Thongprasert, M., 1978, *Solar rice drier: a forced air drier type*, Proceedings of Solar Drying Workshop, Manila, Philippines.
- Thrope, G. R., Wint, A. and Coggan, G.R., 1973, *The mathematical modeling of industrial pneumatic dryers*, Transaction of Institute of Chemical Engineering Research, 51, pp. 339-349.
- Tumambing, J.A., 1978, *Current drying practices and need in ASEAN*, Bulk Handling and Storage of Grain in The Humid Tropics, AICAR Proceedings no.22, Kuala Lumpur, Malaysia, pp. 48-57.
- Ulrich, W., 2002, *Cyclone dryer*, 13th International Drying Symposium (IDS 2002), Beijing, China, Aug. 27-30 2002, Vol. B., pp. 867-873.
- Wang, B., Xu, L.X., Xiao, G.X., Chu, K.W., Yu, A.B., 2003, *Numerical study of gas-solid flow in a cyclone separator*, Third International Conference on CFD in the Minerals and Process Industries, Melbourne, Australia, Dec 10-12 2003; CSIRO, pp. 371-376.
- Wetchacama, S., Soponronnarit, S., Swasdisevi, S., Panich-ing-orn, J. and Suthicharoenpanich, S., 1999, *Drying of high moisture paddy by two-dimensional spouted bed technique*, Proceedings of the First Asian-Australian Drying Conference (ACD'99), Bali, Indonesia, pp. 300-307.

-
- Wicks, M., 1971, *Transport of solids at low concentrations in horizontal pipes*, Advances in solid-liquid flow in pipes and its application., edited by Zandi, I., Pergamon Press, New York.
- Wilhelm, L.R., 1976, *Numerical calculation of psychrometric properties in SI units*, Transaction of the ASAE, pp. 318-328.
- Witt, P.J., and Mittoni, L.J., 1999, *Validation of a CFD model for predicting gas flow in a cyclone*, CHEMECA99, Newcastle, Australia.
- Wratten, F.T., W.D. Poole, J.L. Chesness, S. Bal and V.Ramarao, 1969, *Physical and thermal properties of rough rice*, Transactions of ASAE, 12, pp. 801-803.
- Yen, S.C., Lu, W-M., Shung, S.C., 1990, *Gas-solid heat transfer in gas cyclone*, Journal of Chinese Institute of Chemical Engineering, 21, pp. 197-206.
- Yoshida, H., Saeki, T., Hashimoto, K., and Fujioka, T., 1991, *Size classification of sub-micron powder by air cyclone and three-dimensional analysis*, Journal of Chemical Engineering of Japan, 24, pp. 640-647.
- Yoshida, H., Fukui, K., Yoshida, K., and Shinoda, E., 2001, *Particle separation by Inoya's type gas cyclone*, Powder Technology, 118, pp. 16-23.
- Yuu, S., Jotaki, T., Tomita, Y., and Yoshida, K., 1978, *The reduction of pressure drop due to dust loading in a conventional cyclone*, Chemical Engineering Science, 33, pp.1573-1580.
- Zhou, L.X., and Soo, S. L., 1990, *Gas-solid flow and collection of solids in a cyclone separator*, Powder Technology, 63, pp.45-53.

DEVELOPMENT OF A CYCLONE RICE DRYER

by

Pracha Bunyawanicakul

B.Eng, Kasetsart University; M.Eng, AIT Thailand

School of Engineering

Submitted in fulfillment of the requirement for the degree of

Doctor of Philosophy

APPENDICES



University of Tasmania

Faculty of Science, Engineering and Technology

September 2006

Appendices

<i>Appendix A. MATLAB Source Program for Pneumatic Dryer Simulation.....</i>	226
<i>Appendix B. Drawing of Cyclone Dryer, Rotary Feeder, Heater and Settling Chamber.....</i>	235
<i>Appendix C. Calculation of the Required Air Flow and Total Pressure Drop Across the Drying System.....</i>	264
C.1 Air flow rate.....	265
C.2 System pressure drop.....	265
<i>Appendix D. Three Hole Probe Calibration.....</i>	271
D.1 Probe Construction.....	272
D.2 Detail of Probe Calibration.....	272
D.3 Calibration Results and Data Fitting.....	273
D.4 Error of Fitted Surface.....	277
<i>Appendix E. Experimental Results of Paddy Grain and Silica Gel Particle Drying and Initial Conditions for Cyclone Dryer Simulations....</i>	280

Appendix A.

MATLAB Source Program for Pneumatic Dryer Simulation

Appendix A. Source program for pneumatic dryer Simulation

```

Parameter4;n=1;
Ta(n)=Ta1;W(n)=W1;Tr(n)=Tr1;M(n)=M1;
t(n)=t1;Vr(n)=Vr1;
disp(n)
% Compute the distance
y1=(n-1)*dy;
y(n)=y1;
xx=1;
% Find Relative Humidity of inlet air for initial stage
[RH1]=RHair(Ta1,W1);
RH(n)=RH1;
% Find time and velocity for rough rice kernel movement at the end
% of initial stage
[Ma]=ViscoA(Ta1);
[Da]=DensityA(Ta1,W1);
[Dr]=DensityR(M1);
[Qa]=VolFA(Va,Dd);
[Va]=Vair(Qa,Dd);
[Re]=Reynold1(Da,Va,Vr1,Dp,Ma);
[Dg]=DragC2(Re);
[dVr]=DiffVr(Dg,Da,Dr,Dp,Va,Vr1);
[t2]=Ntime(dVr,Vr1,t1,dy);
[Vr2]=NrVelocity(Vr1,t2,t1,dVr);
t(n+1)=t2;Vr(n+1)=Vr2;
% Find moisture content of rough rice at the end of initial stage
[Me]=Eqmoist(RH1,Ta1);
[D]=Diffuse(Tr1);
%% Set initial moisture distribution
for i=1:1001
    MProf(1,i)=M(n);
end;
MProf_S=MProf;
[M(n+1),MProf(2,:)] = MDistb_Sim2(MProf(1,:),Me,D,t1,t2,Dp);
M2=M(n+1);
[dMdt(n)]=Dryrate(M1,M2,t1,t2);
% Find Humidity ratio of air at the end of initial stage
[mr]=RMflow(mrw,M1);
[ma]=AMflow(Qa,Da);
[W2]=NHumid(W1,mr,ma,M2,M1);
W(n+1)=W2;
% Find air and rough rice temperature at the end of initial stage
s=1;
[Gr]=Rflux(mr,Dd);
[dM]=DiffM(M2,M1,dy);
[Cp]=SHrice(M1);
[Ga]=Aflux(Qa,Da,Dd);
[ap1]=SPareal(mr,t1,t2,Dr,dy,Dp,Dd);
[Mw]=ViscoA(Tr1);
[Ma]=ViscoA(Ta1);
[Minf]=ViscoA(Ta1);
[ka]=Tcond(Ta1);
[Ca]=SHair(Ta1);
[Cv]=SHvap(Ta1);
[Re]=Reynold1(Da,Va,Vr1,Dp,Ma);
[Pr]=Prandtl(Ca,Ma,ka);
[h]=Htcoeff(ka,Dp,Re,Pr,Minf,Mw);
[a(s)]=FRungl(h,ap1,Ta1,Tr1,Ga,Ca,W1,Cv,dy);
[Cw]=SHwater(Tr1);

```

```

[L]=Lheat(Tr1,M1);
[b(s)]=FRung2(h,ap1,Ta1,Tr1,Gr,Cp,M1,Cw,L,Cv,dM,dy);
for s=2:1:4
if s==2&3
Ta1=Ta(n)+(a(s-1)/2);
Tr1=Tr(n)+(b(s-1)/2);
[Mw]=ViscoA(Tr1);
[Ma]=ViscoA(Ta1);
[Minf]=ViscoA(Ta1);
[ka]=Tcond(Ta1);
[Ca]=SHair(Ta1);
[Cv]=SHvap(Ta1);
[Da]=DensityA(Ta1,W1);
[Re]=Reynold1(Da,Va,Vr1,Dp,Ma);
[Pr]=Prandtl(Ca,Ma,ka);
[h]=Htcoeff(ka,Dp,Re,Pr,Minf,Mw);
[Ga]=Aflux(Qa,Da,Dd);
[a(s)]=FRung1(h,ap1,Ta1,Tr1,Ga,Ca,W1,Cv,dy);
[Cw]=SHwater(Tr1);
[L]=Lheat(Tr1,M1);
[b(s)]=FRung2(h,ap1,Ta1,Tr1,Gr,Cp,M1,Cw,L,Cv,dM,dy);
else
Ta1=Ta(n)+a(s-1);
Tr1=Tr(n)+b(s-1);
[Mw]=ViscoA(Tr1);
[Ma]=ViscoA(Ta1);
[Minf]=ViscoA(Ta1);
[ka]=Tcond(Ta1);
[Ca]=SHair(Ta1);
[Cv]=SHvap(Ta1);
[Da]=DensityA(Ta1,W1);
[Re]=Reynold1(Da,Va,Vr1,Dp,Ma);
[Pr]=Prandtl(Ca,Ma,ka);
[h]=Htcoeff(ka,Dp,Re,Pr,Minf,Mw);
[Ga]=Aflux(Qa,Da,Dd);
[a(s)]=FRung1(h,ap1,Ta1,Tr1,Ga,Ca,W1,Cv,dy);
[Cw]=SHwater(Tr1);
[L]=Lheat(Tr1,M1);
[b(s)]=FRung2(h,ap1,Ta1,Tr1,Gr,Cp,M1,Cw,L,Cv,dM,dy);
end;
end;
Ta2=Ta(n)+((a(1)+(2*a(2))+(2*a(3))+a(4))/6);
Ta(n+1)=Ta2;
Tr2=Tr(n)+((b(1)+(2*b(2))+(2*b(3))+b(4))/6);
Tr(n+1)=Tr2;
for n=2:3002
Ta1=Ta(n);W1=W(n);Tr1=Tr(n);M1=M(n);
t1=t(n);Vr1=Vr(n);MProf(1,:)=MProf(2,:);
disp(n)
% Compute the distance
y1=(n-1)*dy;
y(n)=y1;
% Find Relative Humidity of inlet air for nth stage
[RH1]=RHair(Ta1,W1);
RH(n)=RH1;
% Find time and velocity for rough rice kernel movement at the end
% of nth stage
[Ma]=ViscoA(Ta1);
[Da]=DensityA(Ta1,W1);
[Dr]=DensityR(M1);

```

```

[Va]=Vair(Qa,Dd);
[Re]=Reynold1(Da,Va,Vr1,Dp,Ma);
[Dg]=DragC2(Re);
[dVr]=DiffVr(Dg,Da,Dr,Dp,Va,Vr1);
[t2]=Ntime(dVr,Vr1,t1,dy);
[Vr2]=NrVelocity(Vr1,t2,t1,dVr);
t(n+1)=t2;Vr(n+1)=Vr2;
% Find moisture content of rough rice at the end of nth stage
[Me]=Eqmoist(RH1,Ta1);
[D]=Diffuse(Tr1);
[M(n+1),MProf(2,:)] = MDistb_Sim2(MProf(1,:),Me,D,t1,t2,Dp);
M2=M(n+1);
[dMdt(n)]=Dryrate(M1,M2,t1,t2);
if mod(n,100)==1
    MProf_S(xx+1,:)=MProf(2,:);
    xx=xx+1;
end;
% Find Humidity ratio of air at the end of nth stage
[mr]=RMflow(mrw,M1);
[ma]=AMflow(Qa,Da);
[W2]=NHumid(W1,mr,ma,M2,M1);
W(n+1)=W2;
% Find air and rough rice temperature at the end of initial stage
s=1;
[Gr]=Rflux(mr,Dd);
[dM]=DiffM(M2,M1,dy);
[Cp]=SHrice(M1);
[Ga]=Aflux(Qa,Da,Dd);
[ap1]=SPareal(mr,t1,t2,Dr,dy,Dp,Dd);
[Mw]=ViscoA(Tr1);
[Ma]=ViscoA(Ta1);
[Minf]=ViscoA(Ta1);
[ka]=Tcond(Ta1);
[Ca]=SHair(Ta1);
[Cv]=SHvap(Ta1);
[Re]=Reynold1(Da,Va,Vr1,Dp,Ma);
[Pr]=Prandtl(Ca,Ma,ka);
[h]=Htcoeff(ka,Dp,Re,Pr,Minf,Mw);
[a(s)]=FRung1(h,ap1,Ta1,Tr1,Ga,Ca,W1,Cv,dy);
[Cw]=SHwater(Tr1);
[L]=Lheat(Tr1,M1);
[b(s)]=FRung2(h,ap1,Ta1,Tr1,Gr,Cp,M1,Cw,L,Cv,dM,dy);
for s=2:1:4
    if s==2&3
        Ta1=Ta(n)+(a(s-1)/2);
        Tr1=Tr(n)+(b(s-1)/2);
        [Mw]=ViscoA(Tr1);
        [Ma]=ViscoA(Ta1);
        [Minf]=ViscoA(Ta1);
        [ka]=Tcond(Ta1);
        [Ca]=SHair(Ta1);
        [Cv]=SHvap(Ta1);
        [Da]=DensityA(Ta1,W1);
        [Re]=Reynold1(Da,Va,Vr1,Dp,Ma);
        [Pr]=Prandtl(Ca,Ma,ka);
        [h]=Htcoeff(ka,Dp,Re,Pr,Minf,Mw);
        [Ga]=Aflux(Qa,Da,Dd);
        [a(s)]=FRung1(h,ap1,Ta1,Tr1,Ga,Ca,W1,Cv,dy);
        [Cw]=SHwater(Tr1);
        [L]=Lheat(Tr1,M1);
    end
end

```

```

[b(s)]=FRung2(h,ap1,Ta1,Tr1,Gr,Cp,M1,Cw,L,Cv,dM,dy);
else
Ta1=Ta(n)+a(s-1);
Tr1=Tr(n)+b(s-1);
[Mw]=ViscoA(Tr1);
[Ma]=ViscoA(Ta1);
[Minf]=ViscoA(Ta1);
[ka]=Tcond(Ta1);
[Ca]=SHair(Ta1);
[Cv]=SHvap(Ta1);
[Da]=DensityA(Ta1,W1);
[Re]=Reynold1(Da,Va,Vr1,Dp,Ma);
[Pr]=Prandtl(Ca,Ma,ka);
[h]=Htcoeff(ka,Dp,Re,Pr,Minf,Mw);
[Ga]=Aflux(Qa,Da,Dd);
[a(s)]=FRung1(h,ap1,Ta1,Tr1,Ga,Ca,W1,Cv,dy);
[Cw]=SHwater(Tr1);
[L]=Lheat(Tr1,M1);
[b(s)]=FRung2(h,ap1,Ta1,Tr1,Gr,Cp,M1,Cw,L,Cv,dM,dy);
end;
end;
Ta2=Ta(n)+((a(1)+(2*a(2)))+(2*a(3))+a(4))/6;
Ta(n+1)=Ta2;
Tr2=Tr(n)+((b(1)+(2*b(2)))+(2*b(3))+b(4))/6;
Tr(n+1)=Tr2;
end;

function [RH]=RHair(Ta1,W1);
% Function 'RHair.m'
% This function compute Air properties(RH)
pw=(101.325*W1)/(.62198+W1);
pws=exp((-7511.52/(Ta1+273.15))+89.63121+(0.02399897*(Ta1+273.15))...
-(1.1654551*10^-5*((Ta1+273.15)^2))-(1.2810336*10^-8*((Ta1+273.15)^3))...
+(2.0998405*10^-11*((Ta1+273.15)^4))-(12.150799*log(Ta1+273.15)));
RH=pw/pws;

function [Ma]=ViscoA(Ta1);
% Function 'ViscoA.m'
% This function compute the viscosity of air at abitariry temperature
Ma=(1.69111*10^-5)+(4.98424*10^-8*Ta1)-(3.18702*10^-11*Ta1^2)...
+(1.31965*10^-14*Ta1^3);

function [Da]=DensityA(Ta1,W1);
% Function 'DensityA.m'
% This function compute the density of air at abitariry air temperature and humidity ratio
Da= 101.325/(0.28705*(Ta1+273.15)*(1+(1.6078*W1)));

function [Qa]=VolFA(Va,Dd);
% Function 'Vair.m'
% This function compute Air velocity at abitariry flow rate...
% of abitariry dryer diameter
Qa=Va*(pi*Dd^2)/4;

function [VA]=Vair(Qa,Dd);
% Function 'Vair.m'
% This function compute Air velocity at abitariry flow rate...
% of abitariry dryer diameter
VA=(4*Qa)/(pi*Dd^2);

```

```

function [Re]=Reynold1(Da,Va,Vr1,Dp,Ma);
% Function 'Reynold.m'
% This function compute Reynold number
Re=Da*Dp*(Va-Vr1)/Ma;

function [Dg]=DragC2(Re);
% function 'DragC.m'
% This function compute drag coefficient of rice kernel
if Re<1
Dg=24/Re;
elseif Re>=1&Re<1000
Dg=max((24/Re)*(1+(0.15*Re^0.687)),0.44);
elseif Re>=1000&Re<=200000
Dg=0.44;
end;

function [dVr]=DiffVr(Dg,Da,Dr,Dp,Va,Vr1);
% Function 'DiffVr.m'
% This function is the change of Rough rice respect to distance dy
dVr=((3*Dg*Da*((Va-Vr1)^2))/(4*Dr*Dp))-((Dr-Da)*9.81/Dr);

function [t2]=Ntime(dVr,Vr1,t1,dy);
% Function 'Ntime.m'
% This function compute moving time of rough rice for distance dy
a=dVr;
b=Vr1-(2*t1*dVr);
c=(t1^2*dVr)-(t1*Vr1)-dy;
t2=((-1*b)+((b^2)-(4*a*c))^0.5)/(2*a);

function [Vr2]=NrVelocity(Vr1,t2,t1,dVr);
% Function 'NrVelocity.m'
% This function compute velocity of rough rice at distance increment dy
Vr2=Vr1+((t2-t1)*dVr);

function [Me]=Eqmoist(RH,Ta1);
% Function 'Eqmoist.m'
% This function compute equilibrium moisture content of Rough Rice...
% at abritariry air conditions
x=(3.146*10^-6*(273.15+Ta1))^(1/2.464);
y=log(1-RH);
Me=-(y/x)/100;

function [D]=Diffuse(Tr1)
% Function 'Diffuse.m'
% This function compute Diffusion coefficient of water inside Rough...
% Rice kernel at abitariry Air Temperature
D=5.68033*10^-6*exp(-3445.66/(Tr1+273.15));

% This program compute moisture districution inside rice kernel
% at constant drying condition and time t
function [Mav,Mt]=MDistb_Sim2(M0,Me,DF,t1,t2,Dp)
% Find time step and radius increment during simulation
dt=t2-t1;
dDp=Dp/(2*1000);
%Start Calculation
k=1;
t=k*dt;
% Compute radius increment
for i=1:1001
R(i)=(i-1)*dDp;

```

```

end;
% Set initial moisture distribution
MI=M0;
M1=M0;
% Create System of equation for moisture distribution
i=1;
B(i)=-((3/(dDp^2))+(1/(DF*dt)));
C(i)=3/(dDp^2);
D(i)=-(((3/(dDp^2))-(1/(DF*dt)))*M1(i))-(M1(i+1)*3/(dDp^2));
for i=2:999
    A(i)=(1/(2*dDp^2))*(1-(1/(i-1)));
    B(i)=-((1/(DF*dt))+(1/(dDp^2)));
    C(i)=(1/(2*dDp^2))*(1+(1/(i-1)));
    D(i)=-((1/(2*dDp^2))*(1-(1/(i-1)))*M1(i-1))-(((1/(DF*dt))-(1/(dDp^2)))*M1(i))...
        -((1/(2*dDp^2))*(1+(1/(i-1)))*M1(i+1)));
end;
i=1000;
    A(i)=(1/(2*dDp^2))*(1-(1/(i-1)));
    B(i)=-((1/(DF*dt))+(1/(dDp^2)));
    D(i)=-((1/(2*dDp^2))*(1-(1/(i-1)))*M1(i-1))-(((1/(DF*dt))-(1/(dDp^2)))*M1(i))...
        -((1/(2*dDp^2))*(1+(1/(i-1)))*M1(i+1))-((1/(2*dDp^2))*(1+(1/(i-1)))*Me);
% Solve System of equation
% Forward Substitution
for i=2:1000
    A(i)=A(i)/B(i-1);
    B(i)=B(i)-(A(i)*C(i-1));
    D(i)=D(i)-(A(i)*D(i-1));
end;
%Backward Substitution
Mt(1001)=Me;
Mt(1000)=D(1000)/B(1000);
for i=999:-1:1
    Mt(i)=(D(i)-(C(i)*Mt(i+1)))/B(i);
end;
% Find Average Moisture content by Composite Simpson's rule
Mav=0;
b=4/(1000*(Dp^2));
for i=2:1000
    if mod(i,2)==0
        sum=4*b*Mt(i)*(R(i)^2);
        Mav=Mav+sum;
    else
        sum=2*b*Mt(i)*(R(i)^2);
        Mav=Mav+sum;
    end;
end;
sum=b*Mt(1001)*(R(1001)^2);
Mav=Mav+sum;
% Create the average moisture profile
for i=1:1001
    Mf(i)=Mav;
end;

function [mr]=RMflow(mrw,M1);
% Function 'RMflow.m'
% This function compute Flow rate of rough rice dry mass
mr=mrw-(mrw*(M1/(1+M1)));

```

```

function [ma]=AMflow(Qa,Da);
% Function 'AMflow.m'
% This function compute Mass flow rate of dry air
ma=Qa*Da;

function [W2]=NHumid(W1,mr,ma,M2,M1);
% Function 'NHumid.m'
% This function compute humidity ratio of air for next distance dy
W2=W1-((mr/ma)*(M2-M1));

function [Gr]=Rflux(mr,Dd);
% Function 'Rflux.m'
% This function compute the Mass flux of Rough rice across the cross...
% section of dryer
Gr=4*mr/(pi*Dd^2);

function [dM]=DiffM(M2,M1,dy);
% Function 'DiffM.m'
% This function compute change of moisture during distance dy
dM=(M2-M1)/dy;

function [Cp]=SHrice(M1);
% Function 'SHrice.m'
% This function compute specific heat of rough rice
Cp=(1.11+(4.48*(M1/(M1+1))))*10^3;

function [Ga]=Aflux(Qa,Da,Dd);
% Function 'Aflux.m'
% This function compute Mass flux of air across the cross section of dryer
Ga=(4*Da*Qa)/(pi*Dd^2);

function [ap]=SParea1(mr,t1,t2,Dr,dy,Dp,Dd);
% Function 'SParea1.m'
% This function compute specific surface area of rough rice
ap=24*mr*(t2-t1)/(pi*Dr*dy*Dp*Dd^2);

function [ka]=TCond(Ta1);
% Function 'TCond.m'
% This function compute Thermal Conductivity of air at abitary temperature
ka=(2.42503*10^-2)+(7.88913*10^-5*Ta1)-(1.79034*10^-8*Ta1^2)...
-(8.5705*10^-12*Ta1^3);

function [Ca]=SHair(Ta1);
% Function 'SHair.m'
% This function compute specific heat of air at abitary temperature
Ca=1009.26-(4.043033*10^-2*Ta1)+(6.17596*10^-4*Ta1^2)...
-(4.09723*10^-7*Ta1^3);

function [Cv]=SHvap(Ta1);
% Function 'SHvap.m'
% This function compute specific heat of vapor in the air at abitary temperature
Cv=1883-(0.1674*(Ta1+273.15))+(8.439*10^-4*((273.15+Ta1)^2))...
-(2.6967*10^-7*((273.15+Ta1)^3));

function [Pr]=Prandtl(Ca,Ma,ka);
% Function 'Prandtl.m'
% This function compute Prandtl Number
Pr=Ca*Ma/ka;

```

```

function [h]=Htcoeff(ka,Dp,Re,Pr,Minf,Mw)
% Function 'Htcoeff.m'
% This function compute Heat transfer coefficient between Rough rice and moving air
h=(ka/Dp)*((((Minf/Mw)^0.25)*(Pr^0.4)*((0.4*Re^0.5)+(0.06*Re^(2/3))))+2);

function [FR1]=FRung1(h,ap,Ta1,Tr1,Ga,Ca,W1,Cv,dy);
% Function 'FRung1.m'
% This function is the change of air temperature respect ot distance dy
% Solution of this equation solve by Runge-Kutta 4th method
FR1=dy*(-1*h*ap*(Ta1-Tr1))/(Ga*(Ca+(W1*Cv)));

function [Cw]=SHwater(Tr1);
% Function 'SHwater.m'
% This function compute specific heat of water in rough rice
Cw=2822.32+(11.8277*(273.15+Tr1))-(3.5047*10^-2*((273.15+Tr1)^2))...
+(3.601*10^-5*((273.15+Tr1)^3));

function [L]=Lheat(Tr1,M1);
% Function 'Lheat.m'
% This function compute heat of vaporization of water in rough rice
L=(2502-(2.386*Tr1))*(1+(2.49*exp(-21.733*M1)))*1000;

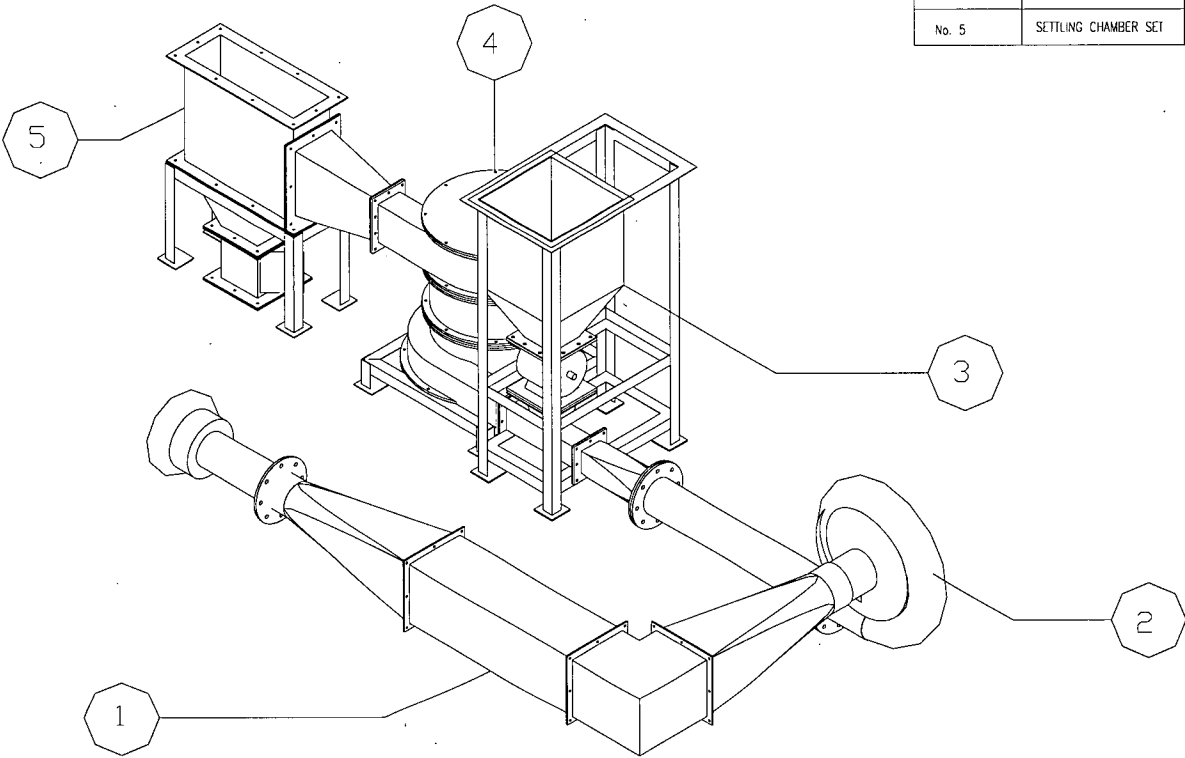
function [FR2]=FRung2(h,ap,Ta1,Tr1,Gr,Cp,M1,Cw,L,Cv,dM,dy);
% Function 'FRung2.m'
% This function is the change of rough rice temperature respect to distance dy...
% Solution of this equation find by Runge-kutta 4th order method
FR2=((h*ap*(Ta1-Tr1)/Gr)+((L+(Cv*(Ta1-Tr1))*dM))*(dy/(Cp+(M1*Cw))));

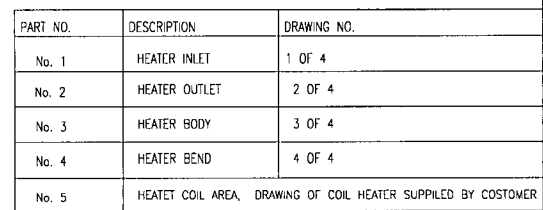
% Program 'Parameter4.m'
% Input parameter of Penumatic rice dryer
disp('Please input parameter for penumatic rice drying')
disp('Air parameter')
Ta1=input('Initial air temperature');
W1=input('Initial humidity ratio of air');
Va=input('Air Inlet Velocity');
disp('Rough rice parameter')
Tr1=input('Initial grain temperature');
M1=input('Initial moisture content of rough rice');
mrw=input('Feed rate of rough rice');
Vr1=input('Initial velocity of rough rice particle');
t1=input('Time at start');
Dp=0.0035;
disp('Dryer parameter')
Dd=input('Diameter of dryer');
dy=input('Hight increment during simulation');

```

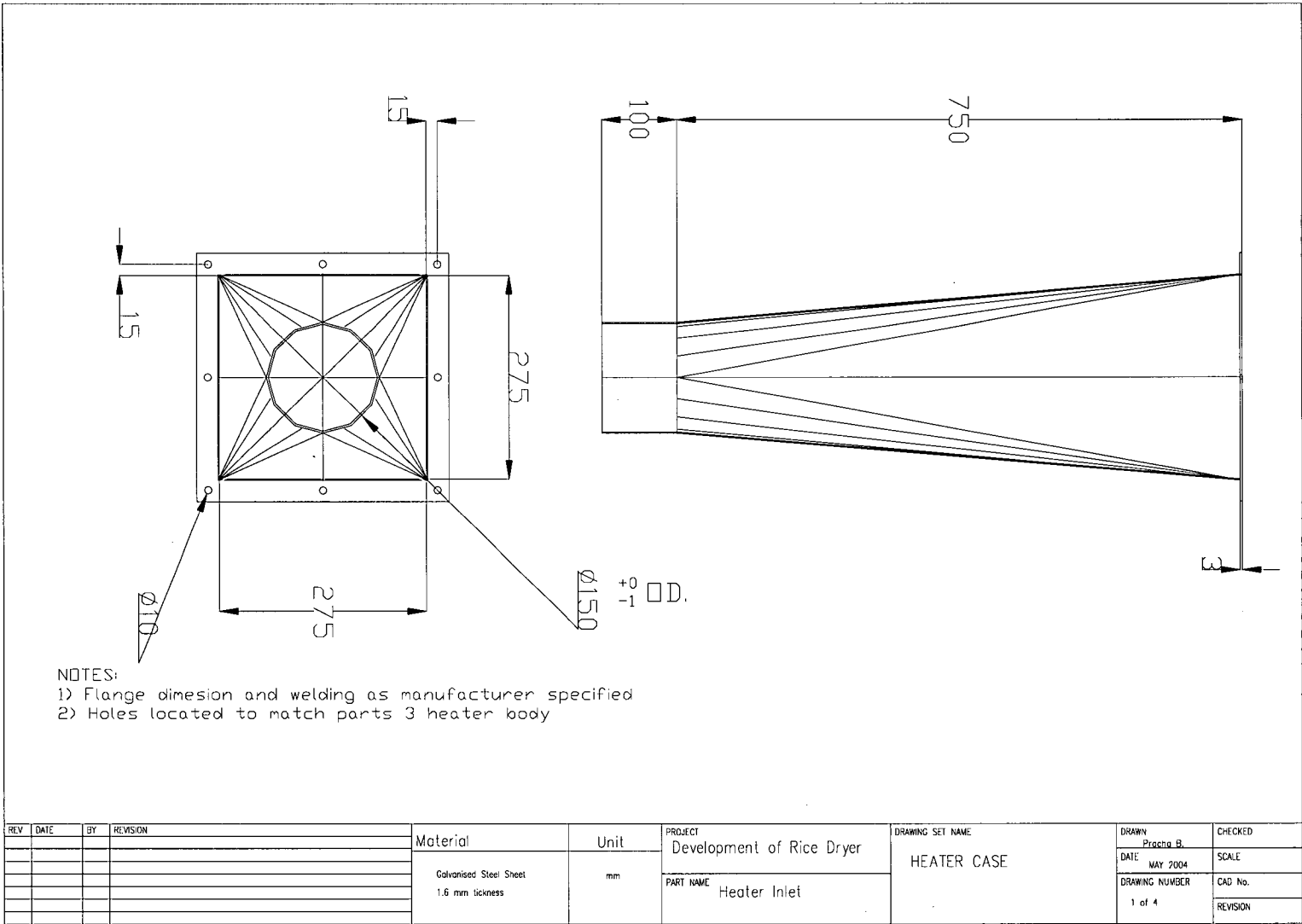

Appendix B.

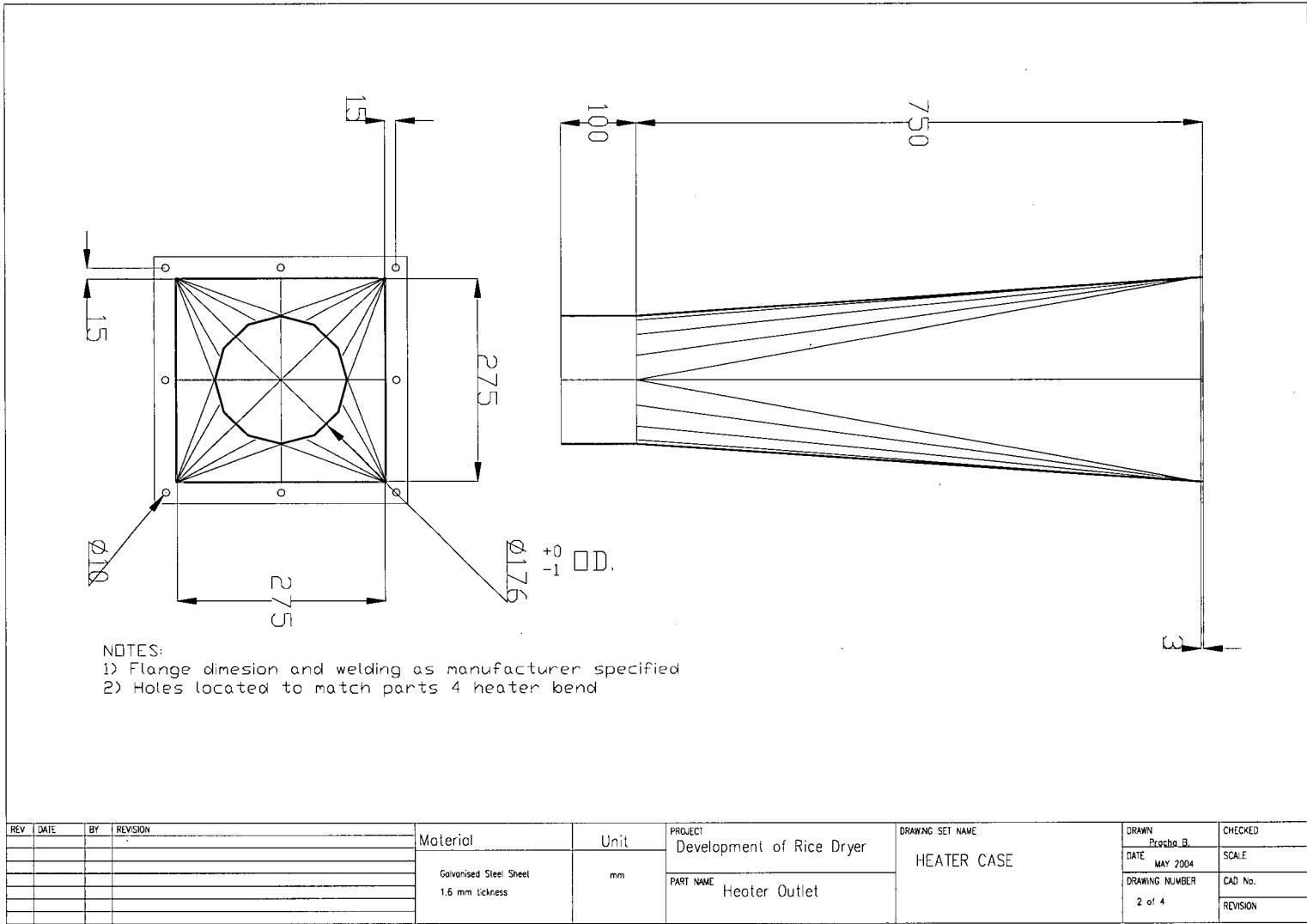
Drawings of Cyclone Dryer, Rotary Feeder, Heater and Settling Chamber

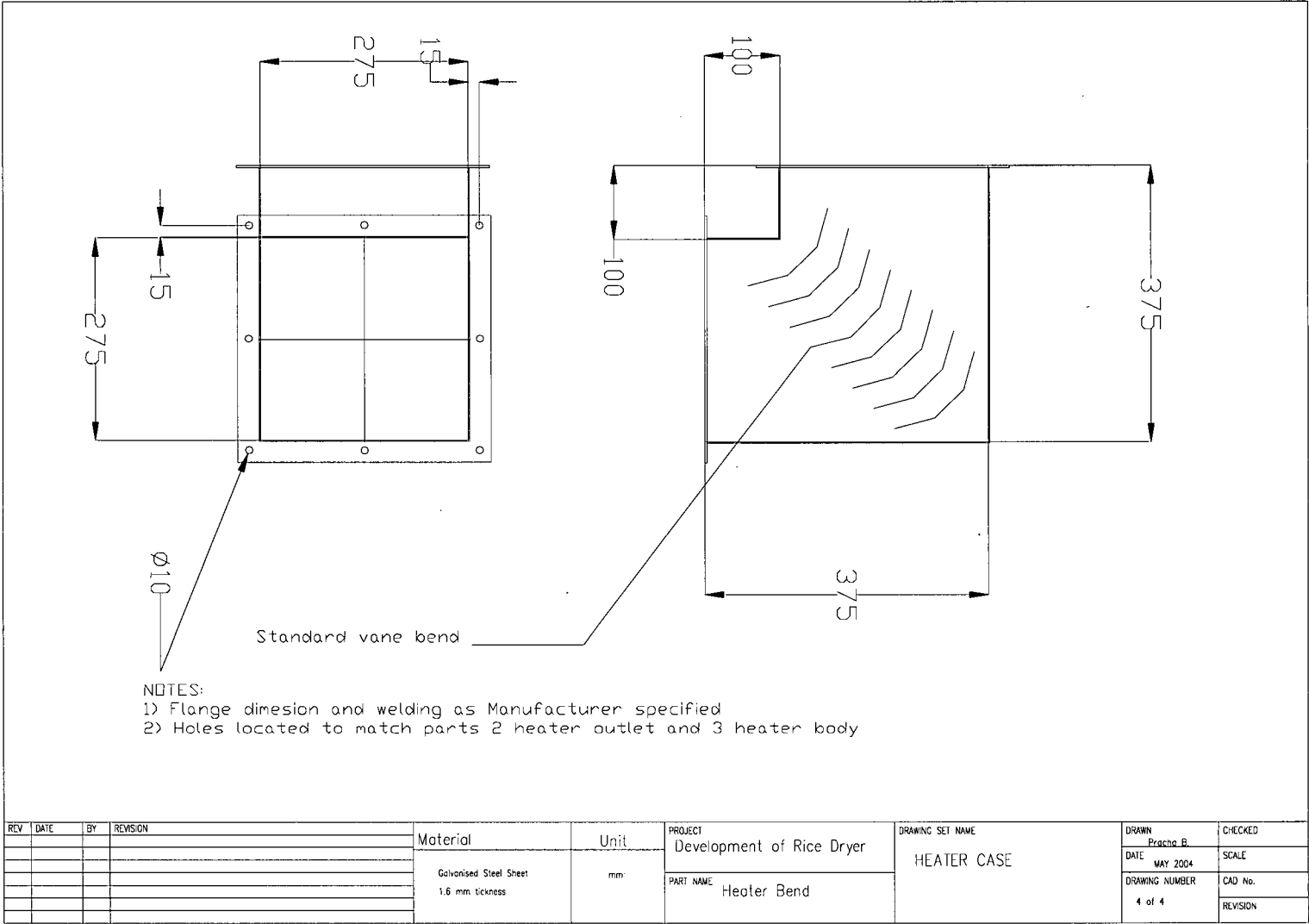




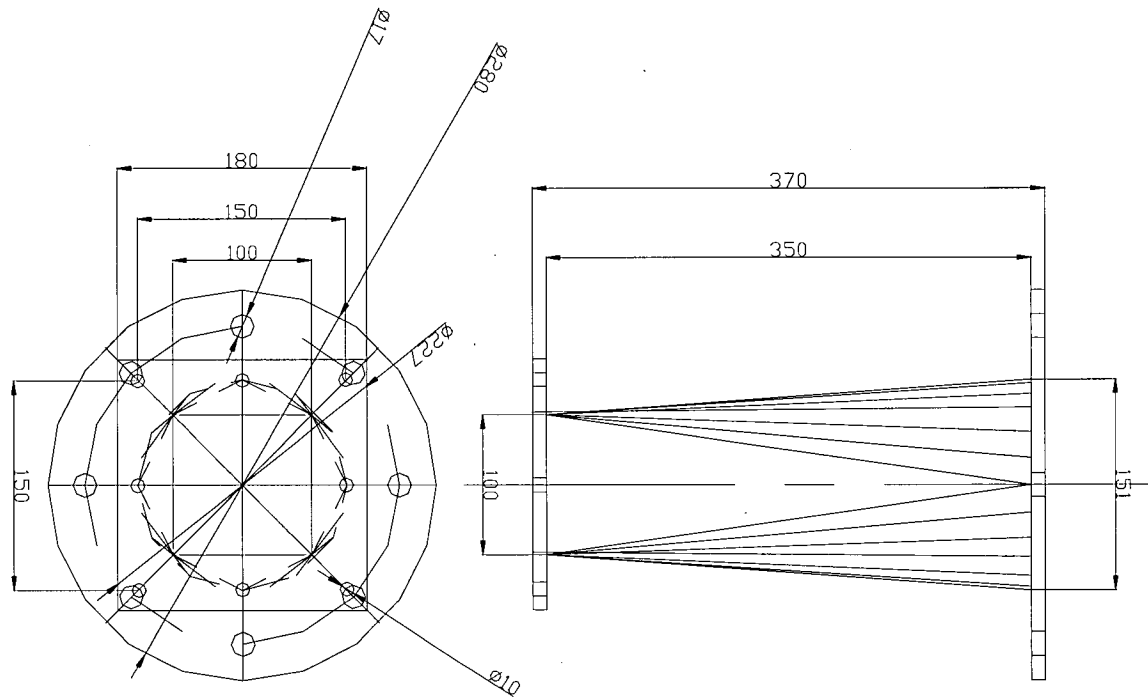
REV	DATE	BY	REVISION	Material	Unit	PROJECT Development of Rice Dryer	DRAWING SET NAME HEATER CASE	DRAWN Prasanna B.	CHECKED	
								Part of Cyclone Dryer	DATE MAY 2004	SCALE
									DRAWING NUMBER	CAD No.
										REVISION



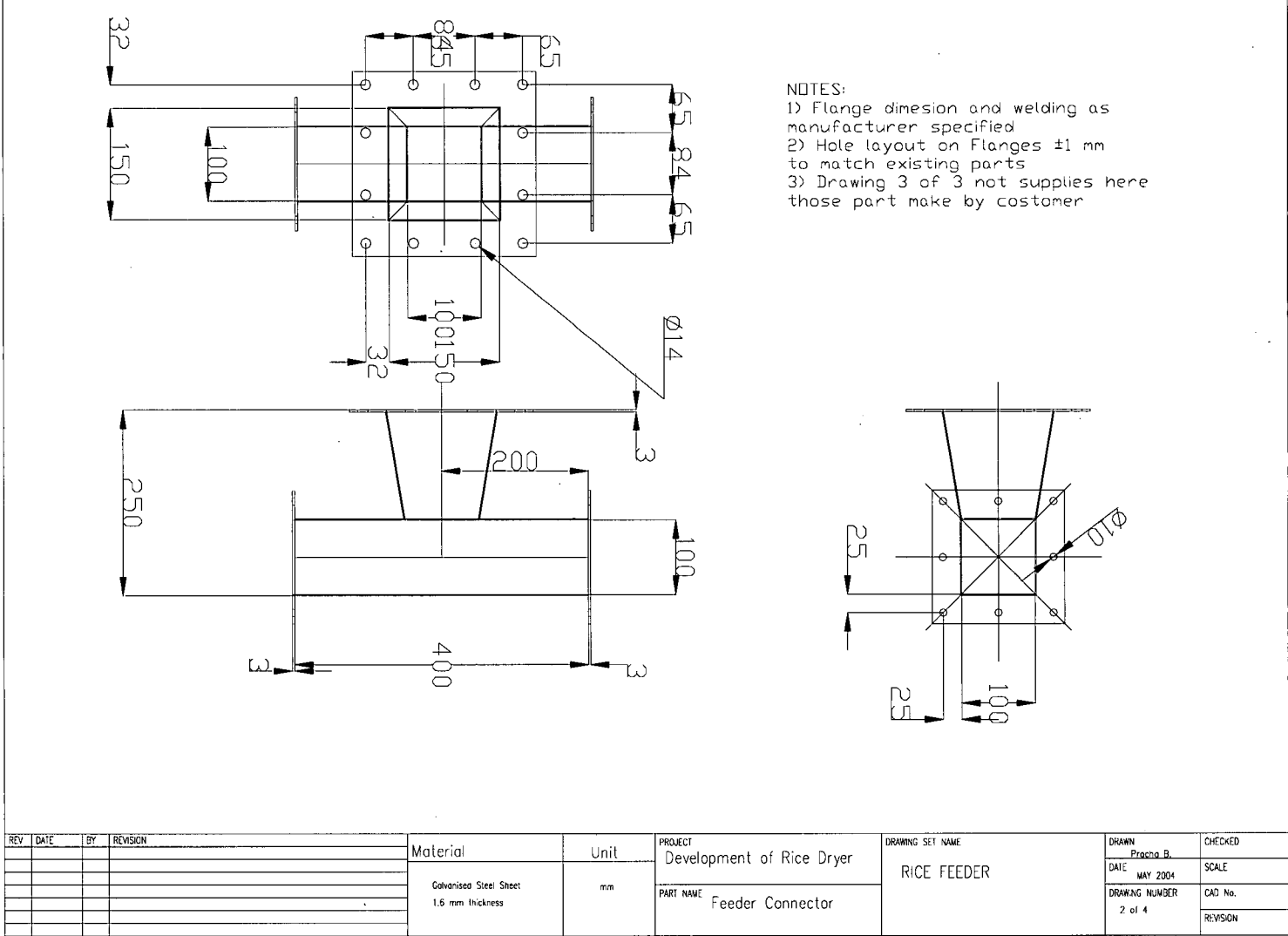


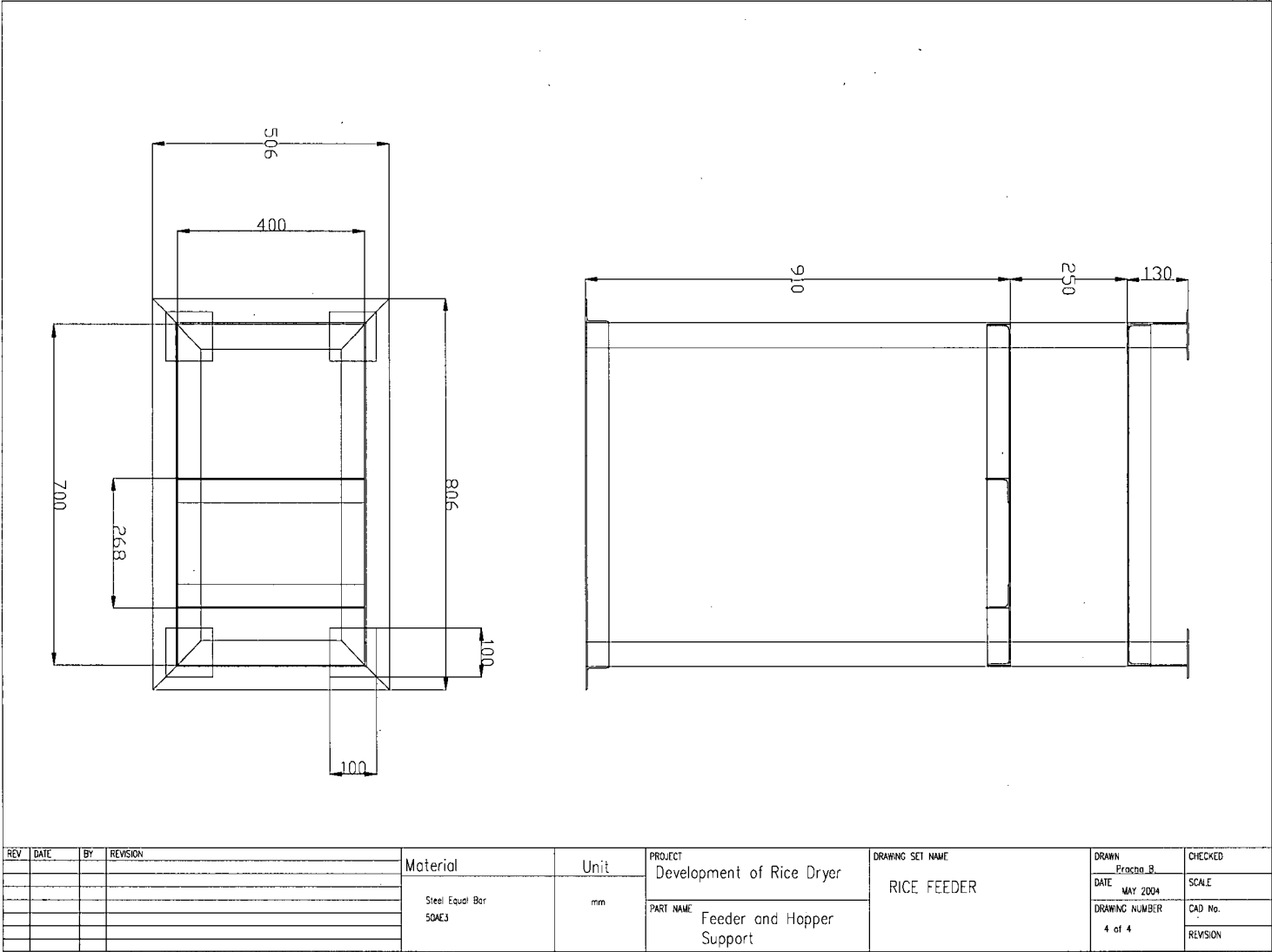


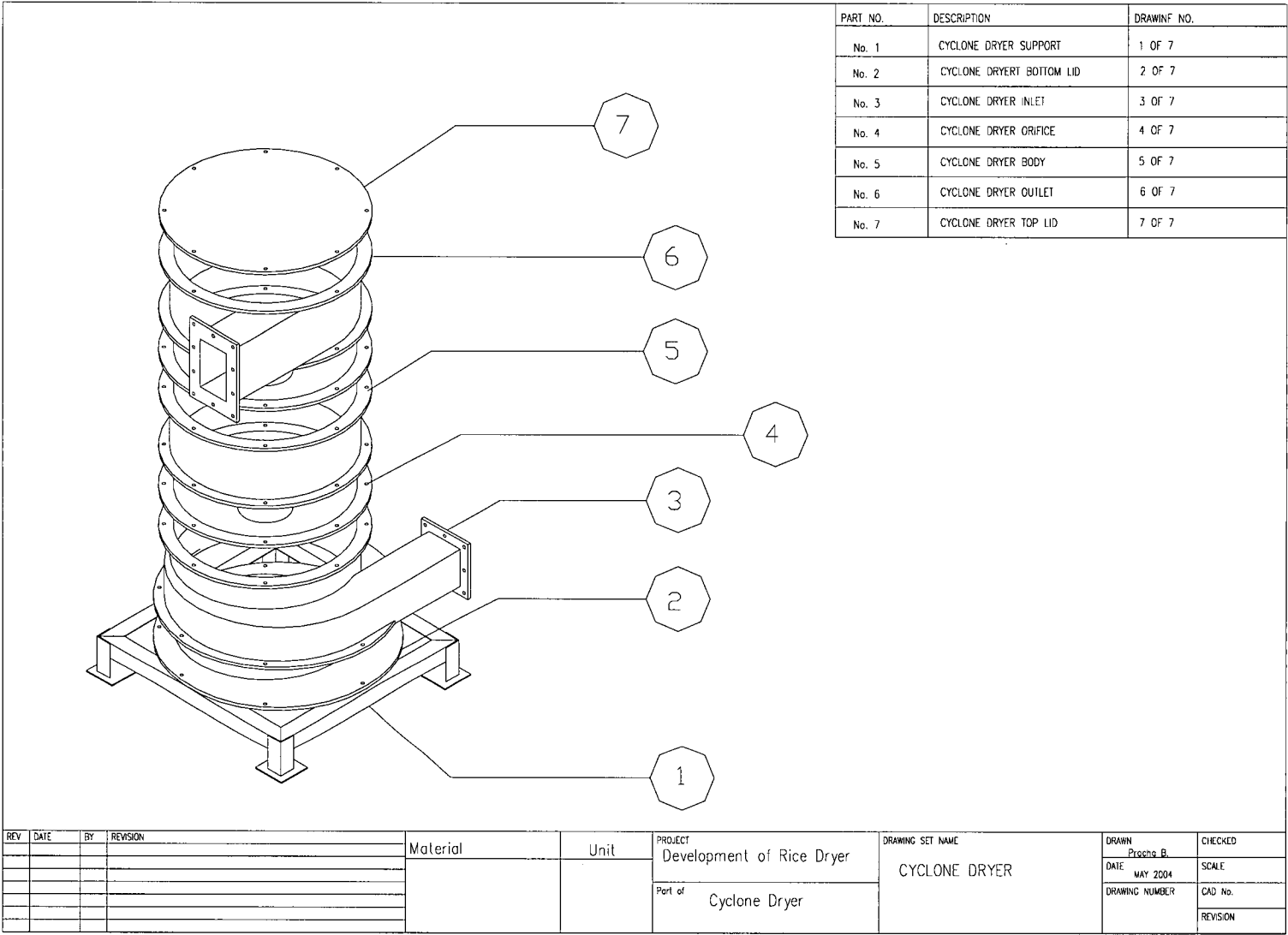
[illegible][illegible]

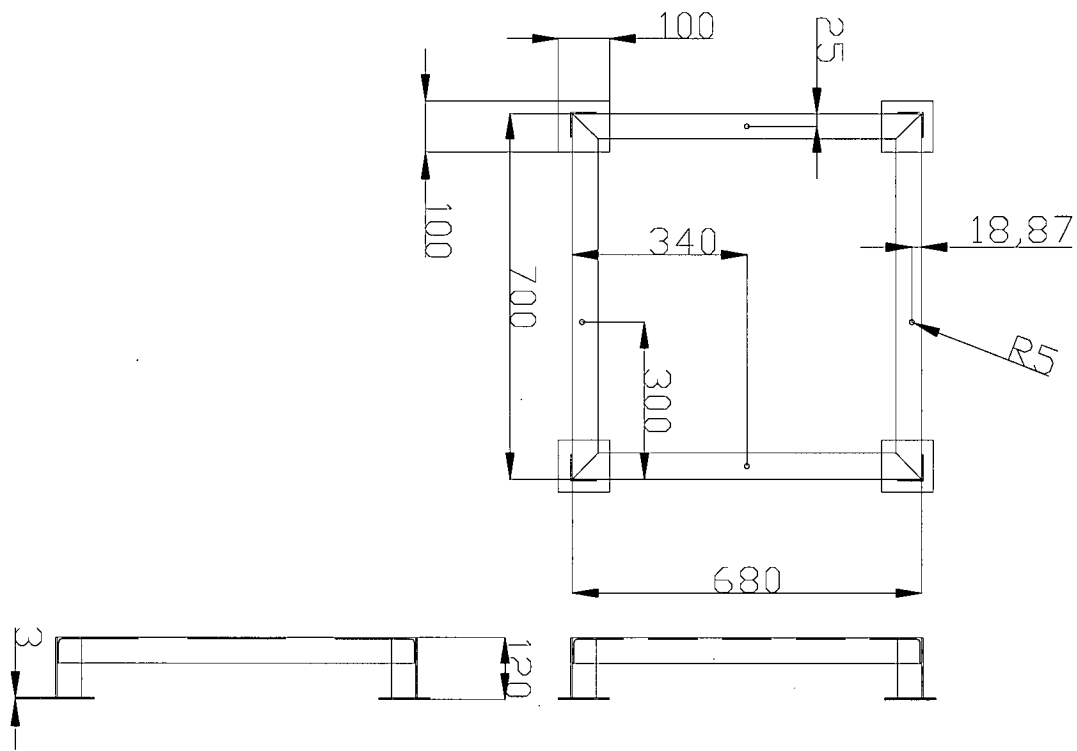


REV	DATE	BY	REVISION	Material	Unit	PROJECT Development of Rice Dryer	DRAWING SET NAME RICE FEEDER	DRAWN Prescho B.	CHECKED
								DATE MAY 2004	SCALE
				Steel Sheet	mm	PART NAME Pipe Contraction		DRAWING NUMBER	CAD No.
				1 mm thickness				1 OF 4	REVISION

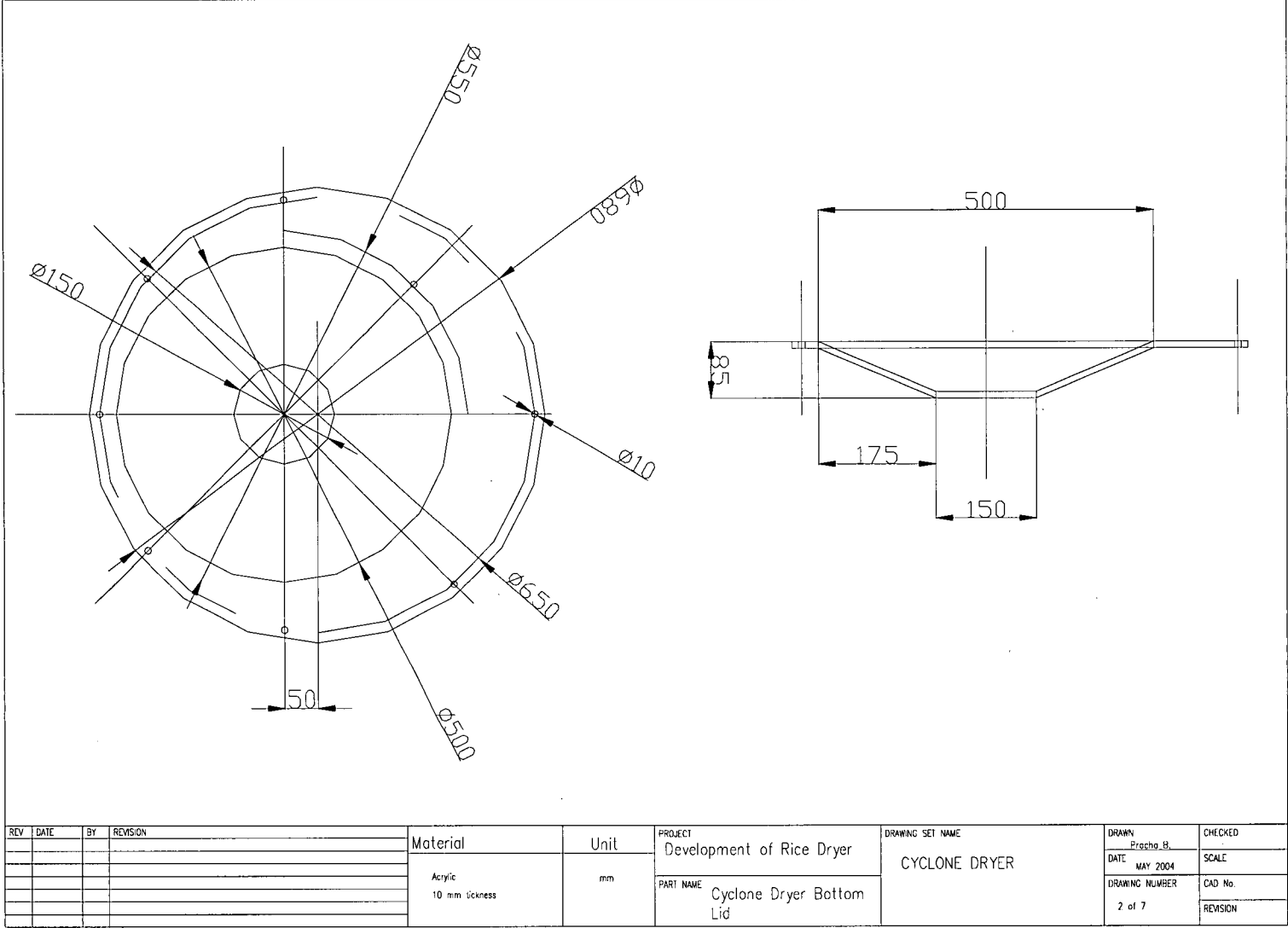


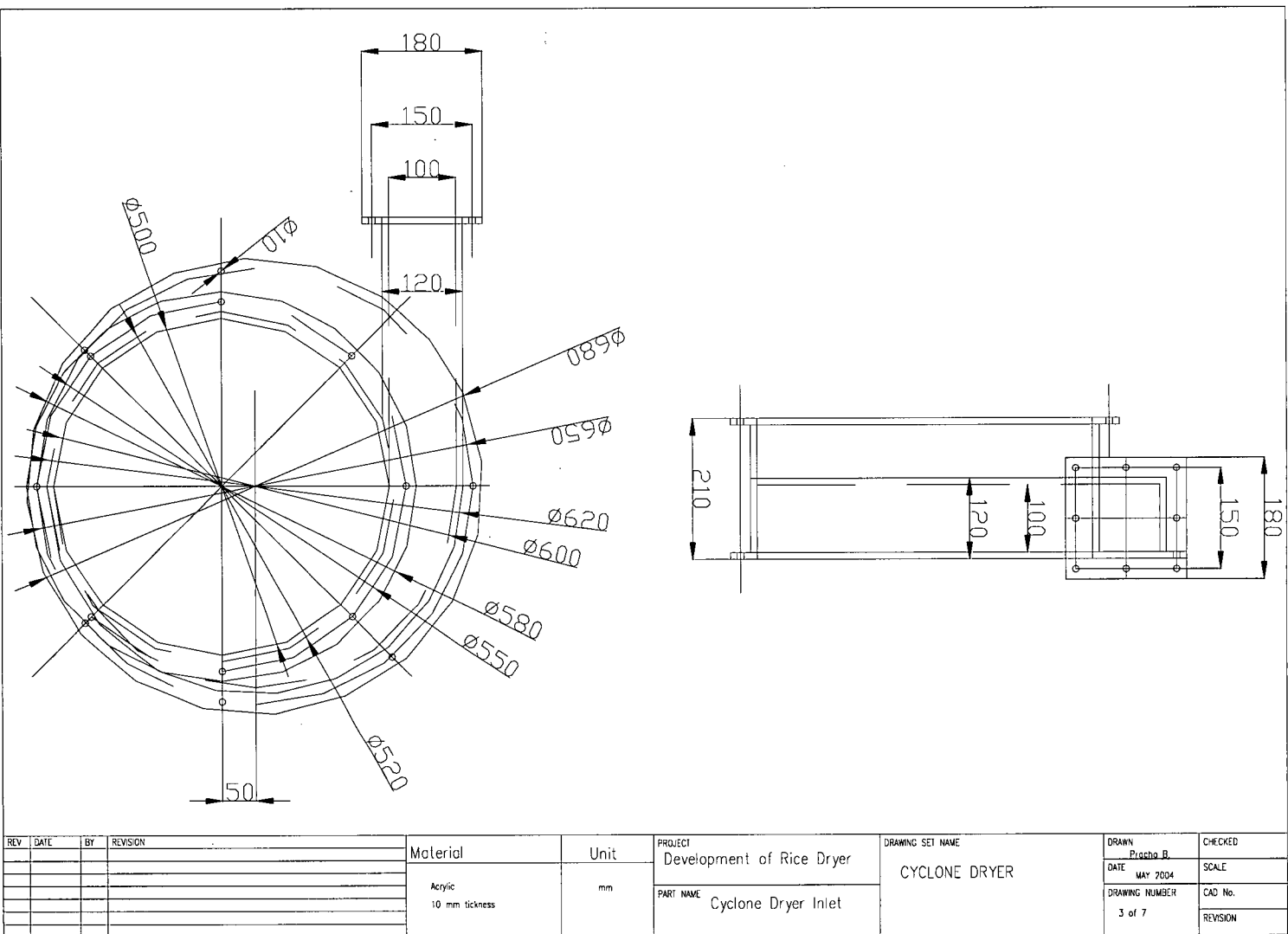


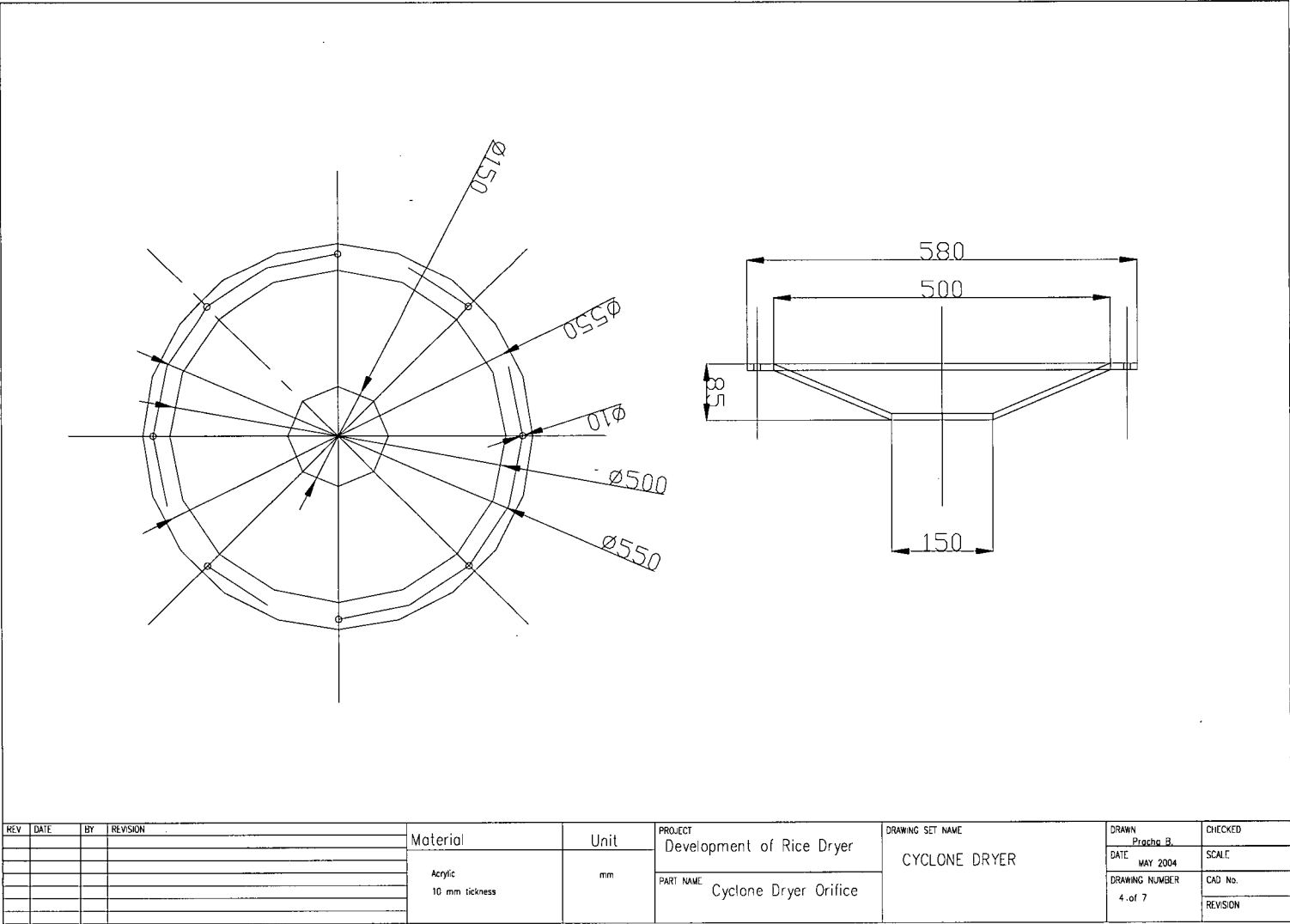


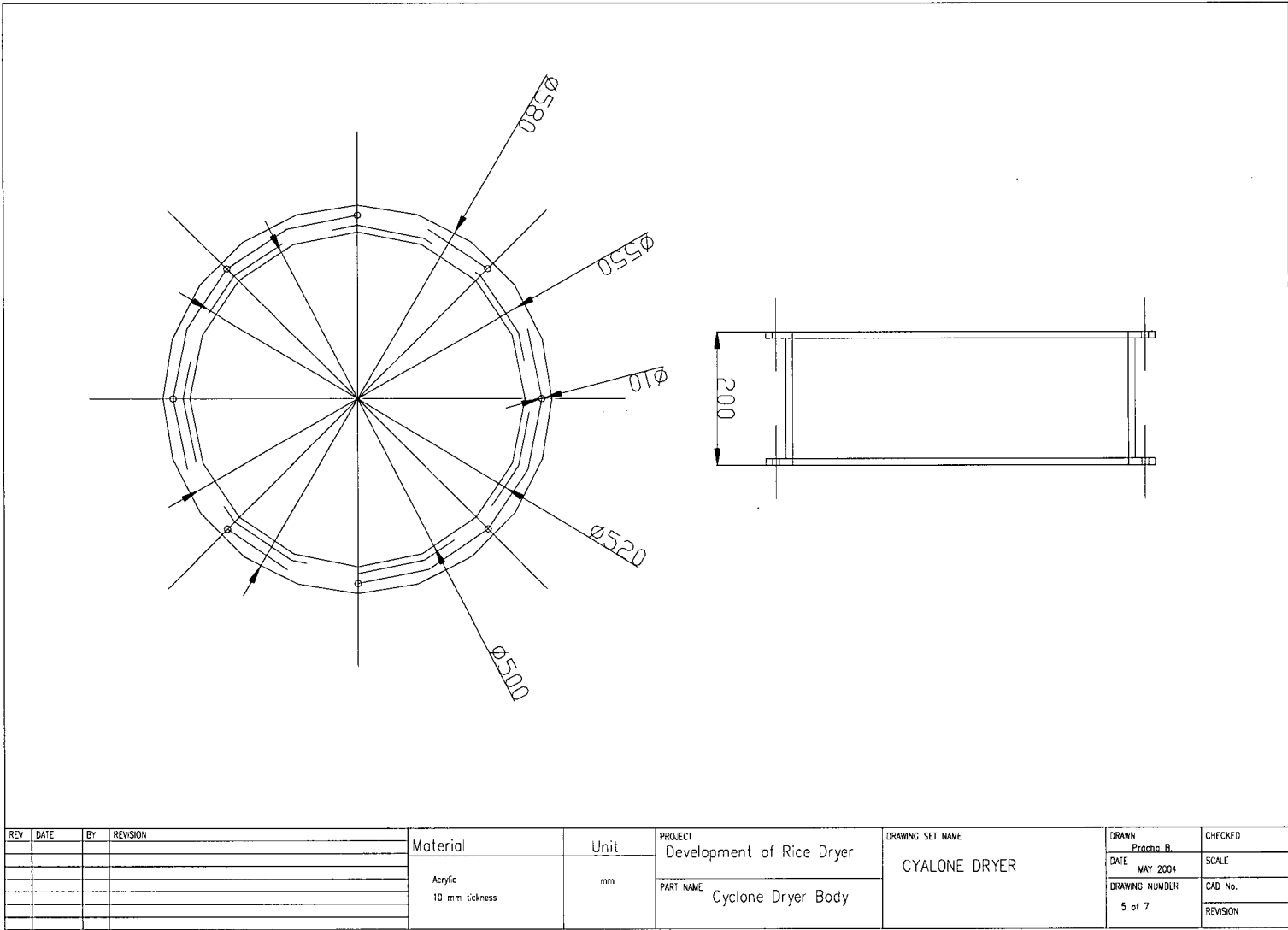


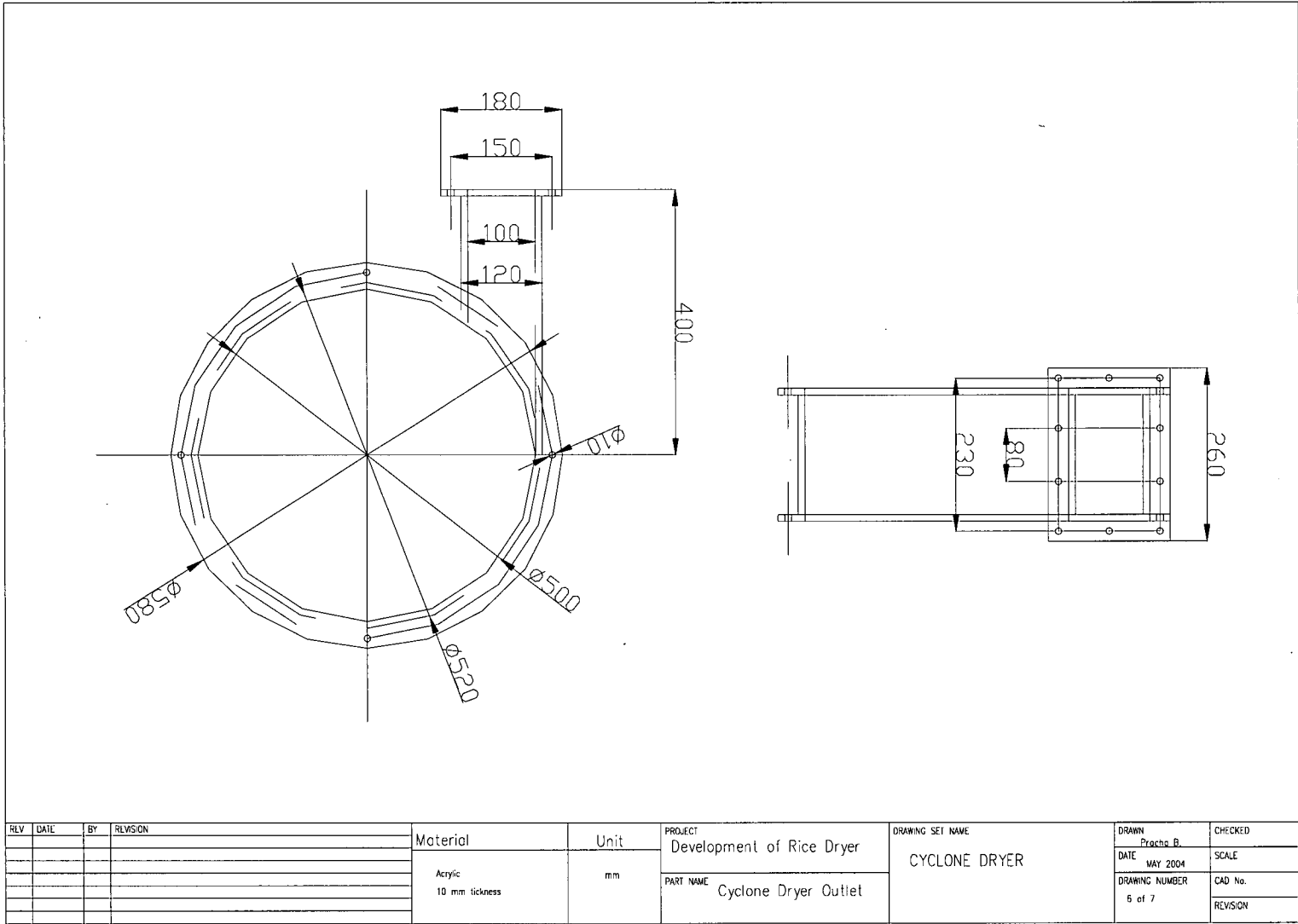
REV	DATE	BY	REVISION	Material	Unit	PROJECT Development of Rice Dryer	DRAWING SET NAME CYCLONE DRYER	DRAWN Prachin B.	CHECKED
				Equal Angle Steel 50AE3	mm	PART NAME Cyclone Dryer Support		DATE MAY 2004	SCALE
								DRAWING NUMBER 1 of 7	CAD No. REVISION

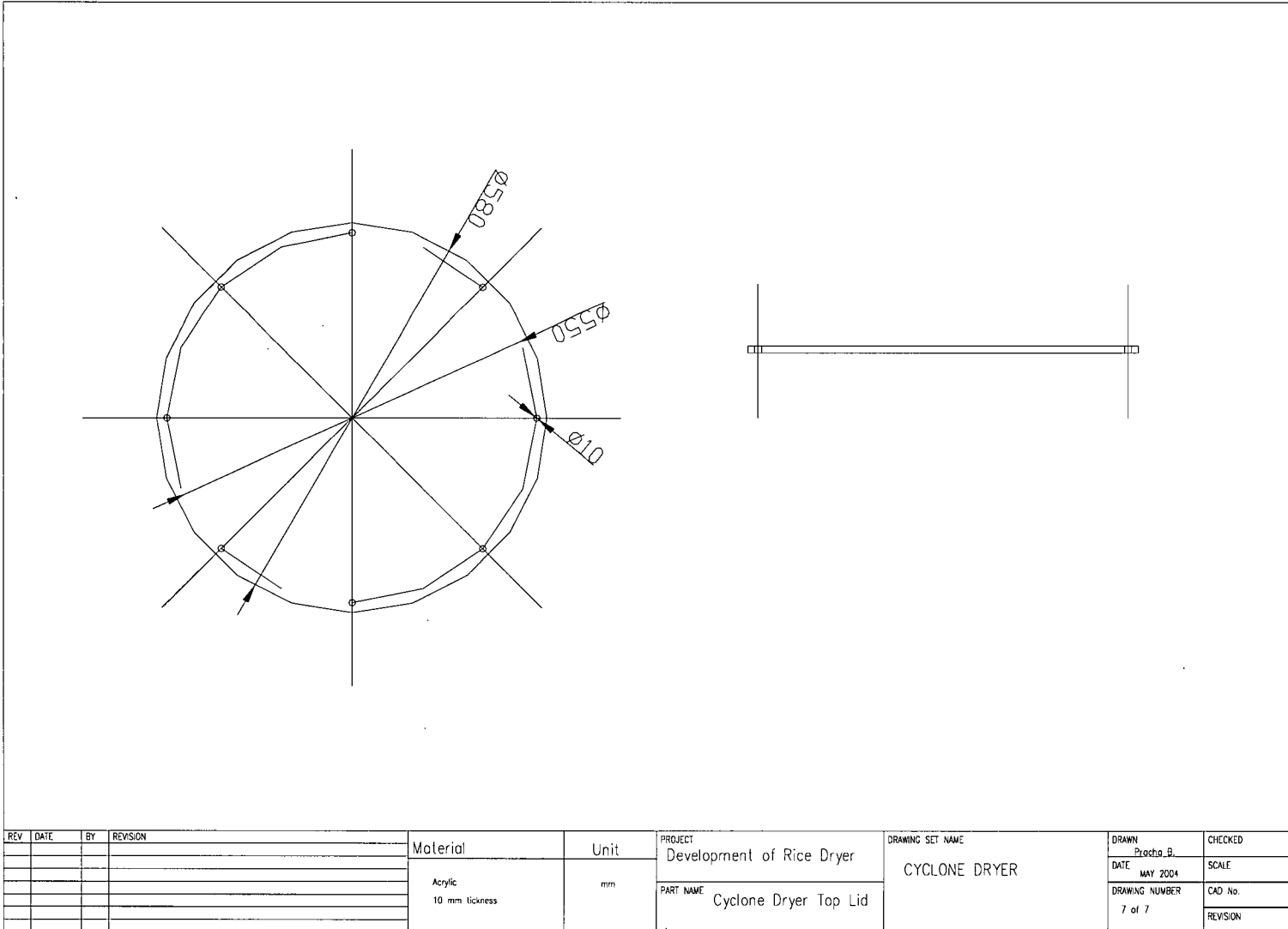


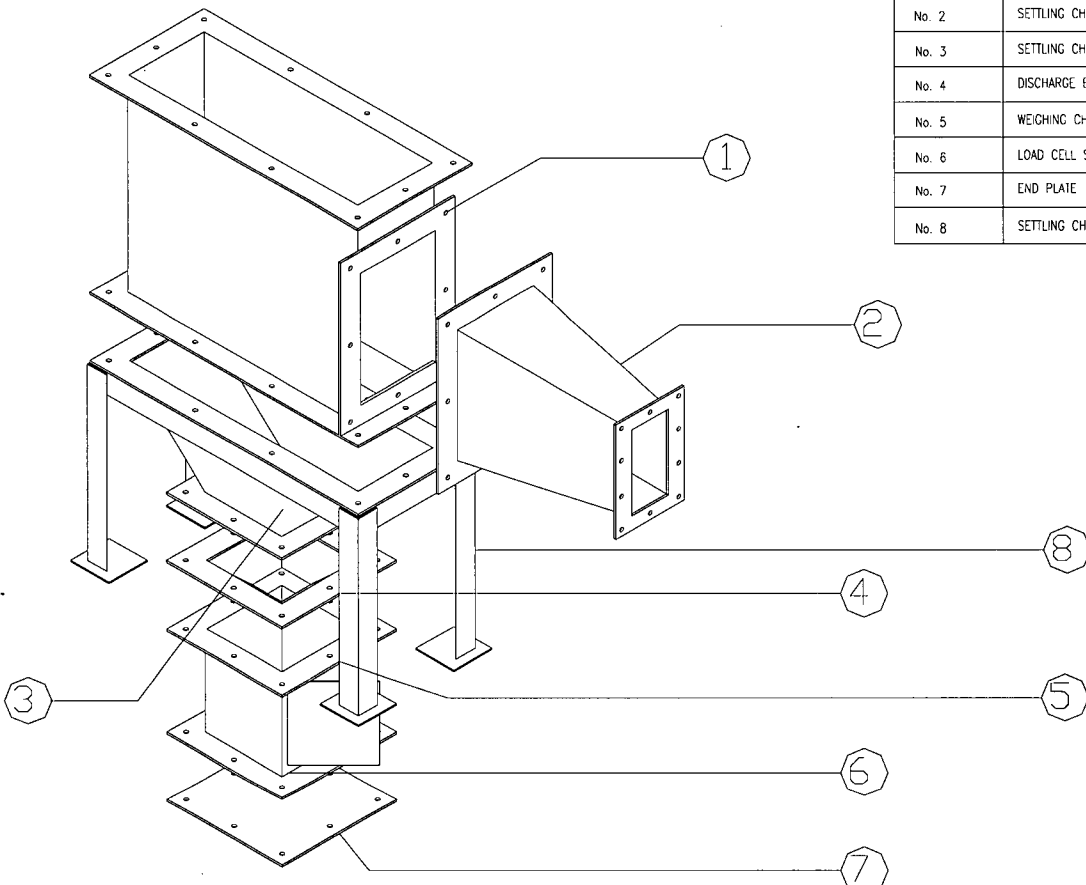


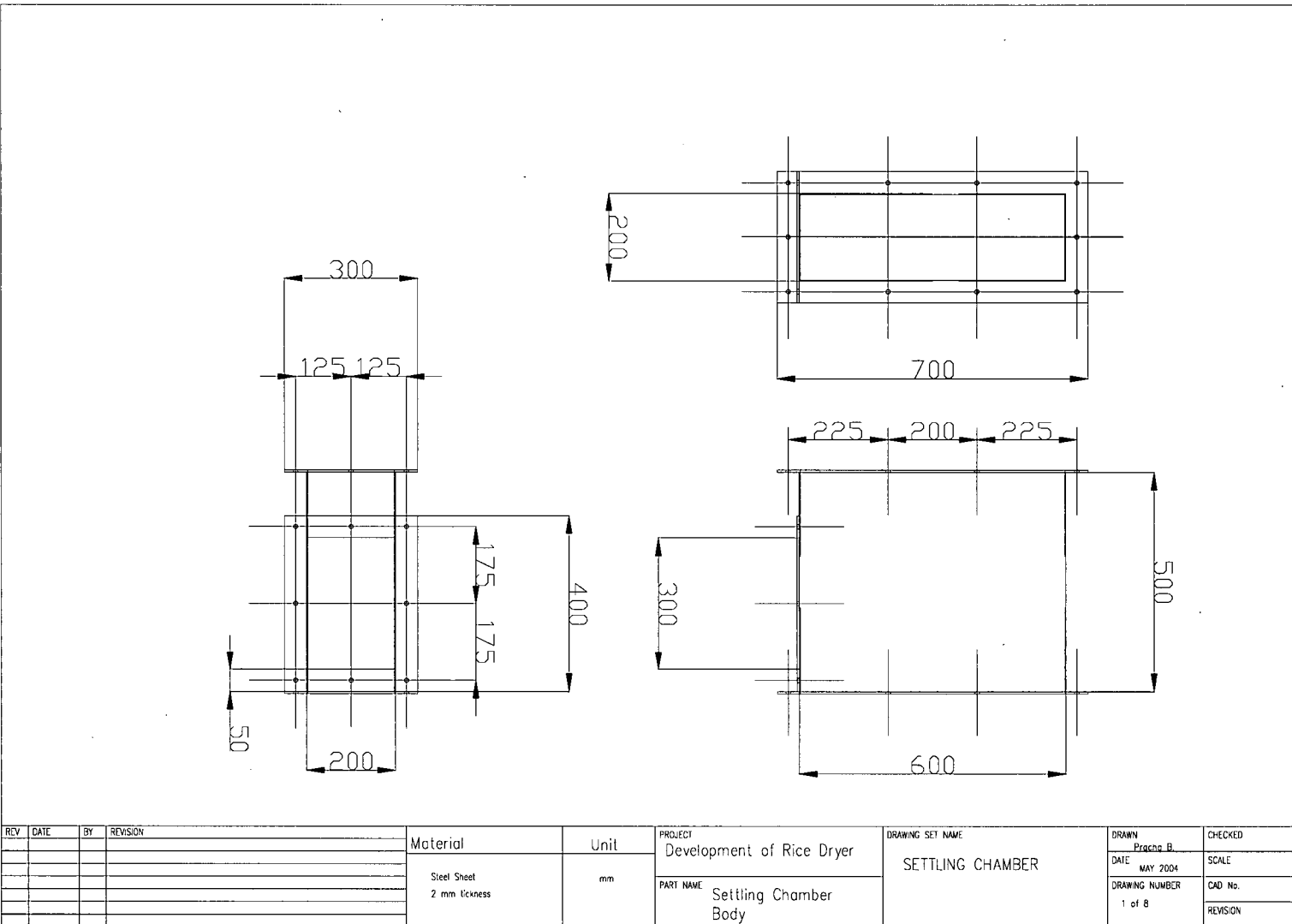


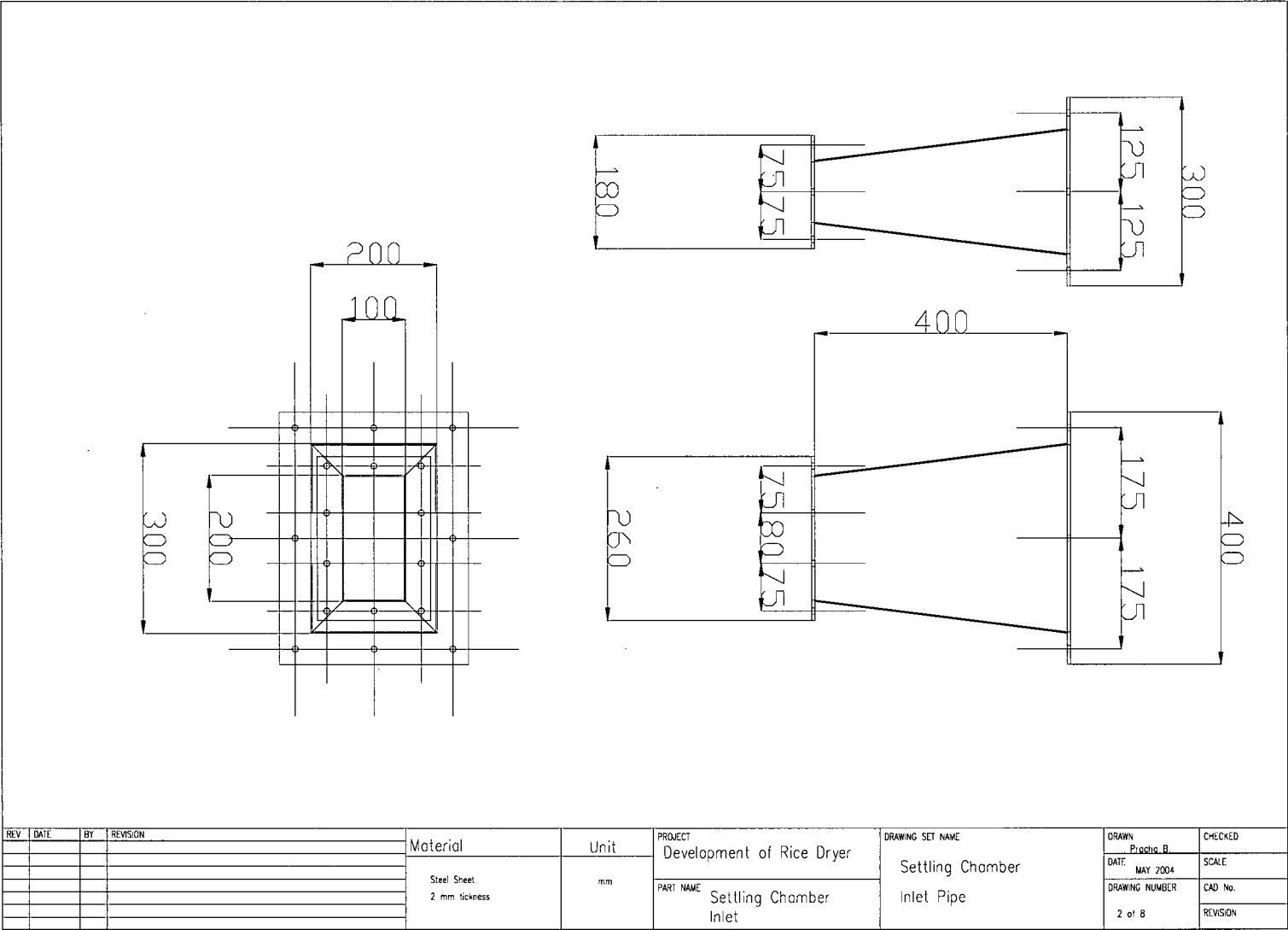


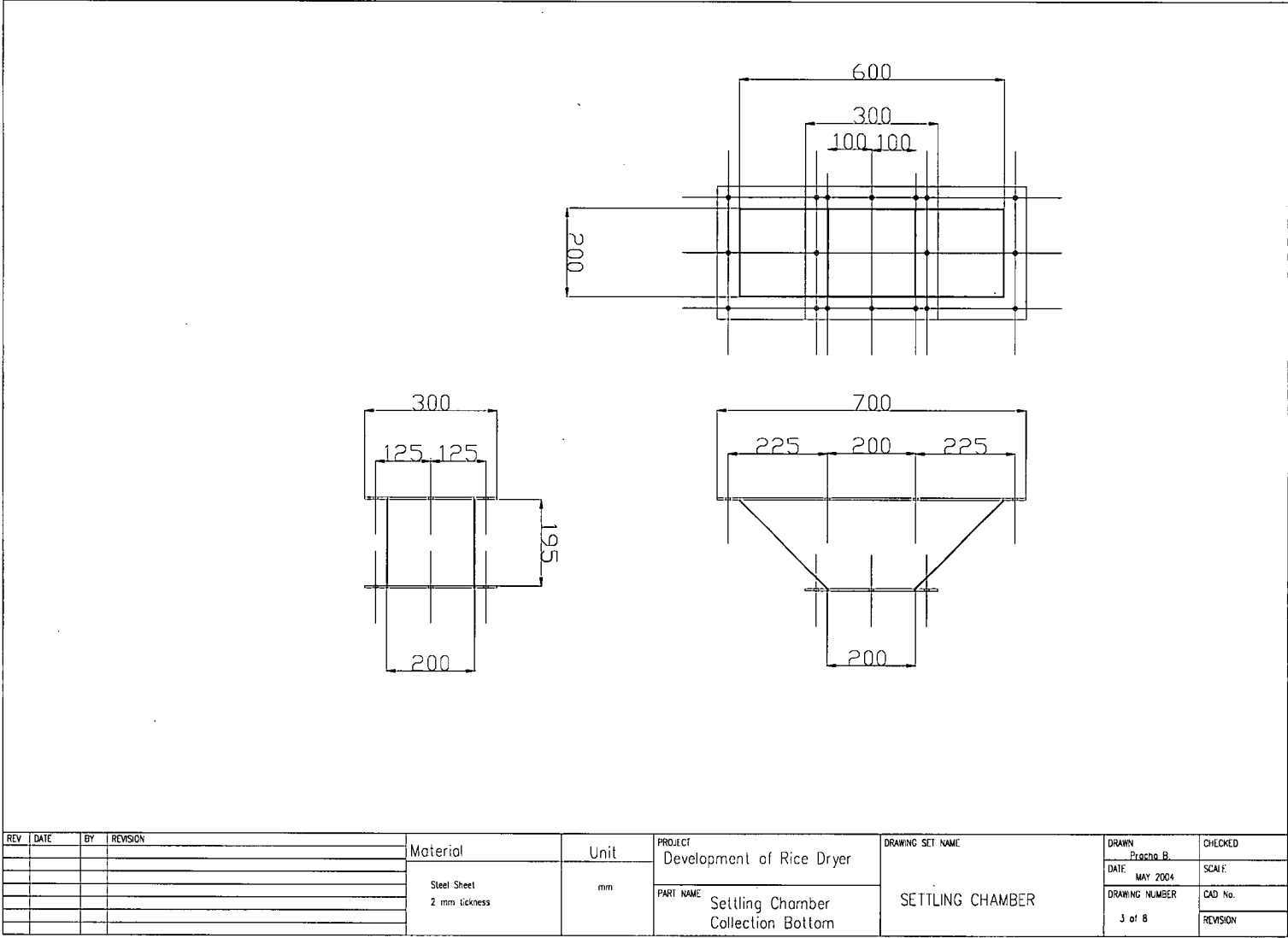


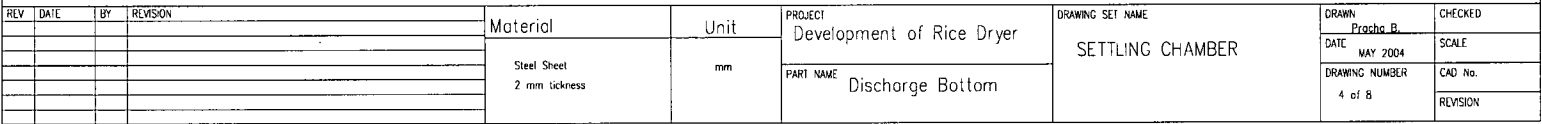


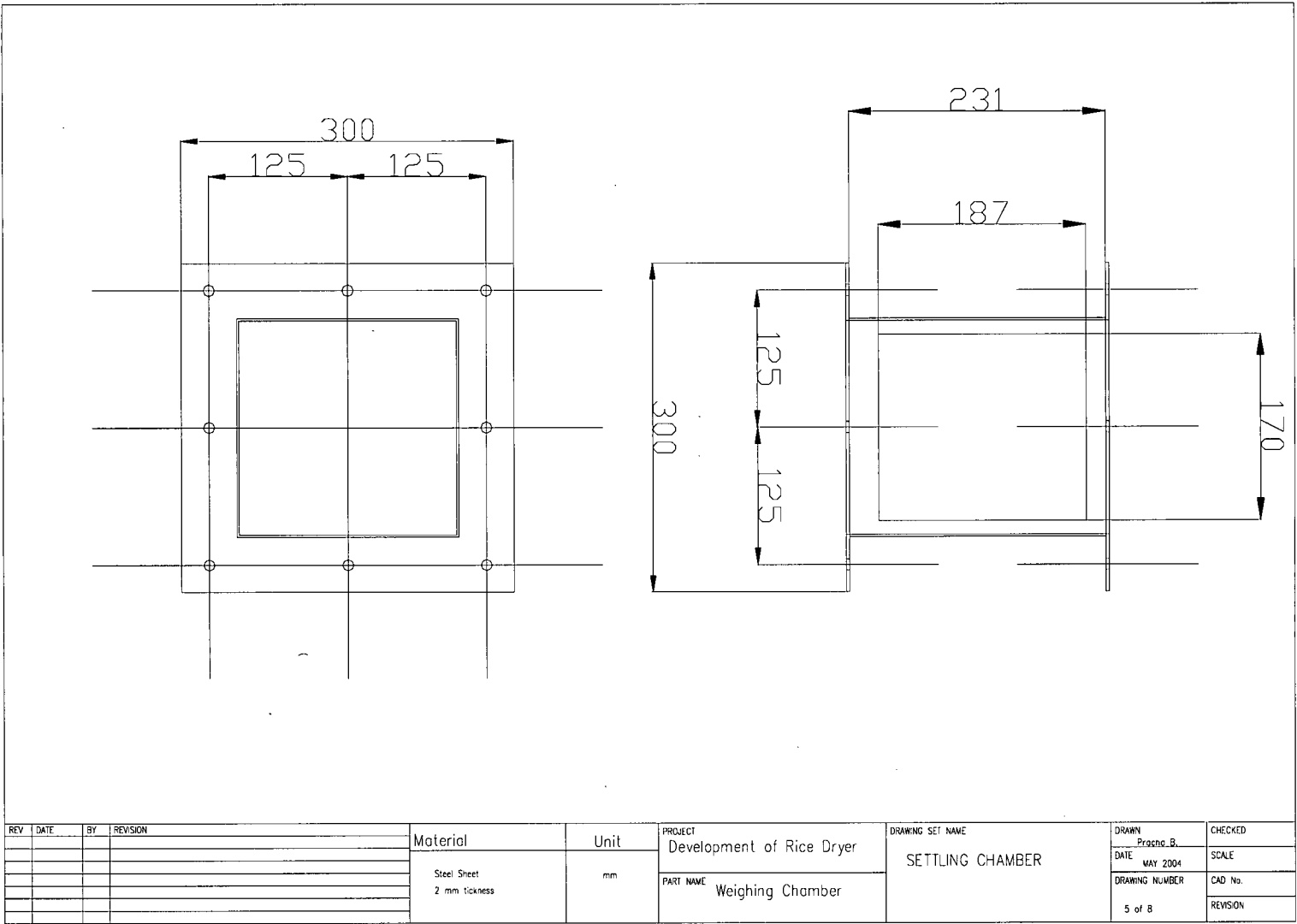


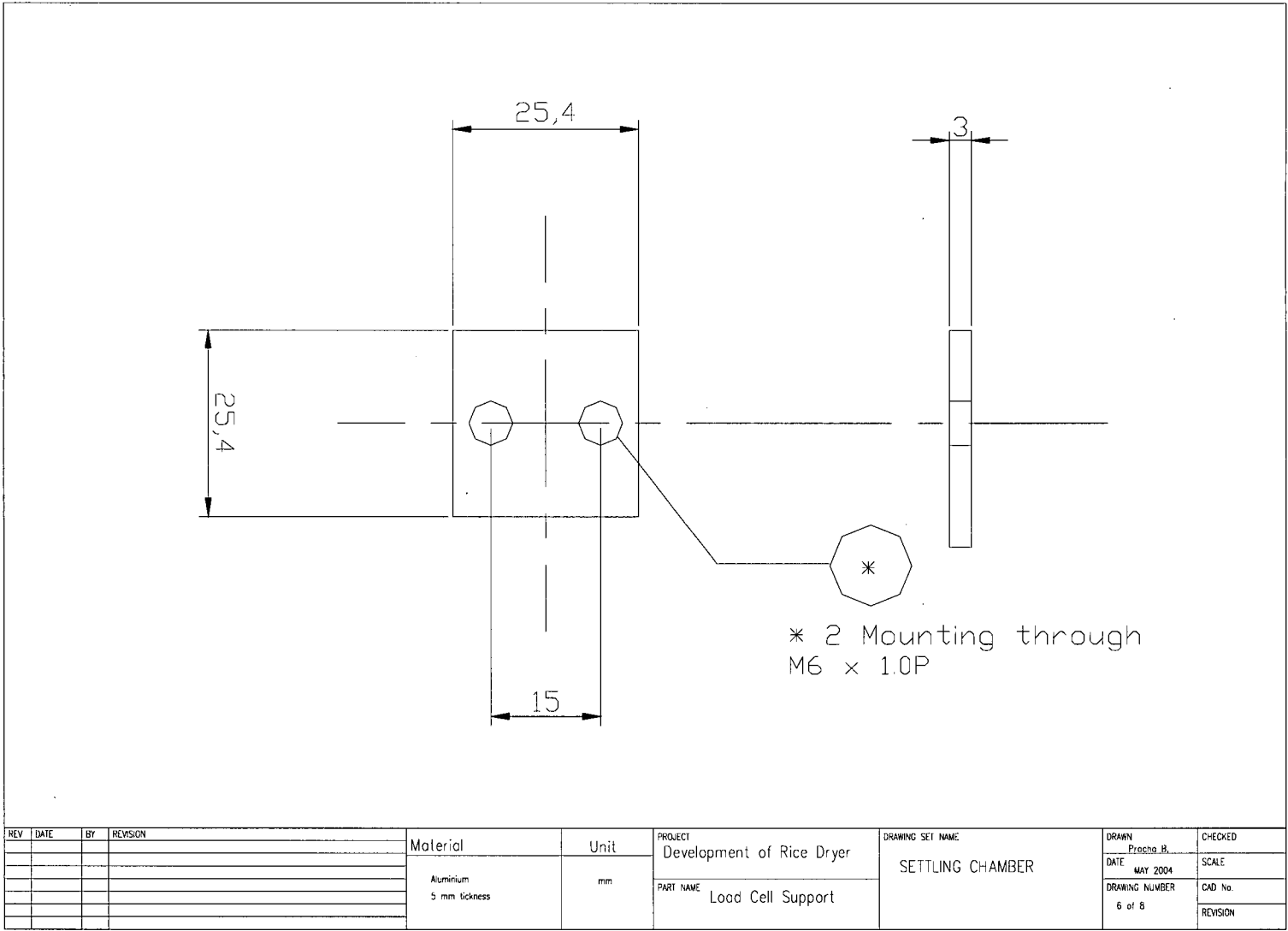


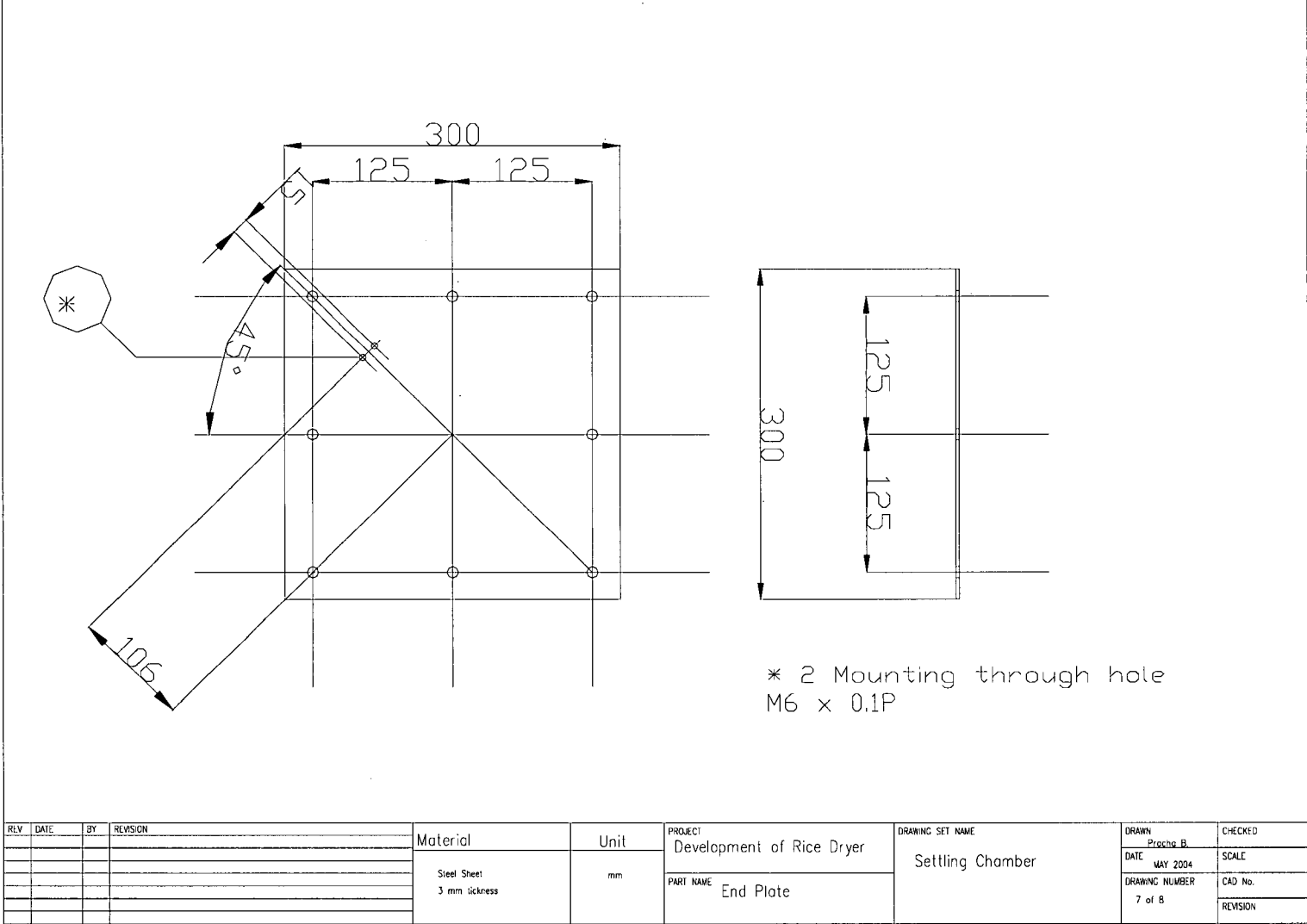


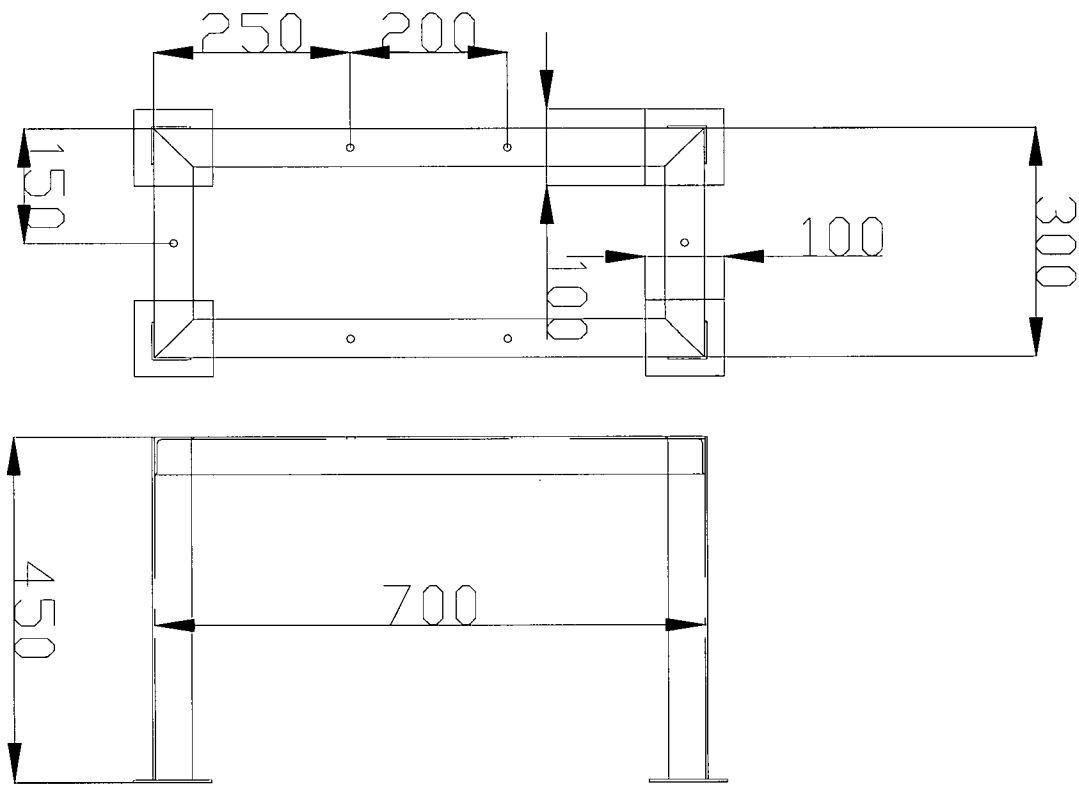












REV	DATE	BY	REVISION	Material	Unit	PROJECT Development of Rice Dryer	DRAWING SET NAME SETTLING CHAMBER	DRAWN Procho B.	CHECKED
				Steel Equal Bar 50AE3	mm	PART NAME Settling Chamber Support 1		DATE MAY 2004	SCALE
								DRAWING NUMBER 1 of 2	CAD No. REVISION

Appendix C.

Calculation of the Required Air Flow and Total Pressure Drop across the Drying System

Appendix C Calculation of the Required Air Flow and Total Pressure Drop Across the Drying System

C.1 Air flow rate of cyclone dryer system

The air flow rate through cyclone dryer system must provide an air velocity greater than the minimum value that will sustain the steady state working of a cyclone dryer. According to the work of Wetchakama (1999), the minimum spouted bed velocity varies between 13 -16 m/s. For 15 cm orifice, the desired air flow was determined by the following relationship, assuming uniform flow in the contracted jet:

$$Q = vA$$

where Q = Volume airflow rate, m^3/s

$$v = \text{Inlet air velocity} = 13 \text{ m/s}$$

$$A = \pi(R_x^2 - R^2) \text{ when } R/R_x = 0.66 \text{ and } R_x = 0.15 \text{ m}$$

Therefore, the desired air flow varies between:

$$Q_{\min} = 13 \pi (1 - 0.66^2) * 0.15^2 / 4 = 0.129 \text{ m}^3/\text{s}$$

$$Q_{\max} = 16 \pi (1 - 0.66^2) * 0.15^2 / 4 = 0.16 \text{ m}^3/\text{s}$$

C.2 System pressure drop

Once the air flow rate is specified, the corresponding pressure losses can be estimated. The system pressure loss is composed of the pressure loss for the individual components, i.e. cyclone dryer chamber, air duct, duct fitting, heater chamber and separation chamber. The layout drawing in Appendix B shows the components installed in the model dryer system. The corresponding pressure loss is being determined by the following procedure:

The calculation of pressure loss is based on the following assumptions:

1. The volume air flow rate: $Q = 0.129\text{-}0.16 \text{ m}^3/\text{s}$
2. Density and viscosity of air at 110°C

$$\rho_f = \text{Air density} = 0.921 \text{ kg/m}^3$$

$$\mu = \text{Air viscosity} = 2.205 \cdot 10^{-5} \text{ kg/ms}$$

3. To calculate friction losses in straight ducts, the Darcy-Weisbach equation is applied:

$$\Delta P = f \left(1000L/D_{eq} \right) \rho_f v^2 / 2 \quad (\text{C-1})$$

where

ΔP = friction loss, Pa

f = friction factor

L = duct length, m

D_{eq} = equivalent diameter, equation (3.14), mm

v = velocity, m/s

ρ_f = density, kg/m³

A simplified formula for calculation of the friction factor f is (ASHRAE 1981):

$$f' = 0.11 \left(\frac{R_\epsilon}{D_{eq}} + \frac{68}{Re} \right)^{0.25} \quad (\text{C-2})$$

where R_ϵ is surface roughness of duct and Re is Reynolds number. If $f \geq 0.018$: $f = f'$, otherwise $f = 0.85f' + 0.0028$ (ASHRAE 1981). Reynolds number Re is calculated by the relationship:

$$Re = \frac{\rho v D_{eq}}{1000\mu} \quad (\text{C-3})$$

4. To calculate dynamic losses that result from disturbances in the flow caused by a fitting, Equation (4.18) is applied:

$$\Delta P = \xi \left(\rho_f v^2 / 2 \right) \quad (\text{C-4})$$

where

ΔP = fitting loss, Pa

ξ = fitting loss coefficient

The following paragraphs expand on the losses of individual components as shown in the layout drawing in Appendix B. The pressure losses can be determined as follows:

(a) Inlet Bellmouth

According to Table F.1 Entry Fitting, Stanford (1988)

$$- r/D = 0.2: \xi_a = 0.03$$

(b) Heater body inlet

See drawing number 1 of 4 heater cases set in Appendix B. Fitting loss coefficient for this diffuser according to Idelchik (1994) diagrams 5-4 and 5-28 is

- Reynolds number = $6 \cdot 10^4$
- Transition angle (α) = 12.2 degree
- Diffuser length (l_d) = 0.75 m
- Area ratio (n_{ar1}) = 4.22
- $\xi_b = 0.433$

(c) Heater bank

Fitting loss coefficient for this diffuser according to Idelchik (1994) diagram 12-30 is

$$- \xi_c = 5.32$$

(d) Heater body outlet

See drawing number 2 of 4 rice feeder set in Appendix B. Fitting loss coefficient for this diffuser according to Idelchik (1994) diagrams 5-4 and 5-28 is

- Reynolds number = $4.7 \cdot 10^4$
- Transition angle (α) = 10.2 degree
- Diffuser length (l_d) = 0.75 m
- Area ratio (n_{ar1}) = 3.1
- $\xi_d = 0.346$

(e) Honey comb (Flow Straightener)

$$- \xi_e = 0.5 \text{ (From manufacturer)}$$

(f) Transition duct from fan to cyclone

See drawing number 1 of 4 rice feeder set in Appendix B. Fitting loss coefficient for this diffuser according to Idelchik (1994) is

- Reynolds number = 4.6×10^4
- Transition angle (α) = 5.45 degree
- Diffuser length (l_d) = 0.4 m
- Area ratio (n_{arl}) = 1.8
- $\xi_f = 0.2$

(g) Cyclone chamber

- $\xi_g = 20$

(h) Separation chamber

- $\xi_h = 1$ (Free flow to atmosphere)

Due to the small duct lengths in the system, the pressure loss in ducts following Equation (C-1) is neglected; The total pressure loss of system according to the sum of items (a) to (f) is shown in equation (C-4),

$$\Delta P = \xi_a \frac{\rho v_a^2}{2} + \xi_b \frac{\rho v_b^2}{2} + \xi_c \frac{\rho v_c^2}{2} + \dots + \xi_h \frac{\rho v_h^2}{2} \quad (C-5)$$

where $v_a = Q / A_a = 4Q / \pi 0.15^2 \quad \text{m/s}^2$

$v_b = Q / A_b = 4Q / \pi 0.15^2 \quad \text{m/s}^2$

$v_c = Q / A_c = Q / 0.075625 \quad \text{m/s}^2$

$v_d = Q / A_d = 4Q / \pi 0.0176^2 \quad \text{m/s}^2$

$v_e = Q / A_e = 4Q / \pi 0.15^2 \quad \text{m/s}^2$

$v_f = Q / A_f = 4Q / \pi 0.15^2 \quad \text{m/s}^2$

$v_g = Q / A_g = Q / 0.01 \quad \text{m/s}^2$

$v_h = Q / A_h = Q / 0.02 \quad \text{m/s}^2$

By substitution of $v_a, v_b \dots v_h$ into Equation 4.19, the system pressure loss curve Equation 4.20 is obtained with varying numbers of chambers.

$$\Delta P = 207739\rho Q^2 \qquad \text{Pa} \qquad \qquad \qquad (C-6)$$

Equation (C-6) gives the total pressure drop across cyclone dryers. Figure C-1 shows typical plots of the system pressure loss and blower characteristic curves for the model dryer system. The operating flow for a particular case is given by the intersection of the corresponding system and blower characteristic curves.

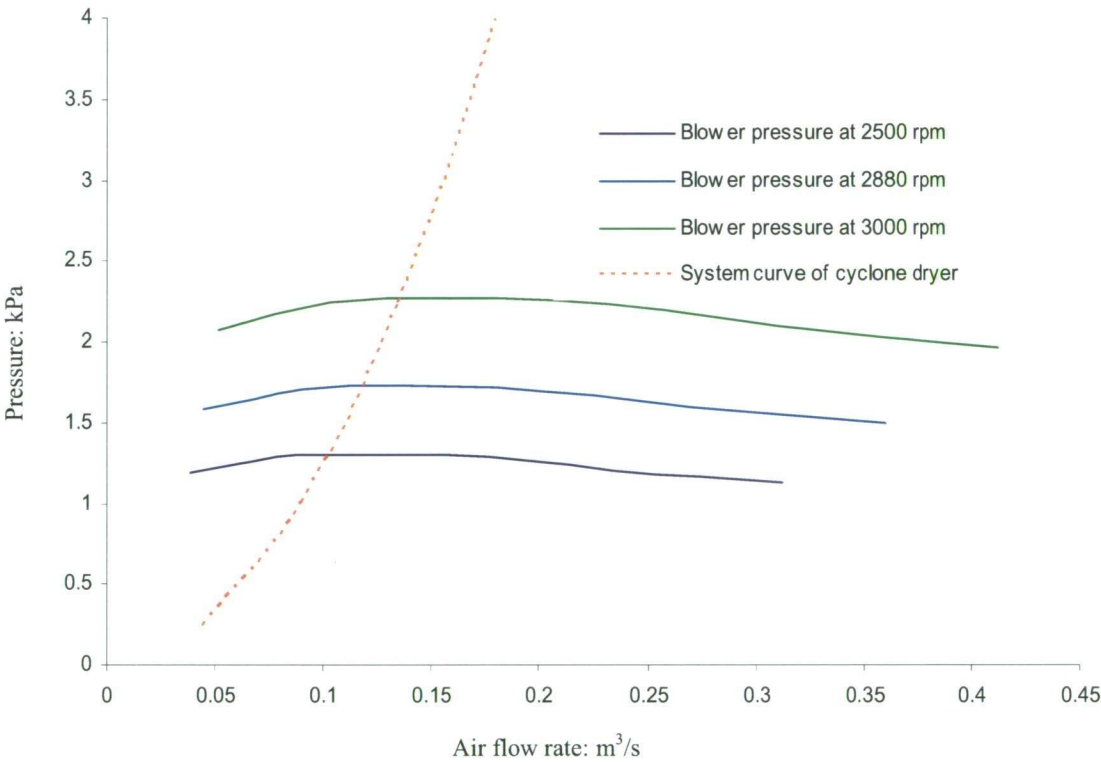


Figure C-1 Operating point at various speeds of the selected blower

The radial bladed centrifugal blower was driven by a 3 kW AC motor equipped with a variable frequency speed controller. The characteristic curves of the blower at 2880 rpm are shown in Figure C-2.

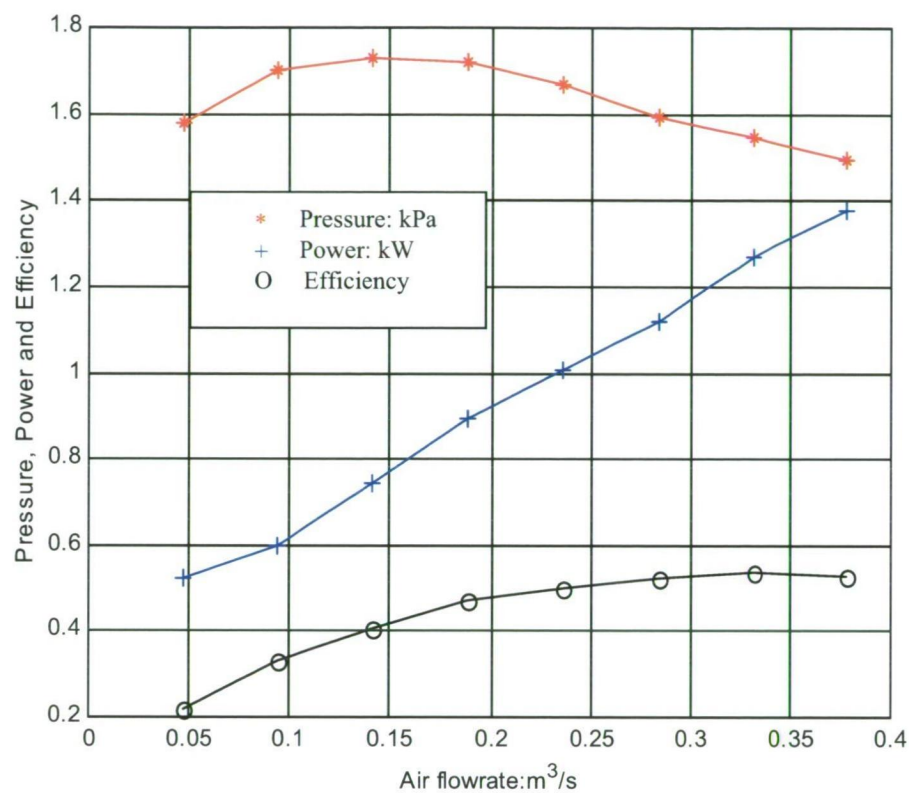


Figure C-2 Characteristic curve of selected blower at 2880 rpm

Appendix D.

Three Hole Probe Calibration

Appendix D. Three Hole Probe Calibrations

D.1 Probe Construction

The three-hole probe is supported by a steel tube of 6.35 mm O.D. The measuring head is a wedge shape with a rounded nose as shown in Figure 5.4. There are three pressure tappings: one is the centre of the nose and one on each side face. Pressures from these tappings are conducted to the measuring device through 0.75 mm O.D. tubes inside the probe support.

This probe can measure flow speed and direction, and total and static pressure. The pressure difference between the top and bottom holes is zero when the probe points directly into the flow. The probe tappings are numbered 1 through 3: nose tapping 1, side tappings 2 and 3.

D.2 Detail of probe calibration

By considering the potential flow around a circular cylinder as an ideal case, three calibration functions f_1 , f_2 and f_3 can be written in forms of the flow angle relative to the probe head (α), the probe geometry, and Reynolds number based on probe diameter ($Re = \rho U d / \mu$).

$$f_1(\alpha, \text{Geometry}, Re) = (P_2 - P_3) / (P_1 - P_3) \quad (D.1)$$

$$f_2(\alpha, \text{Geometry}, Re) = (P_1 - P_3) / (\rho U^2 / 2) \quad (D.2)$$

$$f_3(\alpha, \text{Geometry}, Re) = (P_{\text{tot}} - P_1) / (\rho U^2 / 2) \quad (D.3)$$

where P is the total pressure at the probe and U is the velocity at the probe. For a particular probe the forms of f_1 , f_2 and f_3 can be found at a given Reynolds number by measuring over the range of flow angle. The calibration was carried out by rotating the probe in a closed circuit wind tunnel over the range of 1000-10000 of probe Reynolds number. The three hole probe was mounted in a variable angle support. A Pitot tube placed in the wind tunnel with its static hole at the same axial position as the three hole probe was used as a velocity reference. Pressure differences

between the three probe tapings were obtained with a pressure scanner and Furness FCS421 micromanometer. The scanner channel connections were

Channel 0	Channel1	Channel2	Channel3	Channel4
0	Ptot	P2 (top side)	P1(front side)	Ptot
0	Pstat	P3(bottom side)	P3(bottom side)	P1(front side)

Data from the manometer output signal were acquired by a PC with a National Instruments data acquisition board. Programs were written in National Instruments LabVIEW software (created by Jane Sargison). Pressure signals were typically sampled at 500 Hz for 5-10 seconds, with 2 seconds delay time for steady-state condition to be achieved after switching pressure sources.

D.3 Calibration Results and Data Fitting

The values of f_1 , f_2 and f_3 at different probe Reynolds numbers (Re) are plotted against probe angle (α) in Figures C-1, C-2, C-3. These results show that functions f_1 , f_2 and f_3 vary significantly with Re . This implies that the three functions f_1 , f_2 and f_3 depend on flow velocity.

Least square multiple polynomial regression was used to fit surfaces of f_1 , f_2 and f_3 over ranges of Re and probe angle α , which were considered independent variables. The regression model assumed a fifth order variation with angle α and a third order variation with Reynolds number. This lead to 24 regression coefficients for each of the fractions f_1 , f_2 and f_3 , as indicated in Equations D-4 to D-6.

$$\begin{aligned}
 f_1(\alpha, Re) = & A_{(0,0)} + A_{(0,1)}Re + A_{(0,2)}Re^2 + A_{(0,3)}Re^3 \\
 & A_{(1,0)}\alpha + A_{(1,1)}\alpha Re + A_{(1,2)}\alpha Re^2 + A_{(1,3)}\alpha Re^3 \\
 & A_{(2,0)}\alpha^2 + A_{(2,1)}\alpha^2 Re + A_{(2,2)}\alpha^2 Re^2 + A_{(2,3)}\alpha^2 Re^3 \\
 & A_{(3,0)}\alpha^3 + A_{(3,1)}\alpha^3 Re + A_{(3,2)}\alpha^3 Re^2 + A_{(3,3)}\alpha^3 Re^3 \\
 & A_{(4,0)}\alpha^4 + A_{(4,1)}\alpha^4 Re + A_{(4,2)}\alpha^4 Re^2 + A_{(4,3)}\alpha^4 Re^3 \\
 & A_{(5,0)}\alpha^5 + A_{(5,1)}\alpha^5 Re + A_{(5,2)}\alpha^5 Re^2 + A_{(5,3)}\alpha^5 Re^3
 \end{aligned} \tag{D.4}$$

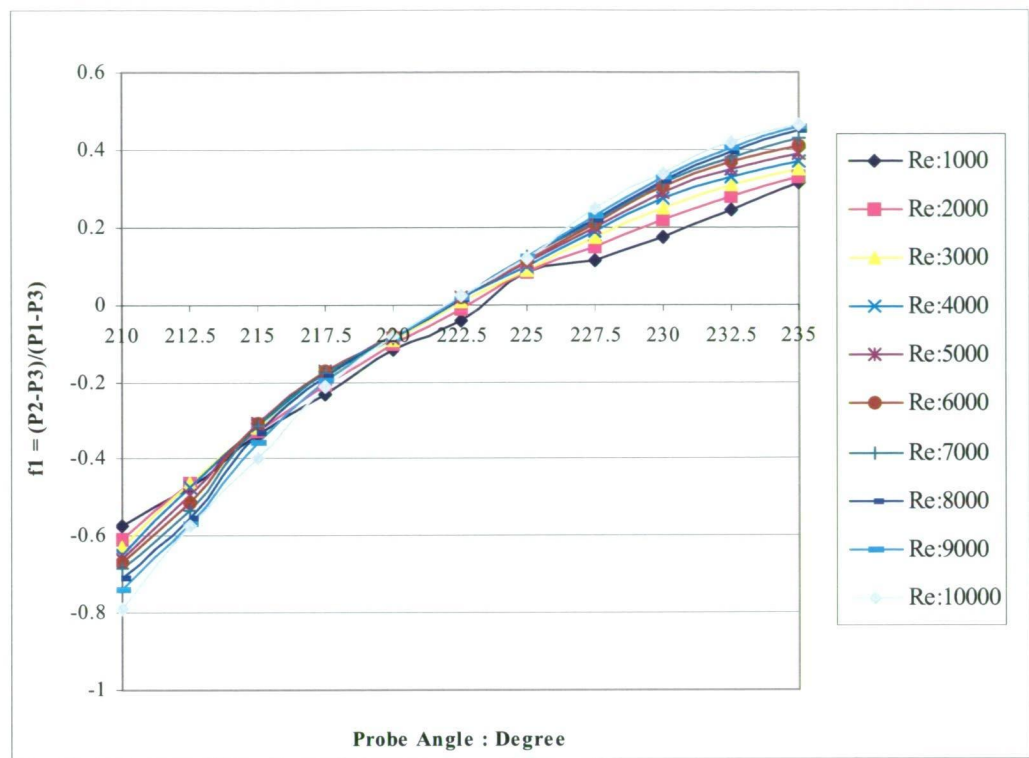


Figure D-1 f1 plotted against probe angle at different Re

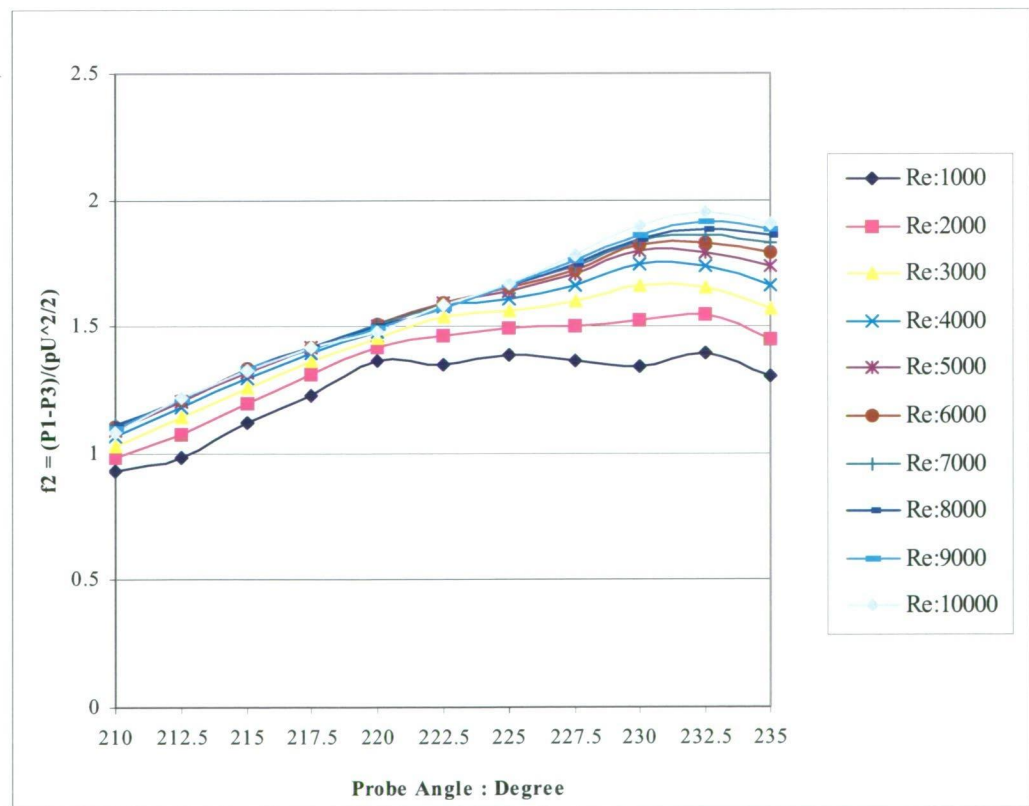


Figure D-2 f2 plotted against probe angle at different Re

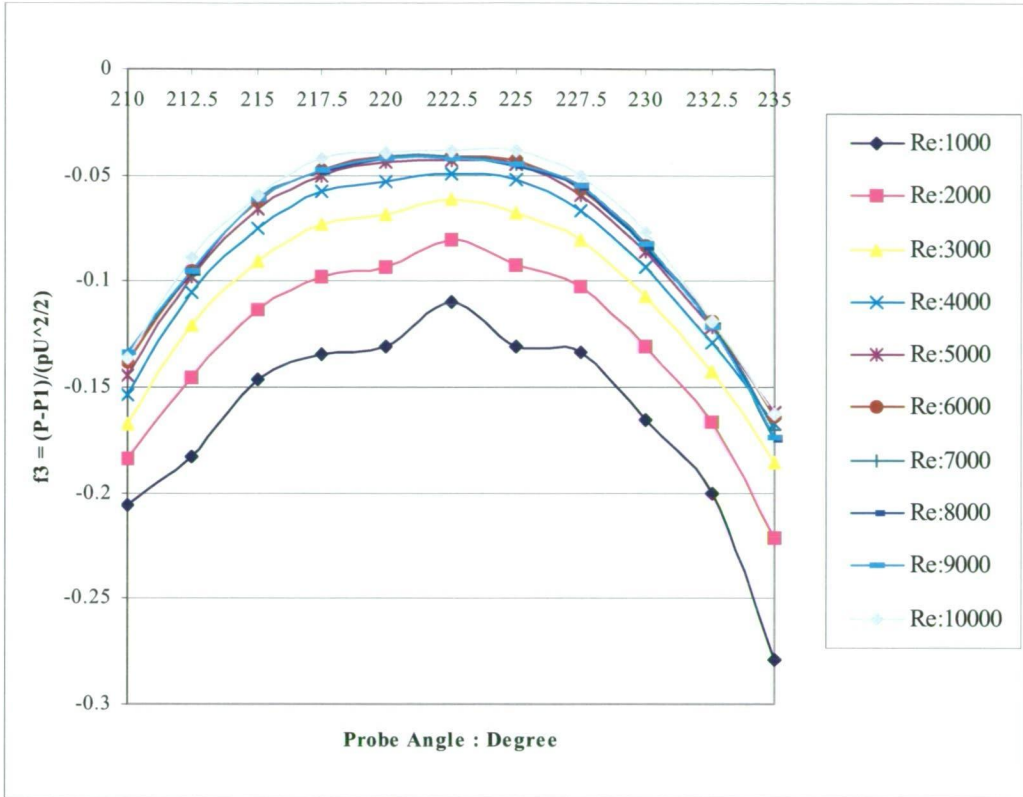


Figure D-3 f_3 plotted against probe angle at different Re

$$\begin{aligned}
 f_2(\alpha, Re) = & B_{(0,0)} + B_{(0,1)}Re + B_{(0,2)}Re^2 + B_{(0,3)}Re^3 \\
 & B_{(1,0)}\alpha + B_{(1,1)}\alpha Re + B_{(1,2)}\alpha Re^2 + B_{(1,3)}\alpha Re^3 \\
 & B_{(2,0)}\alpha^2 + B_{(2,1)}\alpha^2 Re + B_{(2,2)}\alpha^2 Re^2 + B_{(2,3)}\alpha^2 Re^3 \\
 & B_{(3,0)}\alpha^3 + B_{(3,1)}\alpha^3 Re + B_{(3,2)}\alpha^3 Re^2 + B_{(3,3)}\alpha^3 Re^3 \\
 & B_{(4,0)}\alpha^4 + B_{(4,1)}\alpha^4 Re + B_{(4,2)}\alpha^4 Re^2 + B_{(4,3)}\alpha^4 Re^3 \\
 & B_{(5,0)}\alpha^5 + B_{(5,1)}\alpha^5 Re + B_{(5,2)}\alpha^5 Re^2 + B_{(5,3)}\alpha^5 Re^3
 \end{aligned} \tag{D.5}$$

$$\begin{aligned}
 f_3(\alpha, Re) = & C_{(0,0)} + C_{(0,1)}Re + C_{(0,2)}Re^2 + C_{(0,3)}Re^3 \\
 & C_{(1,0)}\alpha + C_{(1,1)}\alpha Re + C_{(1,2)}\alpha Re^2 + C_{(1,3)}\alpha Re^3 \\
 & C_{(2,0)}\alpha^2 + C_{(2,1)}\alpha^2 Re + C_{(2,2)}\alpha^2 Re^2 + C_{(2,3)}\alpha^2 Re^3 \\
 & C_{(3,0)}\alpha^3 + C_{(3,1)}\alpha^3 Re + C_{(3,2)}\alpha^3 Re^2 + C_{(3,3)}\alpha^3 Re^3 \\
 & C_{(4,0)}\alpha^4 + C_{(4,1)}\alpha^4 Re + C_{(4,2)}\alpha^4 Re^2 + C_{(4,3)}\alpha^4 Re^3 \\
 & C_{(5,0)}\alpha^5 + C_{(5,1)}\alpha^5 Re + C_{(5,2)}\alpha^5 Re^2 + C_{(5,3)}\alpha^5 Re^3
 \end{aligned} \tag{D.6}$$

The regression coefficient for the functions f1, f2 and f3 are specified in Tables D-1, D-2 and D-3.

Table D-1 Coefficients of f1(α ,Re)

Coefficient	i = 0	i = 1	i = 2	i = 3
A(0,i)	3.61E+04	-5.87E+01	2.90E-02	-2.11E-06
A(1,i)	-6.99E+02	1.24177526	-6.41E-04	4.67E-08
A(2,i)	5.26095601	-1.05E-02	5.65E-06	-4.15E-10
A(3,i)	-1.90E-02	4.38E-05	-2.49E-08	1.84E-12
A(4,i)	3.24E-05	-9.13E-08	5.48E-11	-4.08E-15
A(5,i)	-1.98E-08	7.56E-11	-4.82E-14	3.61E-18

Table D-2 Coefficients of f2(α ,Re)

Coefficient	i = 0	i = 1	i = 2	i = 3
B(0,i)	1.12E+06	-3.67E+02	5.33E-02	-2.56E-06
B(1,i)	-2.52E+04	8.15E+00	-1.18E-03	5.66E-08
B(2,i)	2.25E+02	-7.24E-02	1.05E-05	-5.00E-10
B(3,i)	-1.00E+00	3.21E-04	-4.64E-08	2.21E-12
B(4,i)	2.24E-03	-7.11E-07	1.03E-10	-4.88E-15
B(5,i)	-2.00E-06	6.30E-10	-9.07E-14	4.30E-18

Table D-3 Coefficients of f3(α ,Re)

Coefficient	i = 0	i = 1	i = 2	i = 3
C(0,i)	2.42E+05	-1.96E+02	3.79E-02	-2.15E-06
C(1,i)	-5.45E+03	4.42E+00	-8.53E-04	4.84E-08
C(2,i)	4.92E+01	-3.98E-02	7.69E-06	-4.36E-10
C(3,i)	-2.22E-01	1.79E-04	-3.46E-08	1.96E-12
C(4,i)	5.01E-04	-4.04E-07	7.79E-11	-4.42E-15
C(5,i)	-4.52E-07	3.63E-10	-7.01E-14	3.97E-18

From (D.1) and (D.2) when the probe Reynolds number is defined as

$$Re = \rho U d / \mu \tag{D.7}$$

we have

$$C2 = f2 Re^2 = 2(p1-p3) \rho d^2 / \mu^2 \tag{D.8}$$

and

$$f2 = C2 / Re^2 \tag{D.9}$$

Substituting (D.7) into (D.5) gives

$$\begin{aligned}
C2 = & B_{(0,0)} Re^2 + B_{(0,1)} Re^3 + B_{(0,2)} Re^4 + B_{(0,3)} Re^5 \\
& B_{(1,0)} \alpha Re^2 + B_{(1,1)} \alpha Re^3 + B_{(1,2)} \alpha Re^4 + B_{(1,3)} \alpha Re^5 \\
& B_{(2,0)} \alpha^2 Re^2 + B_{(2,1)} \alpha^2 Re^3 + B_{(2,2)} \alpha^2 Re^4 + \\
& B_{(2,3)} \alpha^2 Re^5 + B_{(3,0)} \alpha^3 Re^2 + B_{(3,1)} \alpha^3 Re^3 + \\
& B_{(3,2)} \alpha^3 Re^4 + B_{(3,3)} \alpha^3 Re^5 + B_{(4,0)} \alpha^4 Re^2 + \\
& B_{(4,1)} \alpha^4 Re^3 + B_{(4,2)} \alpha^4 Re^4 + B_{(4,3)} \alpha^4 Re^5 + \\
& B_{(5,0)} \alpha^5 Re^2 + B_{(5,1)} \alpha^5 Re^3 + B_{(5,2)} \alpha^5 Re^4 + \\
& B_{(5,3)} \alpha^5 Re^5
\end{aligned} \tag{D.10}$$

where B are numbers taken from Table D-2. With the known values of f1 and C2, Equations (D.4) and (D.10) can be now solved for the probe angle and probe Reynolds number. Velocity is calculated from the probe Reynolds number by using equation (D.7). The Newton-Raphson Iteration method for the system of non-linear equations was employed for this solution. An application program (program UCpct.m) written in was used to desire the flow angle and velocity from the probe measurements.

D.4 Error of fitted surface

In order to assess the error in the calibration process, the probe Reynolds number and probe angle were substituted into (D.4), (D.5) and (D.6) to obtain f1, f2 and f3 at various positions over the calibration range. The difference between the calculated values and real measured data for f1, f2 and f3 is show in Figures D-4, D-5 and D-6, respectively.

The f1 and f2 values of probe angle and Reynolds number calibration range were substituted into Equations (D.7) and (D.10) to obtain the calculated probe angle and air velocity. The errors of probe angle (difference between calculated angle and real angle at the same f1 and f2) and air velocity are shown in Figures D-7 and D-8.

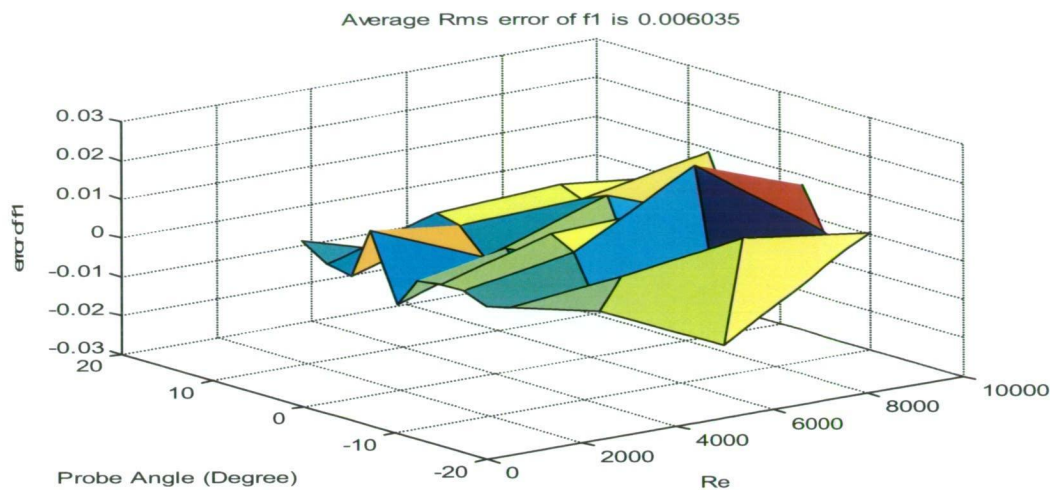


Figure D-4 Error of f1

Average Rms error of f2 is 0.0062111

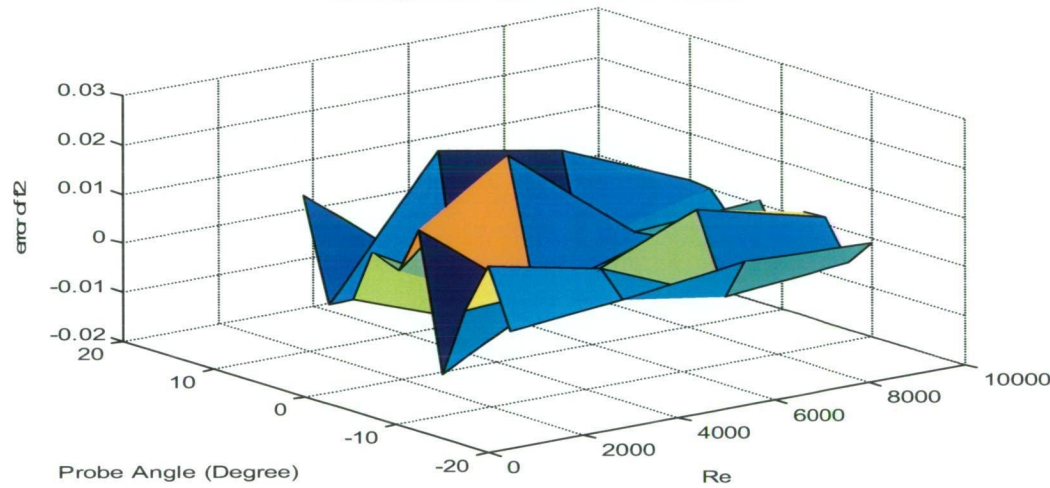


Figure D-5 Error of f2

Average Rms error of f3 is 0.0017526

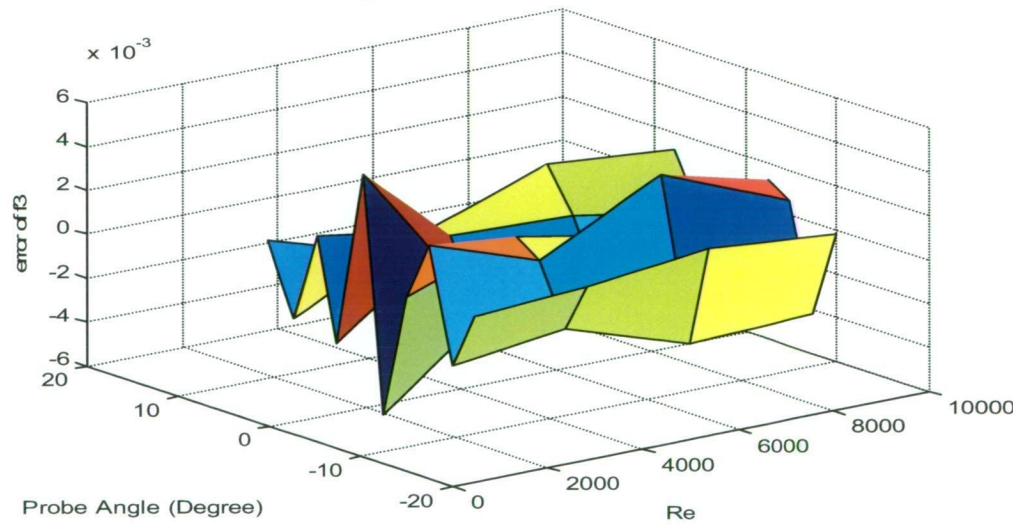


Figure D-6 Error of f3

Average Rms error of Angle is 0.13974°

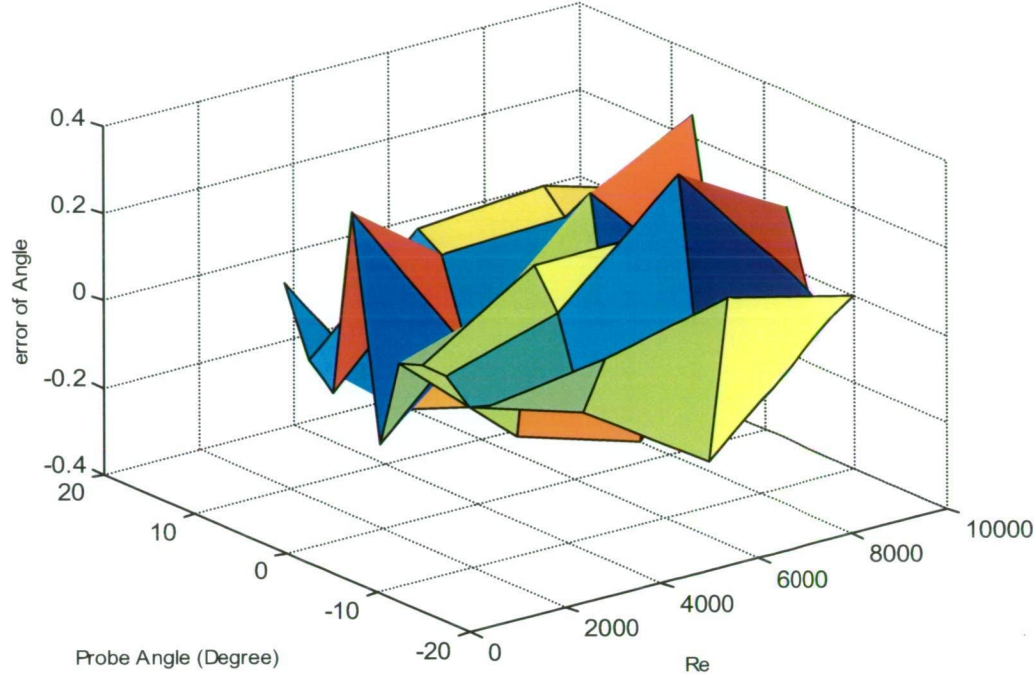


Figure D-7 Error of Calibration Angle

Average Rms error of Air Velocity is 0.02234 ms^{-1}

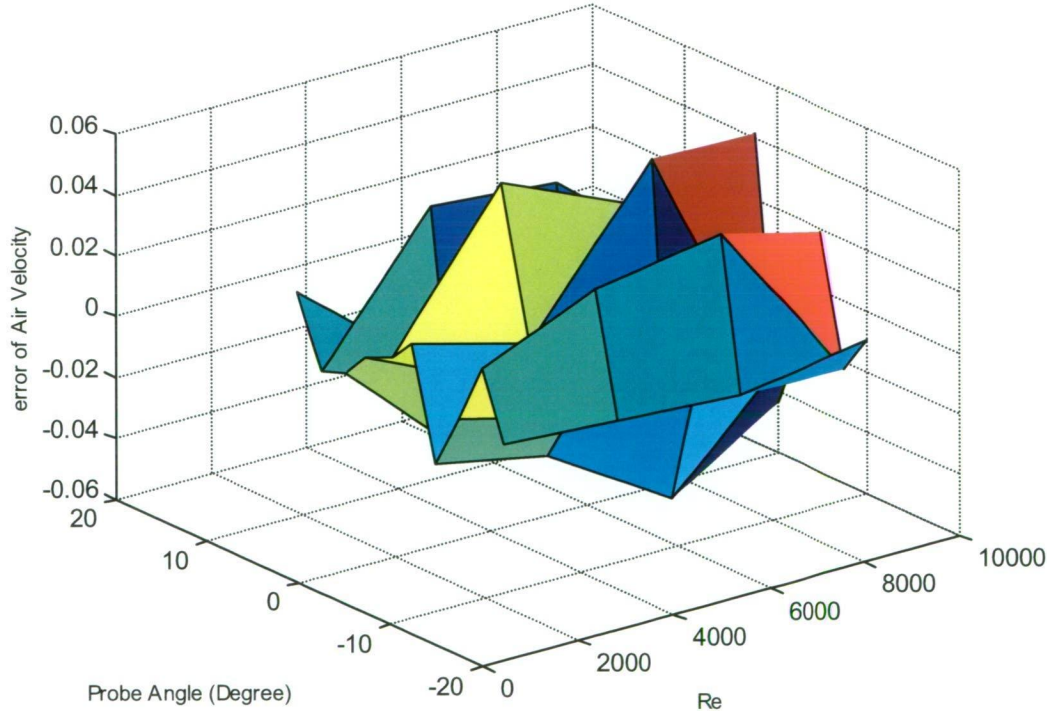


Figure D-8 Error of Air Velocity

Appendix E.

Experimental Results of Paddy Grain and Silica Gel Particle

Drying and

Initial Conditions for Cyclone Dryer Simulations

Table E.1 Experimental results of paddy drying in three-chamber cyclone dryer

TEST	F_a kg/s	T_{in} °C	T_{out} °C	M_i kg/kg	M_a Kg/kg	T_a °C	T_{in} °C	W_i kg/kg	W_a kg/kg	F_a kg/s	MR % db.	Nu	Sh	SPEC MJ/ kg Water
1	0.0298	22.00	43.69	0.32822	0.30122	63.39	46.01	0.00758	0.01182	0.2027	2.40	0.22583	0.00566	10.75
2	0.0298	22.40	52.21	0.32192	0.29253	75.27	54.24	0.00757	0.01219	0.1925	2.94	0.21072	0.00597	12.39
3	0.0298	22.60	57.72	0.32299	0.28489	57.44	60.48	0.00773	0.01341	0.1868	3.81	0.18256	0.00772	11.28
4	0.0298	24.00	48.02	0.34006	0.31430	62.57	49.74	0.00670	0.01041	0.2162	2.58	0.21582	0.00551	11.86
5	0.0298	24.40	53.99	0.34028	0.30691	75.10	55.75	0.00684	0.01131	0.2060	3.34	0.21723	0.00601	11.29
6	0.0298	24.60	60.28	0.34110	0.29826	57.26	62.71	0.00693	0.01279	0.1989	4.28	0.18419	0.00774	10.38
7	0.0298	21.00	46.25	0.41572	0.37662	59.64	47.36	0.00743	0.01229	0.2325	3.91	0.25548	0.00722	8.40
8	0.0298	21.60	54.03	0.41781	0.36927	70.78	55.12	0.00768	0.01461	0.2239	4.85	0.23103	0.01009	8.22
9	0.0298	21.70	62.28	0.42197	0.35572	82.32	63.99	0.00777	0.01602	0.2176	6.63	0.17645	0.01186	7.14
10	0.0411	23.70	40.70	0.35700	0.33555	61.13	44.72	0.00969	0.01368	0.2262	2.15	0.18988	0.00467	10.41
11	0.0411	23.00	46.88	0.35692	0.32818	74.40	52.06	0.00919	0.01479	0.2094	2.87	0.14874	0.00612	9.71
12	0.0411	23.40	47.67	0.35828	0.32615	58.55	57.80	0.00945	0.01595	0.2079	3.21	0.11271	0.00706	10.34
13	0.0411	20.60	38.94	0.36111	0.33547	60.42	45.13	0.00547	0.00979	0.2223	2.56	0.14154	0.00502	9.13
14	0.0411	20.70	45.98	0.35289	0.32202	72.17	53.42	0.00548	0.01111	0.2328	3.09	0.12370	0.00678	10.09
15	0.0411	20.00	50.16	0.36082	0.32598	80.95	58.55	0.00594	0.01238	0.2245	3.54	0.11065	0.00756	9.97
16	0.0411	21.00	42.01	0.31494	0.30574	57.34	44.82	0.00632	0.00791	0.2401	0.92	0.18141	0.00194	22.80
17	0.0411	20.80	43.45	0.36007	0.33514	70.99	50.30	0.00629	0.01073	0.2260	2.49	0.14203	0.00523	11.94
18	0.0411	20.80	47.79	0.31518	0.29176	82.46	57.04	0.00630	0.01107	0.2146	2.34	0.11332	0.00534	14.67
19	0.0611	21.50	38.69	0.42576	0.39759	61.41	40.58	0.00735	0.01590	0.2059	2.82	0.12371	0.00433	4.41
20	0.0611	21.50	41.04	0.42859	0.39470	75.53	44.73	0.00728	0.01671	0.2174	3.39	0.11416	0.00547	5.06
21	0.0611	21.60	43.05	0.42369	0.38814	86.07	49.90	0.00727	0.01829	0.1916	3.55	0.06194	0.00455	6.01
22	0.0611	20.20	38.17	0.38578	0.36112	58.01	42.86	0.00918	0.01514	0.2422	2.47	0.11271	0.00495	6.27
23	0.0611	20.20	43.19	0.39075	0.36623	70.48	48.04	0.00936	0.01400	0.2175	2.45	0.08978	0.00502	7.82
24	0.0611	20.40	43.92	0.38835	0.36192	78.32	50.27	0.00978	0.01656	0.2222	2.64	0.08909	0.00463	8.47
25	0.0611	20.20	38.28	0.38683	0.36129	59.58	41.25	0.00623	0.01307	0.2302	2.55	0.13391	0.00509	6.36
26	0.0611	22.60	41.37	0.38361	0.36260	67.31	45.45	0.00907	0.01390	0.2469	2.10	0.13686	0.00356	9.32
27	0.0611	20.40	45.36	0.38344	0.35117	80.74	52.21	0.00557	0.01433	0.2406	3.23	0.09798	0.00691	7.84

Table E.2 Experimental results of paddy drying in four-chamber cyclone dryer

<i>TEST</i>	<i>F_a</i> kg/s	<i>T_{ai}</i> °C	<i>T_{ao}</i> °C	<i>M_i</i> kg/kg	<i>M_a</i> Kg/kg	<i>T_a</i> °C	<i>T_{ro}</i> °C	<i>W_i</i> kg/kg	<i>W_a</i> kg/kg	<i>F_a</i> kg/s	<i>MR</i> % db.	<i>Nu</i>	<i>Sh</i>	<i>SPEC</i> MJ/ kg Water
1	0.0298	23.60	45.41	0.32870	0.29925	63.30	49.34	0.00516	0.00912	0.2090	2.95	0.14254	0.00440	9.40
2	0.0298	23.40	50.04	0.32259	0.28929	75.67	56.99	0.00510	0.01018	0.2038	3.33	0.10916	0.00556	9.89
3	0.0298	23.40	63.67	0.32817	0.29402	84.67	65.07	0.00514	0.01195	0.2052	4.42	0.14646	0.00749	11.27
4	0.0298	24.10	50.75	0.27194	0.24149	64.54	52.21	0.00726	0.01149	0.2112	3.04	0.16107	0.00461	12.16
5	0.0298	24.40	53.70	0.26471	0.23368	76.73	60.59	0.00730	0.01188	0.2020	3.10	0.09101	0.00486	11.74
6	0.0298	24.60	65.52	0.26524	0.22881	88.99	68.09	0.00755	0.01325	0.1944	3.64	0.11708	0.00593	11.06
7	0.0298	24.80	49.20	0.20908	0.19366	63.50	51.31	0.01038	0.01246	0.2212	1.54	0.15152	0.00227	20.50
8	0.0298	25.00	59.12	0.21043	0.19129	76.67	61.05	0.01033	0.01282	0.2111	1.91	0.13144	0.00264	20.64
9	0.0298	25.50	63.51	0.20729	0.18124	88.49	66.03	0.01059	0.01438	0.2060	2.60	0.13081	0.00396	21.71
10	0.0411	23.00	43.35	0.30565	0.28615	60.50	46.78	0.00868	0.01212	0.2129	1.95	0.13483	0.00322	10.81
11	0.0411	23.20	51.18	0.29547	0.27043	71.15	52.57	0.00853	0.01380	0.2112	2.50	0.16678	0.00490	10.52
12	0.0411	23.40	49.47	0.32307	0.28917	83.25	58.12	0.00808	0.01509	0.2053	3.39	0.09636	0.00646	9.34
13	-	-	-	-	-	-	-	-	-	-	-	-	-	-
14	0.0411	24.20	53.21	0.31571	0.30402	74.51	54.94	0.01066	0.01301	0.2033	1.17	0.15257	0.00215	3.66
15	0.0411	23.80	55.25	0.38807	0.33095	86.29	59.62	0.01068	0.02135	0.2148	5.71	0.12615	0.01032	6.07
16	0.0411	23.80	44.60	0.35109	0.32526	60.78	45.72	0.01130	0.01573	0.2297	2.58	0.21791	0.00439	8.82
17	0.0411	23.80	51.64	0.35321	0.31919	74.10	53.67	0.01125	0.01784	0.2164	3.40	0.16152	0.00633	9.61
18	0.0411	23.90	57.22	0.35125	0.31406	84.42	60.85	0.01136	0.01936	0.2117	3.72	0.12063	0.00758	8.96
19	0.0611	22.20	39.02	0.26519	0.25064	61.02	41.96	0.00663	0.01096	0.2097	1.46	0.13567	0.00291	11.22
20	0.0611	22.20	44.59	0.26044	0.24492	76.79	49.03	0.00657	0.01174	0.1922	1.55	0.09877	0.00310	9.80
21	0.0611	22.60	50.41	0.26687	0.24455	87.13	58.42	0.00666	0.01343	0.1843	2.23	0.06249	0.00380	8.20
22	0.0611	22.30	39.97	0.26581	0.25741	59.26	43.33	0.00812	0.01025	0.2258	0.84	0.12545	0.00155	17.79
23	0.0611	22.00	46.04	0.26709	0.25472	72.29	49.56	0.00794	0.01213	0.1983	1.24	0.10184	0.00263	14.19
24	0.0611	22.30	50.97	0.26766	0.24682	87.47	55.25	0.00817	0.01554	0.1903	2.08	0.08925	0.00436	10.34
25	0.0611	24.20	38.79	0.37727	0.35856	60.42	41.48	0.01013	0.01496	0.2339	1.87	0.16588	0.00363	8.17
26	0.0611	23.90	42.03	0.38506	0.36244	71.58	45.75	0.00998	0.01472	0.2203	2.26	0.13393	0.00133	8.23
27	0.0611	23.80	47.39	0.37284	0.34805	85.51	52.34	0.00993	0.01677	0.2151	2.48	0.10802	0.00465	8.49

Table E.3 Experimental results of silica gel drying in three-chamber cyclone dryer

TEST	F_a kg/s	T_{a1} °C	T_{a2} °C	M_i kg/kg	M_a kg/kg	T_{a3} °C	T_{a4} °C	W_i kg/kg	W_a kg/kg	F_a kg/s	MR % db.	Nu	Sh	SPEC MJ/kg Water
1	0.0585	21.50	44.18	0.25688	0.23564	63.78	44.40	0.01132	0.01727	0.2000	2.12	0.21626	0.003*1	6.39
2	0.0585	19.40	44.73	0.25203	0.22426	73.25	45.17	0.00838	0.01642	0.1789	2.60	0.15570	0.00457	6.17
3	0.0585	21.10	51.56	0.25530	0.21138	84.60	52.74	0.01122	0.02503	0.1940	4.39	0.13016	0.00837	5.07
4	0.0585	19.70	38.61	0.26565	0.24023	57.80	40.54	0.00659	0.01267	0.2434	2.54	0.18604	0.00577	6.80
5	0.0585	20.00	44.15	0.25836	0.23112	69.83	46.26	0.00648	0.01300	0.2429	2.72	0.17025	0.00605	7.10
6	0.0585	19.20	44.30	0.25927	0.22970	76.11	47.30	0.00622	0.01360	0.2473	2.96	0.16124	0.00699	7.45
7	0.0585	21.40	39.46	0.26133	0.23260	58.62	40.94	0.00707	0.01339	0.2484	2.87	0.21135	0.00552	6.05
8	0.0585	21.00	44.26	0.25885	0.22464	70.47	46.30	0.00684	0.01500	0.2504	3.42	0.18231	0.00738	5.92
9	0.0585	24.00	49.27	0.25251	0.20889	81.63	51.52	0.01088	0.02163	0.2265	4.36	0.15228	0.00707	5.48
10	0.0433	21.80	40.07	0.21731	0.19844	61.24	42.47	0.00604	0.00985	0.2134	1.89	0.20810	0.00374	11.15
11	0.0433	21.20	43.68	0.24070	0.20616	72.02	47.30	0.06632	0.01428	0.2032	3.45	0.16725	0.00782	7.37
12	0.0433	22.00	48.12	0.23265	0.18920	85.67	53.22	0.00604	0.01521	0.1912	4.35	0.13475	0.00806	6.84
13	0.0433	19.80	38.98	0.25341	0.23196	58.19	39.59	0.00600	0.00998	0.2299	2.15	0.33476	0.00475	10.35
14	0.0433	20.20	43.74	0.25493	0.21688	68.28	44.85	0.00622	0.01333	0.2186	3.81	0.25513	0.00796	6.86
15	0.0433	20.60	46.64	0.24946	0.21087	80.13	49.20	0.00628	0.01406	0.2105	3.86	0.19269	0.00821	9.00
16	0.0433	23.40	38.50	0.24129	0.22122	60.10	39.93	0.00779	0.01152	0.2411	2.01	0.30500	0.00364	12.65
17	0.0433	21.20	42.42	0.24598	0.22040	68.95	43.66	0.00706	0.01141	0.2528	2.56	0.29257	0.00505	11.76
18	0.0433	21.20	46.54	0.24834	0.21281	79.40	50.27	0.00704	0.01324	0.2524	3.55	0.19136	0.00720	10.19
19	0.0256	22.00	42.65	0.26918	0.21027	58.38	42.85	0.00715	0.01379	0.2272	5.89	0.49917	0.00935	5.96
20	0.0256	21.40	46.48	0.25633	0.19757	70.23	48.96	0.00693	0.01360	0.2187	5.88	0.24909	0.00652	7.00
21	0.0256	21.80	52.59	0.26067	0.18174	84.13	56.15	0.00722	0.01591	0.2187	7.89	0.20962	0.01211	7.13
22	0.0256	23.80	45.92	0.24848	0.20571	59.96	46.60	0.01056	0.01525	0.2372	4.28	0.33278	0.00599	8.59
23	0.0256	21.60	47.68	0.25016	0.18234	67.89	50.00	0.00728	0.01481	0.2365	6.78	0.23937	0.01108	6.79
24	0.0256	21.50	53.37	0.24860	0.16915	79.90	56.80	0.00714	0.01638	0.2272	7.95	0.19563	0.01335	6.94
25	0.0256	19.70	45.68	0.23087	0.15647	57.43	46.01	0.00773	0.01190	0.2519	4.44	0.39829	0.00713	9.18
26	0.0256	21.60	51.34	0.22934	0.17307	68.94	52.68	0.00854	0.01439	0.2387	5.63	0.24389	0.00857	8.49
27	0.0256	20.80	58.81	0.23234	0.15881	81.19	60.80	0.00783	0.01600	0.2338	7.35	0.19489	0.01248	8.01

Table E.4 Experimental results of silica gel drying in four-chamber cyclone dryer

<i>TEST</i>	<i>F_a</i> kg/s	<i>T_{ai}</i> ° C	<i>T_{ao}</i> ° C	<i>M_i</i> kg/kg	<i>M_a</i> Kg/kg	<i>T_a</i> ° C	<i>T_{co}</i> ° C	<i>W_i</i> kg/kg	<i>W_a</i> kg/kg	<i>F_a</i> kg/s	<i>MR</i> % db.	<i>Nu</i>	<i>Sh</i>	<i>SPEC</i> MJ/ kg Water
1	0.0585	22.00	40.62	0.24865	0.22191	60.02	41.18	0.00683	0.01395	0.2376	2.67	0.26061	0.00543	6.25
2	0.0585	22.00	44.51	0.24926	0.21169	72.24	46.36	0.00671	0.01887	0.1949	3.76	0.13144	0.00692	4.77
3	0.0585	22.20	50.30	0.24963	0.020103	90.79	52.22	0.00675	0.02180	0.1999	4.86	0.12969	0.00899	5.08
4	0.0585	23.60	40.50	0.21481	0.21274	62.08	41.51	0.00825	0.01550	0.2414	2.91	0.24320	0.00533	5.95
5	0.0585	24.00	43.85	0.23868	0.20749	72.98	46.27	0.00801	0.01624	0.2275	3.12	0.16656	0.00546	6.56
6	0.0585	24.10	48.82	0.23292	0.19614	85.74	51.30	0.00802	0.01788	0.2171	3.68	0.14478	0.00700	6.61
7	0.0585	21.80	39.52	0.23753	0.21700	58.56	41.05	0.00742	0.01241	0.2378	2.05	0.19943	0.00403	8.03
8	0.0585	22.40	44.04	0.23782	0.20920	69.28	46.37	0.00770	0.01425	0.2427	2.86	0.17019	0.00545	6.33
9	0.0585	22.60	47.85	0.24702	0.21271	83.86	49.93	0.00792	0.01759	0.2061	3.43	0.13965	0.00597	5.82
10	0.0433	22.00	41.91	0.23330	0.20907	58.73	43.19	0.00816	0.01303	0.2201	2.42	0.23151	0.00486	5.19
11	0.0433	24.80	47.57	0.23932	0.20173	75.41	51.70	0.01142	0.01856	0.2150	3.79	0.15669	0.00586	7.14
12	0.0433	24.80	54.91	0.27058	0.21975	90.58	56.38	0.01144	0.02344	0.1794	5.08	0.17239	0.00818	5.04
13	0.0433	22.90	44.00	0.25505	0.22277	69.78	44.56	0.01086	0.01687	0.2270	3.23	0.28027	0.00583	6.56
14	0.0433	23.50	49.00	0.26012	0.21123	70.27	50.58	0.01108	0.02050	0.2248	4.89	0.20107	0.00874	4.76
15	0.0433	24.00	54.82	0.25632	0.19810	81.03	56.06	0.01163	0.02277	0.2246	5.82	0.20238	0.00999	4.96
16	0.0433	21.60	42.71	0.26402	0.23005	59.32	43.03	0.01037	0.01632	0.2380	3.40	0.34616	0.00650	6.71
17	0.0433	22.20	46.46	0.25926	0.22398	68.97	47.66	0.01074	0.01717	0.2348	3.53	0.24474	0.00669	7.79
18	0.0433	21.60	48.79	0.25923	0.22133	80.44	51.50	0.01064	0.01788	0.2100	3.79	0.17956	0.00717	8.07
19	0.0256	23.70	47.23	0.18825	0.15249	61.26	48.32	0.01035	0.01448	0.2134	3.60	0.25248	0.00490	8.90
20	0.0256	23.80	54.27	0.17632	0.14174	71.08	55.47	0.01019	0.01423	0.2128	3.46	0.21582	0.00473	10.44
21	0.0256	23.60	53.79	0.24624	0.15893	80.31	46.71	0.01020	0.01978	0.2152	8.73	0.20713	0.01174	5.80
22	0.0256	21.90	46.84	0.18147	0.15347	59.82	47.61	0.00699	0.01019	0.2288	2.80	0.27203	0.00441	10.73
23	0.0256	22.00	50.65	0.18649	0.14448	68.86	52.15	0.007111	0.01210	0.2240	4.20	0.23305	0.00677	9.05
24	0.0256	22.20	55.63	0.18682	0.13113	81.50	59.92	0.00656	0.01379	0.2119	5.57	0.15592	0.00975	9.39
25	0.0256	21.60	46.25	0.19768	0.15263	57.79	46.83	0.00817	0.01280	0.2422	4.51	0.29078	0.00676	7.85
26	0.0256	22.00	50.67	0.20081	0.14399	66.41	51.87	0.00835	0.01472	0.2383	5.68	0.24129	0.00899	7.91
27	0.0256	21.60	57.05	0.19531	0.13720	79.59	59.21	0.00821	0.01517	0.2282	6.26	0.19497	0.00982	8.84

Table E.5 Summary of simulation cases for silica gel drying in three chamber cyclone dryer

<i>TEST</i>	<i>F_{in}</i> kg/s	<i>T_{in}</i> ° C	<i>M_i</i> kg/kg	<i>F_{out}</i> kg/s	<i>T_{out}</i> ° C	<i>W_i</i> kg/kg	<i>Remark</i>
4	0.0585	19.70	0.26565	0.2434	57.80	0.00659	From E.3
25	0.0256	19.70	0.23087	0.2519	57.43	0.00773	From E.3
26	0.0256	21.60	0.22934	0.2387	68.94	0.00854	From E.3
27	0.0256	20.80	0.23234	0.2338	81.19	0.00783	From E.3
1	-	-	-	0.2519	57.43	0.00773	Compare to Test 25 of E.3
2	0.0433	19.70	0.23087	0.2519	57.43	0.00773	Compare to Test 25 of E.3
3	0.0585	19.70	0.23087	0.2519	57.43	0.00773	Compare to Test 25 of E.3
5	0.0256	19.70	0.23087	0.2519	68.94	0.00773	Compare to Test 25 of E.3
6	0.0256	19.70	0.23087	0.2519	81.19	0.00773	Compare to Test 25 of E.3
8	0.0256	19.70	0.20988	0.2519	57.43	0.00773	Compare to Test 25 of E.3
9	0.0256	19.70	0.40000	0.2519	57.43	0.00773	Compare to Test 25 of E.3

Table E.6 Summary of simulation cases for silica gel drying in three chamber cyclone dryer

<i>TEST</i>	<i>F_a</i> kg/s	<i>T_{in}</i> ° C	<i>M_i</i> kg/kg	<i>F_a</i> kg/s	<i>T_{in}</i> ° C	<i>W_i</i> kg/kg	<i>Remark</i>
10	0.0433	22.00	0.23330	0.2201	58.73	0.00816	From E.4
22	0.0256	21.90	0.18147	0.2288	59.82	0.00699	From E.4
23	0.0256	22.00	0.18649	0.2240	68.86	0.00711	From E.4
24	0.0256	22.20	0.18682	0.2119	81.50	0.00656	From E.4
11	-	-	-	0.2288	59.82	0.00699	Compare to Test 25 of E.4
12	0.0433	21.90	0.18147	0.2288	59.82	0.00699	Compare to Test 25 of E.4
14	0.0585	21.90	0.18147	0.2288	59.82	0.00699	Compare to Test 25 of E.4
15	0.0256	21.90	0.18147	0.2288	68.86	0.00699	Compare to Test 25 of E.4
16	0.0256	21.90	0.18147	0.2288	81.50	0.00699	Compare to Test 25 of E.4
17	0.0256	21.90	0.23330	0.2288	59.82	0.00699	Compare to Test 25 of E.4
18	0.0256	21.90	0.40000	0.2288	59.82	0.00699	Compare to Test 25 of E.4